UNIVERSITY OF Southampton

University of Southampton Research Repository
ePrints Soton

Copyright © and Moral Rights for this thesis are retained by the author and/or other copyright owners. A copy can be downloaded for personal non-commercial research or study, without prior permission or charge. This thesis cannot be reproduced or quoted extensively from without first obtaining permission in writing from the copyright holder/s. The content must not be changed in any way or sold commercially in any format or medium without the formal permission of the copyright holders.

When referring to this work, full bibliographic details including the author, title, awarding institution and date of the thesis must be given e.g.

AUTHOR (year of submission) "Full thesis title", University of Southampton, name of the University School or Department, PhD Thesis, pagination

http://eprints.soton.ac.uk

UNIVERSITY OF SOUTHAMPTON

FACULTY OF SOCIAL AND HUMAN SCIENCES

SCHOOL OF MATHEMATICS

A spectral MHD code for the non-linear study of magnetic neutron stars

BY

Oliver Robertshaw

A thesis submitted for the degree of Doctor of Philosophy

June 2011

UNIVERSITY OF SOUTHAMPTON

ABSTRACT

FACULTY OF SOCIAL AND HUMAN SCIENCES

SCHOOL OF MATHEMATICS

Doctor of Philosophy

A spectral MHD code for the non-linear study of magnetic neutron stars

BY

Oliver Robertshaw

To study the ideal magnetohydrodynamic equations we present a spectral code that uses finite differencing in radius and spherical harmonic expansions in the angles. Convolution replaces spherical harmonic multiplication, giving us an infinite system of PDEs in radius and time to solve; we truncate at some relatively low degree ℓ and may evolve with or without non-zero m to simulate three dimensions or axisymmetry.

Our code crudely models the internal dynamics of a neutron star by placing a magnetized fluid into a spherical shell of fixed radius, surrounded by vacuum. The spherical harmonic decomposition makes it simple to both dynamically calculate the gravitational potential and to use a magnetic vector potential to ensure a divergence-free evolution. A simple friction method is effective at finding the equilibria of stratified stars in the absence of exterior fields and/or rotation. We then investigate the stability of perturbed equilibria by evolving non-linearly in time over many Alfvén time crossings, and briefly analyze the resulting oscillation frequencies.

Contents

List of Figures

Declaration of authorship

I, **Oliver Robertshaw**, declare that this thesis entitled **A spectral MHD code for the non-linear study of magnetic neutron stars** and the work presented in the thesis are both my own, and have been generated by me as the result of my own original research. I confirm that:

- this work was done wholly or mainly while in candidature for a research degree at this University;
- where any part of this thesis has previously been submitted for a degree or any other qualification at this University or any other institution, this has been clearly stated;
- where I have consulted the published work of others, this is always clearly attributed;
- where I have quoted from the work of others, the source is always given. With the exception of such quotations, this thesis is entirely my own work;
- I have acknowledged all main sources of help;
- where the thesis is based on work done by myself jointly with others, I have made clear exactly what was done by others and what I have contributed myself;
- none of this work has been published before submission.

Signed: .....

Date: .....

Acknowledgements

I would like to thank my supervisor Professor Carsten Gundlach for his indefatigable guidance, my friends and colleagues at Southampton University for their support and encouragement, and my parents for setting me on this course in life.

“Some mathematician has said
pleasure lies not in discovering truth,
but in seeking it.”

Stepan Arkadyevitch
Anna Karenina

Chapter 1

Anatomy of a neutron star

In 1932 Sir James Chadwick discovered an uncharged particle with approximately the same mass as a proton, through his studies of the emissions of irradiated beryllium. Such particles had earlier been predicted to exist as the binding of a proton and electron by Rutherford, who called them *neutrons*. Less than two years later, Baade and Zwicky [6] postulated that supernovae, which were poorly understood at the time, can transform an ordinary star into a *neutron star* by removing all of the charged particles.

As our understanding of subatomic physics progressed, it soon became clear that neutron stars, if they existed, would be extremely compact and very difficult to spot. The observation of regular radio pulses from deep space – the emissions of a pulsar – by Bell Burnell and Hewish in 1967 [11] led to increased interest in the study of neutron stars, and the associated exotic physics that is still untestable in Earth-bound laboratories.

Although there exists a general consensus when it comes to many points of neutron star phenomenology, various properties and processes are still poorly understood. This chapter outline the birth and life of a typical neutron star, drawing on information from various sources (for example, [1, 14, 39, 66, 72, 79]).

1.1 Neutron star formation

Up until their death, stars remain in a hydrostatic equilibrium: the inward pull of gravity is chiefly opposed by outward pressure from nuclear fusion. This process continuously combines nuclei within the core, mostly those of hydrogen, forming heavier elements and releasing energy. As it ages the star forms layers of different elements at high concentrations, with mostly hydrogen and helium towards the surface, iron and nickel at the core, and others (such as oxygen and silicon) in between due to differing rates of fusion.

Iron and nickel nuclei have maximal binding energies: they cannot be used to create heavier elements. The density and temperature of the core rises as quantities of these

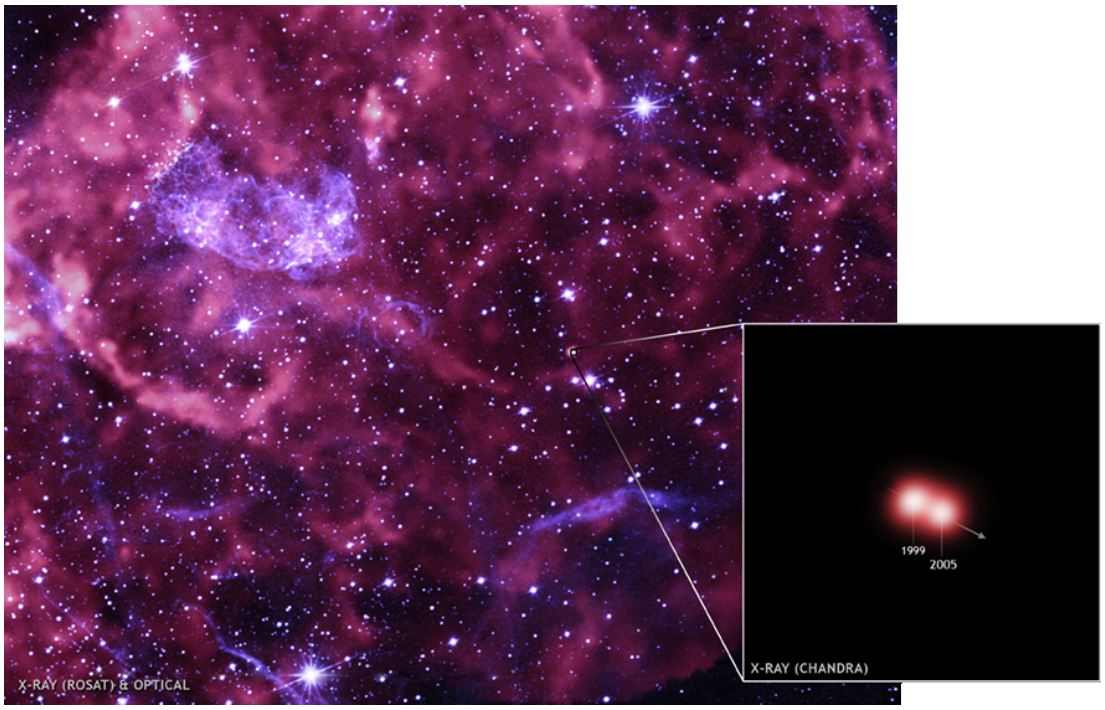

Figure 1.1: Supernova remnant *Puppis A* and the neutron star formed at its centre, currently moving at 10^6 m s^{-1}. *Credit: Chandra: NASA/CXC/Middlebury College/F.Winkler et al; ROSAT: NASA/GSFC/S.Snowden et al.; Optical: NOAO/AURA/NSF/Middlebury College/F.Winkler et al.*

elements build up, with the pressure generated by fusion and electron degeneracy[1] balancing gravity at this point. The collapse of sufficiently massive cores may be triggered by electron capture and/or photo-dissociation and occurs on a time scale of seconds. The former, whereby electrons and protons are combined to form neutrons and electron neutrinos, reduces the overall pressure from electron degeneracy. The latter breaks iron and nickel nuclei into α-particles and neutrons, decreasing the temperature, and hence the thermal support, at the core. Very strong magnetic fields may even accelerate this process [55].

Relatively low mass stars, such as our own Sun, slowly eject their outer layers as they age and leave behind a cooling dwarf star, rather than collapsing. Dying stars between 8 – $20M_\odot$ account for about ninety percent of *core collapse* supernovae. This range of masses typically results in the formation of a neutron star, with masses between 1 – $3M_\odot$ and radii of 10 – 15km, that are gravitationally decoupled from the rest of the star's expelled mass. Neutron star formation is also thought to occur for stars little above $20M_\odot$, but in-falling matter (at least ten percent of the progenitor's mass) will likely cause delayed, accretion induced collapse into a black hole. Stars between 40 – $100M_\odot$ should rapidly collapse straight into a black hole, bypassing any supernova event. The theoretical Eddington limit

[1] A consequence of the Pauli exclusion principle: fermions (which include protons, neutrons and electrons) may not occupy the same quantum state simultaneously. As the uncertainly in the position of the electrons decreases as they are compacted, their momentum uncertainty will increase, and a pressure force results. Neutrons are more massive than electrons and so can exhibit a much greater pressure than electrons when compressed.

should prevent stars more massive than $120M_{\odot}$ from ever reaching a collapse stage as thermal pressure expels the outer layers early on.

The onset of core collapse is marked by a decoupling of the iron–nickel core into a rapidly collapsing *inner core* and a slower moving *outer core*. Approximately 100 ms after the collapse begins, matter is falling into the centre at a sizeable fraction of the speed of light. Once densities comparable to those of an atomic nucleus are reached, on the order of $10^{17}\,\mathrm{kg\,m^{-3}}$, nucleons are so closely packed together that the (usually attractive) strong nuclear force between them becomes repulsive and prevents further collapse. A hot, large ($\sim 100\,\mathrm{km}$ radius) *proto-neutron star* (PNS) is formed mere seconds after the collapse began.

The remaining in-falling mass of the star, primarily the outer core, forms a pressure shock wave as it falls onto the surface of the PNS which propagates outwards; this is commonly referred to as a *bounce* event. It occurs several hundred milliseconds after the collapse begins, heating and further compressing matter within the outer core. Energy is also lost to dissociating the remaining heavy nuclei and the result is a stalled shock front. A number of mechanisms, acting on their own or perhaps coupled to each other, are thought to be able to revive the standing shock and yet give a supernova explosion, but the primary driver is most likely to be neutrinos escaping from the collapsed inner core, depositing their energy within the surrounding stalled matter. This process slowly cools the PNS, contributing in part to its diminishing in size. Other properties of the parent star's core, such as angular momentum and magnetic energy, are transferred to the neutron star, which interact and strongly affect its subsequent evolution.

1.2 Neutron star structure

1.2.1 The interior

Much like how seismology reveals information about the Earth's core, mantle and crust, the oscillations of neutron stars are our best means of directly determining their inner structure. (Other kinds of direct observations, such as the surface temperature or red-shift, help to constrain the various models we care to construct.) These oscillations should be observable[2] within the various signals emitted by *pulsars*, which are magnetized spinning neutron stars that continuously emit a narrow beam of high-energy electromagnetic radiation powered by energy from either the rotation, magnetic field or accretion.

It is the hope that gravitational waves from neutron stars, and other extragalactic sources, will soon be spotted by various detectors such as Advanced LIGO, LISA and VIRGO. These detectors operate by splitting a laser beam down paths at right angles to

[2]Only a handful of (*quasi-*)periodic oscillations (QPOs) have been observed to date, and are generally considered to be intricately linked to either crust dynamics or the magnetosphere [62, 91], neither of which are particularly well-modelled today.

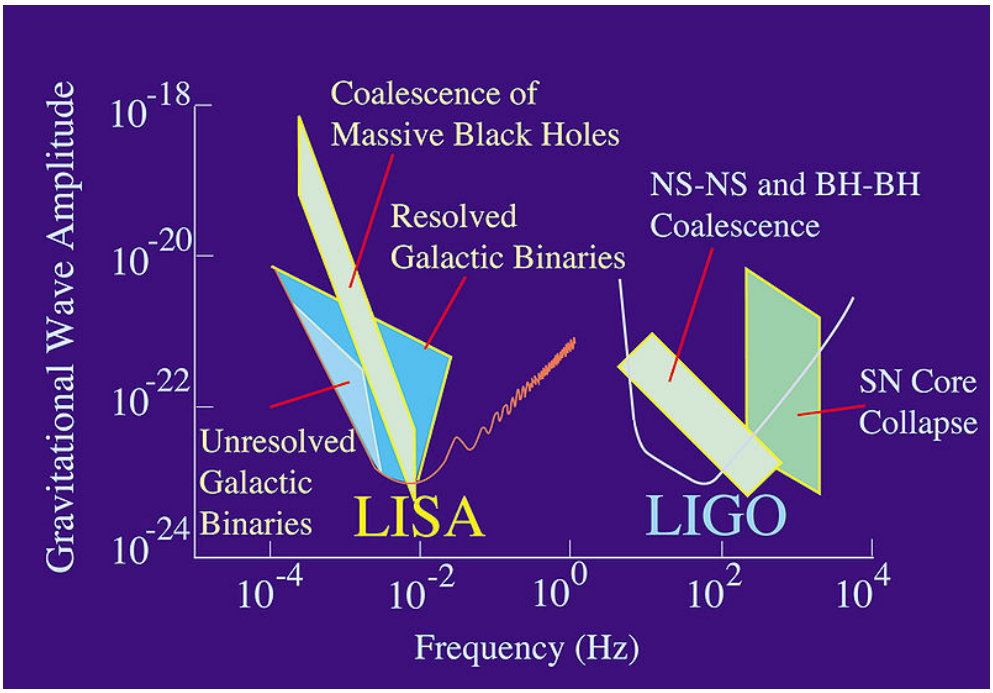

Figure 1.2: Frequency and amplitude detection ranges of LIGO, and the future LISA experiment. ©*NASA/JPL.*

each other: passing gravitational waves will alter the distances travelled by both beams, and an interference pattern should be observable in the recombined beams if the waves are sufficiently powerful. Rapidly rotating neutron stars with large deformations [51] are amongst the potential observation candidates at high-frequencies (figure 1.2) due to the large amounts of gravitational energy they emit, as well as the high detection rate.

The internal structure of a neutron star, or indeed any stellar body – from a rocky asteroid to an entire solar system – is closely related to the equation of state (EOS) of the matter within. A challenge for those constructing an accurate model is to determine a physically realistic EOS, based on observation where possible, and as such there are various different approaches to tackling how quantities such as temperature, entropy and pressure are related. Our model initially adopts a particular simple (and somewhat unrealistic) EOS, whereby the pressure is only dependent on the local density (section 5.1), before moving to the concept of a *stratified* NS where thermal gradients are also important (section 5.6.2).

Beginning at the surface, the one kilometre-thick crust can be described by a gradual change from an outer to an inner region [25] with different properties. The composition of the outer crust, including the surface, may vary widely depending on the initial composition of the parent star or the amount of post-supernova accretion that occurred, but is most likely a solid lattice of heavy elements (such as iron) at sub-nuclear densities. Deeper into the middle of the crust these atoms are more likely to be ionized and neutron-rich, through capture of free electrons.

The crusts of neutron stars with extremely strong magnetic fields, often referred to as

magnetars [35], are thought to undergo regular *cracking* from the massive magnetic strain that can build up, which leads to the release of giant γ-ray flares [67, 78]. We do not currently model any kind of crust more complicated than a container that does not couple to the interior dynamics, except to prevent fluid escaping, although there is, in principle, no reason why such a crust could not be added with more research.

Neutron star *glitches* provide evidence for a rapidly rotating neutron superfluid interior [64, 71] threaded by strong magnetic fields. Observations of sudden spin-up in various pulsars, followed by gradual recovery to the pre-glitch rotation over many days, is thought to be caused by a freely-spinning interior temporarily coupling itself to a solid crust which is also forced to rotate more rapidly before some braking mechanism kicks in.

To support an interior magnetic field, the neutron star bulk is comprised of a neutron superfluid containing a small number of free protons and electrons. However, the composition of the innermost core is unknown: various NS models exist which invoke special states of matter, but many of these have yet to be confirmed or ruled out through observation. Theories regarding the inner core range from the relatively mundane, such as the entire interior being comprised of anisotropic superfluidic neutrons [54], to the exotic-but-plausible, such as a small core of hyperon or quark matter [57, 63], to the purely theoretical, for example the existence of a preon core [50].

1.2.2 The exterior

Due to their strong surface gravity, a typical neutron stars is likely surrounded by very thin atmosphere, perhaps on the order of centimetres in depth. Its composition again depends on the circumstances surrounding the NS formation, but there is evidence to suggest that a typical young neutron star is surrounded by a thin layer of light elements, such as carbon [53].

Observations of *pulsar wind nebulae* require both strong magnetic fields and rapid rotation of the atmosphere region to eject matter from both the poles and equatorial region. One thus expects to find a hot plasma surrounding many neutron stars, although the dynamics of such a *magnetosphere* and its coupling to the NS interior are incredibly complex and certainly less studied than the interior alone.

Alternatively, it is possible that some neutron stars are instead surrounded by a highly charged but very tenuous *electrosphere*. In such cases, there are likely to be constraints [43] on the rotation rates of this region.

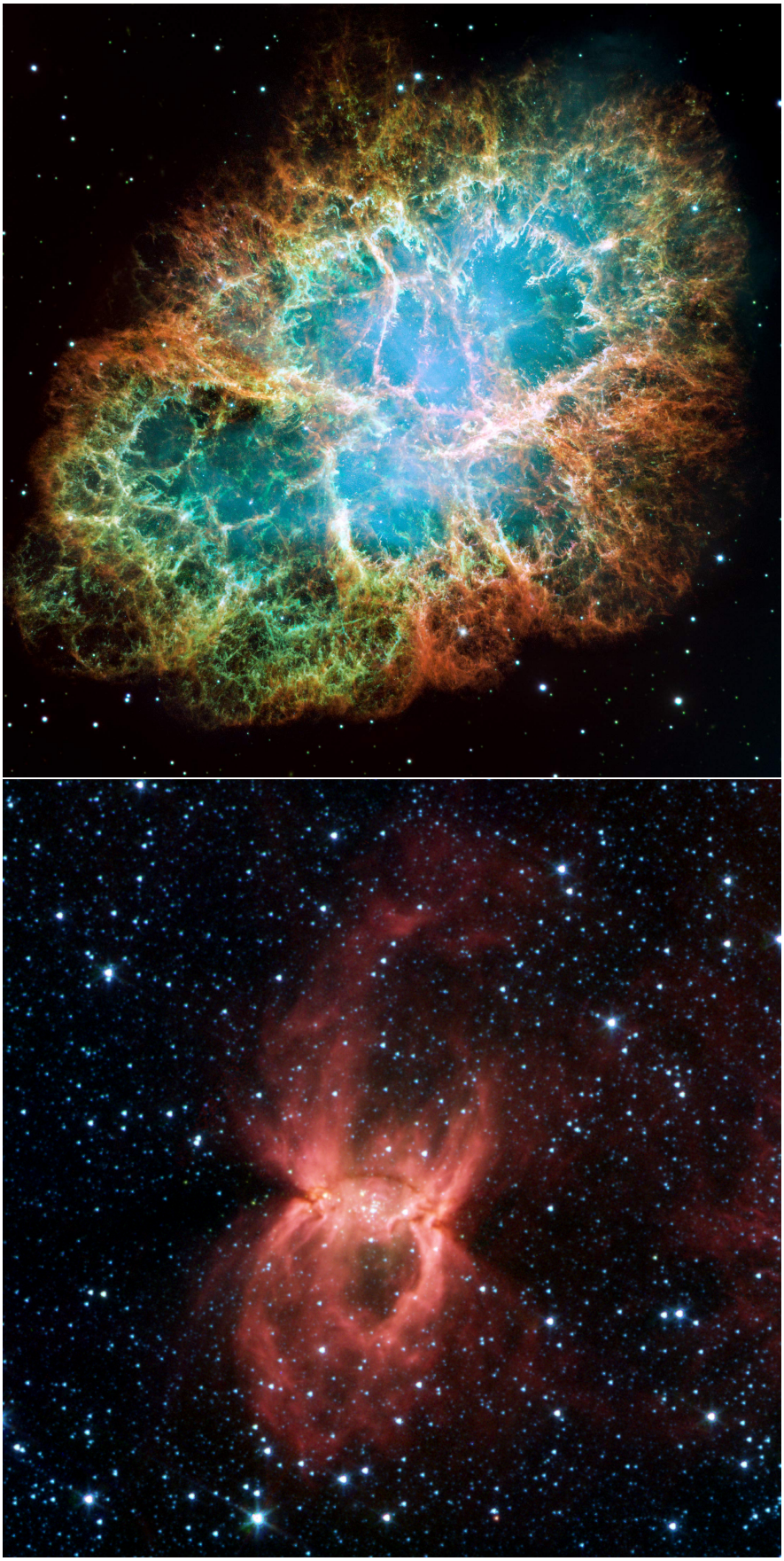

Figure 1.3: The Crab and Black Widow are both examples of pulsar wind nebulae.

Chapter 2

Spectral Method

A spectral expansion of a system of partial differential equations starts by writing the dependent variables as an infinite sum of smooth basis functions of the independent variables. The reason for doing so is to make the system simpler, and (potentially) faster to solve numerically. The most well-known example of this technique, and certainly its first documented application, is the use of Fourier series to solve the 1D heat equation. Ideally the solutions to the systems under study are smooth, or else *Gibb's phenomena* will badly affect the model near discontinuities.

There are various different ways one can go about using such expansions to solve higher dimensional problems but this thesis will investigate a hybrid spectral approach, where functions expressed in spherical polar coordinates (r, θ, φ) have their angular terms expanded over the spherical harmonics. We can then use the orthogonality of spherical harmonics to remove all explicit dependence on θ, φ, and we will be left with PDEs involving just the radial coordinate and time. These will be numerically evolved in time through techniques explained in chapter 3.

Spectral methods have been used to study fluid flow for quite some time, and there are various different conventions and methods used to expand the angular components of scalars and vectors using spherical harmonics [22, 56, 75]. Because of the difficulties that the coordinate singularity at $r = 0$ can create, some authors adopt a fully spectral approach by expanding the radial functions over a limited number of Chebyshev polynomials [15]. There has also been a recent Living Review article on the subject of spectral methods in general relativity [45].

For MHD, spherical harmonic expansions have been used to study the magnetic fields of both the Sun [21] and the Earth [32], and other astrophysical bodies. A very similar convolution technique to our own was perhaps first used by Bullard *et al.* [22] in a similar context, by looking at a rotating dynamo as a simplified model of the Earth's magnetic field. Geppert and Wiebicke [41] later studied how heat flux crossing through the outer crust of a neutron star affects the embedded magnetic field. They make various assumptions that

decouple the hydrodynamics from the magnetic field and entropy, so their main concern is with the evolution of the latter two quantities in a shell, rather than a spherical bulk. More recently, Pons and Geppert [40] used the same method to study how the magnetic field in neutron star crusts decay through nonlinear effects (*Hall drift* and *Ohmic decay*) over long time scales.

This chapter will first define the spherical harmonics and explain how one can expand scalar functions, and then it will introduce a coordinate-free spacetime on which we may introduce derivatives and vector harmonics. Doing so leaves the possibility of extending this formalism to curved spacetimes, and thus a relativistic formulation, even though we are only concerned with flat Newtonian space in this thesis. It then describes how to multiply scalar and vector spherical harmonic expansions, and briefly discusses the real spherical harmonics.

2.1 Spherical harmonics

Spherical harmonics $Y_\ell^m(\theta,\varphi)$ are complex–valued functions that arise when finding separable solutions to Laplace's equation in spherical polar coordinates,

$$\Delta f(r,\theta,\varphi) = 0, \tag{2.1.1}$$

where one rewrites

$$f(r,\theta,\varphi) = R(r)Y(\theta,\varphi) = \sum_{\ell=0}^{\infty}\sum_{m=-\ell}^{\ell} R_\ell^m(r)Y_\ell^m(\theta,\varphi). \tag{2.1.2}$$

for integer *degree* ℓ, *mode* m. The 4π-normalized spherical harmonics (used throughout) are specifically defined by

$$r^2\Delta Y_\ell^m = -\ell(\ell+1)Y_\ell^m \tag{2.1.3}$$

$$\int_{\mathcal{S}} Y_\ell^m Y_L^{M*}\, d\Omega = 4\pi\delta_\ell^L\delta_m^M \qquad (d\Omega = \sin\theta\, d\theta\, d\varphi) \tag{2.1.4}$$

$$\partial_\varphi Y_\ell^m = imY_\ell^m, \tag{2.1.5}$$

$$(Y_\ell^m)^* = (-1)^m Y_\ell^{-m}, \tag{2.1.6}$$

where * represents the complex conjugate, and the angles are represented by the polar $\theta\in[0,\pi)$ (co-latitudinal) and azimuthal $\varphi\in[0,2\pi)$ (longitudinal).

We adopt the notation of [22, 46, 56] and define a *multi-index* γ for a particular degree and mode by

$$\gamma \equiv \ell(\ell+1)+m. \tag{2.1.7}$$

It is a unique integer for every permissible integer degree and mode, and is always represented

by a lower-case Greek symbol in subscript. (2.1.2) can now be rewritten in shorthand as

$$\Delta\left(\sum_{\gamma=0}^{\infty} f_\gamma(r)Y_\gamma(\theta,\varphi)\right)=0. \tag{2.1.8}$$

Furthermore, we introduce the symbol

$$L_\gamma^2=-\ell(\ell+1) \tag{2.1.9}$$

and define a negative multi-index by

$$-\gamma\equiv\ell_\gamma(\ell_\gamma+1)-m_\gamma \qquad \left(Y_{-\gamma}\equiv Y_\ell^{-m}\right) \tag{2.1.10}$$

With this notation we rewrite (2.1.3-2.1.6) as

$$r^2\Delta Y_\gamma=L_\gamma^2 Y_\gamma, \tag{2.1.11}$$

$$\int_{\mathcal{S}} Y_\alpha Y_\beta^* d\Omega=4\pi\delta_{\alpha,\beta}, \tag{2.1.12}$$

$$\partial_\varphi Y_\gamma=im_\gamma Y_\gamma, \tag{2.1.13}$$

$$Y_\gamma^*=(-1)^m Y_{-\gamma}. \tag{2.1.14}$$

Spherical harmonics for a given degree and mode are calculated using the associated Legendre polynomials P_ℓ^m through

$$Y_\ell^m(\theta,\varphi)=\sqrt{(2\ell+1)\frac{(\ell-m)!}{(\ell+m)!}}\,P_\ell^m(\cos\theta)\,e^{im\varphi}, \tag{2.1.15}$$

$$P_\ell^m(x)=\frac{(-1)^m}{2^\ell\ell!}(1-x^2)^{m/2}\frac{d^{\ell+m}}{dx^{\ell+m}}\left[(x^2-1)^\ell\right]. \quad (x\in[-1,1]) \tag{2.1.16}$$

Various recurrence relations exist to calculate these polynomials, some of which are specified in section 3.8. One may use (2.1.16) to show that the spherical harmonics can be expanded in terms of sine and cosine as

$$Y_\ell^m(\theta,\varphi)=\sin^m\theta\left(a_0\cos^{\ell-m}\theta+a_2\cos^{\ell-m-2}\theta+...\right)e^{im\varphi} \tag{2.1.17}$$

for some coefficients $a_i=a_i(\ell,m)$.

2.2 Spectral expansion

The spherical harmonic expansion for a smooth function defined on a sphere, written in terms of both the modes and multi-indexes, is

$$f(t,r,\theta,\varphi) = \sum_{\ell=0}^{\infty} \sum_{m=-\ell}^{\ell} Y_\ell^m(\theta,\varphi) F_l^m(t,r) = \sum_{\gamma=0}^{\infty} Y_\gamma F_\gamma, \tag{2.2.1}$$

where both Y, F are complex functions. We adopt the shorthand of repeated multi-indexes to *often* imply summation, for example

$$f = Y_\gamma F_\gamma. \tag{2.2.2}$$

This notation is not strict in that we sometimes mean summation with only one index, and sometimes not with two or more. Any inferred summation should be taken from the context, for example by the indexes that appear on both sides of an equation, rather than through any strict rules.

Conversely, expansion coefficients may be calculated from the original function, if known, by integrating:

$$F_\gamma = \frac{1}{4\pi} \int f Y_\gamma^* \, d\Omega. \tag{2.2.3}$$

We need to set some maximum value $\ell \leq \ell_m < \infty$ for the expansion in order to carry out computational work; this introduces a truncation error into our calculations. This error will be seen in the recovery of the original variables, as well as the evolved variables in situations where they are coupled. We write this truncated series as

$$\tilde{f} = \sum_{\gamma}^{\ell=\ell_m} Y_\gamma F_\gamma. \tag{2.2.4}$$

Doing so introduces a truncation error

$$E_T = f - \tilde{f} \tag{2.2.5}$$

where we expect $E_T \to 0$ as ℓ_m increases.

2.2.1 Products of spherical harmonics

The product of two (or more) spherical harmonics remains a function of (θ, φ) and thus has its own spherical harmonic expansion,

$$Y_\alpha Y_\beta = \sum_\gamma A_{\alpha\beta\gamma} Y_\gamma, \tag{2.2.6}$$

where $A_{\alpha\beta\gamma}$ is a number that depends on the values of all of the ℓ, m's involved. If we multiply both sides by a particular Y_ϵ^* and integrate, from (2.1.4) and (2.1.6) we have

$$\begin{aligned}\int Y_\alpha Y_\beta Y_\epsilon^* d\Omega &= (-1)^{m_\epsilon} \int Y_\alpha Y_\beta Y_{-\epsilon} d\Omega \\ &= \sum_\gamma A_{\alpha\beta\gamma} \int Y_\gamma Y_\epsilon^* d\Omega = \sum_\gamma 4\pi A_{\alpha\beta\gamma}\delta_{\gamma\epsilon} = 4\pi A_{\alpha\beta\epsilon},\end{aligned} \tag{2.2.7}$$

where $\delta_{\alpha\beta}$ is a Kronecker delta function over both the degrees and modes involved. Hence,

$$A_{\alpha\beta\gamma} = \frac{(-1)^{m_\gamma}}{4\pi} \int Y_\alpha \, Y_\beta \, Y_{-\gamma} \, d\Omega. \tag{2.2.8}$$

This triple integral is often referred to as a *Gaunt coefficient* or *Slater integral* and may be computed using Wigner 3j-symbols:

$$\int Y_\ell^m \, Y_{\ell'}^{m'} \, Y_{\ell''}^{m''} d\Omega = 4\pi\sqrt{(2\ell+1)(2\ell'+1)(2\ell''+1)} \begin{pmatrix} \ell & \ell' & \ell'' \\ 0 & 0 & 0 \end{pmatrix} \begin{pmatrix} \ell & \ell' & \ell'' \\ m & m' & m'' \end{pmatrix}. \tag{2.2.9}$$

The 6-entry brackets are the Wigner 3js, which can in turn be computed using the Racah formula [93]:

$$\begin{aligned}\begin{pmatrix} \ell & \ell' & \ell'' \\ m & m' & m'' \end{pmatrix} &= (-1)^{\ell-\ell'-m''} \sqrt{\frac{(\ell+\ell'-\ell'')!\,(\ell-\ell'+\ell'')!\,(-\ell+\ell'+\ell'')!}{(\ell+\ell'+\ell''+1)!}} \\ &\quad \times \sqrt{(\ell+m)!\,(\ell-m)!\,(\ell'+m')!\,(\ell'-m')!\,(\ell''+m'')!\,(\ell''-m'')!} \\ &\times \sum_t \frac{(-1)^t}{t!(\ell''-\ell'+t+m)!\,(\ell''-\ell+t-m')!\,(\ell+\ell'-\ell''-t)!\,(\ell-t-m)!\,(\ell'-t+m')!}\end{aligned} \tag{2.2.10}$$

where the summation is over the t which gives factorials of zero or positive integers. (Fortran source code is given in appendix B.1.) For the coefficients $A_{\alpha\beta\gamma}$ to be non-zero, we require the following conditions to hold[1]:

$$m'' = -(m+m'), \qquad (\text{"zero-sum"}) \tag{2.2.11}$$

$$|\ell - \ell'| \leq \ell'' \leq \ell + \ell', \qquad (\text{"triangle inequality"}) \tag{2.2.12}$$

$$\ell + \ell' + \ell'' = \text{even}. \qquad (\text{"even sum"}) \tag{2.2.13}$$

Some authors [20] prefer to express these triple integrals through *Clebsch-Gordan* (CG) coefficients and refer to them as such. These originally arose in the field of quantum mechanics when considering angular momentum and spin. They can also be used to

[1] Not *all* integrals that satisfy these condition are necessarily non-zero: for example, it may be shown that $\int Y_{n+1}^{2n+1} Y_{-2n}^{2n+1} Y_{n-1}^{2n} d\Omega = 0$ for $n \geq 1$.

calculate triple integrals [92] through

$$\left\langle \ell'\ell''m_1m_2\middle|\ell'\ell''\ell m\right\rangle = (-1)^{m+\ell'-\ell''}\sqrt{2\ell+1}\begin{pmatrix} \ell' & \ell'' & \ell \\ m_1 & m_2 & -m \end{pmatrix}. \tag{2.2.14}$$

where the term on the left is a CG coefficient.

The coefficient $A_{\alpha\beta\gamma}$ will be used to calculate various products of harmonics later on, so we define

$$\hat{C}_{\alpha\beta\gamma} \equiv \int Y_\alpha Y_\beta Y_\gamma d\Omega, \tag{2.2.15}$$

$$\chi_\gamma \equiv \frac{(-1)^{m_\gamma}}{4\pi}. \tag{2.2.16}$$

Note that the summation over repeated indices rule does not apply to $\chi_\gamma \hat{C}_{\alpha\beta-\gamma}$. These are separated in case one prefers a different phase convention or normalization.

Gaunt coefficients are real valued, as can be seen from the formula for Wigner 3j's. As a result, they are equivalent to coefficients with the opposite sign on the m's:

$$\int Y_\ell^{-m} Y_{\ell'}^{-m'} Y_{\ell''}^{-m''} = (-1)^{m+m'+m''}\int \left(Y_\ell^m Y_{\ell'}^{m'} Y_{\ell''}^{m''}\right)^* = \int Y_\ell^m Y_{\ell'}^{m'} Y_{\ell''}^{m''}. \tag{2.2.17}$$

2.2.2 Products of scalar functions

The foundations laid by the previous section allow us to find the product of two scalar functions in terms of an expansion of spherical harmonics. Consider the multiplication

$$\begin{aligned} & f(r,t,\theta,\varphi) = a(r,t,\theta,\varphi)\, b(r,t,\theta,\varphi) \\ \implies & \sum_\zeta f_\zeta Y_\zeta = \sum_{\alpha,\beta} a_\alpha b_\beta Y_\alpha Y_\beta, \end{aligned} \tag{2.2.18}$$

where the f_ζ etc. are expansion coefficients and functions of (r,t). If we multiply both sides by ${Y_\gamma}^*$ and integrate,

$$\begin{aligned} & 4\pi f_\gamma = \sum_{\alpha,\beta} a_\alpha b_\beta \int Y_\alpha Y_\beta {Y_\gamma}^* d\Omega = \sum_{\alpha,\beta} a_\alpha b_\beta (-1)^{m_\gamma}\int Y_\alpha Y_\beta Y_{-\gamma} d\Omega \\ \implies & f_\gamma = \sum_{\alpha,\beta} \chi_\gamma\, \hat{C}_{\alpha\beta-\gamma}\, a_\alpha b_\beta. \end{aligned} \tag{2.2.19}$$

2.3 Underlying spacetime

Following the notation first introduced by Gerlach and Sengupta [42, 46], we shall work on a spherically symmetric spacetime but set up the appropriate framework before introducing coordinates for numerical treatment.

A four-dimensional spacetime manifold $\mathcal{M}$ is split into 2+2 dimensions, $M^2 \times \mathcal{S}^2$. M^2 represents the 2-dimensional (1+1) reduced spacetime and $\mathcal{S}^2$ the 2-spheres. Slots are represented by Greek indices[2] on $\mathcal{M}$ (with the metric $g_{\mu\nu}$), upper-case Latin indices on M^2 (with the Lorentzian metric g_{AB}), and lower-case Latin on $\mathcal{S}^2$ (with the unit curvature metric γ_{ab}). Thus we write the metric on $\mathcal{M}$ as

$$g_{\mu\nu} = \mathrm{diag}(g_{AB}, r^2\gamma_{ab}), \tag{2.3.1}$$

where r is a coordinate on M^2. We introduce covariant derivatives by writing

$$g_{\mu\nu;\lambda} = 0, \qquad g_{AB|C} = 0, \qquad \gamma_{ab:c} = 0. \tag{2.3.2}$$

on each of $\mathcal{M}$, M^2 and $\mathcal{S}^2$ respectively.

To define vectors we shall also require the totally antisymmetric covariant unit tensor on γ_{ab}, defined by

$$\epsilon_{ab:c} = 0, \qquad \epsilon_{ac}\,\epsilon^{bc} = \gamma_a{}^b. \tag{2.3.3}$$

On flat Newtonian space we will reduce M to a one dimensional manifold with coordinate r, so that $\mathcal{M} = M^1 \times \mathcal{S}^2$. Since this thesis is not concerned with curved space (whilst still laying the groundwork for such an extension) we implicitly assume a 1+2 split where coordinates are concerned. The flat-space metric in spherical polar coordinates is

$$ds^2 = g_{\mu\nu}dx^\mu dx^\nu = dr^2 + r^2\left(d\theta^2 + \sin^2\theta\, d\varphi^2\right), \tag{2.3.4}$$

with components given by

$$\begin{aligned} g^{AA} &= g_{AA} = 1, \\ \gamma_{ab} &= \begin{pmatrix} 1 & 0 \\ 0 & \sin^2\theta \end{pmatrix}, \qquad \gamma^{ab} = \begin{pmatrix} 1 & 0 \\ 0 & \frac{1}{\sin^2\theta} \end{pmatrix}. \end{aligned} \tag{2.3.5}$$

[2]The Greek indices representing harmonic modes are not to be confused with slots on the manifold $\mathcal{M}$. However they never appear in the same expression in this work because of the spacetime splitting, and it should be obvious from the context to which we refer.

2.4 Vector harmonics in 1+2 split

For $\ell \geq 1$ modes we may construct a basis for vectors on $\mathcal{S}^2$ from the scalar spherical harmonics, through

$$Z_{\gamma a} \equiv Y_{\gamma:a}, \qquad \text{(polar)} \tag{2.4.1}$$

$$S_{\gamma a} \equiv \epsilon_a{}^b \, Y_{\gamma:b}. \qquad \text{(axial)} \tag{2.4.2}$$

Note that this implies the relations

$$\begin{aligned} S^a_\alpha S_{\beta a} &= \gamma^{ab}\, \epsilon_b{}^c\, \epsilon_a{}^d\, Z_{\alpha c} Z_{\beta d} = \epsilon^{ac}\, \epsilon_{ad}\, Z_{\alpha c} Z^d_\beta = \epsilon^{ca}\, \epsilon_{da}\, Z_{\alpha c} Z^d_\beta = \gamma^c{}_d\, Z_{\alpha c} Z^d_\beta \\ &= Z^a_\alpha Z_{\beta a}, \end{aligned} \tag{2.4.3}$$

and

$$Z_{\gamma a}{}^{:a} = Y_{\gamma:a}{}^{:a} = L^2_\gamma Y_\gamma, \qquad S_{\gamma a}{}^{:a} = \epsilon^{ab} Y_{\gamma:ab} = -\epsilon^{ab} Y_{\gamma:ab} = 0. \tag{2.4.4}$$

Using γ^{ab} to shift indices, the contravariant components of Z, S are

$$Z^a_\gamma = \left(\partial_\theta Y_\gamma, \frac{1}{\sin^2\theta} \partial_\varphi Y_\gamma \right), \qquad S^a_\gamma = \left(\frac{1}{\sin\theta} \partial_\varphi Y_\gamma, \frac{-1}{\sin\theta}\, \partial_\theta Y_\gamma \right). \tag{2.4.5}$$

It follows that the dot product $Z^a_\alpha S_{\beta a}$ is always zero in axisymmetry ($m = 0$), and zero in 3D iff $\alpha = \beta$.

A tangential, radial vector is formed by multiplying a spherical harmonic with the radial unit vector e^A. Hence, if $\mathbf{v}$ is the velocity field on $\mathcal{M}$, we write it as

$$\mathbf{v}^\mu = v_\gamma Y_\gamma \mathbf{e}^A \oplus (u_\gamma Z^a_\gamma + w_\gamma S^a_\gamma), \tag{2.4.6}$$

where v, u, w are functions of (r, t) only, and $\oplus$ is a direct sum of vector spaces. We adopt similar notation for other vector fields. The covariant form is obtained by using g_{ab} to lower indices:

$$\mathbf{v}_\mu = v_\gamma Y_\gamma \mathbf{e}_A \oplus r^{-2} \left(u_\gamma Z_{\gamma a} + w_\gamma S_{\gamma a} \right). \tag{2.4.7}$$

After reflection through the equator $\theta \to \pi - \theta$ all vector harmonics satisfy either of two outcomes; following Ivers and Phillips [56] we classify them as being *dipolar* or *quadrupolar*:

$$(f^m_\ell)^{(\theta)}(\pi - \theta, \varphi) = \pm (f^m_\ell)^{(\theta)}(\theta, \varphi), \qquad \text{(d/q)} \tag{2.4.8}$$

$$(f^m_\ell)^{(\varphi)}(\pi - \theta, \varphi) = \mp (f^m_\ell)^{(\varphi)}(\theta, \varphi). \qquad \text{(d/q)} \tag{2.4.9}$$

For example, Z^ℓ_ℓ are quadrupolar and S^ℓ_ℓ are dipolar; if $m = 0$ the classification is based on transformation of the non-zero component. This naming convention likely follows from whether or not a given harmonic transforms in the same manner as Z^0_1 or Z^0_2, which are

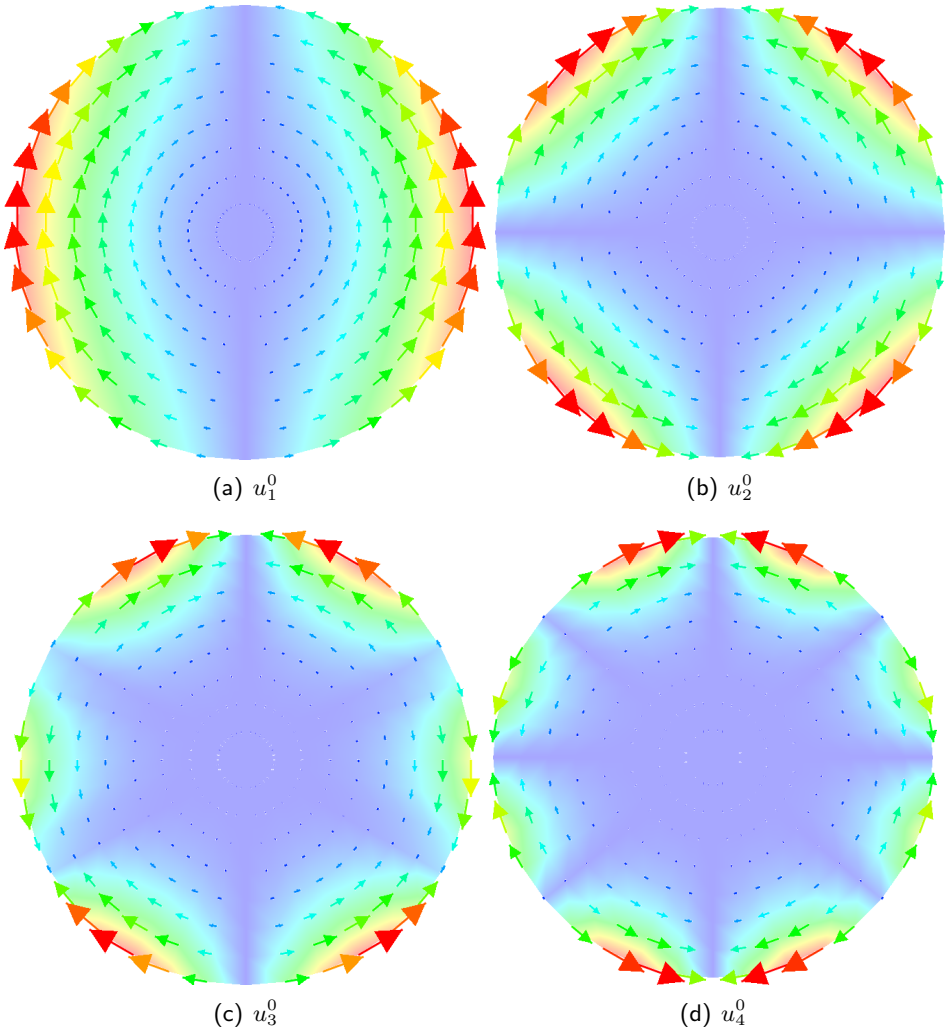

(a) u_1^0 (b) u_2^0

(c) u_3^0 (d) u_4^0

Figure 2.1: Poloidal motion inside a sphere for constant u_γ.

easily seen to describe dipolar/quadrupolar fields (figures 2.1,2.3).

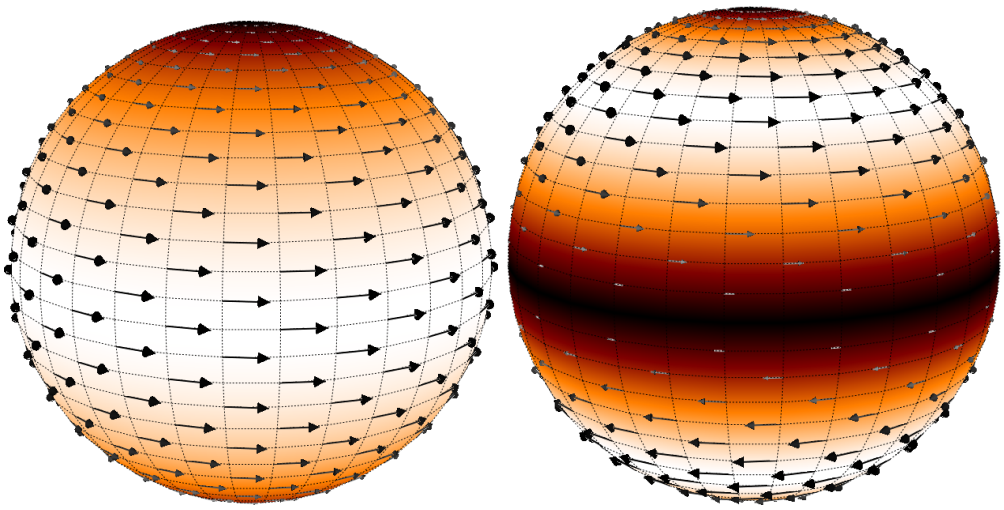

(a) w_1^0 (b) w_2^0

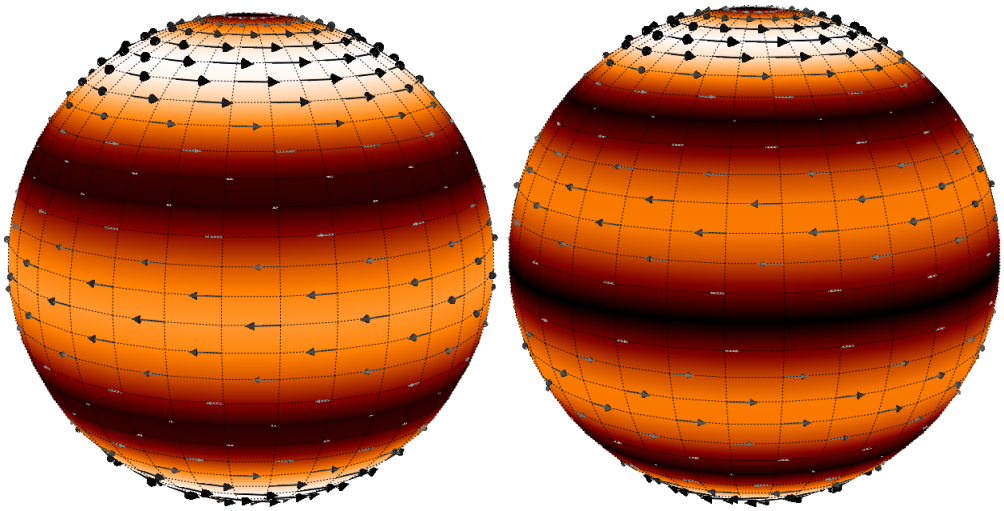

(c) w_3^0 (d) w_4^0

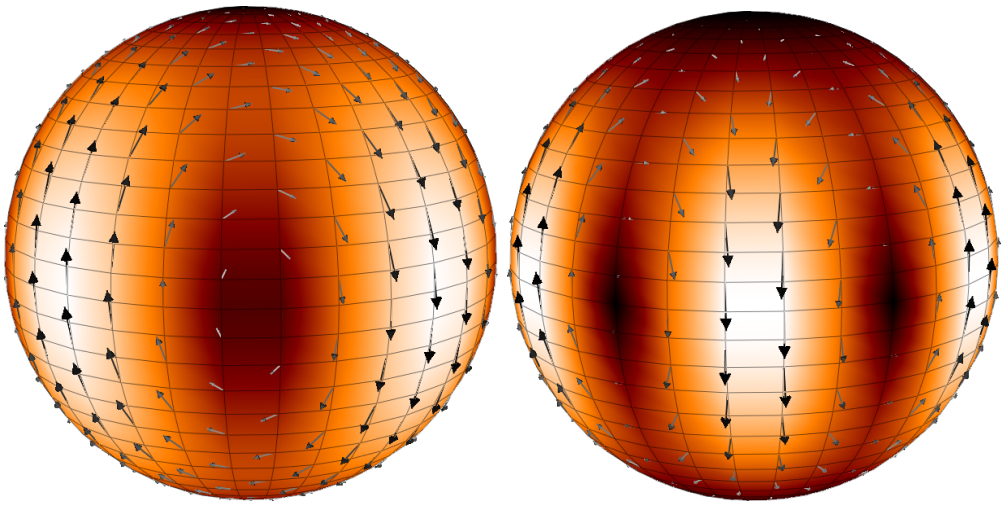

(e) w_2^2 (f) w_3^3

Figure 2.2: Toroidal motion on the surface of a sphere for constant w_γ.

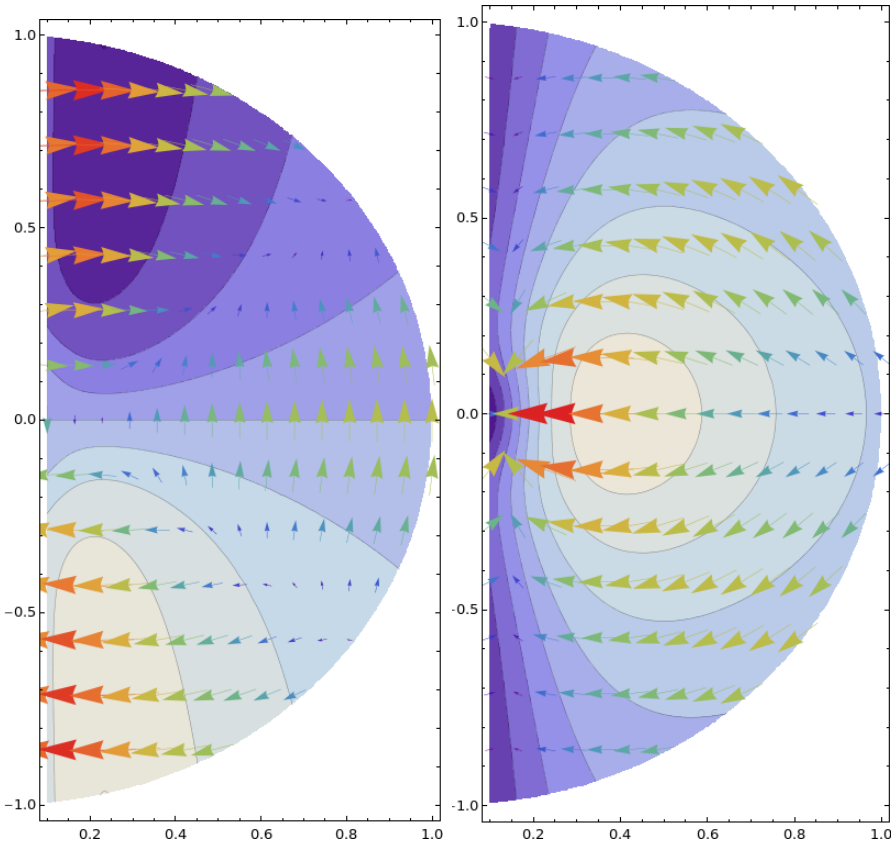

(a) $Z_3^2 + Z_3^{-2}$ (dipolar) (b) $Z_3^3 - Z_3^{-3}$ (quadrupolar)

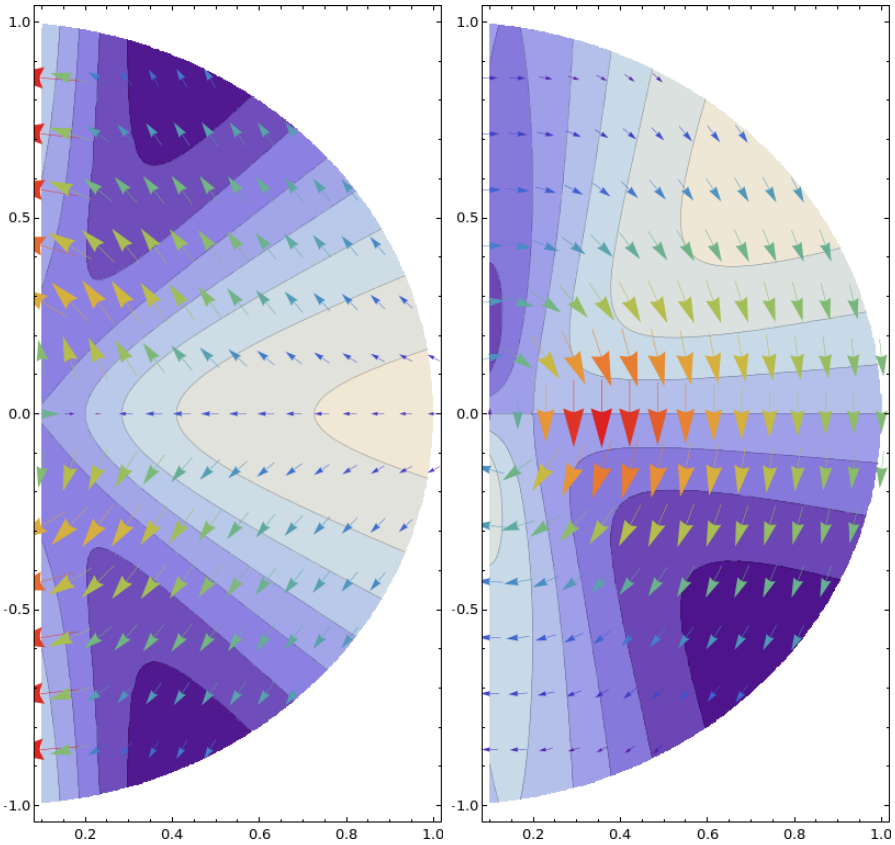

(c) $S_3^2 + S_3^{-2}$ (quadrupolar) (d) $S_3^3 - S_3^{-3}$ (dipolar)

Figure 2.3: Slices of some nonaxisymmetric vector harmonics through $\varphi = 0$. Vectors illustrate the θ-component, and contours the φ-component.

2.4.1 Derivatives of vector harmonics in 1+2 split

To calculate covariant derivatives without introducing coordinates on $\mathcal{S}^2$, the relevant Christoffel symbols must first be found. Starting with the definition of the covariant derivative

$$\nabla_\nu \mathbf{v}^\mu = \partial_\nu \mathbf{v}^\mu + \tfrac{1}{2}\mathbf{v}^\kappa g^{\mu\lambda}\left(\partial_\nu g_{\lambda\kappa} + \partial_\kappa g_{\lambda\nu} - \partial_\lambda g_{\kappa\nu}\right), \tag{2.4.10}$$

we insert our metric (2.3.1) and calculate derivatives for the combinations of radial and angular indices. As an example, we show that

$$\begin{aligned}\nabla_B \mathbf{v}^A &= \partial_B \mathbf{v}^A + \tfrac{1}{2}\mathbf{v}^\kappa g^{A\lambda}\left(\partial_B g_{\lambda\kappa} + \partial_\kappa g_{\lambda B} - \partial_\lambda g_{\kappa B}\right)\\ &= v^A_{\gamma|B} Y_\gamma + \tfrac{1}{2}\mathbf{v}^\kappa g^{AC}\left(\partial_B g_{C\kappa} + \partial_\kappa g_{CB} - \partial_C g_{\kappa B}\right)\\ &= v^A_{\gamma|B} Y_\gamma.\end{aligned} \tag{2.4.11}$$

Derivation of the other quantities follows a similar method and leads to the following useful relations:

$$\nabla_B \mathbf{v}^A = v^A_{\gamma\,|B}\, Y_\gamma, \tag{2.4.12}$$

$$\nabla_B \mathbf{v}^a = (u_{\gamma|B} + r_B u_\gamma) Z^a + (w_{\gamma|B} + r_B w_\gamma) S^a, \tag{2.4.13}$$

$$\nabla_b \mathbf{v}^A = v^A_\gamma Z_{\gamma b} - r^2 r^A (u_\gamma Z_{\gamma b} + w_\gamma S_{\gamma b}), \tag{2.4.14}$$

$$\nabla_b \mathbf{v}^a = r_C v^C_\gamma Y_\gamma \gamma_b{}^a + u_\gamma Z^a_{\gamma:b} + w_\gamma S^a_{\gamma:b}. \tag{2.4.15}$$

It is important to remember to use the metric g to raise and lower indices so that derivatives are cast into this particular form; for example, $\nabla^\alpha \mathbf{v}^\beta = g^{\alpha\mu}\nabla_\mu \mathbf{v}^\beta$.

2.4.2 Gradient, divergence and curl in 1+2 split

Expressions for the gradient of a scalar $\nabla^\mu f$ follow from the definition of the covariant derivative of a scalar function:

$$\nabla_i f = \partial_i f \tag{2.4.16}$$

$$\implies \nabla^A f = \frac{\partial f_\gamma}{\partial r} Y_\gamma, \qquad \nabla^a f = \frac{1}{r^2} f_\gamma Z^a_\gamma. \tag{2.4.17}$$

The divergence of a vector follows from adding (2.4.12,2.4.15):

$$\nabla_i \mathbf{v}^i = (v^A_{\gamma\,|A} + 2 r_A v^A_\gamma + L^2_\gamma u_\gamma) Y_\gamma = \left(v'_\gamma + \frac{2}{r} v_\gamma + L^2_\gamma u_\gamma\right) Y_\gamma. \tag{2.4.18}$$

To find the curl

$$(\nabla \times \mathbf{v})^i = \epsilon^{ijk} \nabla_j \mathbf{v}_k, \tag{2.4.19}$$

we need to find the totally antisymmetric unit tensor ϵ^{ijk} (the Levi-Civita symbol). In 2+1 dimensions, since the slot A only represents one coordinate r, we can write

$$\epsilon^{Aab} = f(r)\,\epsilon^{ab}, \tag{2.4.20}$$

which can then be permuted. Lowering the indices gives

$$\epsilon_{Aab} = \epsilon^{Acd} g_{AA} g_{ac} g_{bd} = r^4 f\,\epsilon_{ab}. \tag{2.4.21}$$

Summation of their product over a, b lets us solve for f:

$$\begin{aligned}\sum_{a,b} \epsilon^{Aab}\epsilon_{Aab} = 2! = r^4 f^2 \epsilon^{ab}\epsilon_{ab} = 2!\; r^4 f^2 \\ \implies f(r) = 1/r^2.\end{aligned} \tag{2.4.22}$$

From this we can find the radial and angular components of the curl

$$\begin{aligned}(\nabla\times\mathbf{v})^A &= \epsilon^{Aab} r^2 \gamma_{bc}\nabla_a \mathbf{v}^c \\ &= \epsilon^{ab}\left(\frac{1}{r} v_\gamma Y_\gamma \gamma_{ab} + u_\gamma Z_{\gamma b:a} + w_\gamma S_{\gamma b:a}\right) \\ &= -L_\gamma^2 Y_\gamma w_\gamma, \\ (\nabla\times\mathbf{v})^a &= \epsilon^{aAb} r^2 \gamma_{bc}\nabla_A \mathbf{v}^c + \epsilon^{abA} g_{AC}\nabla_b \mathbf{v}^C \\ &= -\frac{1}{r^2}\epsilon^{ab}\left(r^2\gamma_{bc}\nabla_A\mathbf{v}^c - g_{AC}\nabla_b\mathbf{v}^C\right) \\ &= -\epsilon^{ab}\left[\left(u'_\gamma + \frac{2}{r}u_\gamma\right) Z_{\gamma b} + \left(w'_\gamma + \frac{2}{r}w_\gamma\right) S_{\gamma b} - \frac{1}{r^2} v_\gamma Z_{\gamma b}\right] \\ &= \left(w'_\gamma + \frac{2}{r}w_\gamma\right) Z^a_\gamma + \left(\frac{1}{r^2}v_\gamma - u'_\gamma - \frac{2}{r}u_\gamma\right) S^a_\gamma.\end{aligned} \tag{2.4.23, 2.4.24}$$

These expressions can be combined to find the vector Laplacian via the identity

$$\Delta\mathbf{v}^i = \nabla^i(\nabla_j\mathbf{v}^j) - (\nabla\times(\nabla\times\mathbf{v}))^i. \tag{2.4.25}$$

2.4.3 Products of vector harmonics (axisymmetric)

Consider the problem of finding, for example, components of the scalar $f = \mathbf{V}^i\mathbf{U}_i$ or the vector $\mathbf{W}^i = (\mathbf{V}\times\mathbf{U})^i$ for some vectors $\mathbf{V}, \mathbf{U}$. It is clear that we will need to calculate integrals involving the vector harmonics Z, S and their derivatives.

In axisymmetry this problem is made somewhat simpler due to orthogonality $\int Z^a_\alpha S_{\beta a} = 0$ causing a large class of these triple integrals to vanish. Integration by parts over the 2-sphere shows

$$\int Z^a_\alpha S_{\beta a} d\Omega = -\int Y_\alpha S^{:a}_{\beta a} d\Omega = 0 \tag{2.4.26}$$

since the second integral vanishes due to (2.4.4). The remaining integrals can be written in terms of $\hat{C}_{\alpha\beta\gamma}$, which we can calculate explicitly. Again integration by parts gives

$$\begin{aligned}
\hat{D}_{\alpha\beta\gamma} \equiv \int Y_\alpha Z^a_\beta Z_{\gamma a} d\Omega &= -\int Y_\beta \left(Z^a_\alpha Z_{\gamma a} + Y_\alpha Z^{:a}_{\gamma a} \right) d\Omega \\
&= -\int Y_\beta \left(Z^a_\alpha Z_{\gamma a} + Y_\alpha Z^{:a}_{\gamma a} \right) d\Omega \\
&= -\hat{D}_{\beta\gamma\alpha} - L^2_\gamma \hat{C}_{\alpha\beta\gamma} \\
&= \hat{D}_{\gamma\alpha\beta} + \left(L^2_\alpha - L^2_\beta \right) \hat{C}_{\alpha\beta\gamma} \\
&= -\hat{D}_{\alpha\beta\gamma} + \left(L^2_\alpha - L^2_\beta - L^2_\gamma \right) \hat{C}_{\alpha\beta\gamma} \\
&= \tfrac{1}{2} \left(L^2_\alpha - L^2_\beta - L^2_\gamma \right) \hat{C}_{\alpha\beta\gamma}, \qquad (2.4.27)
\end{aligned}$$

with the obvious special case

$$\int Z^a_\alpha Z_{\beta a} d\Omega \equiv \int S^a_\alpha S_{\beta a} d\Omega = -4\pi L^2_\alpha \delta_{\alpha,\beta}. \qquad (2.4.28)$$

Other combinations of integrals follow through similar considerations:

$$\int Y_\alpha S^a_\beta S_{\gamma a} = \hat{D}_{\alpha\beta\gamma} \qquad (2.4.29)$$

$$\int Z^a_\alpha Z_{\beta b} Z^b_{\gamma:a} = \hat{E}_{\alpha\beta\gamma} = \frac{1}{4} \left[L^4_\gamma - \left(L^2_\alpha - L^2_\beta \right)^2 \right] \hat{C}_{\alpha\beta\gamma} \qquad (2.4.30)$$

$$\int Z^a_\alpha S_{\beta b} S^b_{\gamma:a} = \hat{E}_{\alpha\beta\gamma} \qquad (2.4.31)$$

$$\int S^a_\alpha S_{\beta b} Z^b_{\gamma:a} = \hat{F}_{\alpha\beta\gamma} = \left[\frac{1}{2} \left(L^4_\alpha + L^4_\beta + L^4_\gamma \right) - \frac{1}{4} \left(L^2_\alpha + L^2_\beta + L^2_\gamma \right)^2 \right] \hat{C}_{\alpha\beta\gamma} \qquad (2.4.32)$$

$$\int S^a_\alpha Z_{\beta b} S^b_{\gamma:a} = -\hat{F}_{\alpha\beta\gamma}, \qquad (2.4.33)$$

$$\int S^a_\alpha S_{\beta b} S^b_{\gamma:a} = 0 \qquad (2.4.34)$$

Symmetries in the integrals may be spotted by swapping the indexes on the L^2 terms, and used to heavily simplify the expansions of systems of ODEs. Note that integrals containing an odd number of S's in them are identically zero in axisymmetry due to the presence of the totally antisymmetric tensor ϵ; in non-axisymmetry we must consider these separately, although equations (2.4.29-2.4.32) will still hold.

2.4.4 Products of vector harmonics (non-axisymmetric)

Consider the integral

$$\begin{aligned}
\hat{G}_{\gamma\alpha\beta} &= \int Y_\gamma Z^a_\alpha S_{\beta a} d\Omega \qquad (m_\alpha \vee m_\beta \neq 0) \\
&= i \int Y_\gamma \csc(\theta) \left(m_\alpha Y_\alpha \partial_\theta Y_\beta - m_\beta Y_\beta \partial_\theta Y_\alpha \right) d\Omega, \qquad (2.4.35)
\end{aligned}$$

which is obviously antisymmetric over α, β, and zero in axisymmetry. The derivative of a spherical harmonic satisfies

$$\partial_\theta Y_l^m = m\cot(\theta)Y_l^m + e^{-i\varphi}\sqrt{s}Y_l^{m+1}, \qquad s=(l-m)(l+m+1), \tag{2.4.36}$$

which lets us rewrite (2.4.35) as

$$\begin{aligned}\hat{G}_{\gamma\alpha\beta} &= i\int (e^{-i\varphi}\csc\theta Y_\gamma)\left(m_\alpha\sqrt{s_\beta}Y_{\ell_\alpha}^{m_\alpha}Y_{\ell_\beta}^{m_\beta+1} - m_\beta\sqrt{s_\alpha}Y_{\ell_\alpha}^{m_\alpha+1}Y_{\ell_\beta}^{m_\beta}\right)d\Omega \\ &= i\int\left(-\sqrt{\frac{3}{2}}\frac{Y_\gamma}{Y_1^1}\right)(...)\,d\Omega. \end{aligned}\tag{2.4.37}$$

Here we choose $m_\gamma > 0$ without loss of generality: we know that at least one of the m's must be positive and so we use the symmetry properties of $\hat{G}$ to place the positive m on the first term in the integral. In this case (2.1.17) shows that dividing a harmonic by $\sin\theta\, e^{i\varphi}$ gives a finite expansion in terms of descending modes,

$$\frac{Y_\ell^{m>0}}{Y_1^1} = a_1 Y_{\ell-1}^{m-1} + a_3 Y_{\ell-3}^{m-1} + ... \tag{2.4.38}$$

Multiplying by $Y_1^1 Y_\ell^{-m}$ and integrating gives the first coefficient through the triangle rule. The remaining coefficients can be found by integrating over descending values of ℓ until $\ell < m-1$:

$$4\pi = a_1\int Y_1^1 Y_{\ell-1}^{m-1}Y_\ell^{-m}d\Omega, \tag{2.4.39}$$

$$0 = a_1\int Y_1^1 Y_{\ell-1}^{m-1}Y_{\ell-2}^{-m}d\Omega + a_3\int Y_1^1 Y_{\ell-3}^{m-1}Y_{\ell-2}^{-m}d\Omega, \tag{2.4.40}$$

and so on to give a recursive relation for the a_i,

$$a_{i+2} = -a_i\frac{\int Y_1^1 Y_{\ell-i}^{m-1}Y_{\ell-i-1}^{-m}d\Omega}{\int Y_1^1 Y_{\ell-i-2}^{m-1}Y_{\ell-i-1}^{-m}d\Omega} = a_i\frac{\sqrt{\frac{(i-\ell+m)(i-1-\ell+m)}{4(i-\ell)^2-1}}}{\sqrt{\frac{(\ell+m-i-2)(\ell+m-i-1)}{(1+2i-2\ell)(3+2i-2\ell)}}}. \tag{2.4.41}$$

where a_1 is given by (2.4.39). It is possible to solve this recursion to write down a closed form expansion for $\hat{G}$ in terms of ℓ, m but the resulting expression is rather unwieldy. We can now express (2.4.37) as a finite sum of Gaunt coefficients, and implement a recursive function in most computer languages to find their values as per

```
recursive function g_hat(l1,m1,l2,m2,l3,m3)
   if(m1>0) ... //loop over a_i as outlined above
   else if(m2>0) return -g_hat(l2,m2,l1,m1,l3,m3)
   else if(m3>0) return -g_hat(l3,m3,l2,m2,l1,m1)
end function
```

An example Fortran function written for this purpose is described in appendix B.2.

The remaining integrals we need are

$$\int S^a_\alpha S^b_\beta S_{\gamma a:b} \equiv \hat{H}_{\alpha\beta\gamma} = \tfrac{1}{2}\left(L^2_\alpha - L^2_\beta + L^2_\gamma\right)\hat{G}_{\alpha\beta\gamma}, \tag{2.4.42}$$

$$\int S^a_\alpha Z^b_\beta Z_{\gamma a:b} = \hat{H}_{\beta\alpha\gamma}, \tag{2.4.43}$$

$$\int Z^a_\alpha S^b_\beta Z_{\gamma a:b} = \hat{H}_{\alpha\beta\gamma}, \tag{2.4.44}$$

$$\int Z^a_\alpha Z^b_\beta S_{\gamma a:b} = -\hat{H}_{\beta\alpha\gamma}, \tag{2.4.45}$$

where the relation to $\hat{G}$ can be shown via integration by parts.

2.5 Products of three or more harmonics

Certain systems may contain cubic-order (or higher) terms, and we should be prepared to handle these. The simplest case, a product of 3 spherical harmonics, is easy enough to deal with:

$$Y_\alpha Y_\beta Y_\nu = \left[\chi_\mu \, \hat{C}_{\alpha\beta-\mu} \, Y_\mu\right] Y_\nu = \chi_\mu\chi_\gamma \, \hat{C}_{\alpha\beta-\mu} \, \hat{C}_{\mu\nu-\gamma} \, Y_\gamma, \tag{2.5.1}$$

where of course repeated indices indicate summation over μ, γ, and α, β, ν are all interchangeable in the final result. Similarly,

$$Y_\alpha Z^a_\beta Z_{\nu a} = Y_\alpha \left[\chi_\mu \hat{D}_{-\mu\beta\nu} Y_\mu\right] = \chi_\mu\chi_\gamma \, \hat{C}_{-\gamma\alpha\mu} \, \hat{D}_{-\mu\beta\nu}, \tag{2.5.2}$$

and so on for other variants.

Taking products in a different order leads to interesting relations between integrals. Consider the following polar vector:

$$Y_\alpha Y_\beta Z^a_\mu = \left(Y_\alpha Y_\beta\right) Z^a_\mu = -\frac{1}{L^2_\gamma}\chi_\nu\chi_\gamma \hat{C}_{\alpha\beta-\nu} \, \hat{D}_{\nu\mu-\gamma} \, Z^a_\gamma \tag{2.5.3}$$

$$= Y_\alpha \left(Y_\beta \, Z^a_\mu\right) = \frac{1}{L^2_\nu L^2_\gamma}\chi_\nu\chi_\gamma \hat{D}_{\beta\mu-\nu} \, \hat{D}_{\alpha\nu-\gamma} \, Z^a_\gamma, \tag{2.5.4}$$

This implies

$$\hat{C}_{\alpha\beta-\nu} \, \hat{D}_{\nu\mu-\gamma} = -\frac{1}{L^2_\nu}\hat{D}_{\beta\mu-\nu} \, \hat{D}_{\alpha\nu-\gamma}, \tag{2.5.5}$$

into which (2.4.27) can be substituted. This leads to a cyclic property over α, β, μ within products of Gaunt coefficients:

$$\hat{C}_{\alpha\beta-\nu}\hat{C}_{\nu\mu-\gamma} \propto \hat{C}_{\beta\mu-\nu}\hat{C}_{\nu\alpha-\gamma}. \tag{2.5.6}$$

From these considerations it becomes clear that some products can be written in different

ways, and it is possible that certain choices may be more desirable than others; the problem is briefly mentioned by Brizuela *et al.* [20]. However one will still get the same *number* regardless of the order, so insofar as a computer code goes the order is almost irrelevant.

Our technique is to reduce products of three or more terms into groups of products of two terms, such as through $a \times b \times c \times d \times e = [(a \times b) \times (c \times d)] \times e$. This means that, if we were to write out the coefficients, the choice of order of multiplication depends on how we group together the terms involved, and sometimes there is a clear choice for this grouping.

One must be careful to include all multiplications when the spectral sum is truncated. For example, consider the cubic product $u = a \times b \times c$. If we expand functions and consider the couplings between $\ell = 1$ modes, then one such term is

$$u_1 = (a_0 b_1 + a_1 b_0) c_0 + \left(a_0 b_0 + \frac{9}{5} a_1 b_1 \right) c_1. \tag{2.5.7}$$

If we define a *pre-multiplication* $F = a \times b$ and truncate at $\ell_m = 1$, then

$$u_1 = F_1 c_0 + F_0 c_1 = (a_0 b_1 + a_1 b_0) c_0 + (a_0 b_0 + a_1 b_1) c_1, \tag{2.5.8}$$

which is different to (2.5.7). However if we calculate and insert F_γ for up to $\ell_m = 2$, then

$$\begin{aligned} u_1 &= F_1 c_0 + F_0 c_1 + \frac{2}{\sqrt{5}} F_2 c_1 + ... = \left[(a_0 b_0 + a_1 b_1) + \frac{4}{5} a_1 b_1 \right] c_1 + ... \\ &= \frac{9}{5} a_1 b_1 c_1 + ..., \end{aligned} \tag{2.5.9}$$

which is now correct.

In general if we have $F = a \times b$ then we need to calculate the coefficients F_γ for up to $2\ell_m$ and then *use* it for up to $2\ell_m$ to properly calculate $F \times c$. Doing so would change the skeleton spectral code we present in section 3.9 and significantly lengthen run-time.

Instead, if we were to write

$$u_\gamma = \sum_{\alpha}^{\ell_m} G_\alpha^{(\gamma)} c_\alpha \tag{2.5.10}$$

where

$$G_\alpha^{(\gamma)} = \sum_{\beta}^{2\ell_m} F_\beta \hat{C}_{\alpha\beta-\gamma} = \sum_{\beta}^{2\ell_m} \sum_{\delta,\epsilon}^{\ell_m} a_\delta b_\epsilon \hat{C}_{\delta\epsilon-\beta} \hat{C}_{\beta\alpha-\gamma}, \tag{2.5.11}$$

then the main loop of the code, represented by (2.5.10), only requires summations up to

ℓ_m. G can be computed up to $2\ell_m$ before this loop. In our example,

$$u_1 = G_0^{(1)} c_0 + G_1^{(1)} c_1, \tag{2.5.12}$$

$$G_0^{(1)} = F_1 = a_0 b_1 + a_1 b_0, \tag{2.5.13}$$

$$G_1^{(1)} = F_0 + \frac{2}{\sqrt{5}} F_2 = a_0 b_0 + \frac{9}{5} a_1 b_1, \tag{2.5.14}$$

$$\implies u_1 = (a_0 b_1 + a_1 b_0) c_0 + \left(a_0 b_0 + \frac{9}{5} a_1 b_1 \right) c_1. \tag{2.5.15}$$

In practice we see such cubic terms in the MHD equations (section 6.1). However we do not yet use this technique, since writing the evolution equations in this new manner would require some effort. The terms that we lose are multiples of the higher modes, which are typically set to be small, and the code is unlikely to differ much (at least in the lower modes that we are most concerned with) without them. One should test a result that is dependent on cubic interactions with a higher ℓ_m to determine if this truncation is important.

2.6 Real spherical harmonics

It is possible to define real-valued spherical harmonics through

$$y_\ell^m \equiv \begin{cases} Y_\ell^0, & (m = 0) \\ \frac{1}{\sqrt{2}} \left(Y_\ell^{-|m|} + (-1)^m Y_\ell^{|m|} \right), & (m > 0) \\ \frac{i}{\sqrt{2}} \left(Y_\ell^{-|m|} - (-1)^m Y_\ell^{|m|} \right). & (m < 0) \end{cases} \tag{2.6.1}$$

They too form a basis for spherical functions, and one may also construct vector harmonics from them.

They have the benefit over the complex-valued counterparts in that calculations need only be performed with real numbers and so should achieve savings in memory and run-time. Although real spherical harmonics are often considered as being harder to manipulate, we only require knowing their actual form for visualization and for calculating the required real-harmonic Gaunt coefficients, defined by

$$\hat{c}_{\alpha\beta\gamma} = \int y_\alpha \, y_\beta \, y_\gamma \, d\Omega. \tag{2.6.2}$$

We should now like to know what requirements there are on the modes that give non-zero integrals.

Firstly, the triangle inequality and and even-sum conditions of the ℓ's should hold. The real harmonics are concerned with changes to the mode numbers; if we were to write (2.6.2) in terms of $\hat{C}_{\alpha\beta-\gamma}$ then the conditions on ℓ are the same.

There are seven permutations of signs on the m's that we need to consider: all positive, one negative and two positive, two negative and one positive, and all negative, as well as the three permutations with a zero mode.

Let us consider the second case, where $M, M' > 0$, $M'' < 0$ and with $M+M'+M'' = 0$. The integral of three such real harmonics is given by

$$\begin{aligned}
&\int y_\ell^M \, y_{\ell'}^{M'} \, y_{\ell''}^{M''} d\Omega \\
&\quad = \frac{i}{2\sqrt{2}} \int \left(Y_\ell^{-M} + (-1)^M Y_\ell^M \right) \left(Y_{\ell'}^{-M'} + (-1)^{M'} Y_{\ell'}^{M'} \right) \left(Y_{\ell''}^{M''} - (-1)^{M''} Y_{\ell''}^{-M''} \right) \\
&\quad = \frac{i}{2\sqrt{2}} \int \left((-1)^{M+M'} Y_\ell^M Y_{\ell'}^{M'} Y_{\ell''}^{M''} - (-1)^{m''} Y_\ell^{-M} Y_{\ell'}^{-M'} Y_{\ell''}^{-M''} \right) \\
&\quad = 0.
\end{aligned} \tag{2.6.3}$$

Of the initial eight terms, six have vanished after integrating as they do not satisfy the condition on the sum of M's. The remaining two cancel each other, since $(-1)^{M''} = (-1)^{M+M'}$ and because the integral of three spherical harmonics is invariant under a sign change on all the M's (2.2.17). Ultimately it should be obvious from comparing real and complex components of (2.6.3) that this integral must vanish. For this very reason, we can conclude that an integral of real spherical harmonics with an odd number of negative m's is zero.

For the remaining combinations of modes, we can reduce a triple-integral of real harmonics into three triple-integrals of complex harmonics, of which only one can satisfy the zero-sum condition.

The condition on the modes for integrating real spherical harmonics is thus: given m, m' we find the m'' that satisfy $\{m + m' - m'' = 0,\, m + m'' - m' = 0,\, m'' + m' - m = 0\}$ and choose from these so that there are not an odd number of negative modes in total. This gives one or two choices for m''. The general form of this integral, for $|m_\alpha| \leq |m_\beta| < |m_\gamma|$, is

$$\hat{c}_{\alpha\beta\gamma} = (-1)^{m_\gamma} f(m_\alpha) \hat{C}^{|m_\alpha|,|m_\beta|,-|m_\gamma|}_{\ell_\alpha,\ell_\beta,\ell_\gamma} \qquad f(m) = \begin{cases} 1 & \text{if } m = 0, \\ \frac{1}{\sqrt{2}} & \text{otherwise.} \end{cases} \tag{2.6.4}$$

For example, the combination $m = -1, m' = 2$ gives the options $m'' = 1, 3, -3$, and we pick $m'' = -3$ so as to have two negative m's. Their integral is

$$\int y_\ell^{-1} y_{\ell'}^2 y_{\ell''}^{-3} = \frac{1}{\sqrt{2}} \int Y_\ell^1 Y_{\ell'}^2 Y_{\ell''}^{-3} = \int y_\ell^1 y_{\ell'}^2 y_{\ell''}^3. \tag{2.6.5}$$

As such, if one were to consider real spherical harmonics as a basis, there is a different, more complicated condition on the values that m can take, but one would expect to achieve further savings in memory (half) and computation time (quarter in axisymmetry,

half otherwise if there is a reality condition to impose). However for ease of manipulation, this thesis concerns itself with the complex harmonics.

Chapter 3

Numerical Toolbox

The systems of equations that we will be interested in are time evolutions of hyperbolic systems: changes in quantities over time are related to the physical (spatial) properties, which are initially prescribed and go on to provide a unique solution. In our case, the spectral expansion we use will reduce these systems so that they only evolve over one spatial dimension, the radial direction r. To do this, we initially[1] generate a grid of N points over the range $0 \leq r \leq r_{\mathsf{max}}$, with constant grid spacing $h = r_{\mathsf{max}}/N$. We update the values of scalars and vectors on the grid at N_t time steps. This chapter will describe a variety of well-known techniques for writing evolution codes on such a fixed grid.

3.1 Numerical differentiation

To calculate derivatives numerically we will use a *finite difference method* of some kind. Taylor's theorem approximates a function at a point if derivatives nearby are known; for some small, fixed h,

$$\begin{aligned} f(r+h) &= f(r) + hf'(r) + \tfrac{1}{2}h^2 f''(r) + ..., \\ f(r-h) &= f(r) - hf'(r) + \tfrac{1}{2}h^2 f''(r) + ... \end{aligned} \tag{3.1.1}$$

Rearranging these expressions lets us evaluate $f'(r)$, as well as higher-order derivatives, in several different ways:

$$f'(r) = \frac{f(r+h) - f(r)}{h} + \mathcal{O}(h) \simeq \frac{\Delta_h[f](r)}{h}, \qquad \text{(forward difference)} \tag{3.1.2}$$

$$= \frac{f(r) - f(r-h)}{h} + \mathcal{O}(h) \simeq \frac{\nabla_h[f](r)}{h}, \qquad \text{(backward difference)} \tag{3.1.3}$$

$$= \frac{f(r+h) - f(r-h)}{2h} + \mathcal{O}(h^2) \simeq \frac{\delta_h[f](r)}{2h}. \qquad \text{(central difference)} \tag{3.1.4}$$

[1] We later consider a *staggered* grid at half-integer spacings

A central difference operator δ_h is the most efficient of these, since it is the only two-point stencil giving $\mathcal{O}(h^2)$ accuracy: it is *second-order accurate*.

Essentially, using one of these finite difference methods lets us approximate derivatives to any order of accuracy. Adding more grid points by decreasing h in turn decreases the error, but it does not change the *order* of the error. A higher order scheme should give a more accurate approximation to the real solution for far less work than increasing the resolution. To do this we need to use more points to calculate derivatives. For example, first derivatives that are fourth-order accurate are given by

$$f'(r) = \frac{-f(r+2h) + 8f(r+h) - 8f(r-h) + f(r-2h)}{12h} + \mathcal{O}(h^4), \tag{3.1.5}$$

and second derivatives by

$$f''(r) = \frac{f(r+h) - 2f(r) + f(r-h)}{h^2} + \mathcal{O}(h^2) \tag{3.1.6}$$

$$= \frac{-f(r+2h) + 16f(r+h) - 30f(r) + 16f(r-h) - f(r-2h)}{12h^2} + \mathcal{O}(h^4). \tag{3.1.7}$$

3.2 Numerical integration

We may also need to calculate the integral of various quantities, for example the energy of a fluid (section 5.5.2), or perhaps to solve the Poisson equation for the gravitational potential. There are a number of different techniques that allow us to do this

One of the simplest ways to numerically integrate is via the *trapezium rule*, whereby the area under a curve is approximated by the area of a trapezium. The same result can be derived by integrating the Taylor series expansion about the lower limit, which has the benefit of giving an error estimate:

$$\begin{aligned}\int_a^{a+h} f(r)\,dr &= \int_a^{a+h} \left[f(a) + (r-a)f'(a) + \tfrac{1}{2}(r-a)^2 f''(a) + ...\right] dr \\ &= hf(a) + \tfrac{1}{2}h^2 f'(a) + \tfrac{1}{6}h^3 f''(a) + ... \\ &= \tfrac{1}{2}hf(a) + \tfrac{1}{2}h\left[f(a) + hf'(a) + ...\right] + ... \\ &= \tfrac{1}{2}h\left[f(a) + f(a+h)\right] + \mathcal{O}(h^3).\end{aligned} \tag{3.2.1}$$

By repeating this process for the interval between each grid point, one has the composite trapezium rule:

$$\begin{aligned}\int_0^{r_{\mathsf{max}}} f(r)\,dr &= h\left[\frac{f(0) + f(r_{\mathsf{max}})}{2} + \sum_{i=1}^{N-1} f(i\,h)\right] + \mathcal{O}(h^2) \\ &\simeq \tfrac{1}{2}h\left[f(0) + 2f(h) + 2f(2h) + ... + f(r_{\mathsf{max}})\right].\end{aligned} \tag{3.2.2}$$

The error estimate has changed since there is a cumulative error $N\mathcal{O}(h^3) \sim \mathcal{O}(h^2)$.

Many more techniques of numerical integration are known. For example, the composite Simpson's rule has a higher order of accuracy:

$$\int_0^{r_{\mathsf{max}}} f(r)\,dr = \tfrac{1}{3}h\left[f(0) + 2\sum_{i=1}^{N/2-1} f(2\,i\,h) + 4\sum_{i=1}^{N/2} f(2\,i\,h-1) + f(r_{\mathsf{max}})\right] + \mathcal{O}(h^4)$$
$$\simeq \tfrac{1}{3}h\left[f(0) + 4f(1) + 2f(2) + 4f(3) + ... + f(r_{\mathsf{max}})\right]. \qquad (3.2.3)$$

3.3 Ghost points

In order to evaluate derivatives at and close to 0 and r_{max}, we introduce a number of *ghost points* on either end of the grid, so that now $-G \leq r \leq r_{\mathsf{max}} + G$. The range $-G \leq r < 0$ is usually referred to the *left ghost zone*, and the range $r_{\mathsf{max}} < r \leq r_{\mathsf{max}} + G$ as the *right ghost zone*. We may sometimes refer to the rest as the *physical* part of the grid. To avoid the obvious recursion of having to add points to evaluate derivatives at the new end-points, we look for alternative ways to calculate the value of f inside these regions, and only bother to find derivatives f' on the physical grid.

For the left ghost zone it will be the case that we deal only with functions that are either even or odd in r, and it should be simple to set $f(-r) = \pm f(r)$ as required.

The right ghost zone will be more complicated since there is (usually) no symmetry condition. One needs to consider what physical conditions may hold for various systems, and then how to express them mathematically: that is, how to turn a *continuum* boundary condition into a numerical boundary condition. For example, a vibrating string with displacement $u(r,t)$ may have the boundary conditions $u(0,t) = u(L,t) = 0$ imposed if it is fixed at both ends.

The particular conditions that we use are explained in more detail in the relevant chapters. Having a boundary condition is necessary for the *well-posedness* of the problem, that is, that a solution exists, is unique, and depends continuously on the initial data.

3.4 Runge-Kutta methods

We will use a forth-order accurate Runge-Kutta method to calculate time derivatives. (Note that, in the following explanation only, the subscripts refer to discrete time steps: $u_n = u(r, t_n)$.) For the problem

$$\dot{u} = f(t,u), \qquad (3.4.1)$$

the RK4 method is given by

$$u_{n+1} = u_n + \frac{h}{6}(k_1 + 2k_2 + 2k_3 + k_4), \tag{3.4.2}$$

where

$$\begin{aligned} k_1 &= f\left(t_n, u_n\right), \\ k_2 &= f\left(t_n + \tfrac{1}{2}\delta t, u_n + \tfrac{1}{2}hk_1\right), \\ k_3 &= f\left(t_n + \tfrac{1}{2}\delta t, u_n + \tfrac{1}{2}hk_2\right), \\ k_4 &= f\left(t_n + \delta t, u_n + hk_3\right). \end{aligned} \tag{3.4.3}$$

The error per time step is $\mathcal{O}(h^4)$ which will be much smaller than that from a second-order accurate finite differencing code.

Another reason as to why we use RK4 is that we only need one set of initial data for a high-order of accuracy. Although a typical RK4 methods requires 4 iterations for each time step, and 4 levels of storage, it is relatively simple to implement and it only requires one set of initial data.

A basic computer implementation of RK4 may actually require 5 levels of storage, due to each of the $u_n + hk_i$ terms. However, *true* 3-level schemes are well known [24], such as the following which is equivalent to (3.4.3):

$$\begin{aligned} U &= u_n \\ G &= U \\ P &= f(t_n, U), \\ \\ U &= U + \tfrac{1}{2}hP \\ G &= P \\ P &= f(t_n + \tfrac{1}{2}\delta t, U), \\ \\ U &= U + \tfrac{1}{2}h(P - G) \\ G &= \tfrac{1}{6}G \\ P &= f(t_n + \tfrac{1}{2}\delta t, U) - \tfrac{1}{2}P, \\ \\ U &= U + hP \\ G &= G - P \\ P &= f(t_n + \delta t, U) + 2P, \\ u_{n+1} &= U + \delta t(G + \tfrac{1}{6}P). \end{aligned} \tag{3.4.4}$$

In our code the size of a time-step δt is proportional to the grid spacing (the *Courant condition*). In addition our equations deal with non-dimensional units set to one, so we evolve with $\delta t = \frac{1}{2}h$. Multiplication by the total number of time steps gives another non-dimensional number that represents the real time simulated (section 5.2.2). If we double the resolution, we need to double the time-steps to represent a synchronous evolution, and should expect to see a four-fold increase in run-time.

3.5 Convergence

The most important check that should be made of a numerical code is that of *convergence*. Essentially, increasing the grid resolution, truncation limit, etc. should mean our numerical solution gives a more accurate representation of the actual solution of the PDE. Convergence can be defined more exactly by saying that we require a numerical solution u representing the exact solution U at any point (x_j, t_n) to satisfy

$$\lim_{h\to 0}\lim_{\delta t\to 0} ||U(x_j,t_n) - u(x_j,t_n)|| = 0. \tag{3.5.1}$$

There are three sources of approximation error in our numerical code: truncation error, from neglecting terms in the series where $\ell > \ell_m$; discretization error, from representing a continuous function as a discrete one; and round-off error, from floating point arithmetic. It is the first two of these which are the most important to analyse, since the latter we can more or less estimate and is usually unimportant when working in double precision arithmetic.

A numerical method is said to be *stable* if it dampens these approximation errors, and *consistent* if the discretization errors tend to zero as the resolution is increased. The Lax Equivalence theorem states that a stable and consistent scheme for a linear initial value problem is convergent, although it can be extended to show the same is true for non-linear systems. For a given system of PDEs, it is difficult to construct an argument to prove that a particular numerical solution does converge to the actual one. Thankfully it is easy to test if it does by comparing the difference between solutions at different levels of resolution.

An n-th order accurate discrete representation of a radial function can be Taylor expanded in some small h as

$$f(r+h) = f(r) + \sum_n^N \frac{h^n}{n!} f^{(n)}(r) + \mathcal{O}(h^{N+1}). \tag{3.5.2}$$

Double the resolution, and then double it again:

$$\begin{aligned} f(r+\tfrac{1}{2}h) &= f(r) + \frac{h^n}{2^n n!} f^{(n)}(r) + \mathcal{O}(h^{n+1}), \\ f(r+\tfrac{1}{4}h) &= f(r) + \frac{h^n}{4^n n!} f^{(n)}(r) + \mathcal{O}(h^{n+1}). \end{aligned} \tag{3.5.3}$$

These expansions should therefore satisfy

$$f(r+h) - f(r+\tfrac{1}{2}h) = \epsilon \left(f(r+\tfrac{1}{2}h) - f(r+\tfrac{1}{4}h) \right), \quad \epsilon = 2^n, \tag{3.5.4}$$

where ϵ is often referred to as the *convergence factor*. For a second-order accurate differencing scheme its value is 4, and for fourth-order, 16.

To check the radial convergence of an evolution code, one could simply run it 3 times at differing resolutions, writing the output to disk at appropriate (i.e. 'shared') time steps and grid points. Post-processing and then plotting the differences allows for visual inspection of convergence. A tool such as gnuplot makes this simple, as one can use a command like

```
plot "< paste res1/data res2/data" u 1:($2-$4),\
     "< paste res2/data res4/data" u 1:(4*($2-$4))
```

to check for second-order convergence without any post-processing. Convergence testing in such a manner allows us to do more than simply check that a certain finite differencing scheme is n-th order accurate: it also lets us ensure the boundary conditions we apply are indeed consistent and stable.

The angular convergence of our code should simultaneously be tested by measuring the difference (at fixed h) between numerical solutions found with increasing ℓ_m. One expects to see exponential angular convergence as a consequence of the spectral method used.

3.6 Artificial dissipation

A form of artificial dissipation may be included in order to suppress fast growing, high frequency components (i.e. oscillations with a wavelength $\leq h$) that may appear in our numerical solution after a finite number of time steps. To remove them in a way that does not affect convergence, we typically implement a *Kreiss-Oliger scheme* [48] whereby a higher order derivative is subtracted, at some or all physical grid points, at every time step.

The general idea for Kreiss-Oliger dissipation is, for a $(2r-2)$–order accurate scheme, to add a term

$$\dot{u} = f(u) + \lambda (-1)^r h^{2r-1} u^{(2r)}. \tag{3.6.1}$$

Subtracting this term is consistent as it tends to zero as h does.

For a second-order accurate code, we should subtract

$$\begin{aligned} \dot{u} &= f(u, u^{(n)}) - S(u), \\ S(u) &= \frac{\lambda}{16\,h} \left(u_{i+2} - 4u_{i+1} + 6u_i - 4u_{i-1} + u_{i-2}, \right) = \lambda\, h^3\, u'''' + \mathcal{O}(h^4) \end{aligned} \tag{3.6.2}$$

where $0 \leq \lambda < 1$ and is the same value for all variables. It is made smaller for higher order accurate finite differencing schemes; in our code we typically set it to be approximately 0.1.

3.7 Finite differencing the wave equation

As we shall see in chapter 4 the wave equation in spherical harmonics can be written as an infinite set of first order PDEs,

$$\dot{\Phi}_\gamma = \Pi'_\gamma, \tag{3.7.1}$$

$$\dot{\Pi}_\gamma = \Phi'_\gamma + \frac{2(\ell+1)}{r}\Phi_\gamma. \tag{3.7.2}$$

Finite differencing this kind of term on a regular grid becomes unstable at the origin with increasing spatial resolution and ℓ (section 4.3). Since stable numerical treatment of this term is later necessary for the hydrodynamic equations (section 5.4) there are a number of alternative methods we can employ, with a *summation–by–parts* (SBP) technique the one we ultimately use.

A second-order accurate, two-point-stencil operator can be written by considering rewriting (3.7.2) in the form

$$\dot{\Pi}_\gamma = (2\ell+3)\frac{\partial(r^{2\ell+2}\Phi_\gamma)}{\partial r^{2\ell+3}}, \tag{3.7.3}$$

the RHS of which can be finite-differenced through applying a second-order central differencing scheme to both the numerator and denominator:

$$(\dot{\Pi}_\gamma)_{(i)} = \frac{r^{2\ell+2}_{(i+1)}(\Phi_\gamma)_{(i+1)} - r^{2\ell+2}_{(i-1)}(\Phi_\gamma)_{(i-1)}}{r^{2\ell+3}_{(i+1)} - r^{2\ell+3}_{(i-1)}} \tag{3.7.4}$$

This scheme cannot be extended to a higher order of accuracy as it would give a zero denominator.

An SBP scheme conserves the energy of a system given appropriate boundary conditions, which eventually allows one to calculate r-dependent *weights* gives to terms in an n-point stencil. Full details are presented in [47]; our code currently employs a 3-point, second-order accurate SBP scheme whose stability for high ℓ or low h is comparable to the two-point operator above. The SBP method can be extended to higher-order accuracy, although the weights are difficult to derive and so left to later work.

3.8 Calculation of spherical harmonics and Gaunt coefficients

For visualization we require expressions for Y, Z^a, S^a, either in Cartesian or polar coordinates. As such we need the following identities and recurrence relations for associated Legendre

polynomials:

$$
\begin{aligned}
P_0^0(\cos\theta) &= 1, \qquad P_1^0(\cos\theta) = \cos\theta, \\
P_{\ell+1}^m(\cos\theta) &= \frac{(2\ell+1)P_\ell^m(\cos\theta)\cos\theta - (\ell+m)P_{\ell-1}^m(\cos\theta)}{\ell-m+1}, \\
P_\ell^{m+1}(\cos\theta) &= \frac{(\ell-m)P_\ell^m(\cos\theta)\cos\theta - (\ell+m)P_{\ell-1}^m(\cos\theta)}{\sqrt{1-\cos^2\theta}}, \qquad P_\ell^{m\neq 0}(\pm 1) = 0, \\
\frac{dP_\ell^m(\cos\theta)}{d\theta} &= -\sin\theta \frac{dP_\ell^m(\cos\theta)}{d(\cos\theta)} = -\sin\theta\left[\frac{\ell P_\ell^m(\cos\theta)\cos\theta - (\ell+m)P_{\ell-1}^m(\cos\theta)}{\cos^2\theta - 1}\right].
\end{aligned}
\tag{3.8.1}
$$

These may be used with (2.1.15) to calculate explicit values of Y_ℓ^m.

In order to calculate Gaunt coefficients we use the method of Wigner 3j symbols, as (2.2.9) is relatively simple to implement (and because we do not need the coefficients in closed-form). We pre-calculate these before running any time evolution, storing their values in a 3-dimensional array where slots are referenced using the multi-indexes. Doing so is somewhat memory inefficient since it does not take advantage of the symmetry of Gaunt coefficients but it is less memory-intensive than allocating a sparse five-dimensional array.

3.9 Skeleton of a simple spectral code

For systems of PDEs that are first-order in time, we shall aim to write down the time derivatives $\dot{u}_\gamma$ on the left-hand side. For each of these γ–modes, of which there are $\mathcal{O}(\ell_m^2)$ to compute, there is a quadratic product on the right hand side, of which there is a sum containing $\mathcal{O}(\ell_m^3)$ terms. Hence we expect the code to scale approximately as $\mathcal{O}(\ell_m^5)$ in full 3D as more angular resolution is added.

In order to avoid zero-valued Gaunt coefficients, we should take account of section 2.2.1 when picking the values of the ℓ's. We will also handle couplings with the 0-mode separately as these expressions will often reduce. Finally, we sum over the degrees and modes because they may appear explicitly in the equations. As such, a pseudo-code (in the style of Fortran) using complex spherical harmonics may read as follows:

```
//Calculate "background" and apply boundary conditions: udot(0) = {0,0}
DO l1 = 1,l_max
DO m1 = 0,l1
   gamma = multiindex(l1,m1)
   gammaneg = multiindex(l1,-m1)
   //Linear terms: udot(gamma) = {0,gamma}
   //Quadratic changes to background: udot(0) += {gamma,gammaneg}
   DO l2 = 1,l_max
   DO m2 = -l2,l2
```

```
      alpha = multiindex(l2,m2)
      m3 = m1-m2
      lower_l3 = MAX(1,l1-l2,ABS(m3))
      IF(is_odd(l1+l2+lower_l3)) lower_l3 = lower_l3 + 1
      upper_l3 = MIN(l_max,l1+l2)
      DO l3 = lower_l3,upper_l3,2
         beta = multiindex(l3,m3)
         //Call or calculate relevant C3 Gaunt coefficients
         //Quadratic couplings: udot(gamma) += {alpha,beta}
      END DO
   END DO
   END DO
   //Similar loop to calculate G3 Gaunt coefficients
   //Apply boundary conditions and dissipation to u(gamma)
   //If m1=0: udot(gamma) = REAL(udot(gamma))
   //If m1>0: udot(gammaneg) = (-1)^m CONJG(udot(gamma))
END DO
END DO
```

This algorithm only deals with the $\hat{C}$ integrals: $\hat{G}$ requires very similar loops over *odd* sums of ℓ's.

If one requires axisymmetry, or only positive m, then the code is easily modified to accommodate this with a switch that returns $0, -\ell$ or ℓ:

```
DO mn = axisymmetry_switch(-ln),axisymmetry_switch(ln) ...
```

Similarly, the `multiindex` function should return ℓ if axisymmetry is required to achieve a significant memory saving.

At first glance this set-up looks well suited for parallelization. If the code is written in such a way that the mode calculations are parallel ℓ, m inner loops to a serial outer time loop, the standard API for Fortran parallelization (OpenMP) incurs serious overhead in creating multiple new threads at every time step. One would prefer to initially create a number of threads equal to the number of available processor cores and pass them work, but this does not seem possible with the current OpenMP API. In any case, we are ultimately interested in comparing evolutions with different parameters and it may be desirable to instead run multiple instances of code on different cores at the same time.

Chapter 4

3D Wave Equation

Before launching straight into fluids and MHD, we first investigate a simpler system whose analysis will help us later on. Consider the linear wave equation in three dimensions,

$$\Box\Phi = 0, \tag{4.0.1}$$

which can be re-written as

$$\begin{aligned}\dot{\Phi} &= \Pi,\\ \dot{\Pi} &= \Delta\Phi = \nabla_j\nabla^j\Phi = \left(\nabla^A\nabla_A + \nabla^a\nabla_a\right)\Phi.\end{aligned} \tag{4.0.2}$$

We now decompose Π, Φ as

$$\begin{aligned}\Pi &= \sum_{\ell,m} Y_\ell^m(\theta,\phi)\ \Pi_\ell^m(r,t) = Y_\gamma\Pi_\gamma,\\ \Phi &= \sum_{\ell,m} Y_\ell^m(\theta,\phi)\ \Phi_\ell^m(r,t) = Y_\gamma\Phi_\gamma,\end{aligned} \tag{4.0.3}$$

and insert them into (4.0.2) to give

$$\begin{aligned}\dot{\Phi}_\gamma &= \Pi_\gamma,\\ \dot{\Pi}_\gamma &= \Phi''_\gamma + \frac{2}{r}\Phi'_\gamma - \frac{\ell(\ell+1)}{r^2}\Phi_\gamma.\end{aligned} \tag{4.0.4}$$

4.1 Regularization

To remove the coordinate singularity in (4.0.4) consider a transformation into Cartesian coordinates:

$$x = r\sin\theta\cos\varphi, \qquad y = r\sin\theta\sin\varphi, \qquad z = r\cos\theta. \tag{4.1.1}$$

We may also set $m = 0$ without loss of generality: from (2.1.17) the highest order terms in Y_ℓ^0 are $(\cos\theta)^\ell$, and thus, to highest order,

$$\Phi = Y_\gamma \Phi_\gamma \sim (\cos\theta)^\ell \Phi_\gamma = \frac{z^\ell}{r^\ell}\Phi_\gamma. \tag{4.1.2}$$

Hence we should rescale as

$$\Phi_\gamma = r^\ell \bar{\Phi}_\gamma, \tag{4.1.3}$$

where it should be clear why we only need the highest power of $\cos\theta$. This is a process we repeat for *all* scalars, including Π, which transforms (4.0.2) into

$$\begin{aligned} \dot{\bar{\Phi}}_\gamma &= \bar{\Pi}_\gamma, \\ \dot{\bar{\Pi}}_\gamma &= \bar{\Phi}''_\gamma + \frac{2(\ell_\gamma + 1)}{r}\bar{\Phi}'_\gamma, \end{aligned} \tag{4.1.4}$$

for each γ-mode.

Parity of spherical harmonics explains why the barred variables are even functions of r. Consider the rotation of a point around the origin to its opposite position, and then a reflection back to the original point:

$$f(r,\theta,\varphi) = f(-r, \pi - \theta, \pi + \varphi). \tag{4.1.5}$$

Using the identity

$$Y_\gamma(\theta,\varphi) = (-1)^\ell Y_\gamma(\pi - \theta, \pi + \varphi), \tag{4.1.6}$$

expanding (4.1.5) for some γ-dependent power x gives

$$r^x Y_\gamma(\theta,\varphi) = (-r)^x Y_\gamma(\pi - \theta, \pi + \varphi) = (-1)^{\ell + x} r^\ell Y_\gamma(\theta,\varphi), \tag{4.1.7}$$

and hence $x = \ell$ plus even integers. The regularization of vectors, which follows in a similar fashion, will be demonstrated in section 5.2.1.

4.2 Reality condition

Physical variables should remain real valued. If we enforce $\Phi \in \mathbb{R}$,

$$\begin{aligned} \Phi &= Y_\gamma \Phi_\gamma, \\ \Phi^* &= {Y_\gamma}^* {\Phi_\gamma}^* = (-1)^m \, Y_{-\gamma} {\Phi_\gamma}^* \end{aligned} \tag{4.2.1}$$

Equating these two implies

$$\Phi_{-\gamma} = (-1)^{m_\gamma} {\Phi_\gamma}^*. \tag{4.2.2}$$

This condition is true for all real variables and can be exploited for memory and time savings (section 3.9) if summations are run only over positive m-modes. It must also be adhered to when generating nonaxisymmetric initial data. We therefore treat all $m \neq 0$ components as complex-valued functions; the $m = 0$ modes *must* be real.

4.3 Second-order in space, first-order in time linear code

To evolve the linear wave equation, following the groundwork laid in chapter 3, we create a physical grid over r, time evolve via RK4, and central finite difference the right hand sides of (4.1.4) for each γ-mode:

$$\begin{aligned}
\dot{\Phi}_{(\mathsf{RK4})(j)} &= \Pi_{(j)}, \\
\dot{\Pi}_{(\mathsf{RK4})(j)} &= \frac{\Phi_{(j+1)} - 2\Phi_{(j)} + \Phi_{(j-1)}}{(\delta r)^2} + \frac{2(\ell+1)}{r_{(j)}} \frac{\Phi_{(j+1)} - \Phi_{(j-1)}}{2\delta r}.
\end{aligned} \tag{4.3.1}$$

Recall that Φ, Π are even functions. The left ghost zone can be populated using the simple scheme $\Phi(-r,t) = \Phi(r,t)$, and similarly for Π. The singular point at the origin can be removed by applying l'Hôpital's rule to Φ'/r, so that

$$\dot{\Pi}_\gamma(0,t) = (2\ell_\gamma + 3)\, \Phi''_\gamma(0,t). \tag{4.3.2}$$

For the right ghost zones, we may for now apply a linear extrapolation scheme to the majority of them. For $j > N$, set

$$\Phi_{(j)} = \Phi_{(N)} + (j-N)\left(\Phi_{(N)} - \Phi_{(N-1)}\right), \tag{4.3.3}$$

and similarly for Π. We can of course extrapolate to higher order if necessary.

We wish to derive boundary conditions that are non-reflecting, so that returning waves do not interfere with the system. To derive such a boundary condition one may investigate the series solution of the linear wave equation. Consider P waves travelling at a speed of 1:

$$\bar{\Phi}_\gamma = \sum_{n=0}^{P} c_{n,\gamma}\, r^{k_\gamma + n}\, f_\gamma^{(n)}(r \pm t). \tag{4.3.4}$$

Inserting into (4.1.4) and dropping the γ's gives

$$\sum_n c_n \left\{ 2f^{(n+1)}\, r^{k+n-1}(1+k+\ell+n) + f_\gamma^{(n)} r^{k+n-2}(k+n)(1+k+2\ell+n) \right\} = 0. \tag{4.3.5}$$

By equating the coefficients of the powers of r to zero we get the following:

$$n = 0 : k(1 + k + 2\ell) = 0, \tag{4.3.6}$$

$$n = i : 2(1 + i + k + \ell)c_i + (1 + i + k)(2 + i + k + 2\ell)c_{i+1} = 0, \tag{4.3.7}$$

$$n = P : 1 + k + \ell + P = 0. \tag{4.3.8}$$

Combining the first and last expressions gives $\{k = 0, P = -\ell-1\}$ and $\{k = -1-2\ell, P = \ell\}$. Since P must be positive only the latter of these is valid. Thus,

$$\bar{\Phi}_\gamma = \sum^{\ell} c_{n,\gamma} r^{-1-2\ell+n} f_\gamma^{(n)}(r \pm t) \tag{4.3.9}$$

where the $c_{n,\gamma}$ are given by the recurrence relation

$$c_{i+1} = \frac{2(i-\ell)}{(i+1)(2\ell-i)} c_i, \tag{4.3.10}$$

which clearly truncates the series at $i = \ell$. This relation can be solved to give the c_i in terms of the Gamma function.

For the $\gamma = 0$ mode, the series reduces to

$$\bar{\Phi}_0 = c_0 \frac{f_0(r \pm t)}{r}, \tag{4.3.11}$$

which can be differentiated once:

$$\bar{\Phi}_0' = \pm\bar{\Pi}_0 - \frac{\bar{\Phi}_0}{r}. \tag{4.3.12}$$

This form is suitable for a central finite differencing scheme for $\ell = 0$ modes. We take outgoing waves, and apply the following scheme to the first ghost point only:

$$\bar{\Phi}_{(N+1)} = 2\delta r \left(-\Pi_{(N)} - \frac{\Phi_{(N)}}{r} \right) + \Phi_{(N-1)}. \tag{4.3.13}$$

For higher modes it might be possible to derive similar boundary conditions; for example,

$$\bar{\Phi}_1 = \frac{c_0 f}{r^3} - \frac{c_0 f'}{r^2} = \frac{\bar{\Phi}_0}{r^2} - \frac{\bar{\Pi}_0}{r}, \tag{4.3.14}$$

which could be used to give $\bar{\Phi}_1$ at the first ghost point. An implementation of proper boundary conditions on higher modes [2, 10] is perhaps unnecessary for this sandbox-code. We can of course place the boundary at a sufficient distance away from the initial data for certain problems under consideration. For simplicity we apply (4.3.13) to *all* ℓ-modes, keeping in mind that convergence may not be guaranteed for higher modes.

When all of these elements are combined into a Fortran program to evolve the linear

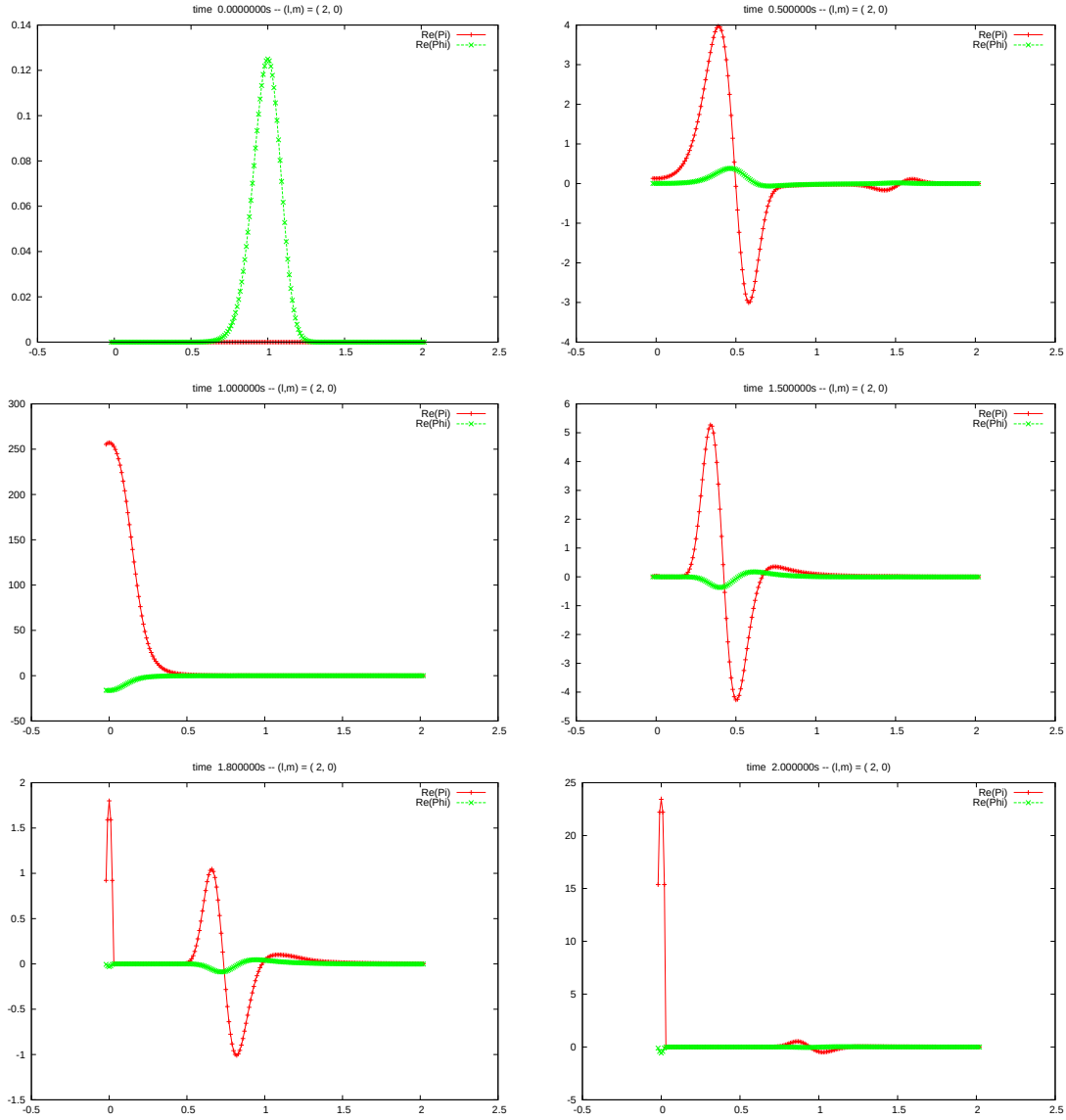

Figure 4.1: An instability at the origin is seen to arise for the second-order linear wave equation code where $\ell_m \geq 2$. Changing the grid spacing, ratio $\delta t/\delta r$, or adding artificial dissipation, do not remove it.

wave equation with Gaussian initial data

$$\Phi_\gamma(0,r) = \lambda_\gamma\, e^{-(r-1)^2}, \qquad \Pi(0,r) = 0, \tag{4.3.15}$$

we do indeed see a travelling Gaussian wave that will reflect off both boundaries (but only very slightly on the right hand side). Unfortunately, instabilities arise at the origin for $\ell = 2$ and above (figure 4.1). It is not immediately clear why this should be, so we shall try to write the equations in such a way that there is no singularity (or special treatment required) at the origin.

4.4 First-order in space linear code

To remove all second-order derivative terms and the necessity of employing l'Hôpital's rule, define a variable $\psi \equiv \Phi'$; time evolutions can now be written as

$$\dot{\Phi}_\gamma = \Pi_\gamma, \tag{4.4.1}$$

$$\dot{\Pi}_\gamma = (2\ell_\gamma + 3)\,\frac{\partial\left(r^{2\ell+2}\,\psi_\gamma\right)}{\partial\left(r^{2\ell+3}\right)}, \tag{4.4.2}$$

$$\dot{\psi}_\gamma = \Pi'_\gamma. \tag{4.4.3}$$

To finite difference this, consider taking derivatives with respect to a non-uniform grid, i.e. $u = r^{2\ell+3}$:

$$\begin{aligned}
&\frac{d(f(r))}{d(g(r))} = \frac{df}{du}\Big/\frac{dg}{du} \\
&\implies \dot{\Pi}_{(i)} = (2\ell+3)\frac{r^{2\ell+2}_{(i+1)}\psi_{(i+1)} - r^{2\ell+2}_{(i-1)}\psi_{(i-1)}}{r^{2\ell+3}_{(i+1)} - r^{2\ell+3}_{(i-1)}}.
\end{aligned} \tag{4.4.4}$$

This is regular at the origin as $2\ell + 3$ is always odd. Reducing to first–order in space also means we do not need values of Π' in the ghost zones, which would otherwise be required for (4.4.4).

We now want to build suitable boundary conditions for the right hand side. Trying a solution of the form $\Phi = f(r-t)/r$, which is only approximate for $\ell > 0$, and calculating $\dot{\Phi}'$ from it, leads to the relation

$$\Pi' + \psi' = -\frac{1}{r}\left[\Pi + 2(l+1)\psi\right]. \tag{4.4.5}$$

A central finite differencing scheme leads to

$$\Pi_{(N+1)} + \psi_{(N+1)} = \Pi_{(N-1)} + \psi_{(N-1)} - 2\frac{\delta r}{r}\left[\Pi_{(N)} + 2(\ell+1)\psi_{(N)}\right]. \tag{4.4.6}$$

This is applied through a method shown to improve stability [23]:

$$\Pi_{(N+1)} = \tfrac{1}{2}\left(\Pi_{(N+1)} + \psi_{(N+1)}\right)_{\text{(wave)}} + \tfrac{1}{2}\left(\Pi_{(N+1)} - \psi_{(N+1)}\right)_{\text{(extrapolated)}}, \tag{4.4.7}$$

$$\psi_{(N+1)} = \tfrac{1}{2}\left(\Pi_{(N+1)} + \psi_{(N+1)}\right)_{\text{(wave)}} - \tfrac{1}{2}\left(\Pi_{(N+1)} - \psi_{(N+1)}\right)_{\text{(extrapolated)}}, \tag{4.4.8}$$

The first set of brackets are given by (4.4.6), and the second by a simple linear extrapolation, as outlined earlier. For the left ghost points, we note that Φ, Π are even functions and therefore $\psi = \Phi'$ is odd.

As hoped, simulations with $\ell_m \leq 9$ and Gaussian initial data (figure 4.2) do not show any problems at the origin. However reflections from the outer boundary seem to introduce numerical oscillations, even if artificial dissipation is introduced. Since we have been applying an approximate solution for high ℓ–modes, Gibbs-like behaviour is seen: the $\ell = 9$ mode is

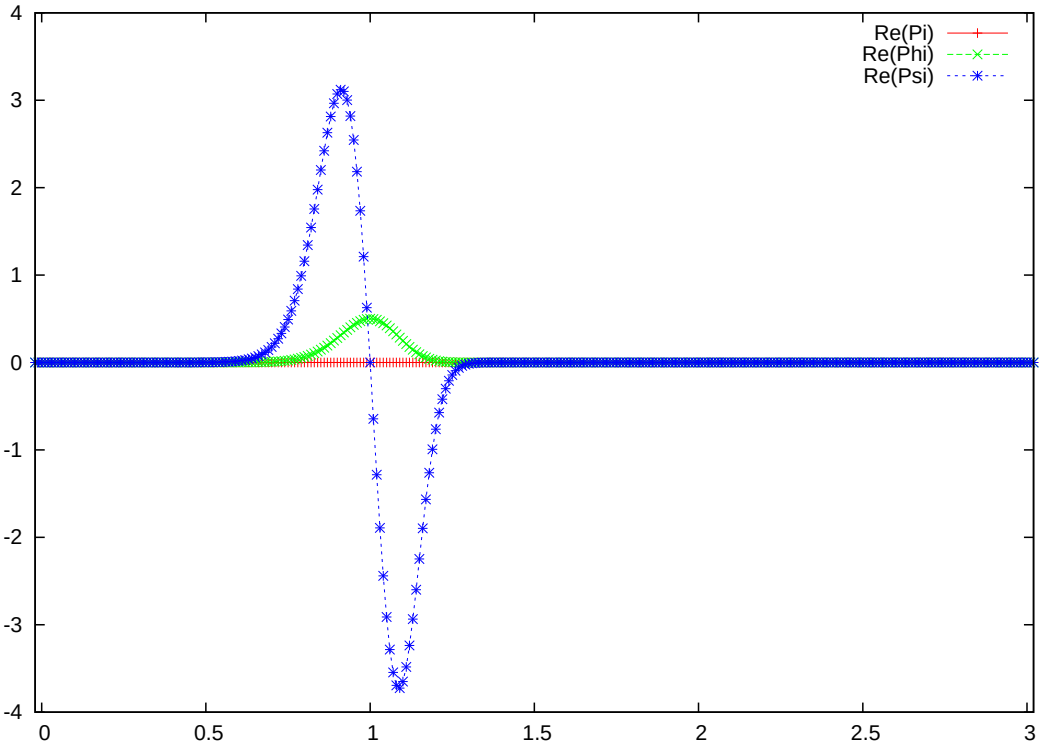

Figure 4.2: Initial data for the $\ell = 0$ mode, within a first-order code. The wave immediately breaks into left- and right-travelling components that move with the same speed. It is centred close to the origin so it reflects from there before any part can reflect off the outer boundary and reach it again.

even observed to oscillate about the origin but not travel along the grid after finite time. It should be possible to derive better behaved boundary conditions from the series solutions.

4.5 Nonlinear quadratic code

Thus far we have not considered any quadratic terms added to the wave equation. We add such a term now so we can use the skeleton code from section 3.9:

$$\Box\Phi = \kappa_2 \Phi^2. \tag{4.5.1}$$

The spectral coefficients satisfy

$$\dot{\bar{\Phi}}_\gamma = \bar{\Pi}_\gamma, \tag{4.5.2}$$

$$\dot{\bar{\Pi}}_\gamma = \bar{\Phi}''_\gamma + \frac{2(l_\gamma + 1)}{r}\bar{\Phi}'_\gamma + \kappa_2\, r^{\ell_\alpha + \ell_\beta - \ell_\gamma}\, \chi_\gamma \hat{C}_{\alpha\beta-\gamma}\, \bar{\Phi}_\alpha \bar{\Phi}_\beta, \tag{4.5.3}$$

where we sum over the multi-indexes α, β and generate the coefficients $\hat{C}_{\alpha\beta-\gamma}$ in some manner.

There is evidence that such a system will blow up in finite time [58] so we shall look for

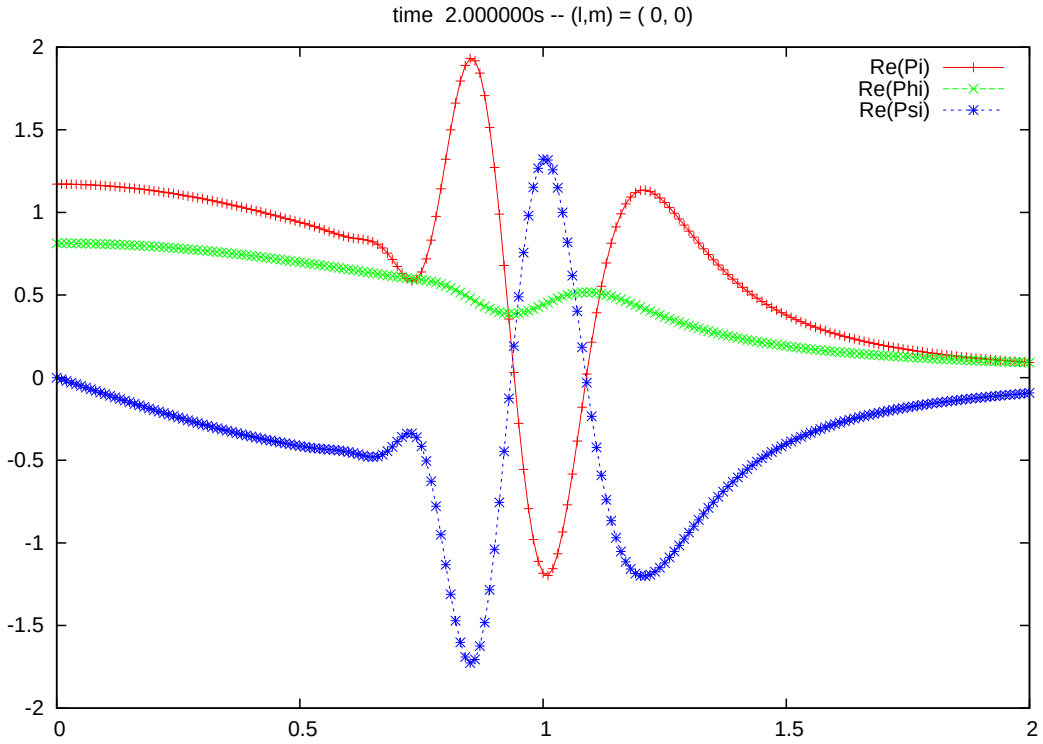

Figure 4.3: Finite-time blow-up in the system $\Box\Phi = 10\Phi^2$ after the wave has reflected from the origin. Setting $\kappa_2 = 1$ takes a very long time for blow-up to occur, whilst with $\kappa_2 = 100$ it is seen very quickly, before a wave-front has reached one of the boundaries.

this behaviour in the code.

To gain extra efficiency, we could consider calculating and storing only the positive m-modes, since Φ, Π are real-valued. This is simple enough to do with the time derivatives (i.e. calculating `udot` for positive-m only) but somewhat more complicated for the right hand sides. Using (4.2.2) where negative m's appear, the quadratic term can be written

$$(\Phi^2)_\gamma = \sum_{\ell_\alpha,\ell_\beta} \chi_\gamma r^{\ell_\alpha+\ell_\beta-\ell_\gamma} \left\{ \bar{\Phi}^0_{\ell_\alpha} \bar{\Phi}^{m_\gamma}_{\ell_\beta} \hat{C}^{-m_\gamma,0,m_\gamma}_{\ell_\gamma,\ell_\alpha,\ell_\beta} + \sum_{m_\alpha>0} \left[\chi_0 \bar{\Phi}_\alpha \bar{\Phi}^{m_\gamma-m_\alpha}_{\ell_\beta} \hat{C}^{-m_\gamma,m_\alpha,m_\gamma-m_\alpha}_{\ell_\gamma,\ell_\alpha,\ell_\beta} + \chi_\alpha \bar{\Phi}_\alpha \bar{\Phi}^{m_\gamma+m_\alpha}_{\ell_\beta} \hat{C}^{-m_\gamma,-m_\alpha,m_\gamma+m_\alpha}_{\ell_\gamma,\ell_\alpha,\ell_\beta} \right] \right\} \tag{4.5.4}$$

This is somewhat unwieldy, and may be excessively difficult to apply properly to the fluid equations. We thus leave it as a possible method to save time and memory in this instance.

With the same Gaussian initial data and outgoing wave boundary condition as previously considered, we see a blow-up in finite time (figure 4.3). This blow-up is only dependent on the value of κ_2 – the larger, the faster – and is independent of ℓ_m or how far away the outer boundary is placed.

4.6 Nonlinear cubic code

We employ the same trick as before, to maintain efficiency and 'recycle' code for the set of equations satisfying

$$\Box\Phi = \kappa_3\Phi^3 \tag{4.6.1}$$

with

$$\Phi^3 = \sum r^l \, g_l^m \, Y_l^m = \sum r^{l'+l''+l'''} \Phi_{l'}^{m'} \Phi_{l''}^{m''} \Phi_{l'''}^{m'''} Y_{l'}^{m'} Y_{l''}^{m''} Y_{l'''}^{m'''} \tag{4.6.2}$$

$$= \sum \chi_\gamma \, \hat{C}_{\alpha\beta-\gamma} \, h_\alpha \Phi_\beta \tag{4.6.3}$$

where h_l^m is understood to be given by (4.5.4). We can precalculate all the required h_γ products in their own loop before using them in the main loop to find time derivatives.

With the same initial data and boundary conditions, similar but faster blow-up (for equal values of κ_2, κ_3) is seen as in the quadratic case.

Chapter 5

Newtonian Fluid Equations

The Navier-Stokes equations describe the motion of a fluid, which we are (crudely) assuming constitutes the interior of a neutron star. They may be derived by considering the flux of mass and momentum across the boundary of a *control volume*, and applying Green's theorem to turn surface into volume integrals. For a compressible, inviscid[1] fluid they reduce to the Euler equations:

$$\frac{\partial \rho}{\partial t} = -\nabla_j(\rho v^j), \tag{5.0.1}$$

$$\rho \frac{dv^i}{dt} = -\nabla^i P - \rho \nabla^i \Phi. \tag{5.0.2}$$

These represent the conservation of mass and momentum, where ρ is the mass density, $\mathbf{v}$ the velocity of a fluid element, P the pressure, and Φ the gravitational potential, given by the Poisson equation

$$\Delta \Phi = 4\pi G \rho. \tag{5.0.3}$$

The discussion in section 5.1 will introduce the *polytropic* equation of state, which defines the relationship

$$P = K\rho^{\Gamma}. \tag{5.0.4}$$

where K is a constant. Because of this EOS there is no need to include an equation for the conservation of energy. One can now divide the equation of momentum conservation by the density:

$$\frac{\partial v^i}{\partial t} = -v^j \nabla_j v^i - \Gamma K \rho^{\Gamma-2} \nabla^i \rho - \nabla^i \Phi. \tag{5.0.5}$$

For simplicity we shall set $\Gamma = 2$ throughout this chapter to keep the equations in *polynomial* form, that is, as a nonlinear system whose variables are raised to integer powers. Non-$\Gamma = 2$

[1] No resistance to flow, so no dissipative terms.

laws, including non-integer laws, are more difficult to handle; one would have to substitute a new variable $R = \rho^{\Gamma-2}$ in (5.0.5), and either specify how R evolves in time (section 5.6.2 introduces the concept of *stratification*), find a (truncated) spherical harmonic expansion of the function, or perhaps even iterate if it can be assumed that ρ is mostly spherical (section 6.2.3).

For our spectral expansion and subsequent time evolutions, we shall place a fluid whose motions are described by the Euler equations into a rigid spherical container fixed at $r_{\text{max}} < 1$. This container is a numerical necessity as we cannot model the discontinuities that a surface/atmosphere interface would introduce with a spectral scheme, or a non-spherical outer boundary formed by rotational or magnetic effects without more mathematical framework, but it can perhaps be thought of as approximating a rigid crust,

5.1 Polytropic equation of state

A simplistic EOS – the *polytrope* – has been studied for some time. 19th century physicists such as Lord Kelvin, Emden and Zeuner began by trying to understand gaseous stars by assuming they had a constant specific heat: changing the pressure or volume of the star would not change the amount of energy needed to increase its temperature. Chandrasekhar [27] explains the derivation: consider an amount of heat energy Q being added to a system, which is equal to the change in internal energy minus the work done:

$$Q = (U - U_0) - W. \tag{5.1.1}$$

If this work is applied to changing the volume of the system, then one can represent an *infinitesimal* change of heat energy by

$$dQ = dU + P\,dV. \tag{5.1.2}$$

An *ideal gas*[2] is one that obeys the equation of state

$$P\,V = R\,T, \qquad U = U(T), \tag{5.1.3}$$

where R is referred to as the gas constant and T is the temperature. For such a gas, the heat energy will change when work is done as per

$$dQ = \frac{dU}{dT}\,dT + P\,dV, \tag{5.1.4}$$

However the equation of state implies that infinitesimal changes in quantities are related by

$$P\,dV + V\,dP = R\,dT, \tag{5.1.5}$$

[2]Under certain conditions fluids can be accurately modelled as a perfect gas.

which can be substituted into (5.1.2) to give

$$dQ = \left(\frac{dU}{dT} + R\right) dT - V\, dP. \tag{5.1.6}$$

If we now define the specific heat c_α of some physical variable α that is held constant to be

$$c_\alpha = \left(\frac{dQ}{dT}\right)_{\alpha=\text{constant}}, \tag{5.1.7}$$

then from (5.1.4) and (5.1.6) we can define the specific heat at constant volume and pressure (i.e. $dV = 0$ and $dP = 0$) by

$$c_V = \frac{dU}{dT}, \qquad c_p = \frac{dU}{dT} + R, \tag{5.1.8}$$

which is useful because their difference gives R. Using this and the equation of state again, we can rewrite (5.1.4) in the form

$$dQ = c_V\, dT + (c_P - c_V)\frac{T}{V} dV. \tag{5.1.9}$$

If a process is *adiabatic* there is no heat transfer to or from the fluid from its surroundings ($dQ = 0$). In this case, if we divide by T and integrate (5.1.9) then

$$c_V \ln T + (c_P - c_V) \ln V = C(s) \tag{5.1.10}$$

for some function C that is a function of entropy. One can rearrange this into the form

$$T \propto V^{1-\Gamma}, \tag{5.1.11}$$

where $\Gamma = c_P/c_V$ is the (constant) ratio of specific heats and is called the *adiabatic index*. This may also be written in the form

$$PV^\Gamma = \text{constant} \quad \Longleftrightarrow \quad P = K(s)\rho^\Gamma \tag{5.1.12}$$

for some function $K(s)$ dependent on the entropy s. If we assume that entropy is constant everywhere, then a fluid that satisfies (5.1.12) with K a constant is referred to as being both *polytropic* (one encounters different types of thermodynamic process with varying γ) and *barotropic* (since the pressure is only a function of density). Otherwise, with varying entropy (which we hold constant for a given particle) we have a *stratified* equation of state (section 5.6.2).

There is also a relation between the internal energy and the volume and pressure:

$$dU = \frac{dU}{dT} dT = c_V dT \tag{5.1.13}$$

$$\Longrightarrow\ U = c_V T, \tag{5.1.14}$$

where the constant of integration has been dropped as we have $U = 0$ at $T = 0$. From the ideal gas relation (5.1.3),

$$U = \frac{c_V}{R} P V \quad \Longleftrightarrow \quad P = (\gamma - 1)\rho U. \tag{5.1.15}$$

This relation lets us calculate the *enthalpy*, defined to be

$$h = U + \frac{P}{\rho} \tag{5.1.16}$$

$$= \frac{\gamma}{\gamma - 1}\frac{P}{\rho}. \tag{5.1.17}$$

5.1.1 The Lane-Emden equation

The gravitational equilibria of stars with a polytropic equation of state have been studied for some time, beginning with Lane (1870). The Lane-Emden equations give the equilibrium of spherical fluid bodies acted on by pressure and gravity. Using the Poisson equation (5.0.3) for the gravitational potential, equilibria are given by combining

$$P' + \rho\Phi' = 0, \qquad \Phi'' + 2\Phi'/r = 4\pi G\rho, \tag{5.1.18}$$

so that

$$\frac{1}{r^2}\frac{d}{dr}\left(\frac{r^2}{\rho}\frac{d(K\rho^\Gamma)}{dr}\right) = -4\pi G\rho. \tag{5.1.19}$$

(5.1.19) has analytical solutions only for $\Gamma = 6/5, 2, \infty$ and can be rewritten in the form

$$\frac{1}{\xi^2}\frac{d}{d\xi}\left(\xi^2\frac{d\theta(\xi)}{d\xi}\right) + \theta(\xi)^n = 0, \tag{5.1.20}$$

where

$$\Gamma = 1 + \frac{1}{n}, \qquad \rho = \rho_c\theta^n, \qquad r = \xi\sqrt{\frac{(n+1)K\rho_c^{\Gamma-2}}{4\pi G}}, \tag{5.1.21}$$

to which numerical solutions are easier to calculate. A set of *Mathematica* routines to achieve this are given in appendix B.4.

Since it is one of the most basic EOS that arguably gives a good description of certain astrophysical interiors, the $\Gamma = 2$ law is one of the most popular and is still in modern research [9, 34, 82]. The $\Gamma = 4/3$ or $\Gamma = 5/3$ laws [12, 18, 83] are chosen when it is suspected that electron degeneracy is the main contributor towards internal pressure, and whether the electrons are moving relativistically or not.

It is more realistic to assume that the pressure depends on both the density and a thermodynamic quantity such as temperature or entropy. Tabulated EOS are often employed in complex core-collapse simulations [66], and further still one can include effects from

particle physics, such as how entropy is affected by neutrino flux [72].

5.2 Spectral evolution in the 1+2 split

Inserting expansions of scalar and vectors (2.2.2, 2.4.6) and their derivatives (section 2.4.1) into the Euler equations, and then integrating, gives the following system that must be satisfied for every γ:

$$\dot{\rho}_\gamma = -\chi_\gamma \left\{ \hat{C}_{\alpha\beta-\gamma} \ \left[\rho_\alpha \left(v'_\beta + 2v_\beta/r + L_\beta^2 u_\beta \right) + \rho'_\alpha \, v_\beta \right] + \hat{D}_{-\gamma\alpha\beta} \ \rho_\alpha u_\beta \right\}, \tag{5.2.1}$$

$$\dot{v}_\gamma = -\chi_\gamma \left\{ \hat{C}_{\alpha\beta-\gamma} \ v_\alpha \, v'_\beta + \hat{D}_{-\gamma\alpha\beta} \ \left[u_\alpha v_\beta - r \left(u_\alpha u_\beta + w_\alpha w_\beta \right) \right] \right\} - 2K\rho'_\gamma, \tag{5.2.2}$$

$$\dot{u}_\gamma = \frac{\chi_\gamma}{L_\gamma^2} \left\{ \hat{D}_{\alpha\beta-\gamma} \ v_\alpha \left(u'_\beta + 2u_\beta/r \right) + \hat{E}_{-\gamma\alpha\beta} \ u_\alpha u_\beta - \hat{F}_{-\gamma\alpha\beta} \ w_\alpha w_\beta \right\} - 2Kr^{-2}\rho_\gamma, \tag{5.2.3}$$

$$\dot{w}_\gamma = \frac{\chi_\gamma}{L_\gamma^2} \left\{ \hat{D}_{\alpha\beta-\gamma} \ v_\alpha \left(w'_\beta + 2w_\beta/r \right) + (\hat{E}_{-\gamma\alpha\beta} \ + \hat{F}_{-\gamma\alpha\beta} \ ) u_\alpha w_\beta \right\}. \tag{5.2.4}$$

Note that we have written $v^A = v_A = v$, time derivatives $\dot{v} \equiv \frac{\partial v}{\partial t}$, and radial derivatives $v' \equiv \frac{\partial v}{\partial r}$.

5.2.1 Regularization

Equations (5.2.1-5.2.4) do not appear to be regular at the origin. In order to regularize vectors one needs to ensure that their components are continuous and finite valued, and to do this we shall rewrite vector components in terms of Cartesian coordinates. The regularization of scalars is the same as in section 4.1.

The directional derivative[3] for the axisymmetric case $m = 0$ is

$$\mathbf{v} \cdot \nabla = \sum_\gamma \left[v_\gamma Y_\gamma \frac{\partial}{\partial r} + u_\gamma Z_\gamma^{(\theta)} \frac{\partial}{\partial \theta} + w_\gamma S_\gamma^{(\varphi)} \frac{\partial}{\partial \varphi} \right] \tag{5.2.5}$$

where $Z^{(\theta)}$ represents the polar component of the vector Z^a, and $S^{(\varphi)}$ the axial component of S^a. The $\partial\varphi$ term is not discarded as it may be the case that we are differentiating a non-axisymmetric term; without it we would be unable to find how to regularize w. From the metric (2.3.1), transforming to Cartesian coordinates gives

$$\begin{aligned} r\frac{\partial}{\partial r} &= x\partial_x + y\partial_y + z\partial_z, \\ r\sin\theta\frac{\partial}{\partial \theta} &= z\left(x\partial_x + y\partial_y\right) - \left(x^2 + y^2\right)\partial_z, \\ \frac{\partial}{\partial \varphi} &= x\partial_y - y\partial_x. \end{aligned} \tag{5.2.6}$$

[3] The frame coefficients for spherical polar coordinates are $v_r\partial_r + v_\theta \frac{1}{r}\partial_\theta + v_\varphi \frac{1}{r\sin\theta}\partial_\varphi$, and is useful for setting initial data and visualization.

In the 1+2 split, we have

$$\epsilon^{ab} = [ab]\frac{1}{\sqrt{\gamma}} = [ab]\frac{1}{\sin\theta}. \tag{5.2.7}$$

All spherical harmonics with $m = 0$ are polynomials of $\cos\theta$:

$$Y^0_\ell = \sum_{n=0}^{\ell} a_n(\cos\theta)^n. \tag{5.2.8}$$

However we need only consider the highest power $n = \ell$, because when we rewrite $(\cos\theta)^n = z^n/r^n$ this gives the 'worst' powers of r in the denominator that need to be cancelled. Thus we approximate by

$$\begin{aligned} Y_\gamma &\simeq (\cos\theta)^\ell, \\ Z^{(\theta)}_\gamma &= \gamma^{\theta\theta}(Y^0_\ell)_{,\theta} \simeq -\ell\sin\theta\,(\cos\theta)^{\ell-1}, \\ S^{(\varphi)}_\gamma &= \epsilon^{\varphi\theta}(Y^0_\ell)_{,\theta} \simeq \ell(\cos\theta)^{\ell-1}. \end{aligned} \tag{5.2.9}$$

Equation (5.2.5) with $\ell \geq 1$ can thus be written

$$\begin{aligned} \mathbf{v} \simeq\ & v_\gamma\frac{z^\ell}{r^\ell}\frac{1}{r}\left(x\partial_x + y\partial_y + z\partial_z\right) - \ell u_\gamma\frac{z^{\ell-1}}{r^{\ell-1}}\frac{1}{r}\left[z\left(x\partial_x + y\partial_y\right) - \left(x^2+y^2\right)\partial_z\right] \\ & + \ell w_\gamma\frac{z^{\ell-1}}{r^{\ell-1}}\left(x\partial_y - y\partial_x\right). \end{aligned} \tag{5.2.10}$$

Making use of the relation $x^2 + y^2 = r^2 - z^2$, the rescaling

$$v_\gamma = r^{\ell-1}\bar{v}_\gamma, \qquad u_\gamma = r^{\ell-2}\bar{u}_\gamma, \qquad w_\gamma = r^{\ell-1}\bar{w}_\gamma, \tag{5.2.11}$$

leads to

$$\mathbf{v}\cdot\nabla \simeq \left(\frac{\bar{v}_\gamma - \ell\bar{u}_\gamma}{r^2}\right) z^\ell(x\partial_x + y\partial_y + z\partial_z) + \ell\bar{u}_\gamma z^{\ell-1}\partial_z + \ell\bar{w}_\gamma z^{\ell-1}(x\partial_y - y\partial_x). \tag{5.2.12}$$

The first term is only regular at the origin $r = 0$ if

$$\bar{v}_\gamma = \ell\bar{u}_\gamma + \mathcal{O}(r^2). \qquad (\bar{v}_\gamma, \bar{u}_\gamma = \mathcal{O}(1)) \tag{5.2.13}$$

By separately considering the case $\ell = 0$, an argument following the above shows that v_0 must be $\mathcal{O}(r)$, and hence $\bar{v}_0 = \mathcal{O}(r^2)$.

Thus far we have shown how to regularize for $m = 0$. It is perhaps reasonable to assume that, since the fluid equations do not contain explicit appearances of m except in the Gaunt coefficients, everything regularizes in a manner dependent only upon the degree ℓ. We have been unable to prove this, but it could be helpful to note that the θ-dependence of all spherical harmonics can be written in terms of $(\cos\theta)^\ell$ or $\sin\theta(\cos\theta)^{\ell-1}$.

The regularized hydrodynamic equations are given by the following system:

$$\dot{\bar{\rho}}_\gamma = -\chi_\gamma r^{\ell_\alpha+\ell_\beta-\ell_\gamma-1}\Big\{\hat{C}_{\alpha\beta-\gamma}\ \left[\bar{\rho}_\alpha\bar{v}'_\beta+\tfrac{1}{r}(\ell_\alpha+\ell_\beta+1)\bar{\rho}_\alpha\bar{v}_\beta+\bar{\rho}'_\alpha\bar{v}_\beta\right] + \tfrac{1}{r}\left(\hat{D}_{-\gamma\alpha\beta}\ +L_\beta^2\hat{C}_{\alpha\beta-\gamma}\ \right)\bar{\rho}_\alpha\bar{u}_\beta\Big\}, \tag{5.2.14}$$

$$\dot{\bar{v}}_\gamma = -\chi_\gamma r^{\ell_\alpha+\ell_\beta-\ell_\gamma-1}\Big\{\hat{C}_{\alpha\beta-\gamma}\ \bar{v}_\alpha\left[\tfrac{1}{r}(\ell_\beta-1)\bar{v}_\beta+\bar{v}'_\beta\right] +\hat{D}_{-\gamma\alpha\beta}\ \left[\tfrac{1}{r}\bar{v}_\alpha\bar{u}_\beta-\tfrac{1}{r}\bar{u}_\alpha\bar{u}_\beta-r\bar{w}_\alpha\bar{w}_\beta\right]\Big\} - 2K\left(\ell_\gamma\bar{\rho}_\gamma+r\bar{\rho}'_\gamma\right), \tag{5.2.15}$$

$$\dot{\bar{u}}_\gamma = \frac{\chi_\gamma}{L_\gamma^2}r^{\ell_\alpha+\ell_\beta-\ell_\gamma-1}\Big\{\hat{D}_{\alpha\beta-\gamma}\ \bar{v}_\alpha\left(\tfrac{1}{r}\ell_\beta\bar{u}_\beta+\bar{u}'_\beta\right)+\tfrac{1}{r}\hat{E}_{-\gamma\alpha\beta}\ \bar{u}_\alpha\bar{u}_\beta -r\hat{F}_{-\gamma\alpha\beta}\ \bar{w}_\alpha\bar{w}_\beta\Big\}-2K\bar{\rho}_\gamma, \tag{5.2.16}$$

$$\dot{\bar{w}}_\gamma = \frac{\chi_\gamma}{L_\gamma^2}r^{\ell_\alpha+\ell_\beta-\ell_\gamma-1}\Big\{\hat{D}_{\alpha\beta-\gamma}\ \bar{v}_\alpha\left[\tfrac{1}{r}(\ell_\beta+1)\bar{w}_\beta+\bar{w}'_\beta\right] +\tfrac{1}{r}(\hat{E}_{-\gamma\alpha\beta}\ +\hat{F}_{-\gamma\alpha\beta}\ )\bar{u}_\alpha\bar{w}_\beta\Big\}. \tag{5.2.17}$$

5.2.2 Dimensional analysis

So far we have been working with dimensionless quantities without properly writing down the equations in a dimensionless form. We should like show that what we have been doing so far is reasonable, and to be able to set parameters corresponding to physically reasonable values. Let us temporarily express dimensionless quantities through *hatted* variables:

$$\hat{r} = r/\left[r\right], \qquad \hat{t} = t/\left[t\right], \qquad \hat{\rho} = \rho/\left[\rho\right], \tag{5.2.18}$$

and so on, where the bracketed variables are appropriate scales chosen so that hatted variables are (usually) order 1.

From conservation of mass, non-dimensionalized as

$$\frac{\partial\hat{\rho}}{\partial\hat{t}} = -\frac{[v][t]}{[r]}\hat{\nabla}\cdot(\hat{\rho}\hat{\mathbf{v}}), \tag{5.2.19}$$

we choose to scale time as $[t]=[r]/[v]$. Conservation of momentum using this scaling can be written

$$\frac{\partial\hat{\mathbf{v}}}{\partial\hat{t}} = -\left(\hat{\mathbf{v}}\cdot\hat{\nabla}\right)\hat{\mathbf{v}} - 2\hat{K}\frac{[K][\rho]}{[v]^2}\hat{\nabla}\hat{\rho} - \frac{[\phi]}{[v]^2}\hat{\nabla}\hat{\phi}, \tag{5.2.20}$$

and, from this, Poisson's equation is

$$\hat{\nabla}^2\hat{\phi} = 4\pi G\frac{[\rho][r]^2}{[v]^2}\hat{\rho} = 4\pi\hat{G}\hat{\rho}, \tag{5.2.21}$$

and we shall usually set $\hat{G}=1$. We shall also use the central density ρ_c as the density scaling, and the radius of the neutron star R as the radial scaling. Hence time has units of

$1/\sqrt{G\rho_c}$.

Let us only assume that we know the mass ($1.5M_\odot$) of a non-rotating neutron star with a polytropic equation of state (5.3.9) whose main constituent is non-relativistic neutron degenerate matter. By integrating over the whole volume of the neutron star we estimate a central density $\rho_c = 7 \times 10^{17}$ kg. By using this as the density scale and setting $\hat{G} = 1$ this implies a time scale of 0.15 ms, which will be equivalent to one unit of time in the code. Finally, the velocity scaling is closely related to the sound speed (5.4.11) and is approximately $10^8\,\mathrm{ms}^{-1}$ $(0.3\,c)$.

5.3 Linear perturbations of static, spherically symmetric stars

Since $Y_0^0 \equiv 1$ the $\ell = m = 0$ mode describes spherical symmetry. For now we shall retain the odd velocity component v_0 instead of writing down the regularized version; this will be useful for when we later describe a necessary change of variables (section 5.4). For a spherically symmetric NS the hydrodynamic equations reduce to

$$\dot{\bar{\rho}}_0 = -\frac{2}{r}\bar{\rho}_0 v_0 - \bar{\rho}_0 v_0' - \bar{\rho}_0' v_0, \tag{5.3.1}$$

$$\dot{v}_0 = -v_0 v_0' - 2K\bar{\rho}_0' - \bar{\phi}_0', \tag{5.3.2}$$

where the Poisson equation in spherical symmetry is

$$\bar{\phi}_0'' + \tfrac{2}{r}\bar{\phi}_0' = 4\pi\hat{G}\bar{\rho}_0. \tag{5.3.3}$$

Recall that scalars ρ, ϕ are regularized with r^ℓ. We shall wish to find static equilibrium solutions to these equations so as to perturb them later on. Note that rotation involves higher ℓ-modes and is a non-linear effect, so it is discussed later on in section 5.7.

It should also be mentioned that, because of the way we have regularized ρ, the central density of the star is given by the value of $\bar{\rho}_0$ at the origin. We often refer to $\bar{\rho}_0$ as the *background density* because $\rho_{(\ell\geq 1)}$ modes will typically be small in comparison.

5.3.1 Spherically symmetric equilibrium solutions

In the absence of a gravitational potential, a simple solution of (5.3.1-5.3.3) is

$$\bar{\rho}_0 = \text{constant}, \quad v_0 = 0. \tag{5.3.4}$$

We henceforth refer to this as the *flat background*.

A more relevant, well-known case can be derived by considering a non-zero gravitational

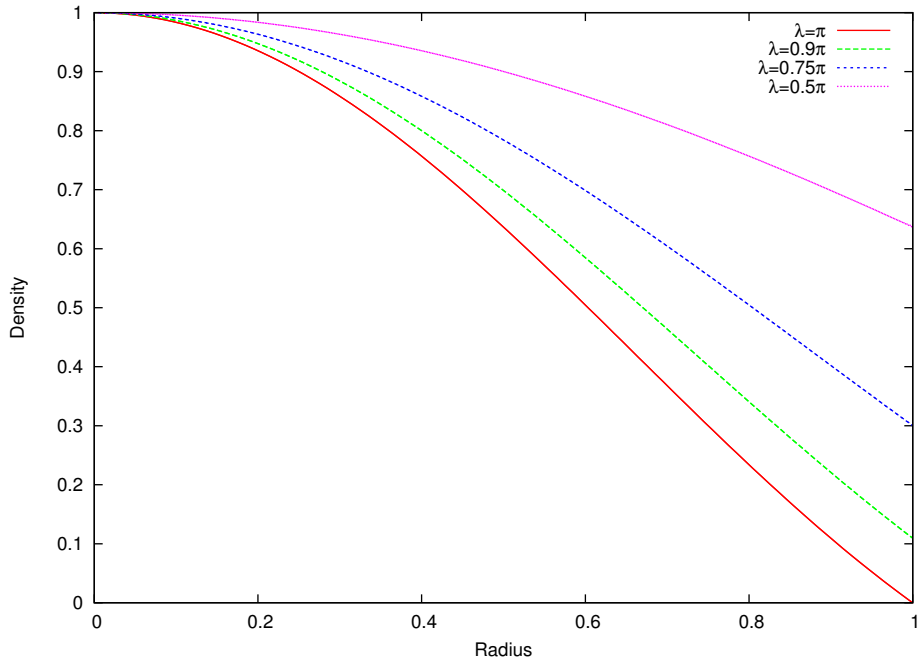

Figure 5.1: Plots of spherically symmetric Lane-Emden $n = 1$ solutions against radial distance for different surface fractions λ. We never set $\lambda \geq \pi$ to avoid zero/negative density.

---

field, leading us to the Lane-Emden solution for a $\gamma = 2$ polytrope. Setting $\bar{v}_0 = 0$ gives

$$\dot{\bar{\rho}}_0 = 0, \qquad 2K\bar{\rho}_0' = -\bar{\phi}_0', \tag{5.3.5}$$

so that the Poisson equation is now

$$2K\bar{\rho}_0'' + \frac{4K}{r}\bar{\rho}_0' - \tilde{G}\bar{\rho}_0 = 0. \tag{5.3.6}$$

This second order ODE is easily solved through substituting $\bar{\rho}_0 = f(r)/r$ For a $\bar{\rho}_0$ that is finite at the origin, we have solutions

$$\bar{\rho}_0 = \frac{\alpha}{r}\sin\left(\sqrt{\frac{\tilde{G}}{2K}}r\right), \qquad \bar{\phi}_0 = 2K\bar{\rho}_0, \tag{5.3.7}$$

where α is an an arbitrary constant that relates to the central density. When we refer to *star-like* initial data, we mean setting

$$\bar{\rho}_0 = \rho_c\frac{\sin(\lambda r)}{\lambda r}, \qquad (\lambda = F\pi) \tag{5.3.8}$$

$$v_0 = 0, \tag{5.3.9}$$

where F is a surface fraction defining how much of the star is inside our box, and ρ_c is a central density scaling: both of these parameters are typically (but not always) set to one.

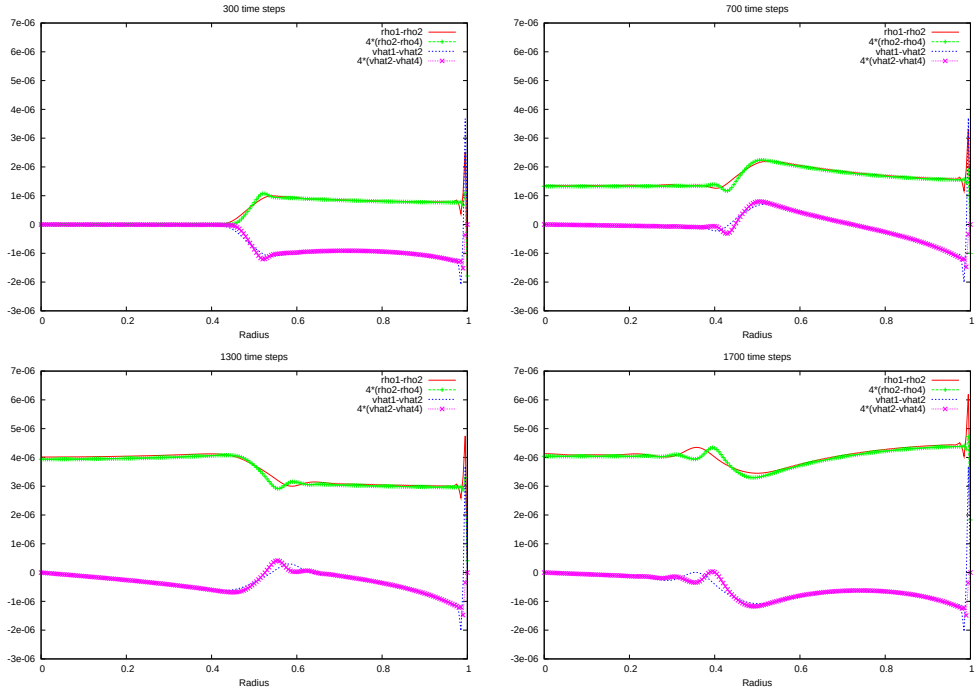

Figure 5.2: Convergence plots of $\ell = 0$ density and velocity components; $rho1$ represents the density evolved at twice the resolution of $rho2$. A spherically symmetric star in equilibrium will be slightly perturbed by the addition of artificial dissipation to every point, but the effect is second-order convergent. The density wave starts at the outer boundary, and then bounces between the two boundaries: each frame shows the wave halfway through a crossing, so the wave is travelling left in the top-left frame. The outer boundary appears to cause a linearly-growing error in the density; a smaller surface fraction greatly reduces this error.

5.3.2 Finite differencing the background equations

One may now try to introduce spherically symmetric perturbations and time-evolve the system, which will of course remain spherically symmetric. Whilst the background equations are regular at the origin, a second– or forth–order accurate finite differencing of these equations on a regularly spaced grid, using l'Hôpital's rule at the origin, is unstable, just as we saw with the wave equation.

Thankfully we can apply our experience with the wave equation and re-cast equation (5.3.1) into the form

$$\dot{v}_0 = -3\bar{\rho}_0 \frac{\partial(r^2 v_0)}{\partial(r^3)} - v_0 \bar{\rho}_0'. \tag{5.3.10}$$

which we then finite difference using one of the schemes described in section 3.7.

To keep this equilibrium code stable for an unlimited number of time-steps, one should initially set $\bar{\phi}_0'$ from $\bar{\rho}_0'$ at grid points, rather than differentiating the analytical solution. This way, in the absence of artificial dissipation, the right-hand sides will exactly cancel out. With dissipation the method is certainly stable for at least four wave crossings (2000 time

steps on an $N = 200$ grid) with convergence shown in figure 5.2.

5.3.3 Non-spherical linear perturbations

We shall now introduce non-spherical $\ell > 0$ perturbations upon these spherical, stable backgrounds. Assuming that these modes are always small in comparison to the background, we can neglect any couplings between non-zero modes since they will be quadratically small. By *linear order* we mean that $\ell = 0$ modes are of $\mathcal{O}(1)$, with higher modes being $\mathcal{O}(\delta)$ for some small parameter δ. Products of $\mathcal{O}(\delta^2)$ are neglected.

Since the harmonic degrees must satisfy the triangle inequality $|\ell_\gamma - \ell_\alpha| \leq \ell_\beta \leq \ell_\gamma + \ell_\alpha$, setting $\ell_\beta = 0$ gives one solution for non-zero Gaunt coefficients: $\ell_\alpha \equiv \ell_\gamma$. Thus, we only have $0, 0, 0$ and $\gamma, \gamma, 0$ couplings to consider. Consequently, since $\chi_\gamma \hat{C}_{\gamma,-\gamma,0} = 1$, and the evolution equations for $\ell = 0$ are unchanged, we need to find the linear γ-mode evolutions. It is a simple matter to find the linear products from equations (5.2.14-5.2.17).

Furthermore we will employ Cowling's approximation whereby perturbations of a spherical gravitational potential are neglected and where the potential is fixed in time. Doing so saves us having to solve Poisson's equation at every time-step, and should be a reasonable approximation to make if the functions $\bar{\rho}_\gamma$ are small. In the non-linear code we shall look again at non-spherical potentials, and later on solve Poisson's equation dynamically. With this the linear evolution equations for non-zero γ are as follows:

$$\dot{\bar{\rho}}_\gamma = -\left[\bar{\rho}_\gamma v_0' + \bar{\rho}_\gamma' v_0 + \frac{1}{r}\bar{\rho}_0 \bar{v}_\gamma' + \frac{1}{r}\bar{\rho}_0' \bar{v}_\gamma + \frac{\ell_\gamma + 2}{r}\bar{\rho}_\gamma v_0 + (\ell_\gamma + 1)\bar{\rho}_0 \left(\frac{\bar{v}_\gamma - \ell_\gamma \bar{u}_\gamma}{r^2}\right)\right], \tag{5.3.11}$$

$$\dot{\bar{v}}_\gamma = -\left[v_0' \bar{v}_\gamma + v_0 \bar{v}_\gamma' + \frac{\ell_\gamma - 1}{r} v_0 \bar{v}_\gamma\right] - 2K\left(\ell_\gamma \bar{\rho}_\gamma + r\bar{\rho}_\gamma'\right), \tag{5.3.12}$$

$$\dot{\bar{u}}_\gamma = -\left[v_0 \bar{u}_\gamma' + \frac{\ell_\gamma}{r} v_0 \bar{u}_\gamma\right] - 2K\bar{\rho}_\gamma, \tag{5.3.13}$$

$$\dot{\bar{w}}_\gamma = -\left[v_0 \bar{w}_\gamma' + \frac{\ell_\gamma + 1}{r} v_0 \bar{w}_\gamma\right]. \tag{5.3.14}$$

These equations are seen to be regular at the origin as $v_0 = \mathcal{O}(r)$. Since 0,γ is the only coupling, modes can only affect themselves and do not filter through into others, and as such we need only ever evolve the modes with non-zero initial data.

On the flat, static background with $v_0 = 0$ we have that $\dot{\bar{\rho}}_0, \dot{v}_0 \equiv 0$. The linear

perturbations on this background reduce to

$$\dot{\bar{\rho}}_\gamma = -\left[\frac{1}{r}\bar{\rho}_0\bar{v}'_\gamma + \frac{1}{r}\bar{\rho}'_0\bar{v}_\gamma + (\ell_\gamma+1)\bar{\rho}_0\left(\frac{\bar{v}_\gamma - \ell_\gamma\bar{u}_\gamma}{r^2}\right)\right], \tag{5.3.15}$$

$$\dot{\bar{v}}_\gamma = -2K\left(\ell_\gamma\bar{\rho}_\gamma + r\bar{\rho}'_\gamma\right), \tag{5.3.16}$$

$$\dot{\bar{u}}_\gamma = -2K\bar{\rho}_\gamma, \tag{5.3.17}$$

$$\dot{\bar{w}}_\gamma = 0. \tag{5.3.18}$$

By taking the time derivative of (5.3.15) one can observe this system obeys the (sound) wave equation:

$$\ddot{\bar{\rho}}_\gamma = 2K\bar{\rho}_0\left[\bar{\rho}''_\gamma + \frac{2(\ell_\gamma+1)}{r}\bar{\rho}'_\gamma\right]. \tag{5.3.19}$$

Note that we impose different boundary conditions to those in the wave equation code we previously considered, so we would not expect density waves to behave in the exact same way.

5.3.4 Boundary conditions

The inner boundary, near the origin, is handled with ease, as we have rescaled variables to be even functions of r. Thus we set $\bar{\rho}(-r) = \bar{\rho}(r)$ etc. for the left-hand ghost zones.

The continuum condition on the outer boundary we apply is to have no fluid escaping the container, imposed by setting $\bar{v}_\gamma(r_{\mathsf{max}}) = 0$. Numerically we implement this as $\dot{\bar{v}}_\gamma = 0$ at $r = r_{\mathsf{max}}$ with compatible initial data. The container is otherwise assumed to be slippery, so we do not impose any stress-related conditions on $\bar{u}, \bar{w}$. To calculate derivatives at and close to the outer boundary we extrapolate to some order, and would likely do the same if we were considering a spherical shell of fluid instead of a sphere.

It is quite common in any stellar modelling to include an atmosphere whereby the density is set to be some small, positive constant in a region outside of vanishing pressure, but we have already pointed out that this is an unworkable scheme within our numerical framework.

5.4 New fluid variables

A central differencing code written to evolve the regularized linear system (5.3.11-5.3.14) is seen to exhibit a numerical instability at the origin even for low ℓ-modes, very similar to that seen in the wave equation code. To solve this issue, we can attempt to recast the equations into a form resembling that of the wave equation and then finite difference over a non-uniform grid. There are two ways in which we could try to achieve this: either by generalizing the finite difference method, or by making a change of variables.

For the first method, recall that we can write derivatives in the form

$$f'(r) + \frac{N}{r} f(r) = (N+1) \frac{\partial \left(r^N f(r) \right)}{\partial (r^{N+1})}, \tag{5.4.1}$$

and then finite difference the right-hand side, assuming $f(r)$ is an odd function. To evaluate this at the origin we require N to be even, but not all the terms in (5.3.11-5.3.14) have even coefficients. However, it is possible to split the terms in the following manner:

$$(N+1) \frac{\partial \left(r^N f(r) \right)}{\partial (r^{N+1})} = \frac{1}{2} \left[(N+2) \frac{\partial (r^{N+1} f(r))}{\partial (r^{N+2})} + N \frac{\partial (r^{N-1} f(r))}{\partial (r^N)} \right]. \tag{5.4.2}$$

So if N is odd, we can turn it into two derivatives that we can evaluate at the origin. As an example, one could rewrite

$$v_0' + \frac{\ell_\gamma}{r} v_0 = \begin{cases} (\ell_\gamma + 1) \dfrac{\partial (r^{\ell_\gamma} v_0)}{\partial (r^{\ell_\gamma + 1})}, & (\ell_\gamma \text{ even}) \\ \dfrac{1}{2} \left[(\ell_\gamma + 2) \dfrac{\partial (r^{\ell_\gamma + 1} v_0)}{\partial (r^{\ell_\gamma + 2})} + \ell_\gamma \dfrac{\partial (r^{\ell_\gamma - 1} v_0)}{\partial (r^{\ell_\gamma})} \right]. & (\ell_\gamma \text{ odd}) \end{cases} \tag{5.4.3}$$

Unfortunately, applying this 'shifting' to every possible term does not help with stability. The code fares no better than when finite differencing on a regularly spaced grid.

We now resort to trying to find a change of variables that naturally gives us wave equation-like terms. The following choice,

$$\begin{aligned} \hat{v}_\gamma &= \frac{\bar{v}_\gamma - \ell_\gamma \bar{u}_\gamma}{r}, \qquad (\hat{v}_0 \equiv v_0) \\ f_\gamma &= \frac{\bar{u}_\gamma' - \hat{v}_\gamma}{r}. \end{aligned} \tag{5.4.4}$$

reduces the linear evolution equations on a flat, static background with $\bar{\rho}_0 = 1$ to

$$\begin{aligned} \dot{\bar{\rho}}_\gamma &= -\left[\hat{v}_\gamma' + \frac{2(\ell_\gamma + 1)}{r} \hat{v}_\gamma + \ell_\gamma f_\gamma \right] = -(2\ell_\gamma + 3) \frac{\partial (r^{2\ell_\gamma + 2} \hat{v}_\gamma)}{\partial (r^{2\ell_\gamma + 3})} - \ell_\gamma f_\gamma, \\ \dot{\hat{v}}_\gamma &= -2K \bar{\rho}_\gamma', \\ \dot{f}_\gamma &= 0, \end{aligned} \tag{5.4.5}$$

which we recognise as the linear wave equation in first-order form. It is important to note that $\hat{v}$ is an odd function of r, whilst f is even. More generally, the linear evolution equations

now read

$$\dot{\bar{\rho}}_\gamma = -\left\{ \hat{v}_0' \bar{\rho}_\gamma + \hat{v}_0 \bar{\rho}_\gamma' + \frac{\hat{v}_0}{r}(\ell_\gamma + 2)\bar{\rho}_\gamma + \bar{\rho}_0 \left[\hat{v}_\gamma' + \frac{2(\ell_\gamma+1)}{r}\hat{v}_\gamma + \ell_\gamma f_\gamma \right] + \frac{\bar{\rho}_0'}{r}\left[r\hat{v}_\gamma + \ell \bar{u}_\gamma \right] \right\}, \tag{5.4.6}$$

$$\dot{\hat{v}}_\gamma = -\left\{ \ell \bar{u}_\gamma \left[\frac{\hat{v}_0'}{r} - \frac{\hat{v}_0}{r^2} \right] + \hat{v}_0' \hat{v}_\gamma + \hat{v}_0 \hat{v}_\gamma' + \frac{\hat{v}_0}{r}\ell_\gamma \hat{v}_\gamma + 2K\bar{\rho}_\gamma' \right\}, \tag{5.4.7}$$

$$\dot{\bar{w}}_\gamma = -\left\{ \hat{v}_0 \bar{w}_\gamma' + \frac{\hat{v}_0}{r}(\ell_\gamma + 1)\bar{w}_\gamma \right\}, \tag{5.4.8}$$

$$\dot{f}_\gamma = -\left\{ \hat{v}_0' f_\gamma + \hat{v}_0 f_\gamma' + \frac{\hat{v}_0}{r}(\ell_\gamma + 1) f_\gamma \right\}. \tag{5.4.9}$$

5.4.1 Discussion of the linear fluid code

One may first ask why we bother to introduce f when it should be possible to finite difference terms such as $\ell\hat{v}/r + \hat{v}'$ in ways similar to that used in the wave equation example. But it seems to be necessary for stability to coax out the travelling-wave part of the density: a code using just $\hat{v}$, or a variable representing $(\bar{v} - \ell\bar{u})/r^2$, almost always becomes unstable near the origin after a reflection there. More dissipation, increasing with ℓ will dampen the effect, but this will become physically unrealistic at some point.

Run-time scales linearly with ℓ_m, as expected. Running on a 3GHz Pentium D processor, a double-complex accurate Fortran code compiled with the Intel Fortran compiler requires about 5ms per time step per mode (without disk activity or dissipation) on an $N = 200$ grid. Using optimized compiler parameters for the particular machine, this figure can be cut to just 1ms. A table of run-time results is listed in section 5.5.1.

Initial data for ℓ-modes is usually set to be a double-Gaussian of the form

$$\begin{aligned} \bar{\rho}_\gamma &= A_\gamma e^{-(r^2-c^2)^2/w^4}, \\ \hat{v}_\gamma &= -(r^2-c^2)\bar{\rho}_\gamma' = 4A_\gamma r \frac{(r^2-c^2)^2}{w^4} e^{-(r^2-c^2)^2/w^4}, \end{aligned} \tag{5.4.10}$$

where A_γ, w, c are coefficients representing the wave amplitudes, width and centre. $\bar{u}, \bar{w}$ may be set in a similar way, and f is derived from them.

5.4.2 Flat background

Starting on a flat background $\bar{\rho}_0 = 1$, figure 5.3 shows a density perturbation on $\ell = 1$ with 200 grid points and artificial dissipation. It immediately breaks into two pieces, one travelling outwards and one inwards, and is shown to be convergent for the first few reflections. 100 time steps at this resolution represents a non-dimensional time of 0.25 ($\delta t = \frac{1}{2}h = 0.0025$).

The failure of finite differencing on a regular $N = 200$ grid with the same initial data and no dissipation is shown in figure 5.4, where an instability always occurs at the origin.

Adding dissipation prevents the code from crashing, but the amount needed to suppress this effect increases (to unphysical quantities) with ℓ.

For higher modes the non-uniform finite differencing scheme begins to lose convergence at this resolution, as demonstrated for $\ell = 5$ (figure 5.5). Doubling the resolution to $N = 400$ remedies this (figure 5.6).

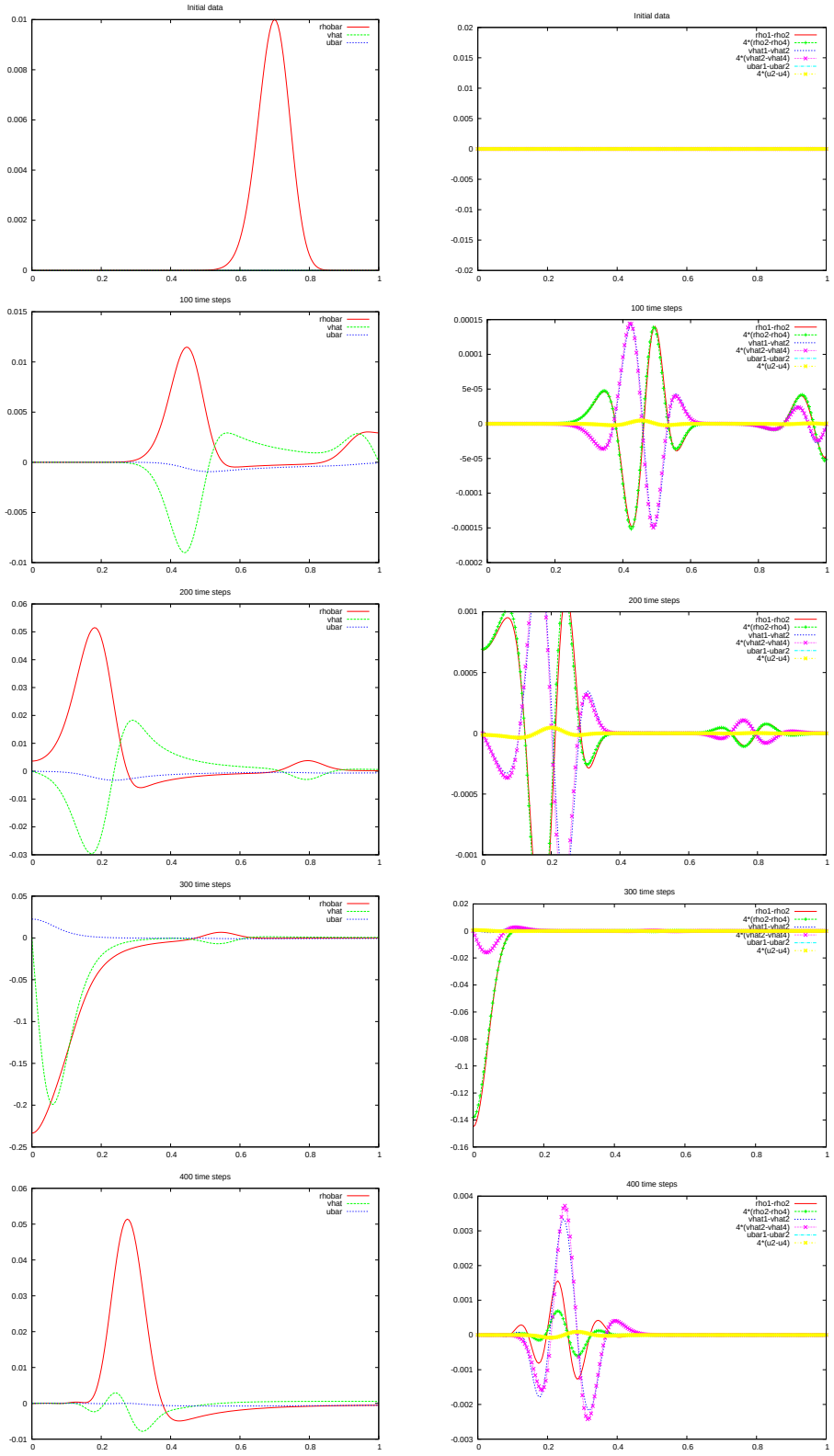

Figure 5.3: An $\ell = 1$ density perturbation on a flat $\bar{\rho}_0 = 1$ background is shown in the plots on the left, before and after a reflection off the outer boundary. Corresponding convergence tests are on the right demonstrating at least second-order convergence.

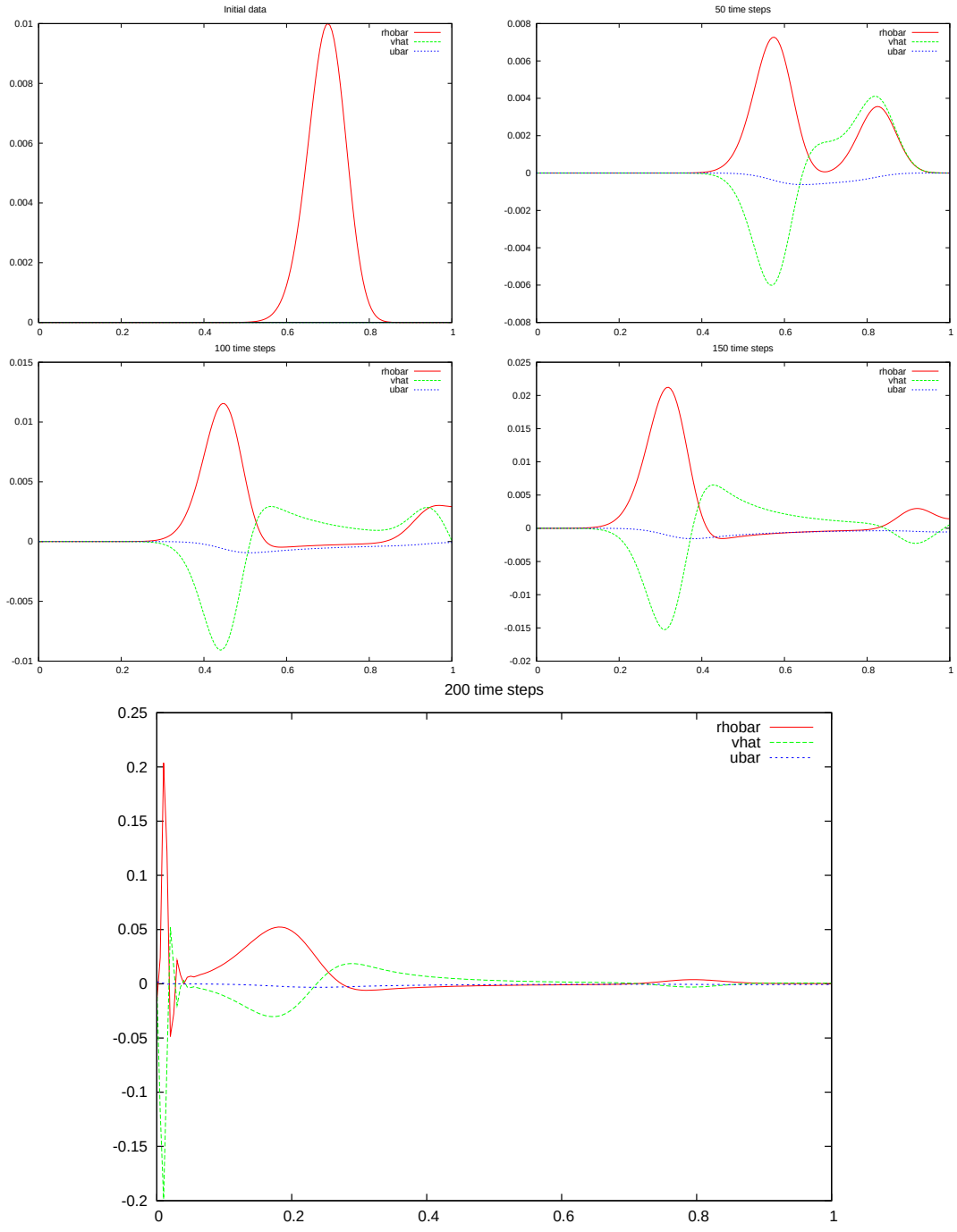

Figure 5.4: Finite differencing an $\ell = 1$ perturbation on a regular $N = 200$ grid fails without artificial dissipation. Small oscillations near the origin in $\bar{\rho}_1, \hat{v}_1$ blowup as the wave approaches this region.

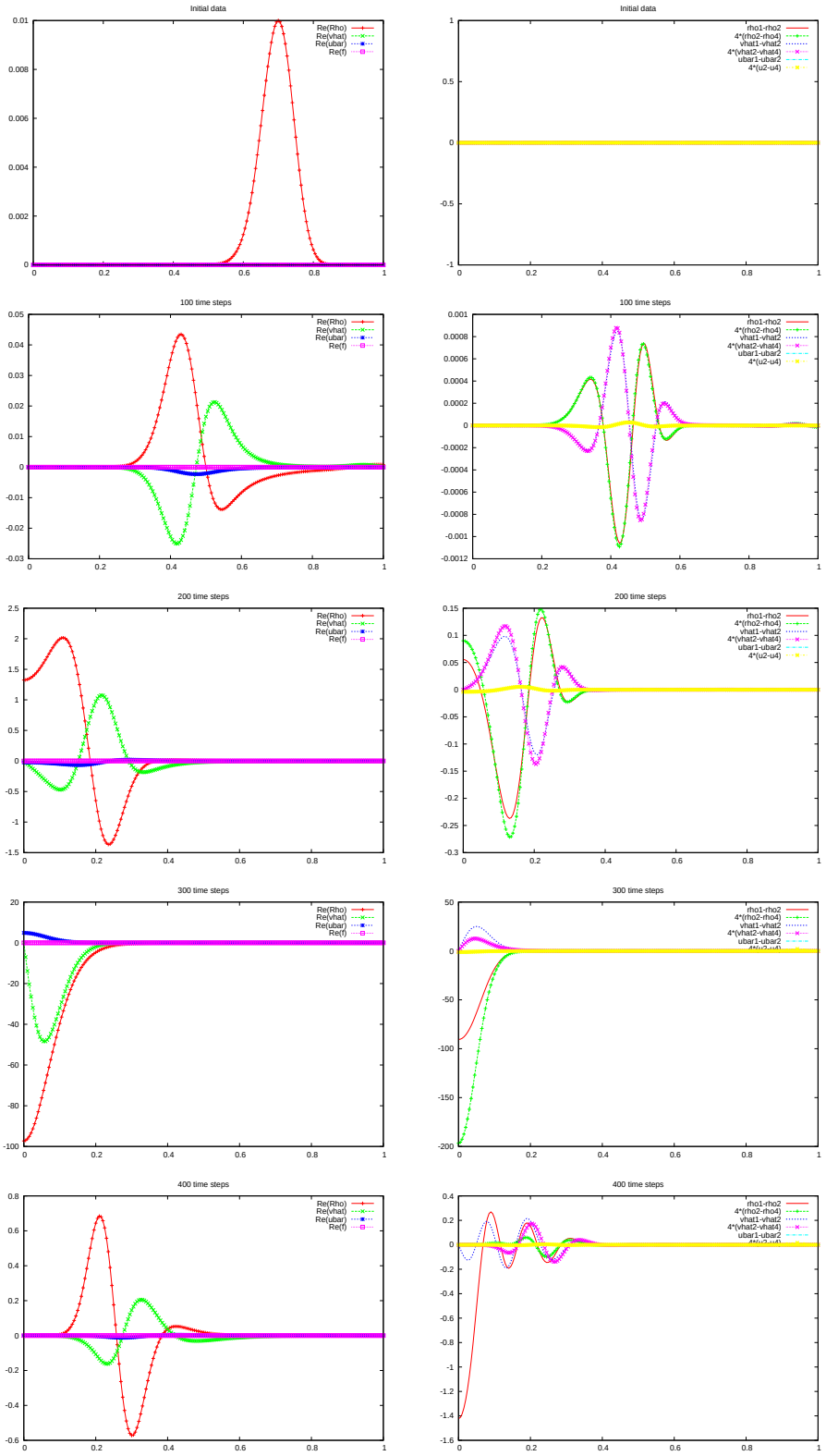

Figure 5.5: A perturbation with $\ell = 5, N = 200$ finite differenced on a non-uniform grid. We begin to encounter problems with convergence after reflections at the origin, as shown in the convergence plots on the right.

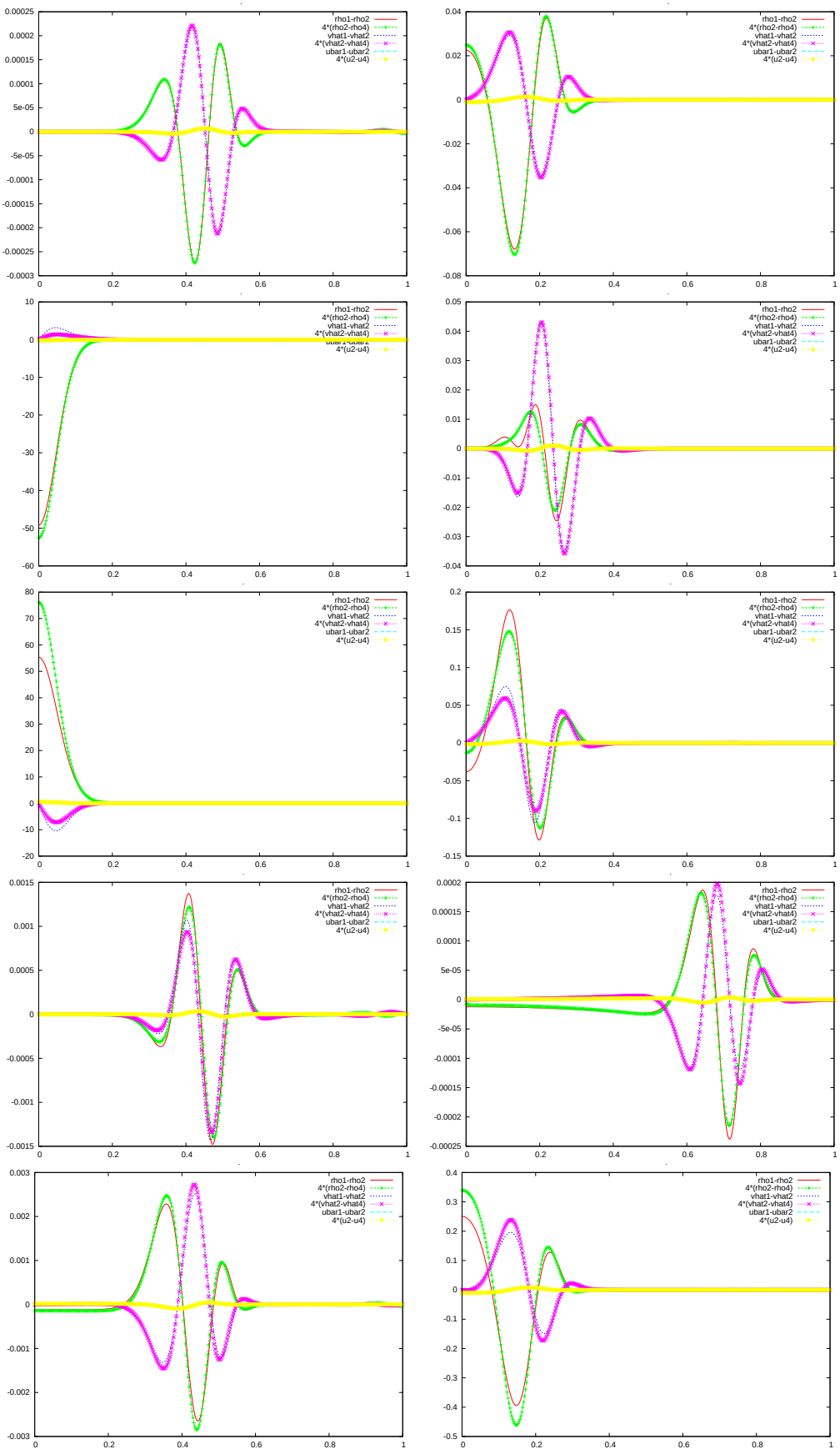

Figure 5.6: Convergence of the same perturbation as in figure 5.5 but with the resolution increased to $N = 400$. Convergence is observed for a period of at least two sound crossings.

5.4.3 Star-like background

On a star-like background $\bar{\rho}_0 = \sin(\lambda r)/(\lambda r)$, figure 5.7 shows reflections of a $\bar{\rho}_1$ perturbation with $N = 200, \lambda = 0.9\pi$. Note that the outgoing waves take longer to reach the outer boundary than on the flat background, since the speed of sound in a material is given by

$$c_s = \sqrt{\frac{\partial P}{\partial \rho}} = \sqrt{2K\rho}. \tag{5.4.11}$$

Figure 5.8 shows the same $\ell = 1$ perturbation but with $\lambda = 0.95\pi$. After a reflection the evolution is no longer second-order convergent, but this can be remedied by increasing the resolution (not shown). At $\lambda = 0.9\pi$ a single sound crossing takes 500 time steps ($t = 1.25$), whilst at $\lambda = 0.95\pi$ it takes 550.

Convergence of an $\ell = 5$ density perturbation with $\lambda = 0.95\pi$ is shown in figure 5.9. The evolution looks similar to $\ell = 1$ so it is not shown. Convergence is lost at the origin when the initially outward-travelling wave piece reaches the origin.

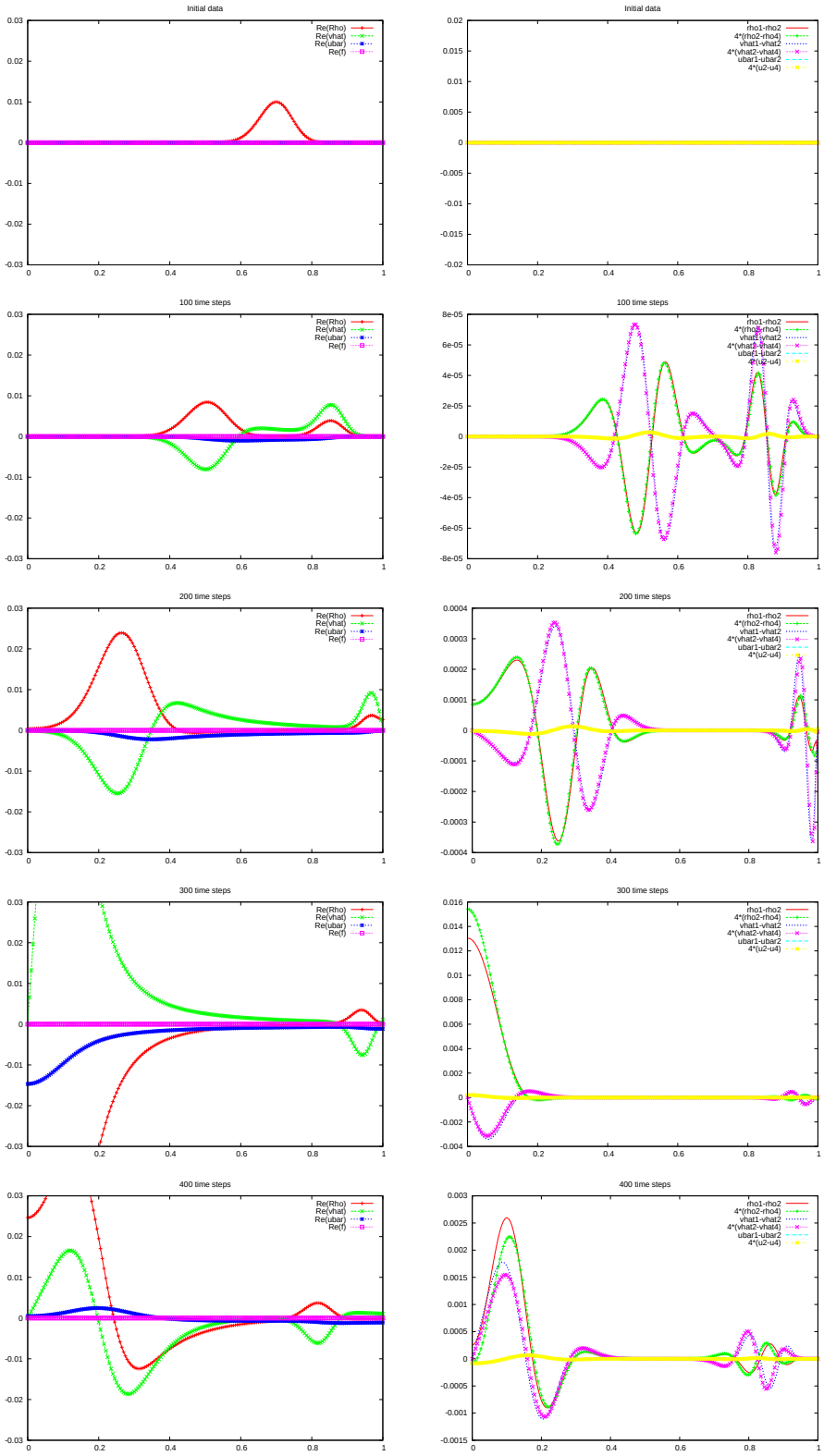

Figure 5.7: An $\ell = 1$ perturbation on an $N = 200, \lambda = 0.9\pi$ star-like background, shown at the same times as figure 5.3 and with convergence plotted in the right-hand column. The density wave takes longer to reach and then reflect off the outer boundary than it would do on a flat background, but is still convergent.

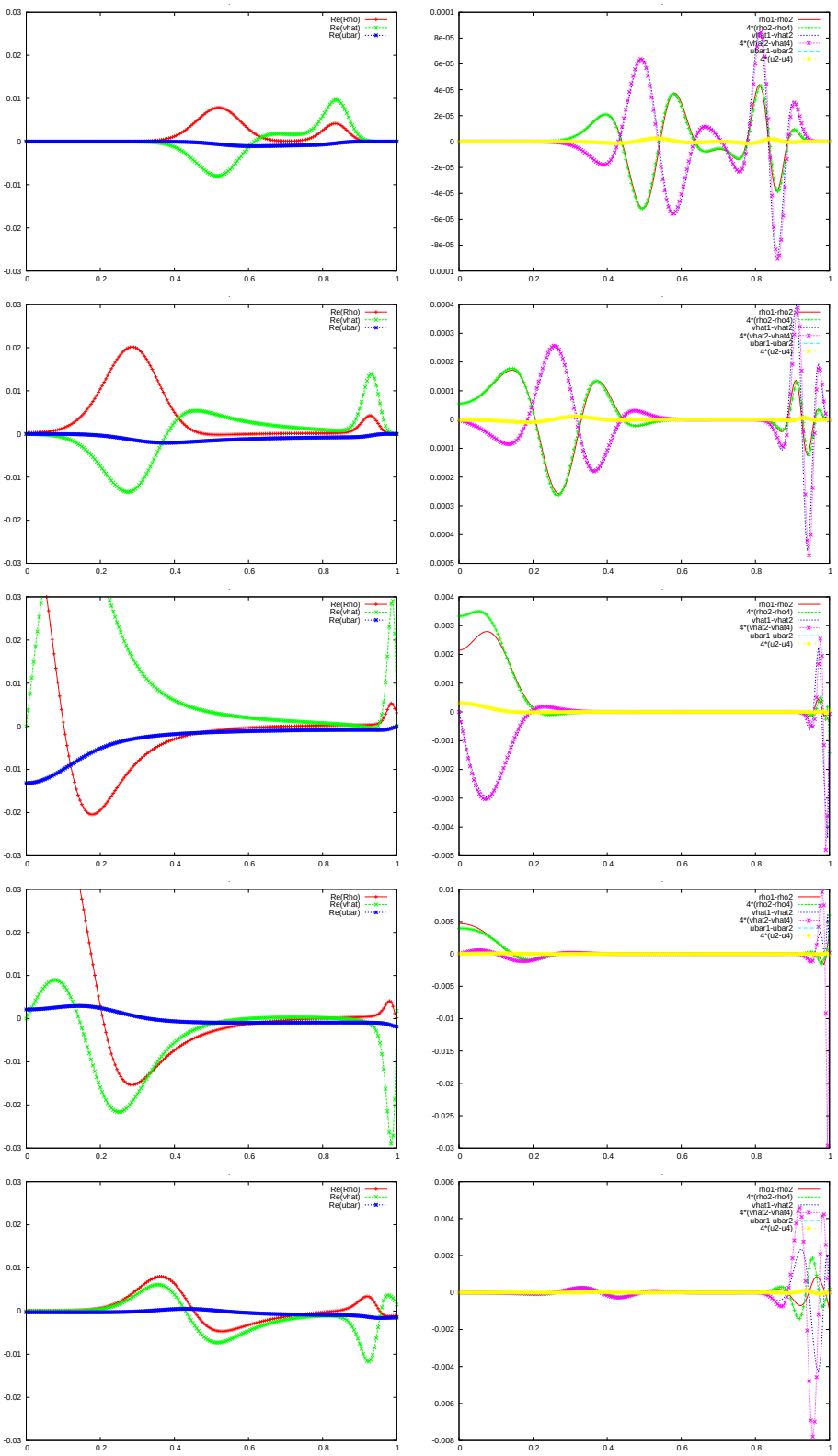

Figure 5.8: The same $\bar{\rho}_1$ initial data as in figure 5.7 but with $\lambda = 0.95\pi$. The density wave takes even longer to reflect off the outer boundary.

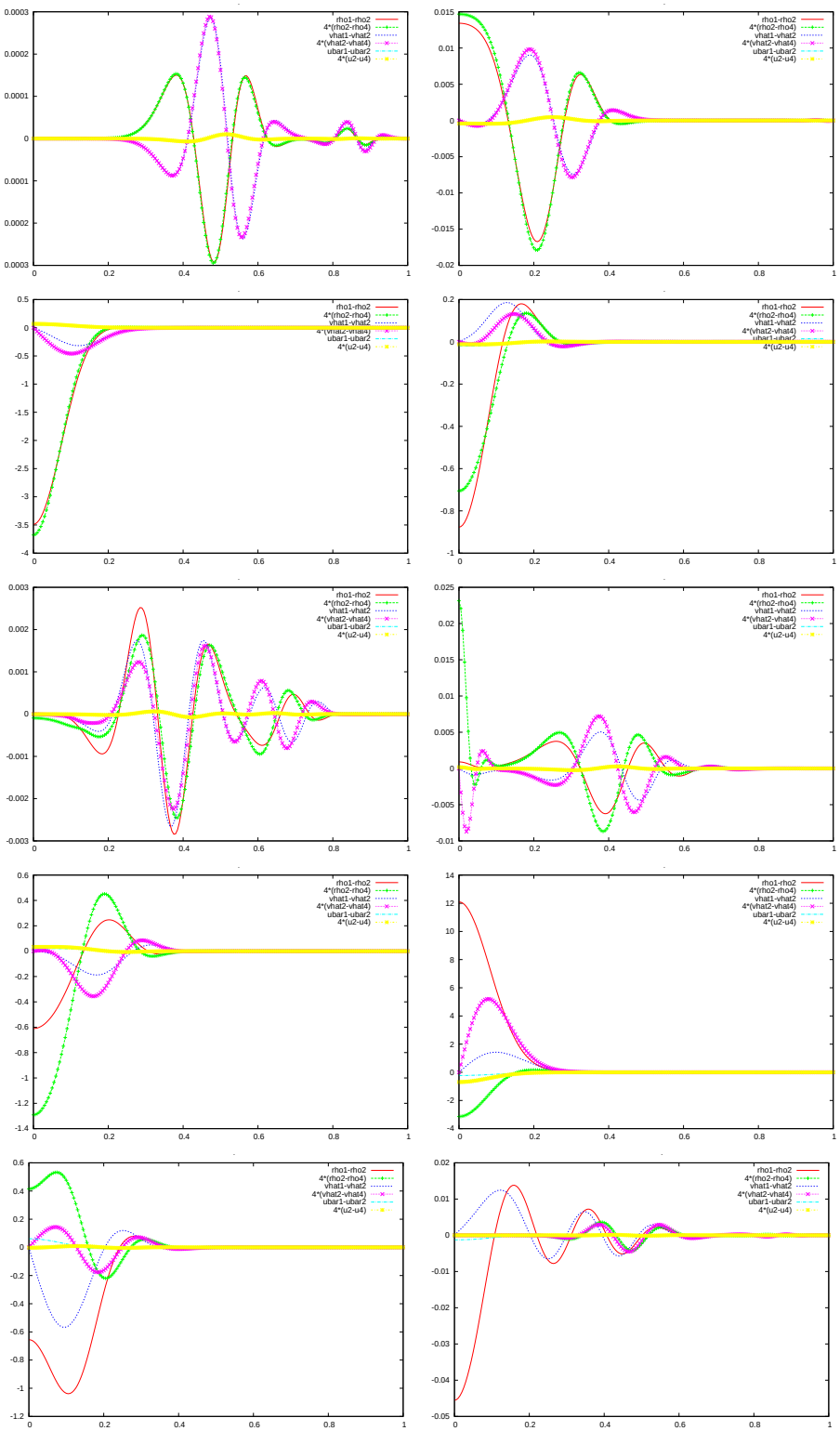

Figure 5.9: Convergence tests of a $\bar{\rho}_5$ perturbation on an $N = 200, \lambda = 0.95\pi$ star-like background. Waves returning from a reflection at the outer boundary lose convergence when reaching the origin. These are plotted for a timescale of just under two sound crossing times.

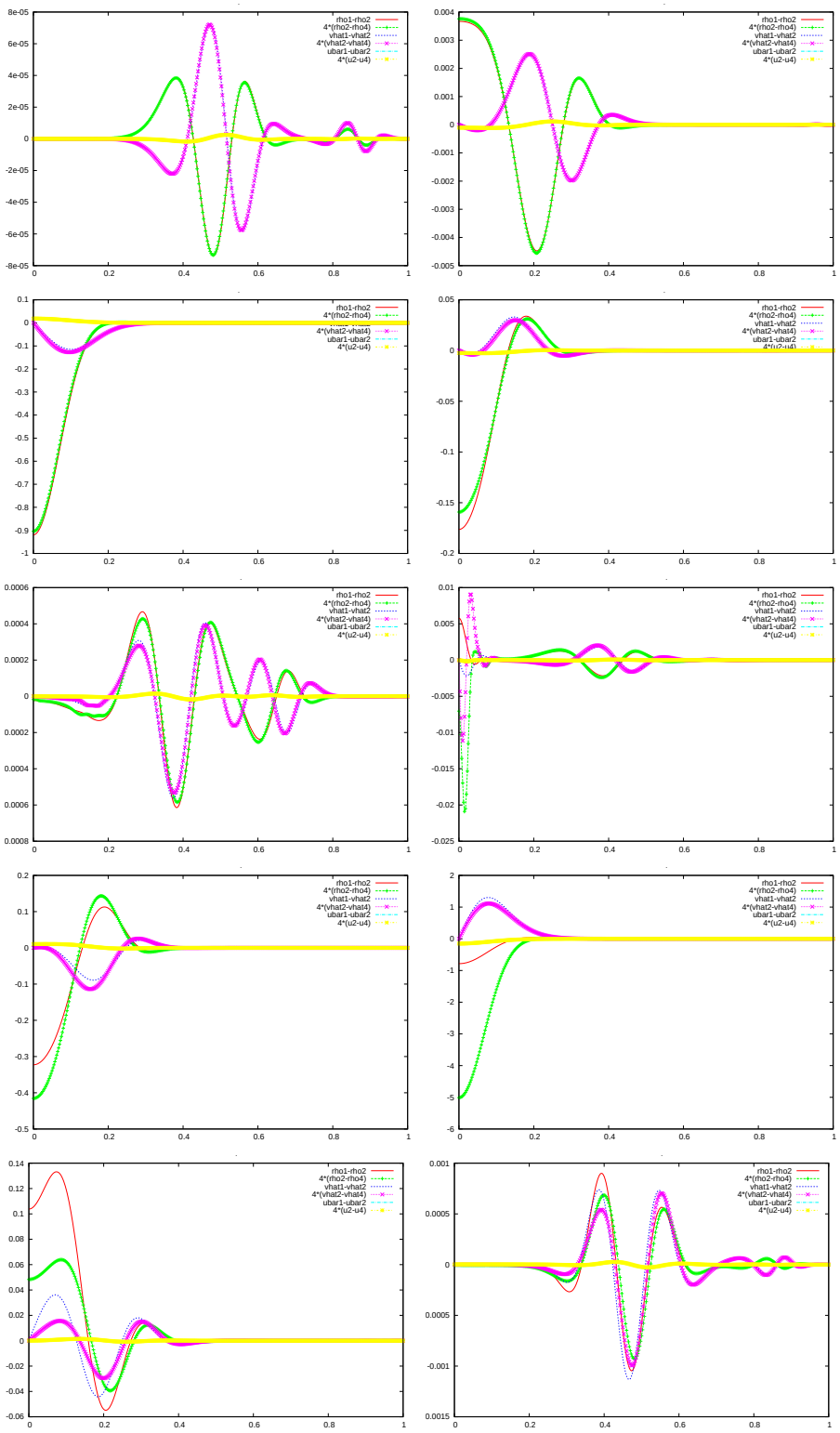

Figure 5.10: Convergence tests of a $\bar{\rho}_5$ perturbation on an $N = 400, \lambda = 0.95\pi$ star-like background, i.e. double the radial resolution of that in figure 5.9. Placing the numerical boundary closer to the physical boundary requires a higher resolution to maintain convergence.

5.5 Non-linear system in new variables $\hat{v}, f$

With a working code for the background and linear perturbations, we now include the non-linear terms. The evolution equations over all modes are thus:

$$\begin{aligned}
\dot{\bar{\rho}}_\gamma =& -\chi_\gamma r^{\ell_\alpha+\ell_\beta-\ell_\gamma}\left\{\hat{C}_{\alpha\beta-\gamma}\left[\bar{\rho}_\alpha\hat{v}'_\beta+\bar{\rho}'_\alpha\hat{v}_\beta+\bar{\rho}_\alpha\ell_\beta f_\beta+\frac{\bar{\rho}'_\alpha}{r}\ell_\beta\bar{u}_\beta+(2+\ell_\alpha+2\ell_\beta)\bar{\rho}_\alpha\frac{\hat{v}_\beta}{r}\right]\right.\\
&\left.+(\ell_\alpha\ell_\beta\hat{C}_{\alpha\beta-\gamma}+\hat{D}_{-\gamma\alpha\beta})\frac{\bar{\rho}_\alpha\bar{u}_\beta}{r^2}\right\}, \qquad (5.5.1)\\
\dot{\hat{v}}_\gamma =& -\chi_\gamma r^{\ell_\alpha+\ell_\beta-\ell_\gamma}\left\{\hat{v}_\alpha\hat{v}'_\beta\hat{C}_{\alpha\beta-\gamma}+\hat{v}_\alpha f_\beta\left(\ell_\beta\hat{C}_{\alpha\beta-\gamma}+\frac{\ell_\gamma\hat{D}_{\alpha\beta-\gamma}}{L_\gamma^2}\right)\right.\\
&+\frac{\hat{v}_\alpha\hat{v}_\beta}{r}\left(2\ell_\alpha\hat{C}_{\alpha\beta-\gamma}+\frac{\ell_\gamma\hat{D}_{\alpha\beta-\gamma}}{L_\gamma^2}\right)+\frac{\bar{u}_\alpha\hat{v}'_\beta}{r}\hat{C}_{\alpha\beta-\gamma}\\
&+\frac{\bar{u}_\alpha f_\beta}{r}\left(\ell_\alpha\ell_\beta\hat{C}_{\alpha\beta-\gamma}+\frac{\ell_\alpha\ell_\gamma\hat{D}_{\alpha\beta-\gamma}}{L_\gamma^2}\right)-\frac{\bar{w}_\alpha\bar{w}_\beta}{r}\left(\hat{D}_{-\gamma\alpha\beta}+\frac{\ell_\gamma\hat{F}_{-\gamma\alpha\beta}}{L_\gamma^2}\right)\\
&+\frac{\hat{v}_\alpha\bar{u}_\beta}{r^2}\left[\ell_\beta\left(\ell_\beta+2\ell_\alpha-1-\ell_\gamma\right)\hat{C}_{\alpha\beta-\gamma}+\hat{D}_{-\gamma\alpha\beta}\right]\\
&\left.+\frac{\bar{u}_\alpha\bar{u}_\beta}{r^3}\left[(\ell_\beta-1)(\ell_\alpha\ell_\beta\hat{C}_{\alpha\beta-\gamma}+\hat{D}_{-\gamma\alpha\beta})+\frac{\ell_\gamma}{L_\gamma^2}\left(\ell_\alpha\ell_\beta\hat{D}_{\alpha\beta-\gamma}+\hat{E}_{-\gamma\alpha\beta}\right)\right]\right\}\\
&-2K\bar{\rho}'_\gamma, \qquad (5.5.2)\\
\dot{\bar{w}}_\gamma =& \chi_\gamma r^{\ell_\alpha+\ell_\beta-\ell_\gamma}\left\{\hat{v}_\alpha\bar{w}'_\beta\frac{\hat{D}_{\alpha\beta-\gamma}}{L_\gamma^2}+\frac{\ell_\alpha\bar{u}_\alpha\bar{w}'_\beta}{r}\frac{\hat{D}_{\alpha\beta-\gamma}}{L_\gamma^2}+(1+\ell_\beta)\frac{\hat{v}_\alpha\bar{w}_\beta}{r}\frac{\hat{D}_{\alpha\beta-\gamma}}{L_\gamma^2}\right.\\
&\left.+\frac{\bar{u}_\alpha\bar{w}_\beta}{r^2}\frac{1}{L_\gamma^2}\left[\ell_\alpha(1+\ell_\beta)\hat{D}_{\alpha\beta-\gamma}+\hat{E}_{-\gamma\alpha\beta}+\hat{F}_{-\gamma\alpha\beta}\right]\right\}, \qquad (5.5.3)\\
\dot{f}_\gamma =& \chi_\gamma r^{\ell_\alpha+\ell_\beta-\ell_\gamma}\left\{f_\alpha f_\beta\frac{\hat{D}_{\alpha\beta-\gamma}}{L_\gamma^2}+\hat{v}_\alpha f'_\beta\frac{\hat{D}_{\alpha\beta-\gamma}}{L_\gamma^2}+\hat{v}'_\alpha f_\beta\frac{\hat{D}_{\alpha\beta-\gamma}}{L_\gamma^2}\right.\\
&+\frac{\hat{v}_\alpha\hat{v}'_\beta}{r}\left(\hat{C}_{\alpha\beta-\gamma}+\frac{\hat{D}_{\alpha\beta-\gamma}-\hat{D}_{\beta\alpha-\gamma}}{L_\gamma^2}\right)+\frac{\ell_\alpha\bar{u}_\alpha f'_\beta}{r}\frac{\hat{D}_{\alpha\beta-\gamma}}{L_\gamma^2}+\frac{2\bar{w}_\alpha\bar{w}'_\beta}{r}\frac{\hat{F}_{-\gamma\alpha\beta}}{L_\gamma^2}\\
&+\frac{\hat{v}_\alpha f_\beta}{r}\left[\ell_\beta\hat{C}_{\alpha\beta-\gamma}+(1+2\ell_\alpha+2\ell_\beta)\frac{\hat{D}_{\alpha\beta-\gamma}}{L_\gamma^2}+\ell_\beta\frac{\hat{D}_{\beta\alpha-\gamma}}{L_\gamma^2}\right]\\
&+\frac{2\hat{v}_\alpha\hat{v}_\beta}{r^2}\left[\ell_\beta\hat{C}_{\alpha\beta-\gamma}+\frac{\ell_\alpha+\ell_\beta}{L_\gamma^2}\hat{D}_{\alpha\beta-\gamma}\right]+\frac{\bar{w}_\alpha\bar{w}_\beta}{r^2}\left[\hat{D}_{-\gamma\alpha\beta}+\frac{\ell_\alpha+\ell_\beta}{L_\gamma^2}\hat{F}_{-\gamma\alpha\beta}\right]\\
&+\frac{\bar{u}_\alpha f_\beta}{r^2}\left[\ell_\alpha\ell_\beta\hat{C}_{\alpha\beta-\gamma}+\ell_\alpha(\ell_\alpha+2\ell_\beta)\frac{\hat{D}_{\alpha\beta-\gamma}}{L_\gamma^2}+\ell_\alpha\ell_\beta\frac{\hat{D}_{\beta\alpha-\gamma}}{L_\gamma^2}+\frac{\hat{E}_{-\gamma\alpha\beta}+\hat{E}_{-\gamma\beta\alpha}}{L_\gamma^2}\right]\\
&+\frac{\hat{v}_\alpha\bar{u}_\beta}{r^3}\left(\hat{D}_{-\gamma\alpha\beta}+\frac{\hat{E}_{-\gamma\alpha\beta}+\hat{E}_{-\gamma\beta\alpha}}{L_\gamma^2}\right)+\frac{\bar{u}_\alpha\bar{u}_\beta}{r^4}\left[\ell_\alpha\ell_\beta(\ell_\beta-1)\hat{C}_{\alpha\beta-\gamma}\right.\\
&\left.\left.+(\ell_\beta-1)\hat{D}_{-\gamma\alpha\beta}+(\ell_\alpha+\ell_\beta-2)\frac{\ell_\alpha\ell_\beta\hat{D}_{\alpha\beta-\gamma}+\hat{E}_{-\gamma\alpha\beta}}{L_\gamma^2}\right]\right\}. \qquad (5.5.4)
\end{aligned}$$

This system contains terms with powers of r as low as $\ell_\alpha + \ell_\beta - \ell_\gamma - 4$, so there are two special cases that need taking into consideration to properly regularize. The first are the terms in the series that satisfy $\ell_\alpha + \ell_\beta - \ell_\gamma = 0$, and the second are those with $\ell_\alpha + \ell_\beta - \ell_\gamma = 2$. (Since $\ell_\alpha + \ell_\beta + \ell_\gamma$ is even, $\ell_\alpha + \ell_\beta - \ell_\gamma$ is also even, and we need only consider these two cases.)

It can be shown that coefficients of terms divided by r either remain regular, have vanishing coefficients, or cancel with cross-terms because they are antisymmetric over α, β. These terms will need l'Hôpital's rule or some other scheme to evaluate the origin.

The variable $\bar{u}$ is still present in these equations, since we have only replaced its derivative. We can either choose to recover $\bar{u}$ by integrating f, or we could time-evolve it alongside the other variables (and perhaps derive f from it instead). Our code time-evolves all five variables as this is easy to do with the current framework, although an integration should, in theory, be faster since there it avoids having to compute a large number of non-linear couplings.

Another issue with this choice is that numerical error and dissipation may cause 'drift' between the derived and time-evolved values of $\bar{u}$, and in the absence of some variable constraint we should monitor both. The easiest way to do the comparison is just to output and display them both graphically.

Finally, we can see from the zero-sum property of the Gaunt coefficients (2.2.11) that a system will remain axisymmetric if it is initially axisymmetric. This is true for the fluid equations, or MHD, or any other time evolution that we can write in this manner.

5.5.1 Discussion of the non-linear fluid code

A non-linear, nonaxisymmetric RK4 code with compiler optimizations and copying negative-m modes (4.2.2) scales with time roughly as $\ell_m^{4.6}$ for modes up to $\ell = 9$. This is a slightly lower figure than we would expect (ℓ_m^5), most likely because of the triangle inequality for the ℓ's. Figure 5.11 lists run-times on the same machine for comparative purposes. We would expect $\ell_m = 10$ to take about 13 seconds per time step with this resolution, about 5 minutes with $\ell_m = 20$, and, in theory, several days with $\ell_m = 100$.

Further optimizations can be made to the nonaxisymmetric code by only considering the modes whose m is a multiple of the lowest present in the initial data: for example, $m = 2$ initial data will only lead to even m. Problems where $m \sim \ell$ in initial data scale more like the axisymmetric code if ℓ_m is not set too high above the initial data maximum ℓ.

Since the quadratic changes we have so far tried have been small, convergence properties are similar to the linear scheme. Setting any kind of initial data on modes $\ell > 0$ will excite other modes. For example, an $\ell = 1$ perturbation will induce perturbations in the $\ell = 2$ mode through self-couplings, which in turn will couple with itself and $\ell = 1$ to induce still higher modes, and so on. For a non-linear evolution we see wave-like behaviour for all modes

	Axisymmetric		Nonaxisymmetric
ℓ_m	Linear	Non-linear	Non-linear
1	1.7ms	1.9ms	3.4ms
2	2.7ms	4.5ms	19ms
3	3.7ms	9.0ms	70ms
4	4.8ms	17ms	220ms
5	5.8ms	28ms	570ms
6	6.9ms	44ms	1.3s
7	8.1ms	65ms	2.6s
8	9.0ms	92ms	4.8s
9	10.4ms	126ms	8.4s
	$\sim \ell_m$	$\sim \ell_m^{2.6}$	$\sim \ell_m^{4.6}$

Figure 5.11: Approximate run-time required per time step on an $N = 200$ second-order accurate evolution with dissipation, optimized to run on a 3GHz Pentium D processor under Linux. Each was run several times over more than 1 time step, and the fastest time recorded, to take account of any background processes.

up to ℓ_m and with it convergence for low modes and a loss after reflection for the higher modes, just as we did in the linear evolutions.

Figure 5.12 shows the value of $\bar{\rho}_1$ at different timesteps on an $N = 200$ grid with different values of ℓ_m. Increasing $\ell_m \geq 2$ shows a larger but fixed difference, although the figure only demonstrates this for $\ell_m = 2, 3$. It seems that $\ell = 2$ is important to the evolution in this case, whilst higher modes are relatively unimportant. Typically we observe that it is most efficient to set ℓ_m equal to the highest initial data mode plus one.

The non-linear code is unstable for $\mathcal{O}(1)$ initial data in $\ell > 0$ velocity terms, regardless of resolution or the values of other parameters, unlike the linear code. As a result we are forced to set initial data that is small compared to the background, and thus perturbations using the non-linear code will generally gives us small, unremarkable differences to evolutions that we have already seen. We should now investigate some important non-linear effects that we could not in the linear evolutions, such as rotation, and later on, magnetic fields.

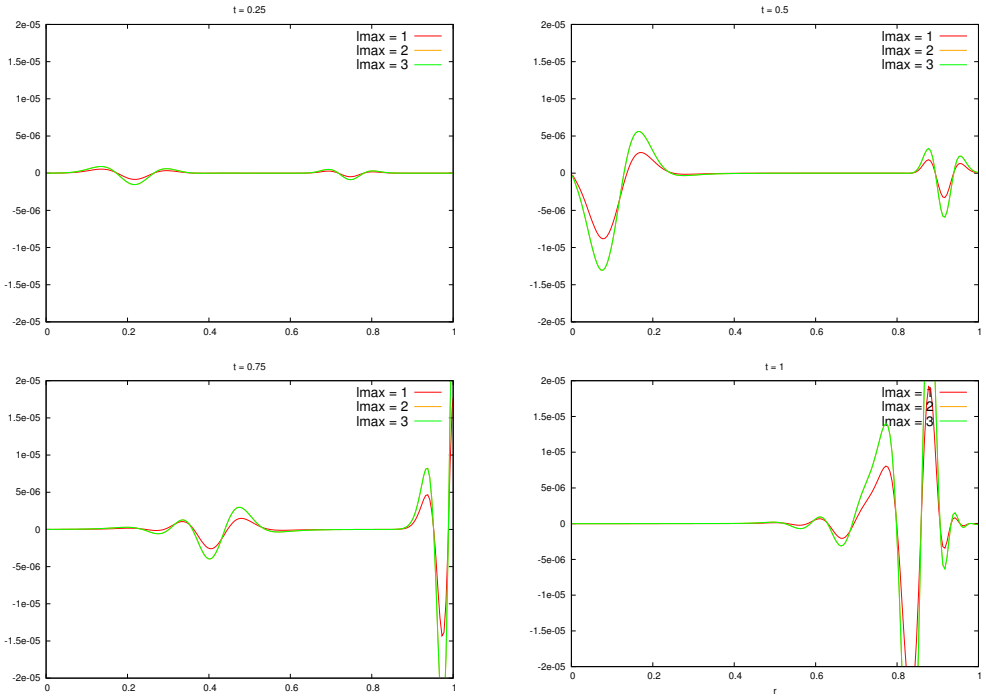

Figure 5.12: Convergence of a non-linear $\bar{\rho}_1$ evolution with increasing ℓ_m. The plots show the difference with a linear evolution having the same initial data; the difference is smaller with $\ell_m = 1$ but for $\ell = 2, 3$ the curves almost exactly overlay each other.

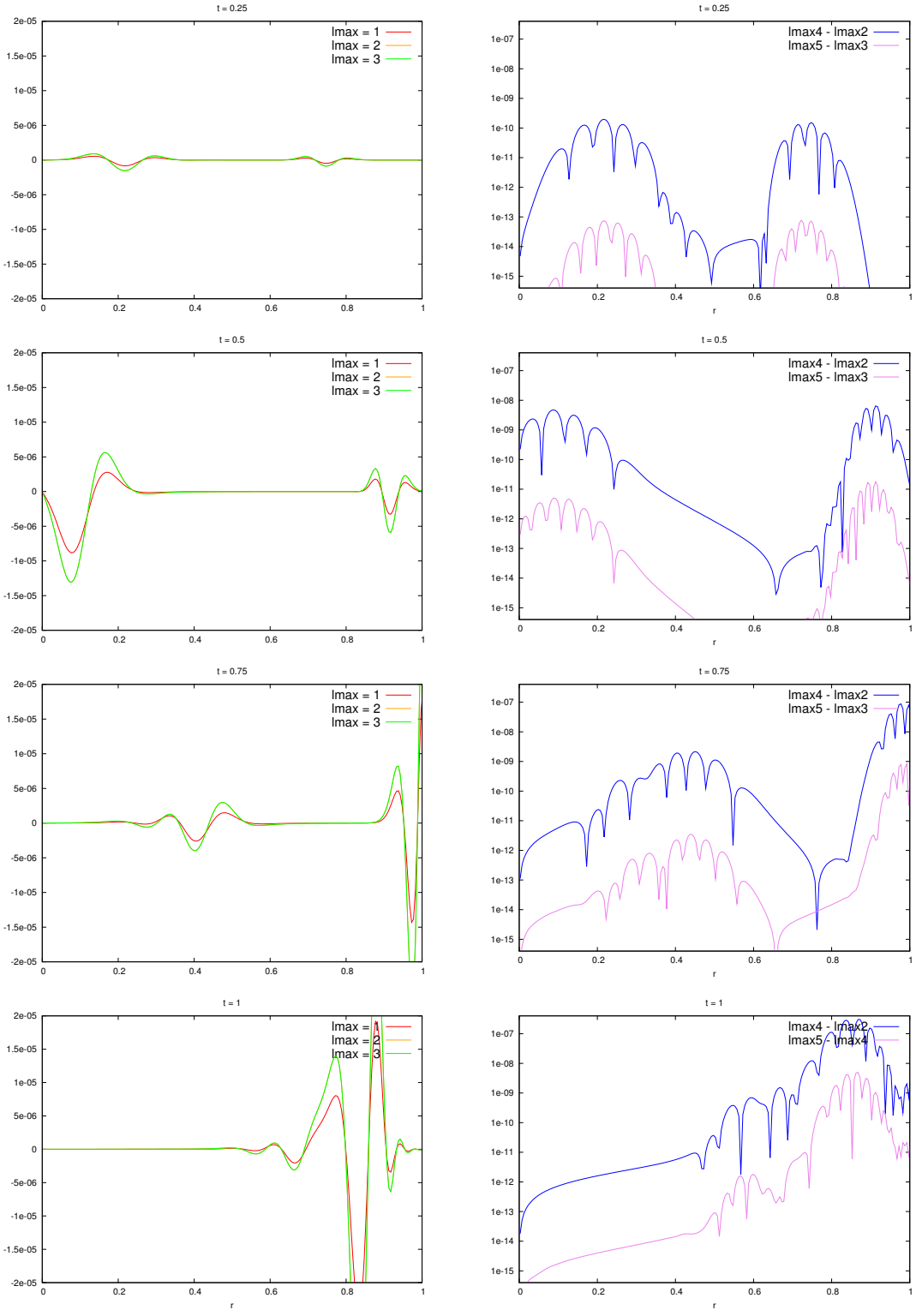

Figure 5.13: Plots demonstrating the convergence of a non-linear $\bar{\rho}_1$ evolution with increasing ℓ_m. The left column is the difference between the linear and non-linear evolutions of the same initial data with increasing ℓ_m; for $\ell_m \geq 2$ this difference is negligible. The right column shows the difference between non-linear evolutions $|(\ell_m = 4) - (\ell_m = 2)|$,$(\ell_m = 5) - (\ell_m = 3)|$.

5.5.2 Energy

A good test of a fluid code is to ensure that, in the absence of sources or sinks, energy conservation is obeyed. The conservation of energy can be written in the form

$$\frac{\partial \mathfrak{D}}{\partial t} + \nabla_j \mathfrak{F}^j = 0, \tag{5.5.5}$$

where $\mathfrak{D}$ is the energy density and $\mathfrak{F}$ the energy flux across surfaces. It can be shown [13] that the energy of an ideal fluid is described by

$$\frac{\partial}{\partial t}\left[\rho\left(\tfrac{1}{2}v^2 + U + \Phi\right)\right] + \nabla_j\left[\rho v^j\left(\tfrac{1}{2}v^2 + h + \Phi\right)\right] = 0, \tag{5.5.6}$$

where the pressure

$$P = (\gamma - 1)\rho U = K\rho^\gamma \tag{5.5.7}$$

gives the following expressions for the internal energy U, from (5.1.15), and enthalpy h, for a polytrope:

$$\begin{aligned} U &= \frac{K}{\gamma - 1}\rho^{\gamma-1}, \\ h &= U + \frac{P}{\rho} = \frac{\gamma K}{\gamma - 1}\rho^{\gamma-1}. \end{aligned} \tag{5.5.8}$$

These expressions can be combined to show

$$\nabla h = \frac{\nabla P}{\rho}. \tag{5.5.9}$$

To find the total energy $\mathfrak{E}$ we integrate the energy density over the (fixed) volume of the star and apply the divergence theorem, noting that the energy flux across the outer boundary is zero:

$$\mathfrak{E} = \int_V \left(\tfrac{1}{2}\rho v^2 + K\rho^\gamma + \rho\Phi\right) dV = \mathfrak{T} + \mathfrak{U} + \mathfrak{W}, \tag{5.5.10}$$

where $\mathfrak{T}, \mathfrak{U}, \mathfrak{W}$ are the kinetic, internal and gravitational energies, respectively.

To calculate these energies we need to find the spherical harmonic expansions of the integrands:

$$\begin{aligned}
\mathfrak{T} &= \frac{1}{2}\int \rho v^2 dV \\
&= \frac{1}{2}\int Y_\gamma \rho_\gamma \left[Y_\alpha Y_\beta v_\alpha v_\beta + r^2\left(Z^a_\alpha Z_{\beta b} u_\alpha u_\beta + S^a_\alpha S_{\beta b} w_\alpha w_\beta\right)\right] r^2 dr\, d\Omega \\
&= \frac{1}{2}\int r^{\ell_\gamma+\ell_\alpha+\ell_\beta}\bar{\rho}_\gamma \left[(Y_\gamma Y_\alpha Y_\beta)\bar{v}_\alpha\bar{v}_\beta + (Y_\gamma Z^a_\alpha Z_{\beta b})\bar{u}_\alpha\bar{u}_\beta + (Y_\gamma S^a_\alpha S_{\beta b}) r^2\bar{w}_\alpha\bar{w}_\beta\right] dr\; d\Omega \\
&= \frac{1}{2}\int r^{\ell_\gamma+\ell_\alpha+\ell_\beta}\bar{\rho}_{-\gamma}\left[\hat{C}_{\alpha\beta-\gamma}\;\bar{v}_\alpha\bar{v}_\beta + \hat{D}_{-\gamma\alpha\beta}\;\left(\bar{u}_\alpha\bar{u}_\beta + r^2\bar{w}_\alpha\bar{w}_\beta\right)\right] dr, \qquad (5.5.11) \\
\mathfrak{U} &= \int K\rho^2 dV \\
&= K\int Y_\alpha Y_\beta d\Omega \int \rho_\alpha\rho_\beta\; r^2 dr \\
&= 4\pi K(-1)^{m_\beta}\delta_{\alpha,-\beta}\int r^{\ell_\alpha+\ell_\beta+2}\bar{\rho}_\alpha\bar{\rho}_\beta\; dr \\
&= 4\pi K(-1)^{m_\gamma}\int r^{2\ell_\gamma+2}\bar{\rho}_\gamma\bar{\rho}_{-\gamma}\; dr, \qquad (5.5.12) \\
\mathfrak{W} &= \frac{1}{2}\int \rho\,\Phi dV \\
&= 2\pi(-1)^{m_\gamma}\int r^{2\ell_\gamma+2}\bar{\rho}_\gamma\bar{\Phi}_{-\gamma}\; dr. \qquad (5.5.13)
\end{aligned}$$

We can then use some of the techniques mentioned in section 3.2 to integrate these quantities numerically over r.

The energy of a test system, a linear $\bar{\rho}_1$ perturbation on a flat background with artificial dissipation, is shown in figure 5.14. The kinetic energy $\mathfrak{T}$ initially grows through pressure differentials between high and low areas of density. It then decreases as one part of the density wave hits the outer surface and matter builds up on the outer shell. A local minimum appears to be reached halfway through the reflection, just before the rebound, but it does not drop to zero as there is still matter travelling towards the centre. The total energy slowly decreases because of the artificial dissipation, but varies on the order of 10^{-6} over the time scale shown (figure 5.15), a small change even when compared against the $\mathcal{O}(10^{-4})$ kinetic/internal energies.

Without artificial dissipation the energy curves look almost identical. The total energy remains constant to one part in 10^{-6} and does not appear to globally increase or decrease.

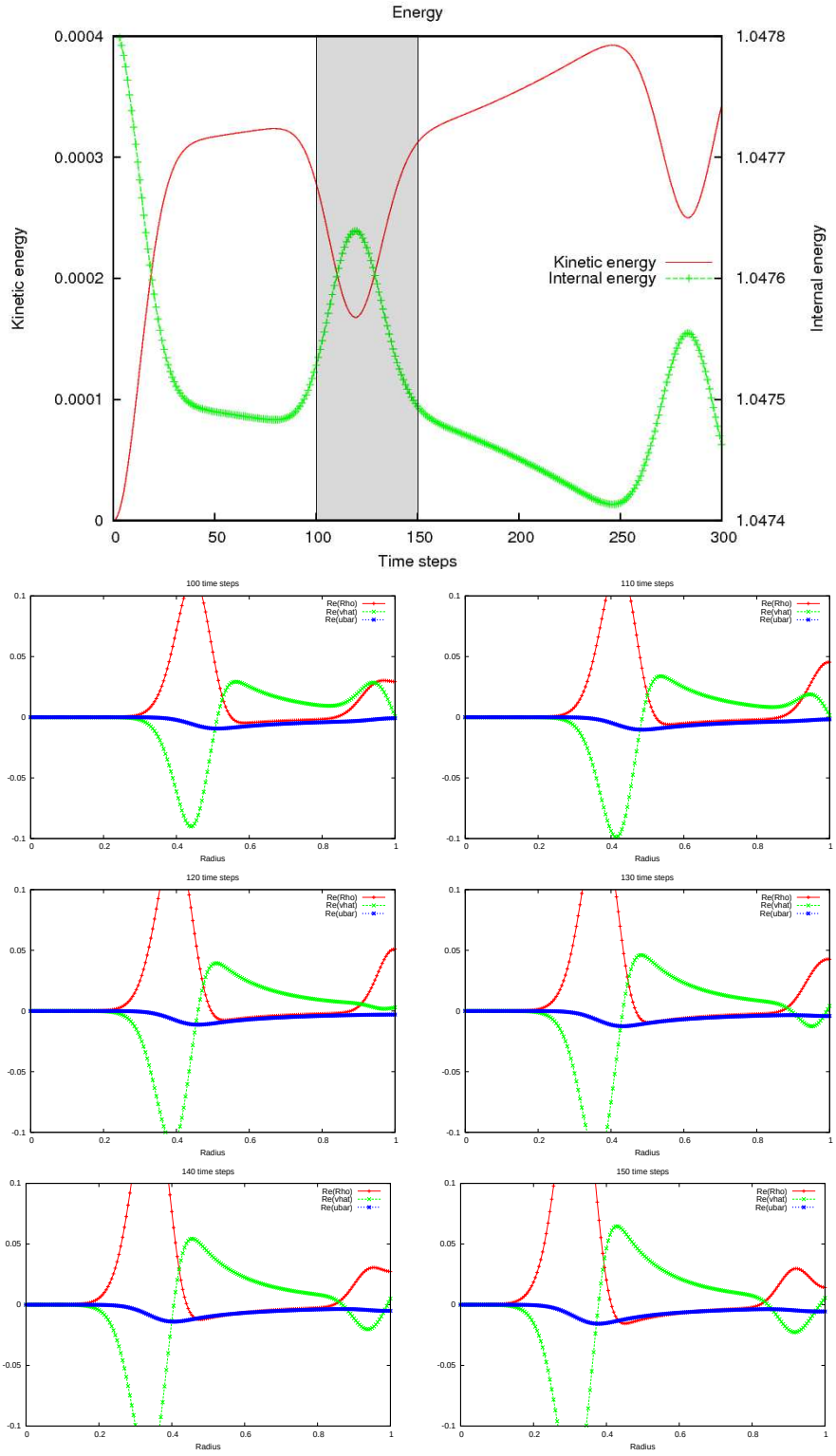

Figure 5.14: Plots of the kinetic and internal energy (top) of a flat star with an initial $\ell = 1$ density perturbation. The evolution of the $\ell = 1$ mode is shown for the shaded region underneath.

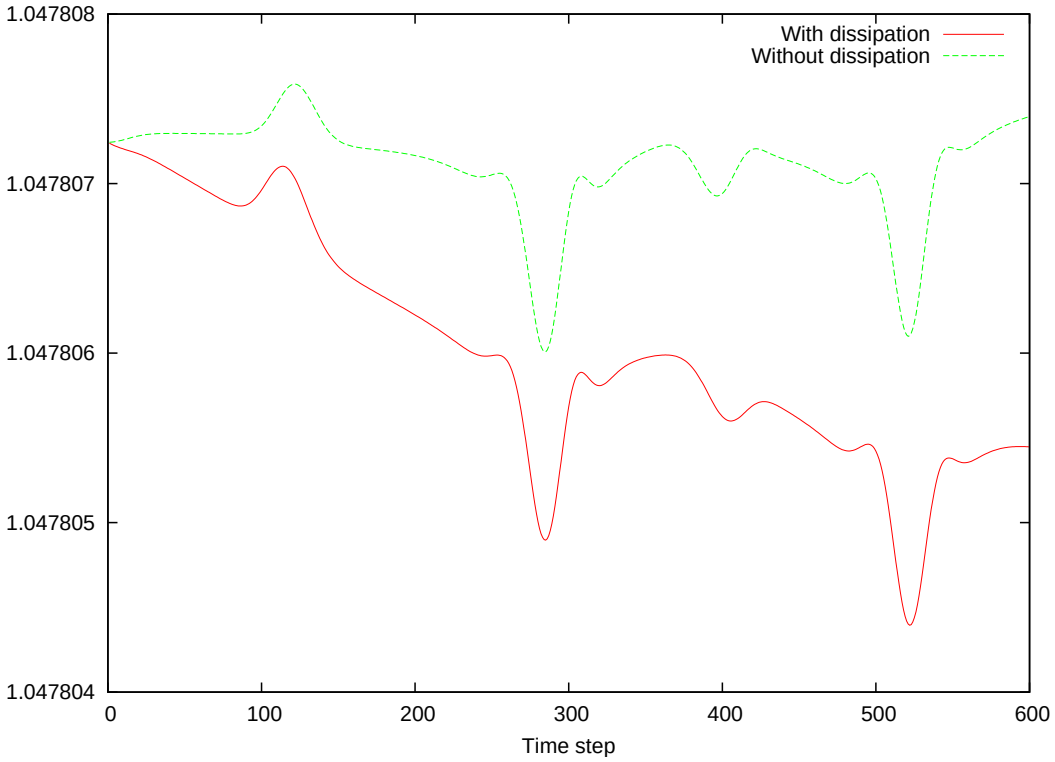

Figure 5.15: The total energy of the same system shown over twice as many time steps. Numerical dissipation is clearly removing energy from the system but apparently not in a way that affects the evolution.

5.6 Improvements to the model

5.6.1 Solving Poisson's equation

Up until now we have used gravitational potentials that remain fixed in time, and which are often spherical. We now show how to solve Poisson's equation to find ϕ: its expansion in spherical harmonics gives

$$\bar{\phi}''_\gamma + \frac{2(\ell_\gamma + 1)}{r}\bar{\phi}'_\gamma = 4\pi G\bar{\rho}_\gamma, \tag{5.6.1}$$

for every γ. In vacuum (presumably the region outside R) this has solution

$$\bar{\phi} \propto r^{-2\ell+1} \tag{5.6.2}$$

on the condition that $\bar{\phi} \to 0$ as $r \to \infty$.

By writing $\eta_\gamma = \bar{\phi}'_\gamma$, the solutions can be written as

$$\eta_\gamma(r) = 4\pi G\frac{r^{-(2\ell_\gamma+2)}}{2\ell+3}\int_0^r \bar{\rho}_\gamma r^{(2\ell_\gamma+2)}dr, \tag{5.6.3}$$

$$\bar{\phi}_\gamma(r) = \int_0^r \eta_\gamma dr. \tag{5.6.4}$$

The two boundary conditions we need are $\eta_\gamma(0) = 0$ and (5.6.2), which means setting $\bar{\phi}_\gamma(R) = \frac{-R}{2\ell_\gamma+1}\eta_\gamma(R)$. Numerically this would suggest that one starts by integrating (5.6.3) *up* from $r = 0$, apply the boundary condition to find $\bar{\phi}(R)$, and then integrate (5.6.4) *down* from $r = R$, as per

$$\bar{\phi}_\gamma = \bar{\phi}(R) - \int_r^R \eta_\gamma dr. \tag{5.6.5}$$

One can evaluate these integrals by using the trapezium rule:

$$\zeta_{(i+1)} = \zeta_{(i)} + \left(r_{(i+1)}^{2\ell+3} - r_{(i)}^{2\ell+3}\right)\frac{\bar{\rho}_{(i+1)} + \bar{\rho}_{(i)}}{2}, \tag{5.6.6}$$

$$\eta_{(i)} = \frac{2K\lambda^2\zeta_{(i)}}{(2\ell+3)}\frac{1}{r^{2\ell+2}}, \tag{5.6.7}$$

$$\bar{\phi}_{(i)} = \bar{\phi}_{(i+1)} - h\frac{\eta_{(i+1)} + \eta_{(i)}}{2}. \tag{5.6.8}$$

where one may set

$$\zeta_{(0)} = \begin{cases} 0, & \text{(regular grid)} \\ r_{(0)}^{2\ell+3}\bar{\rho}_{(0)}. & \text{(staggered grid)} \end{cases} \tag{5.6.9}$$

5.6.2 Stratification

A wider range of equations of state are available for study if we consider some kind of *stratification* where the neutron star is not barotropic, but its pressure additionally depends on some other quantities such as the entropy or chemical composition. Stratification implies the presence of some composition gradient which provides a buoyancy force. Neutron stars are expected to be *stably stratified* [73], meaning that an object in equilibrium will oscillate around its initial position at the *Brunt-Väisälä* frequency if perturbed.

In our framework the stratification $\mathcal{K}$ is set via a modified equation of state

$$P = \mathcal{K}(s)\rho^{\Lambda}, \tag{5.6.10}$$

where initial data for $\mathcal{K}$ can be set using the numerical solution of the corresponding Lane-Emden problem $P = K\rho^{\Gamma}$ for a given K, Γ. The requirement for stable stratification [73] comes from the polytropic relation (5.1.12) which can be rearranged as

$$\mathcal{K} \propto \rho^{\Gamma-\Lambda}. \tag{5.6.11}$$

If $\Gamma < \Lambda$ then an increase in $\mathcal{K}$ gives a decrease in the density. Note that if $\Gamma \simeq \Lambda$ then $\mathcal{K}$ is close to constant, and the stratification is *weak*.

The Euler equation is now

$$\frac{\nabla P}{\rho} = \Lambda\mathcal{K}\rho^{\Lambda-2}\nabla\rho + \rho^{\Lambda-1}\nabla\mathcal{K}, \tag{5.6.12}$$

and so we shall continue to set $\Lambda = 2$, and initially specify $\mathcal{K}$ from some numerical solution to the $\Gamma < 2$ Lane-Emden equation. The stratification is advected with the fluid since entropy is constant for a particle ($\frac{Ds}{Dt} = 0$):

$$\dot{\mathcal{K}} + v^i\nabla_i\mathcal{K} = 0. \tag{5.6.13}$$

5.7 Cylindrically symmetric rotation and equilibrium

In section 5.3 we investigated the equilibria of static stars. By now introducing rotation, one now needs to balance the outwards-acting centrifugal force with pressure and gravity. For now we shall concern ourselves with relatively simple rotation laws in axisymmetry.

Consider a rotation profile where the angular velocity Ω depends only on the distance from the rotation axis $\varpi = r\sin\theta$. The conservation of momentum equation (5.0.5) can be integrated in this case because the centrifugal force is given by the gradient of a potential

[49, 83, 84], giving

$$\Phi + \int \frac{1}{\rho} dP - \int \Omega^2 \varpi \, d\varpi = \text{constant}. \tag{5.7.1}$$

There are at least three well-known examples of ϖ-dependent rotation:

$$\Omega(\varpi) = \begin{cases} \Omega_c, & \text{(rigid)} \\ \dfrac{j_0}{A^2 + \varpi^2}, & (j\text{-constant}) \\ \dfrac{v_0}{\sqrt{A^2 + \varpi^2}}. & (v\text{-constant}) \end{cases} \tag{5.7.2}$$

The latter two are named for the limit of Ω as $\varpi \gg A$; for j-constant, one has constant specific angular momentum ($L = \varpi^2 \Omega$), and for v-constant, one has constant linear velocity ($v = \varpi \Omega$). These can all be inserted into (5.7.1) and integrated, using the $\gamma = 2$ polytropic EOS, to give closed-form expressions:

$$\begin{aligned} &\Phi + 2K\rho - \Psi = \zeta, && (\zeta = \text{constant}) \\ &\Psi = \begin{cases} \frac{1}{2}\Omega_c^2 \varpi^2 & \text{(rigid)} \\ \dfrac{-j_0^2}{2(A^2 + \varpi^2)} & (j\text{-constant}) \\ \frac{1}{2} v_0^2 \ln(A^2 + \varpi^2) & (v\text{-constant}) \end{cases} \end{aligned} \tag{5.7.3}$$

To translate these expressions into a spectral form, we need the expansions for Φ, ρ, as well as ϖ:

$$\varpi^2 = r^2(1 - \cos^2\theta) = \frac{2r^2}{3}\left(Y_0^0 - \frac{Y_2^0}{\sqrt{5}}\right). \tag{5.7.4}$$

In addition one should be aware of how to set the axial component of the velocity given some rotation profile. Ignoring other components, and in axisymmetry, the velocity derivative is

$$\begin{aligned} \mathbf{v} \cdot \nabla &= r\Omega \sin\theta \left(\frac{1}{r\sin\theta}\frac{\partial}{\partial\varphi}\right) = \Omega \frac{\partial}{\partial\varphi} \\ &= r^{\ell-1} \bar{w}_\gamma S_\gamma^{(\varphi)} \frac{\partial}{\partial\varphi}. \end{aligned} \tag{5.7.5}$$

If one assumes a system is rigidly rotating, nondimensionalizing the Euler equation gives the unit-less quantity

$$\hat{\Omega}_c^2 = \frac{\Omega_c^2}{G\rho_c}. \tag{5.7.6}$$

This in turn gives us the rotation period

$$t = \frac{2\pi}{\Omega_c} = \frac{2\pi}{\hat{\Omega}_c}[t], \tag{5.7.7}$$

implying that the time units for one rotation are simply given by $2\pi/\hat{\Omega}_c$. To get an idea of physically reasonable rotation frequencies, PSR J1748-2446ad is the fastest (confirmed) spinning pulsar so far observed; at $\sim 2M_\odot$and rotating at 716Hz [52] we could model this with $\hat{\Omega}_c = 1/\sqrt{3}$.

5.7.1 Rigid rotation

Through equation (5.7.5), and noticing that $S_1^{(\varphi)} = \sqrt{3}$, rigid rotation $\Omega(\varpi) = \Omega_c$ corresponds to setting $\bar{w}_1 = \Omega_c/\sqrt{3}$. To seek equilibrium solutions, we expand the density and gravitational potential terms in (5.7.3) and then equate the coefficients of spherical harmonics:

$$\phi + 2K\rho = \tfrac{1}{2}\Omega_c^2\varpi^2 + \zeta \tag{5.7.8}$$

$$\implies \sum_\gamma \left(\bar{\phi}_\gamma + 2K\bar{\rho}_\gamma\right) r^{\ell_\gamma} Y_\gamma = \frac{\Omega_c^2 r^2}{3}\left(Y_0^0 - \frac{Y_2^0}{\sqrt{5}}\right) + \zeta Y_0^0. \tag{5.7.9}$$

Using Poisson's equation to remove $\bar{\rho}_\gamma$ gives second-order ODEs to be solved:

$$\sum_\gamma \left[\bar{\phi}_\gamma + \frac{1}{\lambda^2}\left(\frac{2(\ell_\gamma+1)}{r}\bar{\phi}'_\gamma + \bar{\phi}''_\gamma\right)\right] r^\ell Y_\gamma = \frac{\Omega_c^2 r^2}{3}\left(Y_0^0 - \frac{Y_2^0}{\sqrt{5}}\right) + \zeta Y_0^0. \tag{5.7.10}$$

The homogeneous problem has solutions that can be written in terms of spherical Bessel functions,

$$\begin{aligned} \bar{\phi}_\gamma &= -2KC_\gamma r^{-\alpha} J_\alpha(\lambda r), \\ \bar{\rho}_\gamma &= C_\gamma r^{-\alpha} J_\alpha(\lambda r). \qquad\qquad (\alpha = \tfrac{1}{2} + \ell_\gamma) \end{aligned} \tag{5.7.11}$$

The modes with rotational terms ($\ell = 0, 2$) admit the following solutions, which are regular at the origin:

$$\begin{aligned} \bar{\phi}_0 &= \frac{r^2\Omega_c^2}{3} - \frac{2\Omega_c^2}{\lambda^2} - \zeta - 2KC_0\frac{\sin(\lambda r)}{\lambda r}, \\ \bar{\rho}_0 &= \frac{\Omega_c^2}{K\lambda^2} + C_0\frac{\sin(\lambda r)}{\lambda r}, \end{aligned} \tag{5.7.12}$$

and

$$\bar{\phi}_2 = -\frac{\Omega_c^2}{3\sqrt{5}} - \frac{C_2\sqrt{2}\left[3r\lambda\cos(\lambda r) + (r^2\lambda^2 - 3)\sin(\lambda r)\right]}{r^5\sqrt{\lambda^5}}, \tag{5.7.13}$$

$$\bar{\rho}_2 = C_2\left[\frac{3r\lambda\cos(\lambda r) + (r^2\lambda^2 - 3)\sin(\lambda r)}{Kr^5\sqrt{2\lambda^5}}\right]. \tag{5.7.14}$$

We now need to find the constants C_γ and ζ, and we start by setting C_0 so that $\bar{\rho}_0(r = 0) = \rho_c$. The remainder (one for each mode) must be found by matching to the exterior of the star (section 5.6.1), where the gravitational potential E satisfies

$$\frac{2(\ell+1)}{r}\bar{E}'_\gamma + \bar{E}''_\gamma = 0 \tag{5.7.15}$$

$$\implies \bar{E}_\gamma = A - B\frac{r^{-1-2\ell}}{(1+2\ell_\gamma)}. \tag{5.7.16}$$

We then set $A = 0$ so that $\lim_{r\to\infty}\bar{E} = 0$. In a more realistic model the surface of the star would be given by the function $r^*(\theta,\varphi)$ but we match the potentials at the spherical shell $r^* \equiv 1$, where

$$\bar{E}_\gamma = \bar{\phi}_\gamma, \qquad \bar{E}'_\gamma = \bar{\phi}'_\gamma, \tag{5.7.17}$$

$$\implies \bar{\phi}'_\gamma = (2\ell_\gamma + 1)\bar{\phi}_\gamma \qquad (\text{at } r = 1). \tag{5.7.18}$$

This constraint lets us determine the remaining constants:

$$\bar{\rho}_\gamma = \begin{cases} \dfrac{\Omega_c^2}{K\lambda^2} + \left[\rho_c - \dfrac{\Omega_c^2}{K\lambda^2}\right]\dfrac{\sin(\lambda r)}{\lambda r}, & (\gamma = 0) \\ \sqrt{5}\Omega_c^2\dfrac{\left[3\lambda r\cos(\lambda r) + (r^2\lambda^2 - 3)\sin(\lambda r)\right]}{6Kr^5\lambda^2(\lambda\cos\lambda - \sin\lambda)}, & (\gamma = 2) \\ 0. & (\text{otherwise}) \end{cases} \tag{5.7.19}$$

An oblate-contoured star generated from this profile with $\rho_c = 2, \Omega_c = \sqrt{3}/2$ is shown in figure 5.16.

One must be careful to avoid setting a negative density, which is lowest at the poles. By reconstructing $\rho(r,\theta)$ from (5.7.19), one can see that

$$\rho_c \geq \Omega_c^2\frac{\lambda(5\lambda^2 + 6\cos\lambda + 9\lambda\cot\lambda - 9) - 6\sin\lambda}{6K\lambda^2(\lambda\cos\lambda - \sin\lambda)} \tag{5.7.20}$$

for the condition $\rho \geq 0$ to hold in the spherical shell.

A numerical issue arises when trying to set $\bar{\rho}_2$ initial data, because of the division by r^5 near the origin: round-off error gives 'kinks' in the data, which dissipation fails to remove. The effect is obviously worse at higher resolution, which hampers convergence.

Rather than devising an elaborate interpolation scheme for the first few grid points, one could instead approximate $\bar{\rho}_2$ by its Taylor expansion about $r = 0$ up to some desired order

for the first few grid points, and then *blend* it with the analytical solution:

$$\bar{\rho}_2 \to e^{-(r/0.1)^4}\text{Series}(\bar{\rho}_2, r=0) + (1-e^{-(r/0.1)^4})\bar{\rho}_2. \tag{5.7.21}$$

5.7.2 Perturbing rigid rotation

Figure 5.17 shows an $\ell = 1$ density perturbation and its convergence on a rigidly rotating $N = 400$ star, with $\ell_m = 4$ and artificial dissipation, $\Omega_c = \sqrt{3}/2, \lambda = 0.9\pi, \rho_c = 2(\mathfrak{T}/|\mathfrak{W}| \simeq 0.06)$, for a few hundred time steps. (Section 5.2.2 will determine how many rotations this represents.) We then show similar data and convergence plots for the other modes.

We observe that f_γ develops problems at the origin quite early on for $\ell > 2$ (figure 5.19) which is not removed by dissipation. The major contributors to the evolution are terms in the summation terms that satisfy $\ell_\gamma - \ell_\alpha + \ell_\beta = 0$, which we briefly referred to in section 5.5. The evolution of f_3 is dominated by a term $\bar{w}_1\bar{w}_2'/r$, where $\dot{\bar{w}}_2$ is dominated by $\bar{w}_1\hat{v}_1/r$, which in turn is generated by the $\bar{\rho}_1$ perturbation. These terms use l'Hôpital's rule to evaluate the origin, and if $\hat{v}$ is small, $\hat{v}/r$ will start to diverge near the origin from its expected value. Under second-order accurate finite differencing one immediately gets non-smooth first, and higher order, derivatives of $\bar{w}_2$, which cause problems in f_3 and higher modes.

We have investigated writing such terms as derivatives over a non-uniform grid where possible, for example as

$$\frac{\hat{v}}{r} = \frac{3}{2}\frac{\partial(r^2\hat{v})}{\partial(r^3)} - \frac{1}{2}\hat{v}'. \tag{5.7.22}$$

Doing so does not make a significant difference to convergence.

This problem appears to have little effect on the $\ell = 1$ mode: the system is still convergent even after a few reflections, and similar to what we saw earlier (section 5.5.1) it turns out that there is little change to this mode if one sets $\ell_m > 2$ anyway. It is not clear to us how to modify the code to fix this error, other than by setting very slow rotation.

We also show the absolute difference between the values of $\bar{\rho}_1(r)$ with increasing ℓ_m in figure 5.20 on an $N = 200$ grid: that is, we plot $|\bar{\rho}_1(\ell_m = 2) - \bar{\rho}_1(\ell_m = 3)|$ and so on. The figure, and similar plots of other variables, suggests that higher odd modes are more important to the evolution of $\bar{\rho}_1$ in this case and there is little point in setting even ℓ_m.

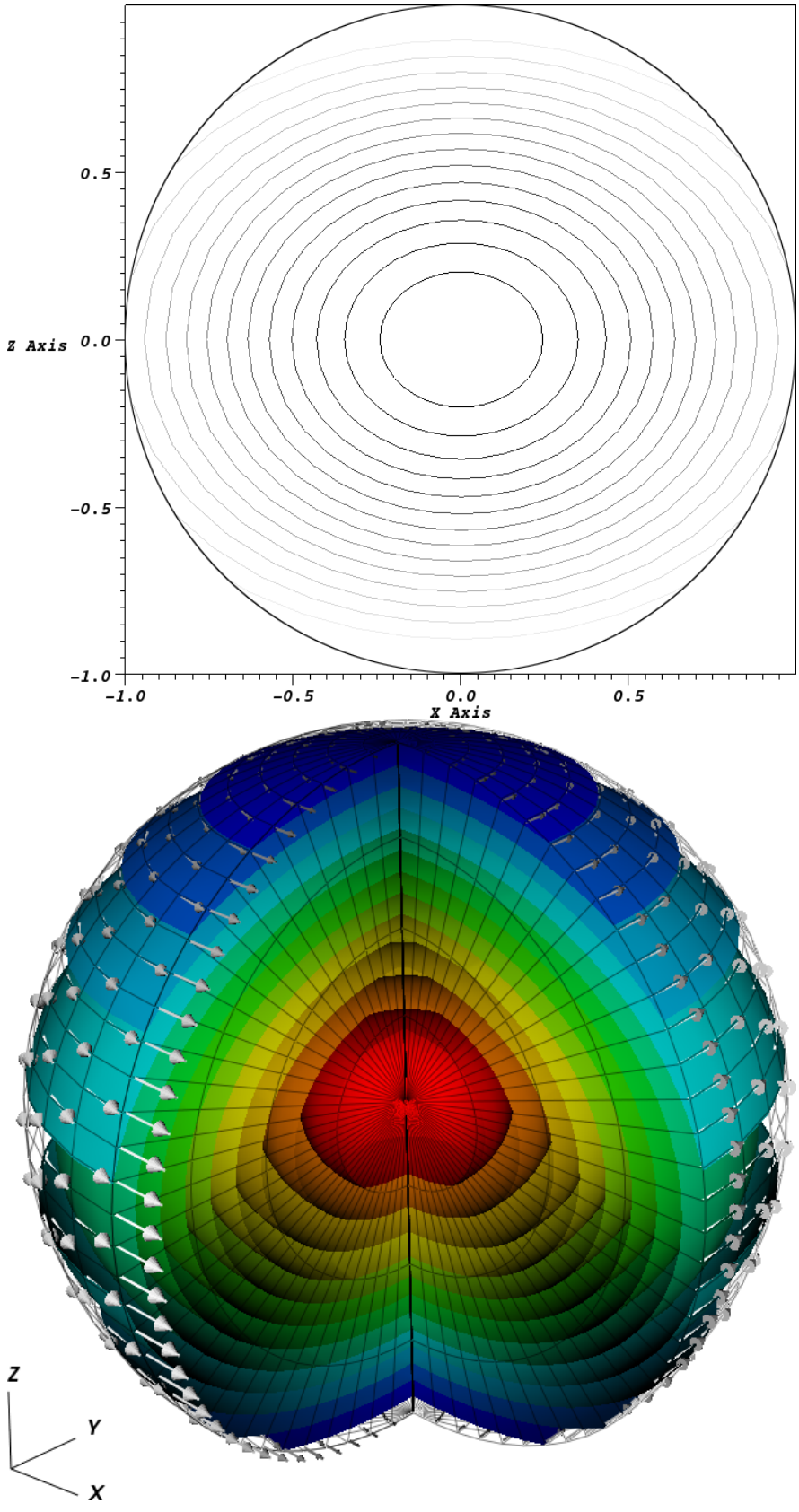

Figure 5.16: The density contours of a polar slice through a rigidly rotating star in equilibrium ($\rho_c = 2, \Omega_c = 0.5$) is shown at the top. The contours are cut off at $r = 1$ because of the spherical shell. Underneath is a 3D visualization using VisIt, available from http://visit.llnl.gov, which includes arrows to show the direction and magnitude of the velocity field.

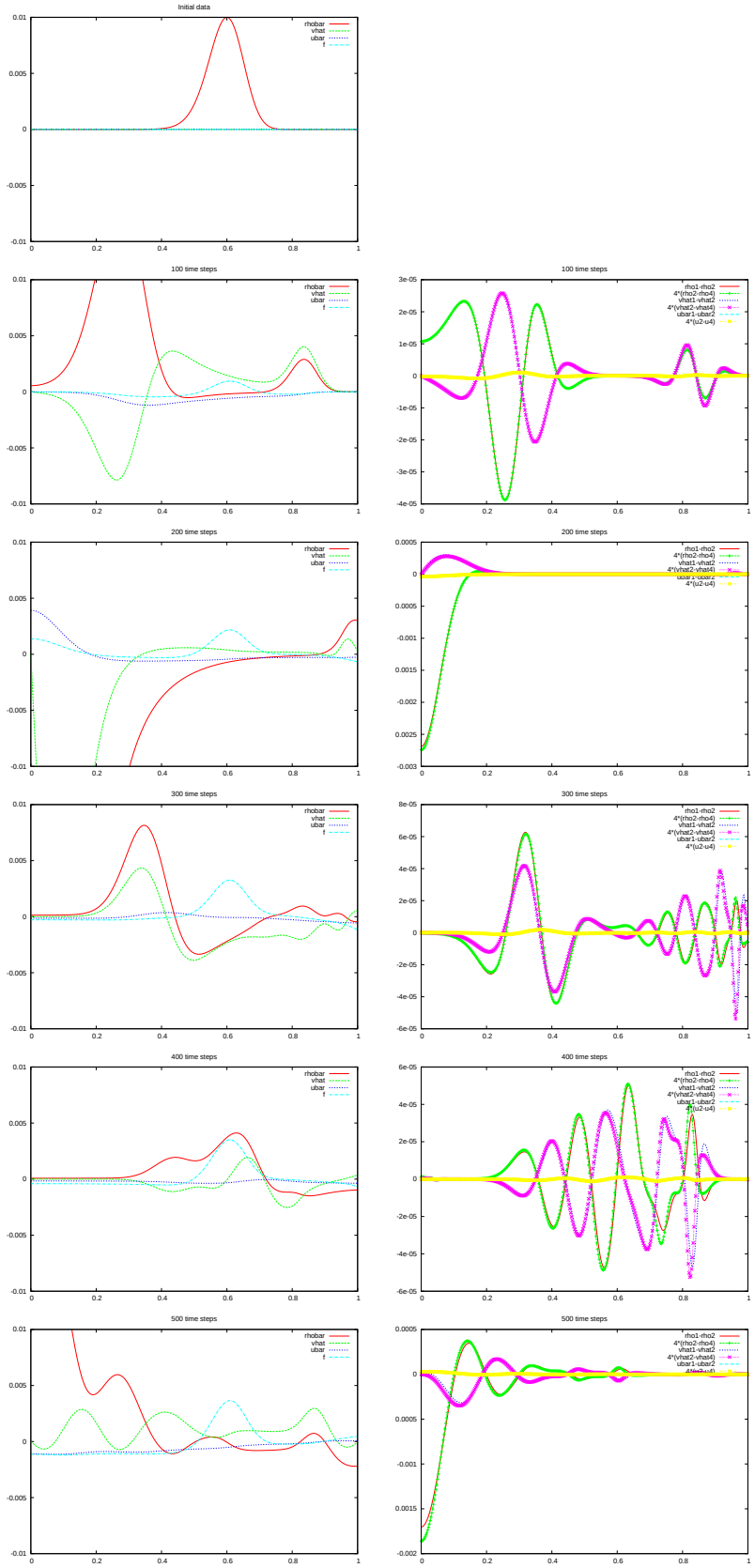

Figure 5.17: An $\ell = 1$ density perturbation of a rigidly rotating star, showing the variables $\bar{\rho}_1, \hat{v}_1, \bar{u}_1$. Plots of second-order convergence of these variables are shown on the right.

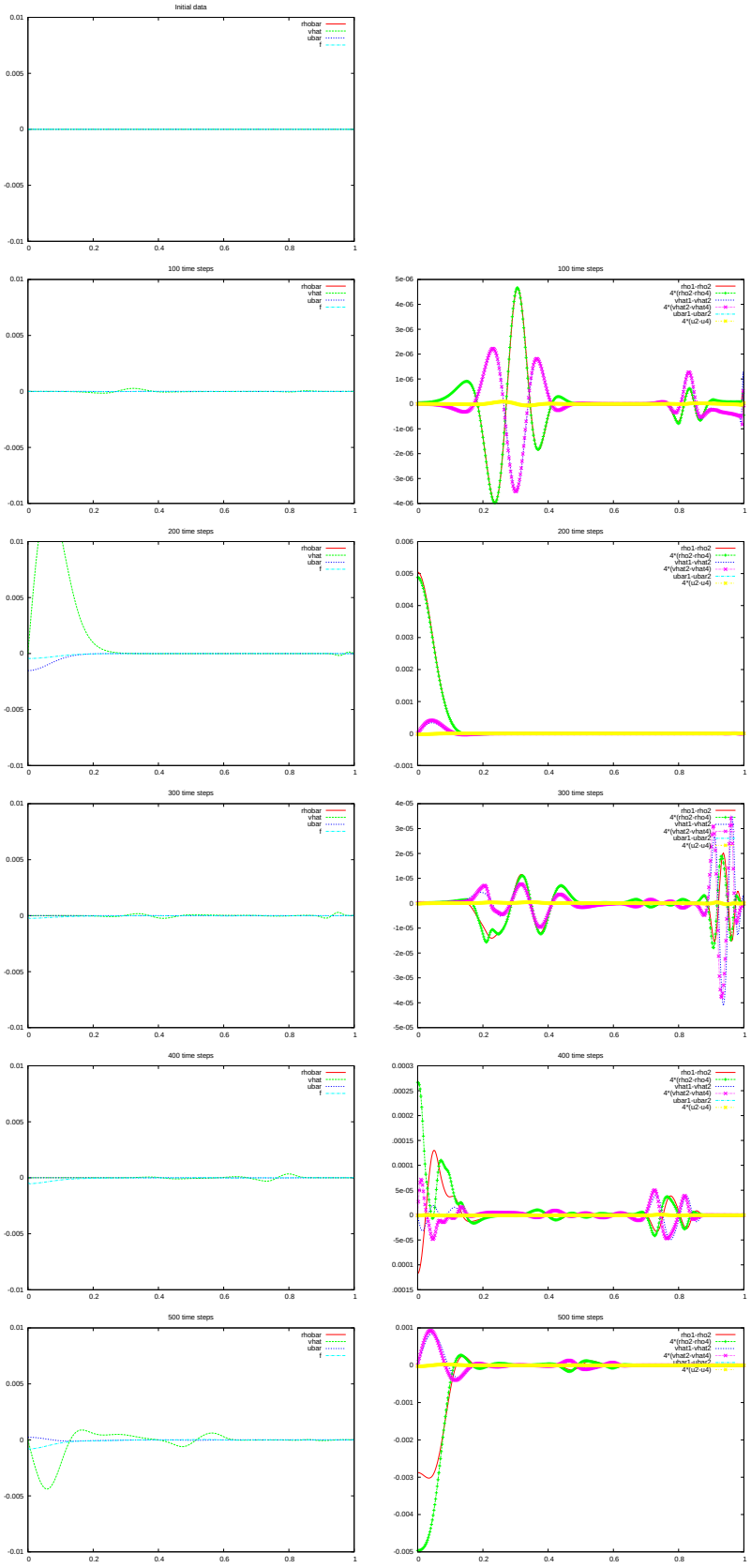

Figure 5.18: Evolution of the $\ell = 2$ mode and corresponding convergence plots.

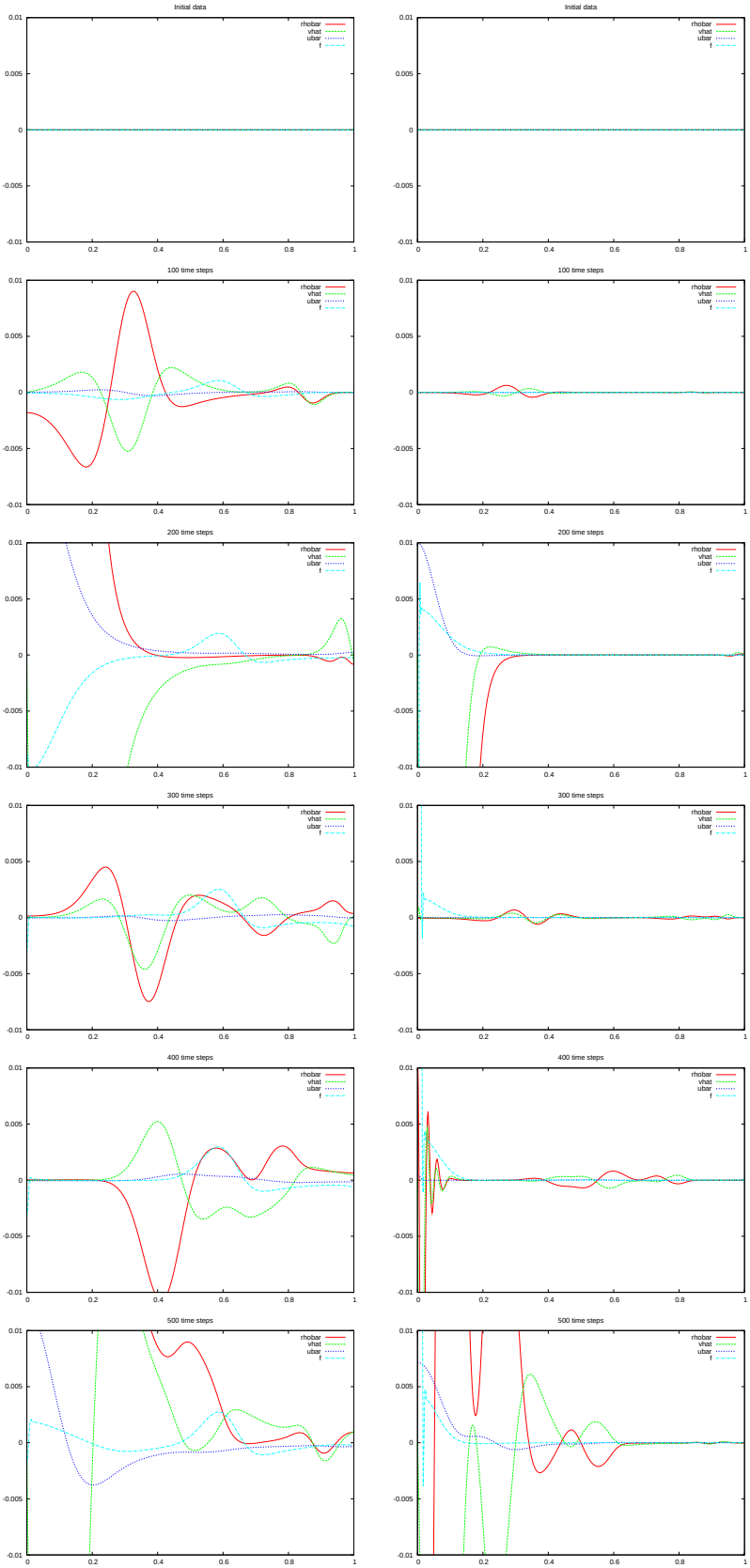

Figure 5.19: Evolution of the $\ell = 3, 4$ modes, which develop problems with the auxiliary variable f.

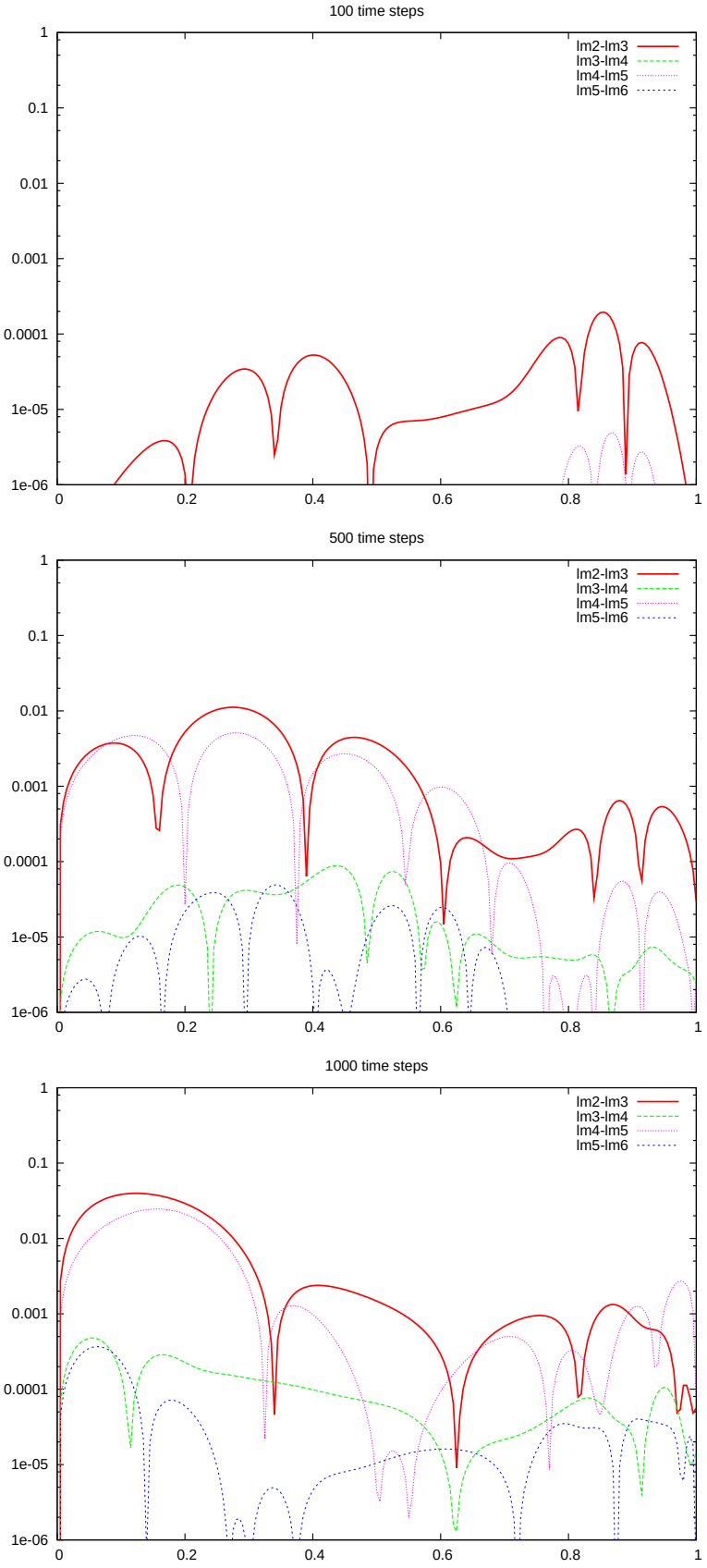

Figure 5.20: Convergence of $\bar{\rho}_1$ with higher ℓ_m and $N = 200$: the differences $|\bar{\rho}_1(\ell_m) - \bar{\rho}_1(\ell_m + 1)|$ are plotted logarithmically.

5.7.3 j-constant differential rotation

The differential rotation profiles in (5.7.3) are not immediately expressible as series of $\sin\theta$ and $\cos\theta$. We shall now look at how we can approximate j-constant differential rotation, although the analysis is similar for other types. If $d = \varpi/A$ is small, i.e. the rotation is almost rigid, then

$$\Omega = \frac{j_0}{A^2+\varpi^2} = \frac{j_0}{A^2}\sum_{n=0}^{\infty}(-1)^n\left(\frac{\varpi}{A}\right)^{2n} = \frac{j_0}{A^2}\left[1-\frac{\varpi^2}{A^2}+\mathcal{O}(d^4)\right]$$
$$= \frac{j_0}{A^2}\left[1-\frac{r^2}{A^2}+\frac{r^2\cos^2\theta}{A^2}+...\right]. \quad (5.7.23)$$

Compare this expression with the general expansion of the axial component of the velocity, from (5.7.5):

$$\mathbf{v} = w_\gamma S_\gamma^{(\varphi)}\frac{\partial}{\partial\varphi} = \left[\sqrt{3}\bar{w}_1 + 3\sqrt{5}\bar{w}_2\cos\theta + \frac{\sqrt{7}}{2}r^2\bar{w}_3(-3+15\cos^2\theta)+...\right]\frac{\partial}{\partial\varphi}. \quad (5.7.24)$$

Thus corresponding axial velocity modes we should set for up to $\mathcal{O}(A^{-4})$ are

$$\bar{w}_1 = \frac{j_0}{\sqrt{3}A^2}\left(1-\frac{4r^2}{5A^2}\right), \qquad \bar{w}_2 = 0, \qquad \bar{w}_3 = \frac{2j_0}{15\sqrt{7}A^4}. \quad (5.7.25)$$

When integrated, (5.7.23) gives

$$\Psi = \frac{j_0}{2A^2}\left(\frac{\varpi^2}{A^2}-\frac{\varpi^4}{A^4}+\frac{\varpi^6}{A^6}\right). \quad (5.7.26)$$

We do not discard terms of $\mathcal{O}(d^4)$ or smaller here; the equation for $\dot{\hat{v}}_0$ contains a term $r^6\bar{w}_3^2$ which needs to be balanced for equilibrium. Because of the underlying reason for this, if $\bar{w}_\gamma$ is set up to a mode κ, $\bar{\rho}_\gamma$ needs to be found for modes up to and including 2κ for *any* kind of rotation profile.

Putting these pieces into the equilibrium condition, we have

$$\sum_\gamma\left[\bar{\phi}_\gamma+\frac{1}{\lambda^2}\left(\frac{2(\ell+1)}{r}\bar{\phi}'_\gamma+\bar{\phi}''_\gamma\right)\right]r^{\ell_\gamma}Y_\gamma = \left[\alpha+\frac{j_0^2r^2}{A^4}\left(\frac{1}{3}-\frac{4r^2}{15A^2}+\frac{8r^4}{105A^4}\right)\right]Y_0$$
$$-\frac{j_0^2r^2}{A^4}\left[\frac{1}{3\sqrt{5}}-\frac{8r^2}{21\sqrt{5}A^2}+\frac{8r^4}{63\sqrt{5}A^4}\right]Y_2$$
$$-\frac{4j_0^2r^4}{A^6}\left[\frac{1}{105}-\frac{2r^2}{285A^2}\right]Y_4-\frac{8j_0^2r^6}{693\sqrt{13}A^8}Y_6. \quad (5.7.27)$$

With matching to a vacuum exterior, solutions are lengthy; suffice to say, even density modes up to $\ell = 6$ go as functions of $\mathrm{sinc}(\lambda r)$ and $\cos(\lambda r)$ and once again give oblate stars. There is more division by high powers of up to $r^{2\ell+1}$, so once again one needs to be careful to set

initial data that is smooth to prevent artificial dissipation creating problems near the origin.

This analysis may be repeated for a general $\Omega = C_0 + C_1\varpi^2 + ...$ cylindrically symmetric differential rotation law, where C_i are arbitrary constants. One could set these parameters to calculate the density profiles for v-constant rotation, or contra-rotating shells, for example.

5.7.4 Generic rotating equilibria

We shall now describe a method by which we may attempt to evolve an arbitrary (i.e. not necessarily cylindrically symmetric) rotating configuration to equilibrium by including artificial friction terms. Consider the velocity evolution equations (5.0.2), re-written as

$$\dot{\mathbf{v}}^i = (\mathcal{V} + \mathcal{A})v^i \tag{5.7.28}$$

where $\mathcal{V}, \mathcal{A}$ are the advection and total acceleration operators. We shall subtract a *friction term* proportional to the velocity as

$$\dot{\mathbf{v}}^i = (\mathcal{V} + \mathcal{A})v^i - \lambda_F(v^i - \mathbf{v}_I^i), \tag{5.7.29}$$

where λ_F is a friction parameter that is to be set, and $\mathbf{v}_I$ is the initial data for the velocity field, usually the toroidal rotation profile. Ideally this term will cause both the accelerations and velocities to vanish, rather than just the former: if the friction balances itself against other forces then we end up with a situation analogous to terminal velocity.

Since we have analytical solutions to rigid rotation, we can investigate what the optimal values of λ are for varying rotation. Initial data is a spherically symmetric Lane-Emden solution with constant $\bar{w}_1 = \Omega/\sqrt{3}$ rotation painted on. We have set $\ell_m = 2$ as we know from the analytical solution that this is sufficient to describe rigid rotation. In addition we use 4th-order dissipation and 2nd-order extrapolation at the outer boundary.

For rapid rigid rotation $\Omega = 0.4\sqrt{3}$, fastest relaxation is achieved by $\lambda_F \simeq 5$, although $\lambda_F \simeq 20$ is best for longer relaxations (figure 5.21). Similar values also seem to hold for a wide range of Ω. The system can become over-damped for values much larger than this, with large residual velocity components and longer relaxation times. At twice the radial resolution the residual velocity is smaller by a factor of four at later times ($t \sim 50$) but the relaxation time scale does not change.

One caveat of this method is that we are usually left with a different central density to that desired, although the relative change in total mass is typically small ($\mathcal{O}(10^{-3})$). Taking a spherically symmetric background that is in equilibrium and suddenly spinning it will noticeably alter the $\ell = 0$ density distribution, which the friction eventually freezes into place. The relaxed $\bar{\rho}_0$ solution that we find with $\Omega = 0.4$ approximates an analytical solution with $\rho_c = 0.92$ with a maximum relative error between them of 10^{-3}, independently of the value of λ. Smaller Ω will of course give solutions closer to $\rho_c = 1$, and different initial $\bar{\rho}_0$

configurations will lead to drastically different central densities.

The scalar virial test [59, 80] is a popular technique for evaluating the accuracy of numerical equilibria: by integrating the product of the Euler equation with the position vector, over the entire volume of the star, one can equates a sum of energies to the second time derivative of the moment of inertia, which is zero for a system in (analytical) equilibrium. A numerical equilibrium code encompassing an entire star should find the sum equal to a relatively small number that converges to zero. Our model does not include a surface with vanishing pressure, so instead we could measure

$$VC = \frac{|2\mathfrak{T} + \mathfrak{W} + \int_V r\frac{\partial P}{\partial r} dV|}{|\mathfrak{W}|} \simeq 0. \tag{5.7.30}$$

In the case of both analytical and relaxed rigid rotation for $\Omega = 0.4, N = 80$, we find $VC = \mathcal{O}(10^{-3})$.

However, we prefer to take a measure of the size of acceleration terms as a gauge of equilibrium accuracy, as these are what we are trying to minimize with the relaxation method. Again in case of rigid rotation $\Omega = 0.4$, a freely-evolved analytical solution has $\mathcal{A}_{\hat{v}_2} \sim \mathcal{O}(10^{-5})$, while for freely-evolved relaxed solution where $\lambda_F = 5$, then $\mathcal{A}_{\hat{v}_2} \sim \mathcal{O}(10^{-6})$. At $t = 1$, $\mathcal{A}_{\hat{v}_2} \sim \mathcal{O}(10^{-2})$ on the analytical solution, while it remains $\mathcal{O}(10^{-6})$ for the relaxed state. Doubling the resolution still reduces the acceleration by a factor of 4.

It should now be clear that this relaxation method works very well for finding the equilibria of rigidly rotating polytropes, although the initial central density parameter should be scaled appropriately. We have also checked the method against j-constant differential rotation and it appears to work just as well, and so we conclude that this method is a fast and relatively robust method for finding the rotational equilibria of polytropes.

The same cannot be said for rotating stratified equilibria. The system takes longer to relax: whilst $\dot{\rho}, \dot{\mathbf{v}}$ were observed to decrease exponentially for a polytrope, the stratified $n = 3/2$ star takes logarithmic time. The free evolution oscillates with an amplitude that grows approximately linearly in time: after relaxing up to $t = 100$ with $\lambda_F = 10$, $\mathcal{A}_{\hat{v}_2} \sim \mathcal{O}(10^{-3})$ at $t = 101$, $\mathcal{A}_{\hat{v}_2} \sim \mathcal{O}(10^{-2})$ at $t = 120$, and $\mathcal{A}_{\hat{v}_2} \sim \mathcal{O}(10^{-1})$ at $t = 300$.

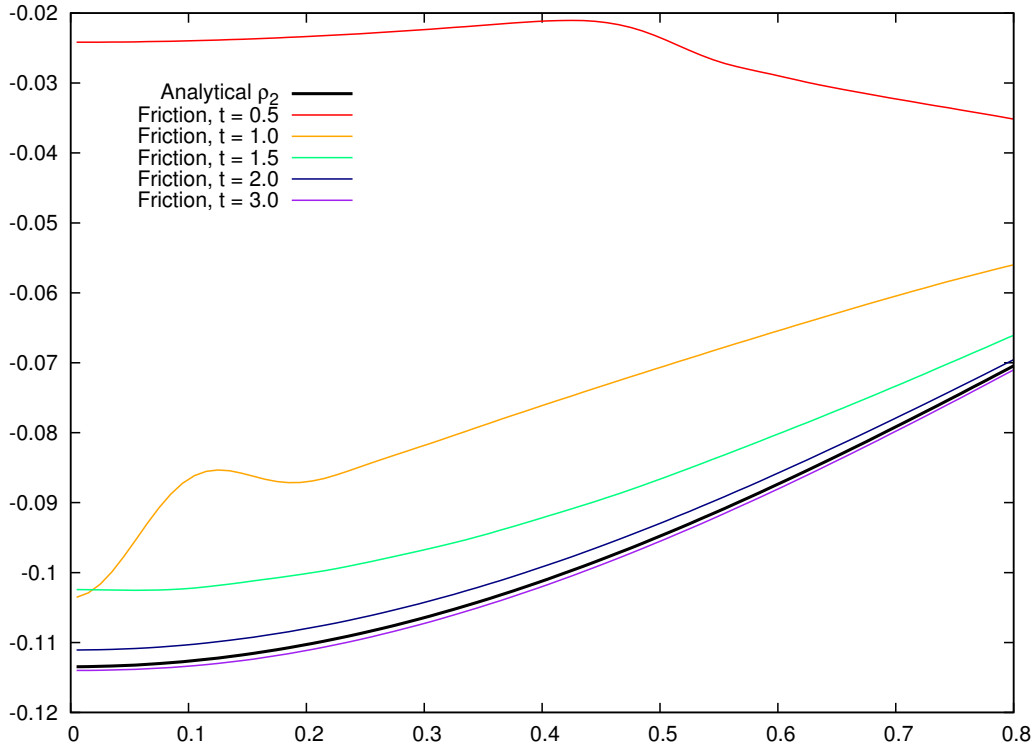

(a) The evolution of $\bar{\rho}_2$ with friction $\lambda_F = 5$ and rigid rotation $\Omega = 0.4\sqrt{3}$. It has approached the analytical solution in a time shorter than it takes for one rotation ($t = 9$).

λ_F	Max$\lvert\dot{u}_0\rvert$	Max$\lvert\hat{v}_2\rvert$	Max$\lvert\bar{w}_2 - \Omega\rvert$
0.5	10^{-2}	2×10^{-2}	5×10^{-4}
1	8×10^{-4}	10^{-3}	2×10^{-5}
5	10^{-7}	2×10^{-7}	2×10^{-7}
10	6×10^{-7}	8×10^{-6}	4×10^{-7}
20	3×10^{-6}	2×10^{-4}	4×10^{-6}
50	10^{-3}	7×10^{-4}	6×10^{-6}

(b) $t = 10$

λ_F	Max$\lvert\dot{u}_0\rvert$	Max$\lvert\hat{v}_2\rvert$	Max$\lvert\bar{w}_2 - \Omega\rvert$
0.5	10^{-6}	4×10^{-6}	10^{-5}
1	6×10^{-7}	7×10^{-7}	5×10^{-6}
5	10^{-7}	2×10^{-7}	2×10^{-7}
10	7×10^{-8}	10^{-7}	6×10^{-8}
20	3×10^{-8}	6×10^{-8}	2×10^{-8}
50	2×10^{-7}	2×10^{-6}	2×10^{-8}

(c) $t = 50$

Figure 5.21: Varying the friction parameter λ_F for a rotating polytrope with $\Omega = 0.4\sqrt{3}$. A moderate $\lambda_F = 5$ is best for short evolutions, but larger parameters are better over longer times. In any case this method rapidly gives equilibria that are close to the analytical solutions.

Chapter 6

Newtonian Ideal MHD

Consider a fluid, similar in nature to that used in the last section, but which can interact with a magnetic field. The governing equations are a combination of the fluid equations and Maxwell's equations:

$$\frac{\partial \rho}{\partial t} = -\nabla_j(\rho v^j), \tag{6.0.1}$$

$$\frac{\partial B^i}{\partial t} = B^j \nabla_j v^i - v^j \nabla_j B^i - B^i \nabla_j v^j + \frac{1}{\mu_0 \kappa_e} \nabla_j \nabla^j B^i, \tag{6.0.2}$$

$$\rho \frac{dv^i}{dt} = \frac{1}{\mu_0} \left[B^j \nabla_j B^i - \tfrac{1}{2} \nabla^i (\mathbf{B}_j B^j) \right] - \rho \nabla^i \Phi - \nabla^i P, \tag{6.0.3}$$

$$\nabla^j \nabla_j \Phi = 4\pi G \rho. \tag{6.0.4}$$

In order, these represent the conservation of mass, the induction equation for a magnetic field $\mathbf{B}$ with non-zero conductivity κ_e, momentum conservation with magnetic permeability μ_0, and a Poisson equation for the gravitational potential. Note the addition of a Lorentz force $\mathcal{L}$ (the combination of magnetic terms) to the Euler equation (6.0.2). The magnetic field has no divergence and is thus constrained by

$$\nabla_j B^j = 0. \tag{6.0.5}$$

When the approximations of an inviscid, perfectly conducting fluid medium are made, we refer to the *ideal* MHD equations. The conductivity is set to be infinite, and the induction equation now reads

$$\frac{\partial B^i}{\partial t} = B^j \nabla_j v^i - v^j \nabla_j B^i - B^i \nabla_j v^j. \tag{6.0.6}$$

This approximation is made throughout.

To non-dimensionalize the system, we need the unit-less number

$$\hat{\mu}_0 = \frac{1}{\mu_0}\frac{[B]^2}{[\rho][v]^2} \tag{6.0.7}$$

in addition to the previously defined $\hat{K}, \hat{G}$. In vacuum, $\mu_0 = 4\pi \times 10^{-7}\,\mathrm{m\,kg\,s^{-2}\,A^{-2}}$, giving a typical field strength of $10^{14}G$ when $\hat{\mu}_0 = 1$.

6.1 Quadratic form of the equations

We should recast the momentum equations (6.0.3) into quadratic form, for insertion into our spectral code. Currently there are three terms multiplying each other in the Lorentz force term; we have seen that a cubic term is easiest handled through a temporary variable storing all of the multiplications of two of the terms, although the method we use does not take account of all the possible mode couplings (see the end of section 2.5). We will also need to fix an equation of state: we may either choose a polytropic $P = K\rho^2$, producing a linear pressure term, or a stratified $P = \mathcal{K}\rho^2$ with a quadratic pressure term.

We can reduce the momentum equations to quadratic order by introducing a rescaled magnetic field variable

$$\mathbf{b} = \mathbf{B}/\rho \tag{6.1.1}$$

$$\implies \dot{v}^i = -v^j\nabla_j v^i - \nabla^i\Phi - 2K\nabla^i\rho - \frac{1}{\mu_0}\left[b_j\nabla^i B^j - b^j\nabla_j B^i\right], \tag{6.1.2}$$

where the division by ρ is non-problematic as the vacuum exterior is excluded from our evolutions. It is also possible to write down induction equations for this rescaled variable,

$$\dot{b}^i = b^j\nabla_j v^i - v^j\nabla_j b^i, \tag{6.1.3}$$

which must be divergence-free:

$$\nabla_j(\rho\, b^j) = 0. \tag{6.1.4}$$

Alternatively, it is possible to calculate the Lorentz force terms (6.0.3) and place them into temporary storage before multiplying by $1/\rho$.

One must now ask which variables should be evolved in time, and which should be derived from others. One approach that does not involve dividing by ρ would be to time evolve $\mathbf{b}$, deriving $\mathbf{B} = \rho\mathbf{b}$ at every time step. However one then needs to find an initial field satisfying (6.1.4), which becomes a complex problem for anything not on a spherically symmetric background.

An alternative method would be to time-evolve $\mathbf{B}$ and calculate $1/\rho$ in some manner. An iterative method to find this quantity is outlined in section 6.2.3. The main benefit of

using the original field variables is that finding a divergence-free field consists of choosing some B profile and calculating C quite easily from it (6.2.5).

However both of these approaches do not remove the concern over the divergence of $\mathbf{B}$. When we set initial data, although it may be divergence-free in the continuum, the numerical evolution may violate this condition. For example, dissipation and truncation ℓ_m will give non-solenoidal evolutions, although these are expected to converge. Various techniques exist to help with this issue, for example, some kind of divergence cleaning mechanism [3, 61].

A third approach, which could also be considered as an extension to the second, is to evolve a vector potential; by writing

$$\mathbf{B} = \nabla \times \mathbf{A}, \tag{6.1.5}$$

it is automatically true that the divergence vanishes. The choice of gauge[1]is irrelevant to the evolution, and we shall see that the time evolution equations for the components of $\mathbf{A}$ are easily derived. In fact this approach turns out to be exactly the same as solving $\nabla \cdot \mathbf{B} = 0$ for the polar component and inserting into the equations. It does however give a term involving a third-derivative in the equation for $\dot{f}$.

6.2 Spherical harmonic expansion

In order to write the MHD equations in terms of spectral coefficients, one starts by defining a magnetic field in a similar way to the velocity field:

$$\mathbf{B} = BY_\gamma e^A \oplus \left(C_\gamma Z^a_\gamma + D_\gamma S^a_\gamma\right). \tag{6.2.1}$$

The conservation of mass equation is of course unchanged with the addition of a magnetic field. We neglect to write the Lorentz terms in the Euler equation here due to length, but the components of the ideal induction equation (6.0.6) are

$$\dot{B}_\gamma = -\chi_\gamma \left\{ v_\alpha \left(B'_\beta + \frac{2B_\beta}{r} \right) - v_\alpha C_\beta \hat{D}_{\alpha\beta-\gamma} \; + u_\alpha B_\beta \left(L^2_\alpha \hat{C}_{\alpha\beta-\gamma} \; + \hat{D}_{\alpha\beta-\gamma} \right) \right\}, \tag{6.2.2}$$

$$\begin{aligned} \dot{C}_\gamma = -\frac{\chi_\gamma}{L^2_\gamma} \Bigg\{ & B_\alpha u'_\beta \hat{D}_{-\gamma\alpha\beta} \; - v_\alpha \left(C'_\beta + \frac{2C_\beta}{r} \right) \hat{D}_{-\gamma\alpha\beta} \; - v'_\alpha C_\beta \hat{D}_{-\gamma\alpha\beta} \\ & + u_\alpha C_\beta \left(\hat{E}_{-\gamma\beta\alpha} \; - \hat{E}_{-\gamma\alpha\beta} \; - L^2_\alpha \hat{D}_{-\gamma\alpha\beta} \right) \Bigg\}, \end{aligned} \tag{6.2.3}$$

$$\begin{aligned} \dot{D}_\gamma = -\frac{\chi_\gamma}{L^2_\gamma} \Bigg\{ & B_\alpha w'_\beta \hat{D}_{-\gamma\alpha\beta} \; + w_\alpha C_\beta \left(\hat{E}_{-\gamma\alpha\beta} \; - \hat{F}_{-\gamma\alpha\beta} \right) - v_\alpha \left(D'_\beta + \frac{2D_\beta}{r} \right) \hat{D}_{-\gamma\alpha\beta} \\ & - v'_\alpha D_\beta \hat{D}_{-\gamma\alpha\beta} \; + u_\alpha D_\beta \left(\hat{F}_{-\gamma\alpha\beta} \; - \hat{E}_{-\gamma\alpha\beta} \; - L^2_\alpha \hat{D}_{-\gamma\alpha\beta} \right) \Bigg\}. \end{aligned} \tag{6.2.4}$$

[1]Since the curl of a gradient is zero, it must be the case that one can add an arbitrary function $\nabla\zeta$ to $\mathbf{A}$ and get the same field.

The divergence-free property of the magnetic field requires

$$L_\gamma^2 C_\gamma + B'_\gamma + \frac{2B_\gamma}{r} = 0 \tag{6.2.5}$$

for each γ.

6.2.1 Magnetic vector potential

As previously mentioned, writing $\mathbf{B} = \nabla \times \mathbf{A}$ and evolving $\dot{\mathbf{A}}$ ensures the magnetic field is always divergence-free. Writing this expression in terms of spherical harmonics is relatively straightforward; without the introduction of coordinates, the curl of a vector $\mathbf{A}$ is

$$B^i = \epsilon^{ijk}\nabla_j \mathbf{A}_k, \qquad \mathbf{A} = \mathcal{A}_\gamma Y_\gamma e^A \oplus \left(\mathcal{B}_\gamma Z_\gamma^a + \psi_\gamma S_\gamma^a\right). \tag{6.2.6}$$

From the curl (2.4.24), we can equate components as

$$B_\gamma = -L_\gamma^2 \psi_\gamma, \qquad C_\gamma = \psi'_\gamma + \frac{2}{r}\psi_\gamma, \qquad D_\gamma = \frac{1}{r^2}\mathcal{A}_\gamma - \mathcal{B}'_\gamma - \frac{2}{r}\mathcal{B}_\gamma, \tag{6.2.7}$$

with regularized components

$$\bar{B}_\gamma = -L_\gamma^2 \bar{\Psi}_\gamma, \quad \bar{C}_\gamma = (\ell_\gamma + 1)\bar{\Psi}_\gamma + r\bar{\Psi}'_\gamma, \quad \bar{D}_\gamma = \frac{1}{r^2}\bar{\mathcal{A}}_\gamma - \frac{\ell_\gamma}{r^2}\bar{\mathcal{B}}_\gamma - \frac{1}{r}\bar{\mathcal{B}}'_\gamma \tag{6.2.8}$$

This is easily verified to give a divergence-free field, since

$$\begin{aligned}\left[\nabla_j B^j\right]_\gamma &= L_\gamma^2 C_\gamma + B'_\gamma + \frac{2}{r}B_\gamma \\ &= L_\gamma^2\left(\psi'_\gamma + \frac{2\psi_\gamma}{r}\right) + (-L_\gamma^2\psi'_\gamma) + \frac{2}{r}(-L_\gamma^2\psi_\gamma) \\ &= 0.\end{aligned} \tag{6.2.9}$$

In fact, equations (2.4.23,2.4.24) are identical to the expression of $\nabla_j B^j = 0$ in spherical harmonics (6.2.5). Solving the latter and replacing C with B, B' is synonymous with evolving the vector potential.

The gauge freedom in choosing a potential is demonstrated through the transformations

$$\begin{aligned}&\mathbf{A}^i \to \mathbf{A}^i + \nabla^i \zeta \\ &\quad \implies \mathcal{A}_\gamma \to \mathcal{A}_\gamma + \zeta'_\gamma, \qquad \mathcal{B}_\gamma \to \mathcal{B}_\gamma + \zeta_\gamma/r^2, \qquad \psi_\gamma \to \psi_\gamma.\end{aligned} \tag{6.2.10}$$

It is easy to verify that the components of $\mathbf{B}$ are invariant under these.

6.2.2 Regularized MHD equations using a magnetic vector potential

We should now regularise the equations for use in a spectral code, retaining the fluid variables $\hat{v}, f$ as defined in section 5.5. Using the standard vector regularization as derived in section 5.2.1, we have

$$b_\gamma = r^{\ell_\gamma - 1}\bar{b}_\gamma, \quad c_\gamma = r^{\ell_\gamma - 2}\bar{c}_\gamma, \quad d_\gamma = r^{\ell_\gamma - 1}\bar{d}_\gamma, \quad \psi_\gamma = r^{\ell_\gamma - 1}\bar{\Psi}_\gamma, \quad D_\gamma = r^{\ell_\gamma - 1}\bar{D}_\gamma. \tag{6.2.11}$$

For the rescaled magnetic field, we introduce a new variable

$$\hat{b}_\gamma = \frac{\bar{b}_\gamma - \ell_\gamma \bar{c}_\gamma}{r} = \mathcal{O}(r), \tag{6.2.12}$$

which we use in place of $\bar{b}$, to simplify the equations for the case $\ell_\gamma = \ell_\alpha + \ell_\beta$. The magnetic field components evolve as follows:

$$\begin{aligned}
\dot{\bar{\Psi}}_\gamma = -\frac{\chi_\gamma}{L_\gamma^2} r^{\ell_\alpha+\ell_\beta-\ell_\gamma} \Big\{ & \hat{v}_\alpha \bar{\Psi}'_\beta \left[\hat{D}_{-\gamma\alpha\beta} \; - \ell_\beta(\ell_\beta+1)\hat{C}_{\alpha\beta-\gamma} \right] \\
& - \frac{\hat{v}_\alpha \bar{\Psi}_\beta}{r} \left[\ell_\beta(\ell_\beta+1)^2 \hat{C}_{\alpha\beta-\gamma} \; - (\ell_\beta+1)\hat{D}_{-\gamma\alpha\beta} \right] \\
& + \frac{\bar{u}_\alpha \bar{\Psi}'_\beta}{r} \left[\ell_\alpha \hat{D}_{-\gamma\alpha\beta} \; - \ell_\alpha \ell_\beta(\ell_\beta+1)\hat{C}_{\alpha\beta-\gamma} \right] \\
& + \frac{\bar{u}_\alpha \bar{\Psi}_\beta}{r^2} \left[\ell_\alpha \ell_\beta(\ell_\alpha - \ell_\beta)(\ell_\beta+1)\hat{C}_{\alpha\beta-\gamma} \; + (\ell_\alpha - \ell_\beta)(\ell_\beta+1)\hat{D}_{-\gamma\alpha\beta} \right] \\
& + \hat{v}_\alpha \bar{D}_\beta \hat{G}_{\alpha\beta-\gamma} \; + \frac{\bar{u}_\alpha \bar{D}_\beta}{r} \ell_\alpha \hat{G}_{\alpha\beta-\gamma} \; + \frac{\bar{w}_\alpha \bar{\Psi}_\beta}{r} \ell_\beta(\ell_\beta+1)\hat{G}_{\alpha\beta-\gamma} \Big\},
\end{aligned} \tag{6.2.13}$$

$$\begin{aligned}
\dot{\bar{D}}_\gamma = -\frac{\chi_\gamma}{L_\gamma^2} r^{\ell_\alpha+\ell_\beta-\ell_\gamma} \Big\{ & -(\hat{v}_\alpha \bar{D}'_\beta + \hat{v}'_\alpha \bar{D}_\beta)\hat{D}_{\alpha\beta-\gamma} \; - \ell_\alpha f_\alpha \bar{D}_\beta \hat{D}_{\alpha\beta-\gamma} \\
& - \frac{\bar{u}_\alpha \bar{D}'_\beta}{r} \ell_\alpha \hat{D}_{\alpha\beta-\gamma} \; + \frac{\bar{\Psi}_\alpha \bar{w}'_\beta}{r} \ell_\alpha(\ell_\alpha+1)\hat{D}_{\alpha\beta-\gamma} \\
& + \frac{\bar{\Psi}'_\alpha \bar{w}_\beta}{r}(\hat{E}_{-\gamma\alpha\beta} \; - \hat{F}_{-\gamma\alpha\beta}\,) - \frac{\hat{v}_\alpha \bar{D}_\beta}{r}(1 + 2\ell_\alpha + \ell_\beta)\hat{D}_{\alpha\beta-\gamma} \\
& + \frac{\bar{u}_\alpha \bar{D}_\beta}{r^2} \left[\ell_\alpha(1-\ell_\beta)\hat{D}_{\alpha\beta-\gamma} \; - \hat{E}_{-\gamma\alpha\beta} \; + \hat{F}_{-\gamma\alpha\beta} \right] \\
& + \frac{\bar{\Psi}_\alpha \bar{w}_\beta}{r^2} \left[\ell_\alpha(\ell_\beta - 1)(\ell_\alpha+1)\hat{D}_{\alpha\beta-\gamma} \; + (\ell_\alpha+1)(\hat{E}_{-\gamma\alpha\beta} \; - \hat{F}_{-\gamma\alpha\beta}\,) \right] \\
& + (\text{3D terms involving } \hat{G}_{\alpha\beta-\gamma}\,) \Big\},
\end{aligned} \tag{6.2.14}$$

where a number of terms that reduce to zero in axisymmetry have been omitted from (6.2.14) for brevity.

It is interesting to note that one cannot generate a poloidal field from a purely toroidal one in axisymmetric ideal MHD, regardless of the velocity or density profile, because (6.2.13) only depends on $\bar{\Psi}$. This has been pointed out by Chandrasekhar [26]; as he put it,

> "There is ... no 'feedback' from the toroidal to the poloidal field. However, there is a feedback from the poloidal to the toroidal field through a coupling with the rotational motions ... [which only exists] in the case of non-uniform rotation."

The last part of this is true in the sense that coefficients of $\bar{w}_1$ in (6.2.14) can be shown to always vanish, and setting $\bar{w}_1' = 0$ removes the other poloidal couplings. Of course in non-ideal MHD such couplings can occur and results in twisting of field lines: certain types of sunspots are thought be created by the so-called α-*effect* [69].

Using this vector potential to evolve the magnetic field also trivializes the resistivity term present in (6.0.2). The vector Laplacian (2.4.25) reduces to adding terms in the induction equation as per

$$\dot{\bar{\Psi}}_\gamma = ... + \frac{1}{\mu_0 \kappa_e}\left[\bar{\Psi}_\gamma'' + \frac{2(\ell+1)}{r}\bar{\Psi}_\gamma'\right], \tag{6.2.15}$$

$$\dot{\bar{D}}_\gamma = ... + \frac{1}{\mu_0 \kappa_e}\left[\bar{D}_\gamma'' + \frac{2(\ell+1)}{r}\bar{D}_\gamma'\right]. \tag{6.2.16}$$

6.2.3 Calculating the rescaled field variables $\mathbf{b} = \mathbf{B}/\rho$

This formulation requires the components of $\mathbf{b}$ be calculated at every time-step. Although we do not have a simple way to divide spherical harmonics, there are two potential ways we could calculate the quantity $1/\rho$, one of which is an iterative scheme.

Consider the quantity $q = 1/\rho$, which satisfies

$$q\rho = q(\rho_0 + \tilde{\rho}) = 1, \tag{6.2.17}$$

where $\tilde{\rho}$ is expected to be small. This can be arranged into the form

$$q = \frac{1}{\rho_0}\left(1 - q\tilde{\rho}\right), \tag{6.2.18}$$

and then written in terms of spherical harmonics as

$$Y_\gamma q_\gamma = \frac{1}{\rho_0}\left(Y_0 - Y_\alpha q_\alpha Y_\beta \tilde{\rho}_\beta\right). \tag{6.2.19}$$

It therefore suggests an iterative scheme based on the Jacobi method:

$$q_\gamma^{(i+1)} = \frac{1}{\rho_0}\left[\delta_{\gamma,0} - \chi_\gamma \hat{C}_{\alpha\beta-\gamma}\, q_\alpha^{(i)} \tilde{\rho}_\beta\right] \qquad \text{where} \quad \tilde{\rho_\beta} = \begin{cases} \rho_\beta, & (\beta \neq 0) \\ 0, & (\beta = 0) \end{cases}$$

$$q_\gamma^{(0)} = \delta_{\gamma,0}\frac{1}{\rho_0}. \tag{6.2.20}$$

To save time one could considering using the previous calculated value of q at the start of

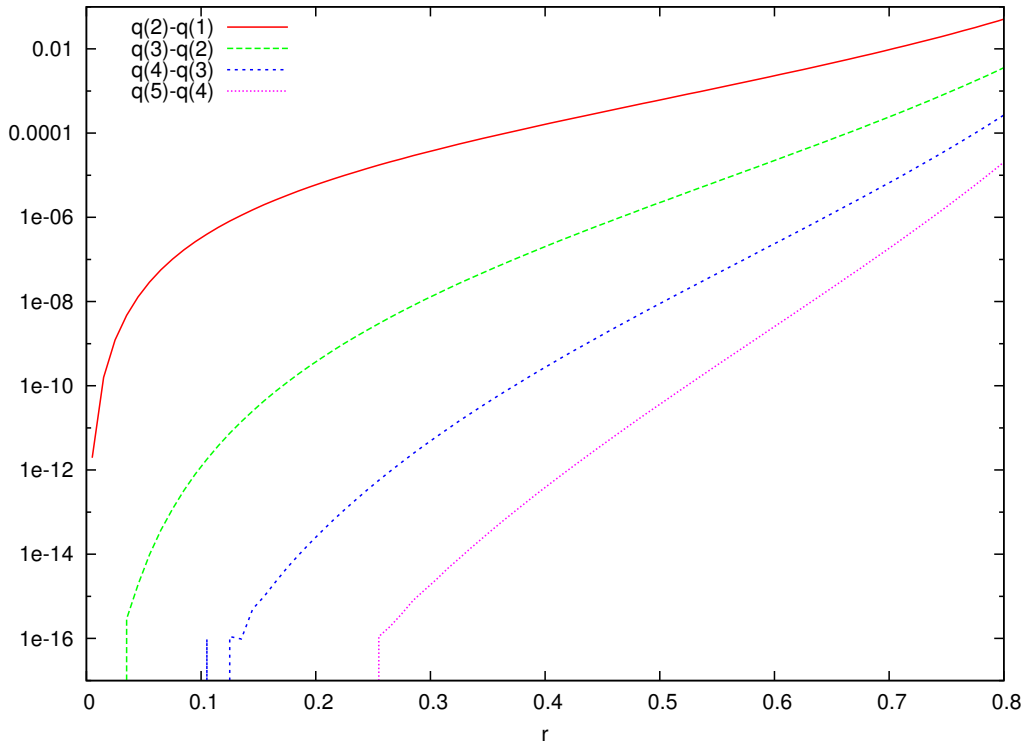

Figure 6.1: The differences between the iterated $\bar{q}_2$ with increasing iteration steps. The density profile being divided is the analytical solution for a rigidly rotating polytrope.

the iteration. This method can also be written in terms of differences between successive iterations, which makes it easier to write an efficient stopping rule (for example, when the L2-norm of the δq's becomes sufficiently small). The iterative procedure converges at different rates, as shown in figure 6.1, and one sees the largest error at the outer boundary, vanishing at approximately a linear rate and expected because of the vanishing density.

It is also possible, and perhaps more efficient, to time-evolve this quantity. If we first notice that

$$\dot{q} = -\dot{\rho}/\rho^2, \qquad \nabla_j q = -\frac{1}{\rho^2}\nabla_j \rho, \tag{6.2.21}$$

manipulating (5.0.1) gives

$$\dot{q} = q\nabla_j v^j - v^j \nabla_j q \tag{6.2.22}$$

$$\begin{aligned} \Longrightarrow \dot{\bar{q}}_\gamma = -\chi_\gamma\, r^{\ell_\alpha+\ell_\beta-\ell_\gamma} \Bigg\{ &\left[\hat{v}_\alpha \bar{q}'_\beta - \hat{v}'_\alpha \bar{q}_\beta - \ell_\alpha f_\alpha \bar{q}_\beta + (\ell_\beta - 2\ell_\alpha - 2)\frac{\hat{v}_\alpha \bar{q}_\beta}{r}\right] \hat{C}_{\alpha\beta-\gamma} \\ &+ \frac{\bar{u}_\alpha \bar{q}'_\beta}{r}\ell_\alpha \hat{C}_{\alpha\beta-\gamma} + \frac{\bar{u}_\alpha \bar{q}_\beta}{r^2}\left(\ell_\alpha \ell_\beta \hat{C}_{\alpha\beta-\gamma} + \hat{D}_{-\gamma\alpha\beta}\right)\Bigg\}. \end{aligned} \tag{6.2.23}$$

However it would still be necessary to use the iterative method to generate $\bar{q}$ initial data, and our code chooses to use the iterative method at every time step.

Regardless of the method one chooses to use, the last step in the process is to generate $\hat{b}, \bar{c}, \bar{d}$ from $\bar{q}, \bar{\Psi}, \bar{D}$ as follows:

$$\hat{b}_\gamma = \chi_\gamma \, r^{\ell_\alpha+\ell_\beta-\ell_\gamma} \left[\frac{\bar{q}_\alpha \bar{\Psi}_\beta}{r}(\ell_\beta+1) \left(\ell_\beta \hat{C}_{\alpha\beta-\gamma} \; + \frac{\ell_\gamma \hat{D}_{\alpha\beta-\gamma}}{L_\gamma^2} \right) + \bar{q}_\alpha \bar{\Psi}'_\beta \frac{\ell_\gamma \hat{D}_{\alpha\beta-\gamma}}{L_\gamma^2} \right], \tag{6.2.24}$$

$$\bar{c}_\gamma = -\frac{\chi_\gamma}{L_\gamma^2} r^{\ell_\alpha+\ell_\beta-\ell_\gamma} \left[\bar{q}_\alpha \bar{\Psi}_\beta(\ell_\beta+1) + r\bar{q}_\alpha \bar{\Psi}'_\beta \right] \hat{D}_{\alpha\beta-\gamma} \, , \tag{6.2.25}$$

$$\bar{d}_\gamma = -\frac{\chi_\gamma}{L_\gamma^2} r^{\ell_\alpha+\ell_\beta-\ell_\gamma} \bar{q}_\alpha \bar{D}_\beta \hat{D}_{\alpha\beta-\gamma} \, . \tag{6.2.26}$$

One may prefer to write a code to find $\bar{B}, \bar{C}$ from $\bar{\Psi}$ first to find components of $\mathbf{b}$ and other quantities, such as the magnetic energy (section 6.2.5).

6.2.4 Exterior field

As our model is surrounded by a spherical shell, with cut-off at non-zero density, the simplest boundary condition on the magnetic field we could impose would be $\mathbf{B} = \mathbf{0}$. In the absence of dissipation, such initial data would automatically satisfy $\dot{\mathbf{B}} = \mathbf{0}$; although we may not apply dissipation to the magnetic variables (section 6.3.2) we still use this relation at the outer boundary.

Although this *buried* field is relatively straightforward to model, theoretical and observational evidence [43] generally points towards neutron stars having strong exterior magnetic fields coupled to the interior through field lines *frozen* into the crust.

Suppose instead that the NS was surrounded by a vacuum atmosphere (section 1.2.2), where there are no charged particles that could carry an electric current. Such a situation is unlikely to exist in nature, as it is widely believed [43] that the electric fields generated at the NS surface by rotation and magnetism would generate a force along field lines several orders of magnitude stronger than that provided by gravity. It would thus be impossible to maintain an equilibrium (in the absence of some exotic physics in the crust). Nonetheless, the non-rotating vacuum-exterior model is still a starting point for our considerations.

In this vacuum exterior, $\mathbf{j} = \nabla \times \mathbf{B}^\epsilon = 0$ and hence $\mathbf{B}^\epsilon$ is given by a scalar potential ∇f satisfying

$$\nabla \cdot \mathbf{B}^\epsilon = \Delta f = 0. \tag{6.2.27}$$

The radial component of $\mathbf{B}^\epsilon$ should vanish at infinity; although the curl of the vector potential is zero in the exterior, we may still equate $\bar{B}^\epsilon_\gamma = -L_\gamma^2 \bar{\Psi}^\epsilon_\gamma$, and so from (6.2.27) we find

$$\bar{\Psi}^\epsilon_\gamma(r) \propto r^{-(2\ell+1)}. \tag{6.2.28}$$

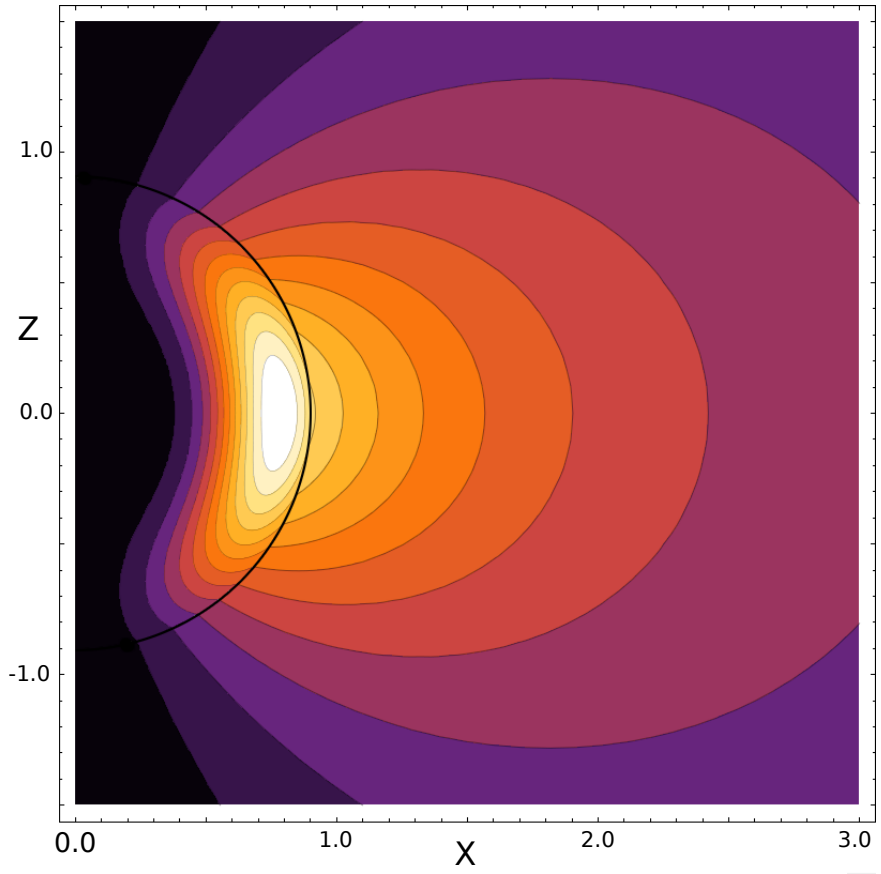

Figure 6.2: The contours of an $\ell = 1$ streamfunction u (section 6.3.1) including the exterior, dipolar component.

The constant of integration is fixed with the value of the interior field on the boundary as

$$\bar{\Psi}^{\epsilon}_{\gamma}(r) = \left(\frac{r}{R}\right)^{-(2\ell+1)} \bar{\Psi}_{\gamma}(R), \tag{6.2.29}$$

$$\bar{D}^{\epsilon}_{\gamma}(r) = 0, \tag{6.2.30}$$

where of course we now have $\bar{\Psi}_{\gamma}(R) \neq 0$ to avoid triviality. This falloff is easily implemented in the outer ghost zone, replacing extrapolation. As we shall see in section 6.3.3 constructing equilibrium exterior fields requires extra numerical considerations within our model.

6.2.5 Magnetic energy

The total energy of the (interior) magnetic field is given by

$$\mathfrak{B} = \frac{1}{2\mu_0}\int |\mathbf{B}|^2 dV \tag{6.2.31}$$

$$= \frac{1}{2\mu_0}\int \left[Y_\alpha Y_\beta B_\alpha B_\beta + r^2\left(Z^a_\alpha Z_{\beta a} C_\alpha C_\beta + S^a_\alpha S_{\beta a} D_\alpha D_\beta\right)\right] r^2 dr\, d\Omega$$

$$= \frac{1}{2\mu_0}\int Y_\alpha Y_\beta d\Omega \int r^{\ell_\alpha+\ell_\beta}\left[\bar{B}_\alpha\bar{B}_\beta + \ell_\beta(\ell_\beta+1)\left(\bar{C}_\alpha\bar{C}_\beta + r^2\bar{D}_\alpha\bar{D}_\beta\right)\right] dr$$

$$= (-1)^{m_\gamma}\frac{1}{2\mu_0}\int r^{2\ell_\gamma}\left[\bar{B}_\gamma\bar{B}_{-\gamma} + \ell_\gamma(\ell_\gamma+1)\left(\bar{C}_\gamma\bar{C}_{-\gamma} + r^2\bar{D}_\gamma\bar{D}_{-\gamma}\right)\right] dr. \tag{6.2.32}$$

This has a lengthier form when written in terms of the vector potential.

A similar integral gives the energy contained in the exterior field, which we know to vanish at infinity (6.2.28):

$$\mathfrak{B}^\epsilon = \frac{1}{2\mu_0}\int_{r=R}^{\infty} |\mathbf{B}^\epsilon|^2 dV \tag{6.2.33}$$

$$= \frac{2\pi}{\mu_0} R^{2\ell-3}\ell^2(\ell+1)(\ell(3+2\ell) + R^2(5+7\ell+2\ell^2))(\bar{\Psi}_\gamma(R))^2 \tag{6.2.34}$$

$$= \frac{4\pi}{35R\mu_0}(5+14R^2)(\bar{\Psi}_1(R))^2 + ... \tag{6.2.35}$$

6.3 Magnetic equilibria

Finding magnetic equilibrium states of stars, physically realistic or otherwise, has long been a challenge faced by astrophysicists [29, 30, 76]. The structure and evolution of magnetic fields of the Sun and Earth themselves are still poorly understood, let alone those of more exotic extrasolar bodies. Early attempts at solving a linear equilibrium problem started by assuming structures described by incompressible polytropes, and an important magneto-rotational instability effect (MRI) was first realized through a model of cylindrically symmetric accretion disks [7].

Our interest lies in numerically finding *stationary* solutions to the non-linear problem, where there is no velocity field except perhaps for some axial rotation. The problem is to balance gravity, the centrifugal force, fluid pressure and magnetic pressure, with the latter typically being the smallest in magnitude. We discuss the stability of these equilibria to various perturbations in section 6.4.

Force-free fields ($\mathcal{L} = 0$) are known to be mathematically given by spherical Bessel functions [31], although their astrophysical significance is dubious. We note a recent argument by Reisenegger [74] that such configurations should simply not exist. If the Lorentz force is integrated over some spherical volume that contains the star, one obtains an expression involving the total magnetic energy and a surface integral that vanishes as

the volume increases towards infinity. From this it must be the case that the Lorentz force is non-zero if there is any magnetic energy, unless there are infinite Lorentz forces on the stellar surface (i.e. a delta function in the original integral).

Techniques have been developed to model the simplest possible NS models, i.e. polytropes with axisymmetric magnetic fields. From the numerically-derived equilibria one may go on to investigate the stability properties and oscillation modes (section 6.4 and chapter 7) although we will later review evidence to suggest magnetized barotropes cannot be in equilibrium.

6.3.1 Grad-Shafranov formalism

There are various *self-consistent field methods* used to iteratively find the equilibria of axisymmetric, rotating polytropes [49]. Recently these have been modified to include the Grad-Shafranov equation [44] to find rigidly rotating, magnetic equilibria [36, 59, 90].

Starting by writing the equilibrium condition in the form

$$\frac{\mathcal{L}}{\rho} - \nabla h - \nabla\Phi + \tfrac{1}{2}\nabla(r\Omega\,\sin\theta)^2 = 0, \qquad \left(\nabla h = \frac{\nabla P}{\rho}\right) \tag{6.3.1}$$

where h is the enthalpy (section 5.5.2) and the centrifugal term has been written as a potential, then the curl can be taken and integrated to give

$$\mathcal{L} = \rho\nabla M, \tag{6.3.2}$$

where M is some scalar function; since $\mathbf{B}\cdot\nabla M = 0$ it is constant along field lines. Next, by introducing a stream function $u(r,\theta)$ defined through

$$\mathbf{B} = \frac{1}{r^2\sin\theta}\frac{\partial u}{\partial\theta}\mathbf{e}_r - \frac{1}{r\sin\theta}\frac{\partial u}{\partial r}\mathbf{e}_\theta + B_\varphi\mathbf{e}_\varphi = \frac{1}{\varpi}\nabla u\times\mathbf{e}_\varphi + B_\varphi\mathbf{e}_\varphi, \tag{6.3.3}$$

it is automatically true that $\nabla\cdot\mathbf{B} = 0$ (using the standard spherical basis). In addition $\mathbf{B}\cdot\nabla u = 0$ so that u is constant along field lines, and thus $M = M(u)$. In terms of vector potentials it is easy to show that the toroidal component of $\mathbf{A}$ satisfies $u = \varpi A_\varphi$. Taking the curl of $\mathbf{B}$ gives the current

$$4\pi\mathbf{j} = \frac{1}{\varpi}\nabla(\varpi B_\varphi)\times\mathbf{e}_\varphi - \frac{1}{\varpi}\Delta_* u\;\mathbf{e}_\varphi, \tag{6.3.4}$$

where

$$\Delta_* u = \frac{\partial^2 u}{\partial r^2} - \frac{\sin\theta}{r^2}\frac{\partial}{\partial\theta}\left(\frac{1}{\sin\theta}\frac{\partial u}{\partial\theta}\right) \tag{6.3.5}$$

which can also be expressed as the Laplacian of a three dimensional term:

$$\frac{1}{\varpi}\Delta_* u \equiv \frac{1}{\sin\varphi}\Delta\left(\frac{u\sin\varphi}{\varpi}\right) = \frac{1}{\sin\varphi}\Delta(A_\varphi \sin\varphi). \tag{6.3.6}$$

We may now rewrite the Lorentz force as

$$4\pi\mathcal{L} = 4\pi\mathbf{j}\times\mathbf{B} = -\frac{1}{\varpi^2}\Delta_* u\nabla u - \frac{1}{\varpi}B^\varphi\nabla F(u) = 4\pi\rho\nabla M(u), \tag{6.3.7}$$

giving the standard form of the Grad-Shafranov equation

$$4\pi\rho\frac{dM}{du} = -\frac{1}{\varpi^2}\left(\Delta_* u + F(u)\frac{dF}{du}\right). \tag{6.3.8}$$

Interestingly, this equation can be used to replace the GS operator in (6.3.4) to give

$$\mathbf{j} = \frac{1}{4\pi}\frac{dF}{du}\mathbf{B} + \rho\,\varpi\frac{dM}{du}\mathbf{e}^\varphi \tag{6.3.9}$$

$$\implies \mathcal{L} = \rho\,\varpi\frac{dM}{du}(\mathbf{B}\times\mathbf{e}^\varphi). \tag{6.3.10}$$

Equating (6.3.9) with (6.3.4) and inverting the Laplacian as per (6.3.6) gives an integral form of the GS equation which is used as the basis for an iterative procedure (see e.g. [59] for more details). The values of $\frac{dF}{du}, \frac{dM}{du}$ are respectively related to the poloidal/toroidal field strength, and the distortion of the star due to magnetic and centrifugal forces, and are (independently) specified.

Although this procedure requires the use of spherical harmonics in evaluating the integral, it also requires vanishing enthalpy on the outer boundary which is not satisfied in our numerical model. In addition, the pressure term cannot be rewritten as the gradient of enthalpy if the fluid is stratified.

Regardless of this, the poloidal components of $\mathbf{B}, \mathbf{j}$ are parallel if the toroidal component of the Lorentz force vanishes (assuming that the field is mixed). It follows from comparing (6.3.3,6.3.4) that

$$\varpi B_\varphi = F(u) \tag{6.3.11}$$

for an arbitrary function F. This is an important condition on axisymmetric magnetic equilibria first noted by Chandrasekhar and Prendergast [30], who express it in terms of frame components,

$$\varpi^2 B^{(\varphi)} = F(\varpi^2 A^{(\varphi)}). \tag{6.3.12}$$

6.3.2 Equilibria through relaxation

We shall now describe the steps we take to relax a buried, mixed field to equilibrium with stratification and without rotation by subtracting an unphysical friction term (section 5.7.4). Consider an $\ell = 1$ field with a toroidal component that is a constant multiple of the poloidal part,

$$\begin{aligned}\bar{\Psi}_1(r,0) &= \psi_1(R^2 - r^2)\left[e^{-(r-c)^2/w^2} + e^{-(r+c)^2/w^2}\right], \\ \bar{D}_1(r,0) &= d_1(R^2 - r^2)\left[e^{-(r-c)^2/w^2} + e^{-(r+c)^2/w^2}\right].\end{aligned} \tag{6.3.13}$$

where we shall set $R = 0.8, w = 0.1, c = 0.4$. Such a field initially satisfies (6.3.11). Our aim is to be determine the stability of a variety of different field configurations, and to generate stable backgrounds on which to study nonaxisymmetric modes (section 7.3).

We first note that this relaxation does not work for unstratified fluids: the density and magnetic field still evolves significantly at several hundred t with strong friction, and the system oscillates violently, blowing up if the field is strong enough. Typically we observe that mixed fields with a strong poloidal component slowly sink towards the origin, eventually crashing the code if the field is initially (and thus always) zero at the origin. Strongly toroidal fields do not appear to sink to the same extent, but the friction method still fails to find a stable configuration. While we do not rule out the existence of special "islands" of stability for magnetic fields embedded in unstratified media [59] with unknown stability properties, it certainly seems unlikely that one can time-evolve arbitrary configurations into stable equilibria without extra physics or unphysical numerical tricks [19].

For stratification, we first set the $\ell = 0$ background from the Lane-Emden solution with $n = 3/2$ (section 5.6.2). A buried field following (6.3.13) with $\psi_1 = 0.01, d_1 = 0.1$ is painted on top. Approximately 45% of the magnetic energy of this profile is contained within the toroidal component, which is very small in relation to the total internal energy ($\mathfrak{B}/\mathfrak{U} = 5 \times 10^{-5}$). We evolve this system with some λ_F up to $t = 100$ with varying ℓ_m, applying forth-order dissipation (with dissipation coefficient 0.02) to all variables except the magnetic field and extrapolating to second-order at the outer boundary. Higher order schemes are observed to sometimes cause boundary instabilities (with our spherical container preventing radial escape of fluid) at late times.

We find that setting $\lambda_F = 5$ for $t < 10$, $\lambda_F = 1$ for $t \geq 10$ is a good choice for minimizing $\dot{\bar{\rho}}_\gamma, v_\gamma, \mathcal{L}_{\bar{w}}$ at $t = 100$ when compared to a fixed λ_F, although we do not claim that it is optimal. During the evolution the magnetic field sinks[2], recentering itself at 0.38, with final energies at $\ell_m = 2, 4, 6$ of $\mathfrak{B}_T/\mathfrak{B} = 0.51, 0.51, 0.51$ and $\mathfrak{B}/\mathfrak{U} = 2.7 \times 10^{-5}, 4.6 \times 10^{-5}, 6.4 \times 10^{-5}$. The final state is illustrated by figure 6.3.

Continuing the evolution without friction appears to be stable for up to $t = 100 + 400$,

[2] If the field is frozen during the relaxation stage, it sinks in a similar manner as soon as the friction term is switched off, although the resulting oscillations are larger in magnitude.

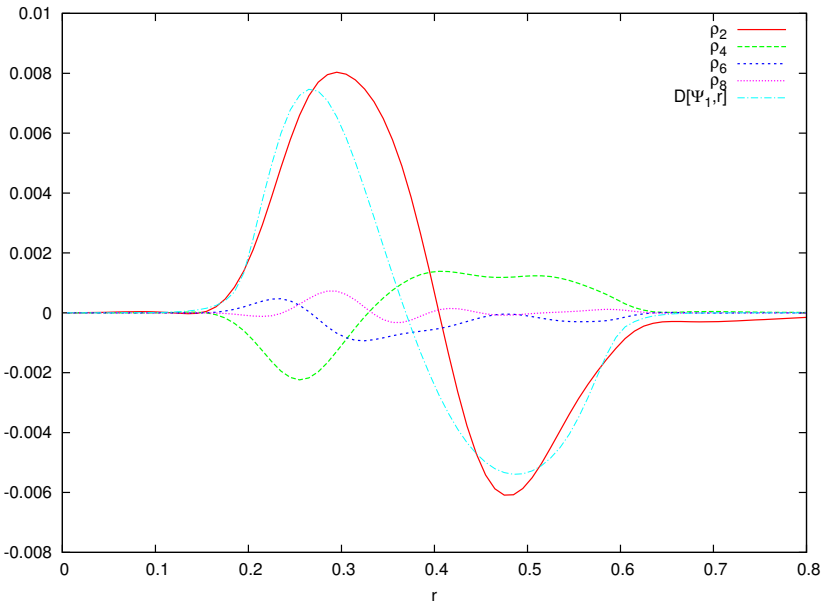

(a) The even-ℓ unregularized density components after relaxation, compared with the (rescaled) derivative of $\bar{\Psi}_1$.

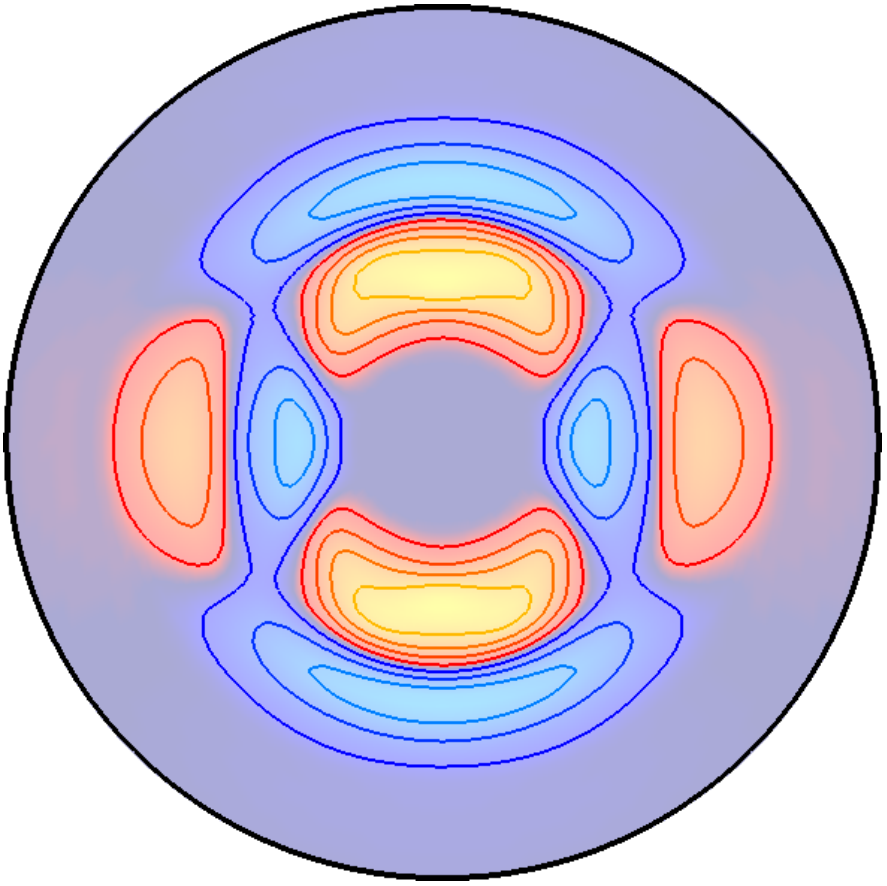

(b) Contours of the deviation of the relaxed density distribution from the spherically symmetric background ($\rho - \rho_0$ at $\ell_m = 8$) with red/blue areas indicating a positive/negative difference.

Figure 6.3: The density at $t = 100$ after evolving a mixed field with friction.

regardless of whether or not the velocity is reset to 0, so long as f is set from $\hat{v}, \bar{u}$ often enough (for example after every time step). Freely evolving the $\ell_m = 2, 4, 6$ relaxed states gives a maximum $|v_2|$ amplitude of $10^{-3}, 3\times10^{-4}, 4\times10^{-4}$ in $100 < t < 100 + 200$. At $\ell_m = 4$, the final energy ratio is $\mathfrak{B}_T/\mathfrak{B} = 0.53$, and there has been a relative mass increase of 0.006 and relative total energy increase of 0.002. These figures are little different if the field is relaxed over some longer $t > 100$. The residual velocity field is proportional in magnitude to the square of the background field (and inversely proportional to the resolution) during both the relaxation and subsequent free evolution indicating that these relaxed states represent linear-regime equilibria. These non-linear oscillations are actually observed to become damped (their time derivatives globally decrease in magnitude) after around $t = 100 + 150$.

We may apply the same relaxation and subtraction techniques to test the stability of generic magnetic fields, including non-mixed forms, to axisymmetric perturbations. The relaxed density distribution of the purely poloidal field $\psi_1 = 0.01$ has a very similar density distribution to the mixed field we previously looked at, and a range of ρ_2 profiles are shown in figure 6.4.

All of these fields, including the purely poloidal (red) and toroidal (purple) fields, are stable to free evolutions (i.e. with no residual acceleration subtracted or perturbations) tested up to $t = 100 + 400$. Their evolutions are typically characterized by initially large oscillations in velocity terms near the origin, which are eventually ($t = \mathcal{O}(100)$) damped.

6.3.3 Equilibria through relaxation: exterior fields

We now turn to the equilibria of exterior fields. Braithwaite [18, 19] found equilibria by evolving arbitrary initial configurations and applying a *hyper-diffusion* operator, with the aim of studying the stability properties. To be able to study neutron stars with realistic (and important) external fields we should like to see if our friction method lets us evolve to an equilibrium.

First recall that an $\ell = 1$ poloidal field suffers an r^{-3} fall-off (6.2.28) in vacuum. Gaussian initial data can not not have smooth derivatives at the outer boundary with this constraint. Since we require derivatives of $\bar{\Psi}$ up to third order ($\dot{f}$ contains such a term) to avoid large unphysical numerical quantities, and want to prescribe both the radial location of the field maximum and its magnitude, we set $\bar{\Psi}_1$ from a polynomial with five free parameters as per

$$\bar{\Psi}_1(r) = \lambda(r^2 + ar^4 + br^6 + cr^8 + dr^{10}). \tag{6.3.14}$$

For example, the polynomial

$$\bar{\Psi}_1 \simeq \lambda(r^2 - 5.29\,r^4 + 11.14\,r^6 - 10.78\,r^8 + 3.98\,r^{10}) \tag{6.3.15}$$

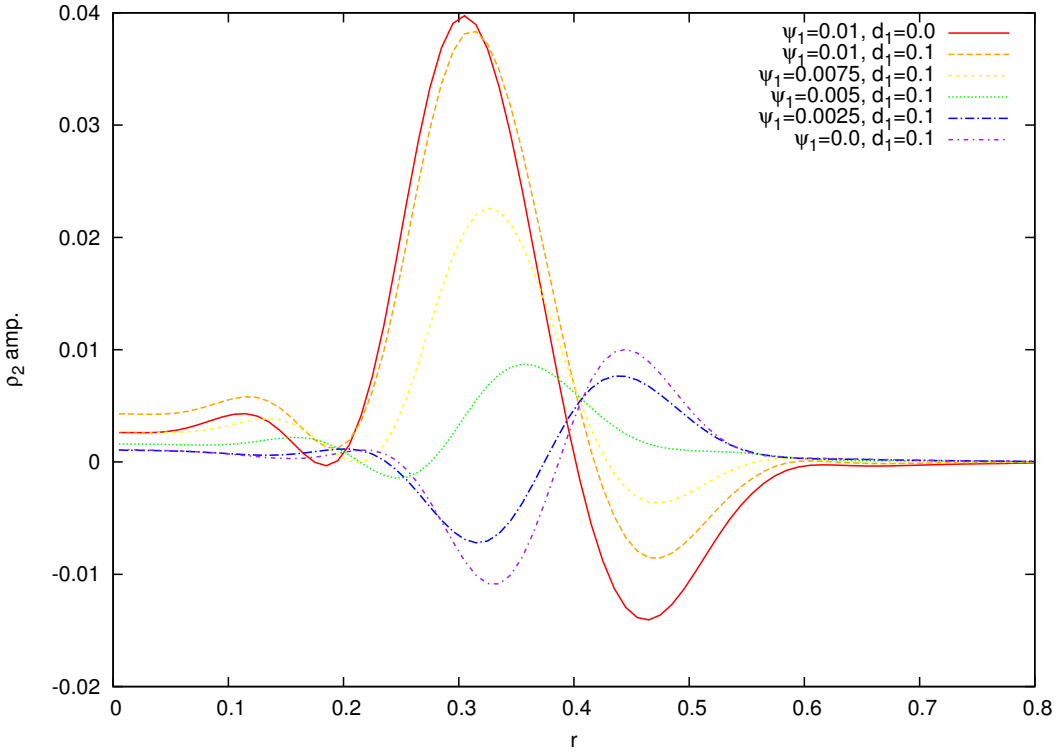

Figure 6.4: A range of relaxed ρ_2 profiles with fixed $\bar{D}_1$ and varying $\bar{\Psi}_1$. The density profile for a purely poloidal field is shown for comparison (red).

---

has a maximum at $r = 0.4$ and matching derivatives to an exterior field (up to third order) when the surface is given by $R = 0.8$.

Toroidal fields are set from a Heaviside function to avoid surface/exterior currents:

$$\varpi B^\varphi = H(x/x_0 - 1)(x - x_0)(x/x_0 - 1), \qquad (x = \varpi A^\varphi) \tag{6.3.16}$$

where x_0 is some minimum value of x where the toroidal field exists. The maximum of ϖA_φ using our example $\bar{\Psi}_1$ is found at $r = 0.8, \theta = \pi/2$ and we should set x_0 to greater than or equal to this. $\bar{D}_\gamma$ is found through numerical integration of (6.3.12): using

$$\varpi B^\varphi = \varpi^2 r^{\ell-1} \bar{D}_\gamma S^\varphi_\gamma = F(\varpi A^\varphi) \tag{6.3.17}$$

implies

$$\bar{D}_\gamma = \frac{1}{2L^2_\gamma} \frac{1}{r^{\ell+1}} \int_0^\pi F(\varpi A^\varphi) \partial_\theta Y_\gamma d\theta, \tag{6.3.18}$$

where we have used the identity $S_\varphi = -\sin\theta \partial_\theta Y$. The toroidal field may now be rescaled through multiplication by an arbitrary constant. Figure 6.5 shows this process, along with the first few $\bar{D}_\gamma$ returned by this particular choice of $\bar{\Psi}_1, F$. This function can be verified to give toroidal Lorentz components that converge to zero with both ℓ_m and resolution (at second-order), as shown for $\ell = 2$ in figure 6.6.

We now relax this magnetic field, with appropriate boundary conditions (6.2.29), again with a changing friction $\lambda_F = 5 : t < 10$ and $\lambda_F = 1 : t \geq 10$.

The background density and magnetic field configurations change very little, with the majority of poloidal magnetic energy remaining in the $\ell = 1$ component. Figure 6.7 shows the total accelerations acting on $\bar{v}_2, \bar{w}_2$ at different times. Although the initial poloidal accelerations shrink by several orders of magnitude, the toroidal acceleration (i.e. the Lorentz force) at $\ell = 2$ grows, reaching a maximum at about $t = 150$. The higher ℓ toroidal accelerations (tested with $\ell = 4, 6, 8$) roughly halve in amplitude from their initial states.

Continuing an evolution without friction leads to global blow-up of the velocity components. Similar blow-up is observed in axisymmetric perturbations to these states, where the initial (unperturbed) acceleration is subtracted at every time step to create an artificial equilibrium, with a time scale independent of the perturbation amplitude. Unfortunately we are forced to conclude that our relaxation technique does not find (stable) equilibria in this case: given the similar issue we have with stratification and rotation, it is possible that friction and the outer boundary conditions are somehow incompatible.

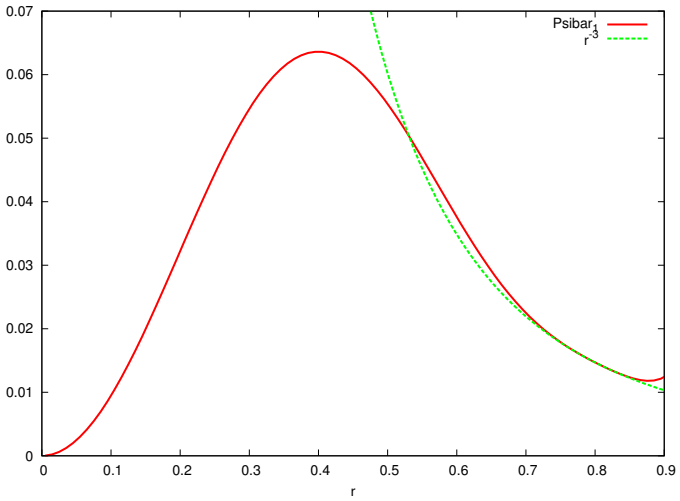

(a) To avoid large unphysical derivatives at the boundary, exterior magnetic fields can be initially set to exhibit the correct fall-off up to third derivatives.

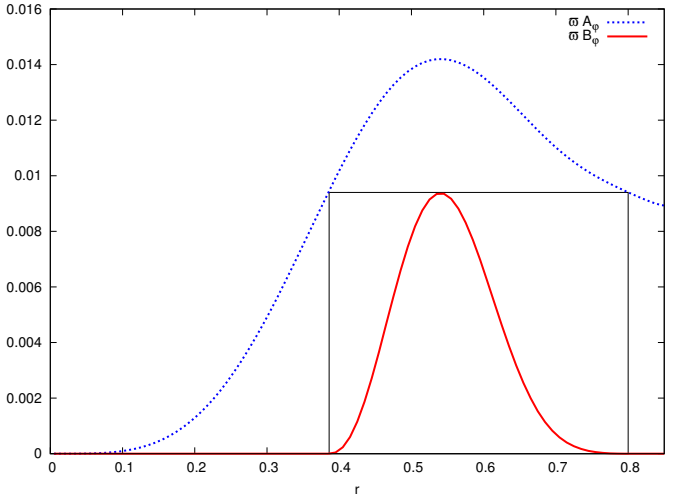

(b) A plot of $\varpi A_\varphi, \varpi B_\varphi$ (rescaled) along the equator $\theta = \pi/2$. The box illustrates why we have chosen a Heaviside function.

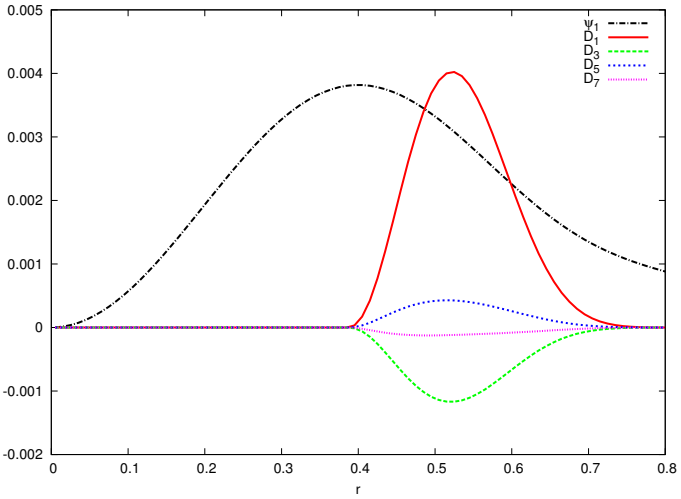

(c) $\bar{D}_\gamma$ can be found from the numerical integration of $F(\varpi A_\varphi)$. The first few unregularized functions are shown above.

Figure 6.5: Satisfying the equilibrium condition (6.3.12) with external fields.

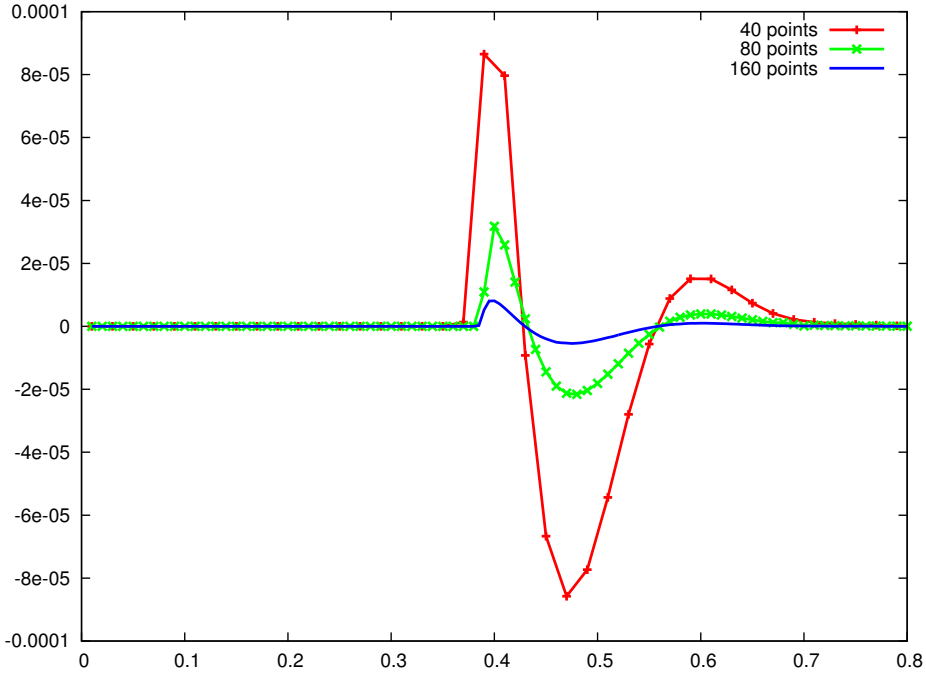

(a) Second-order convergence with increasing resolution at $\ell_m = 4$.

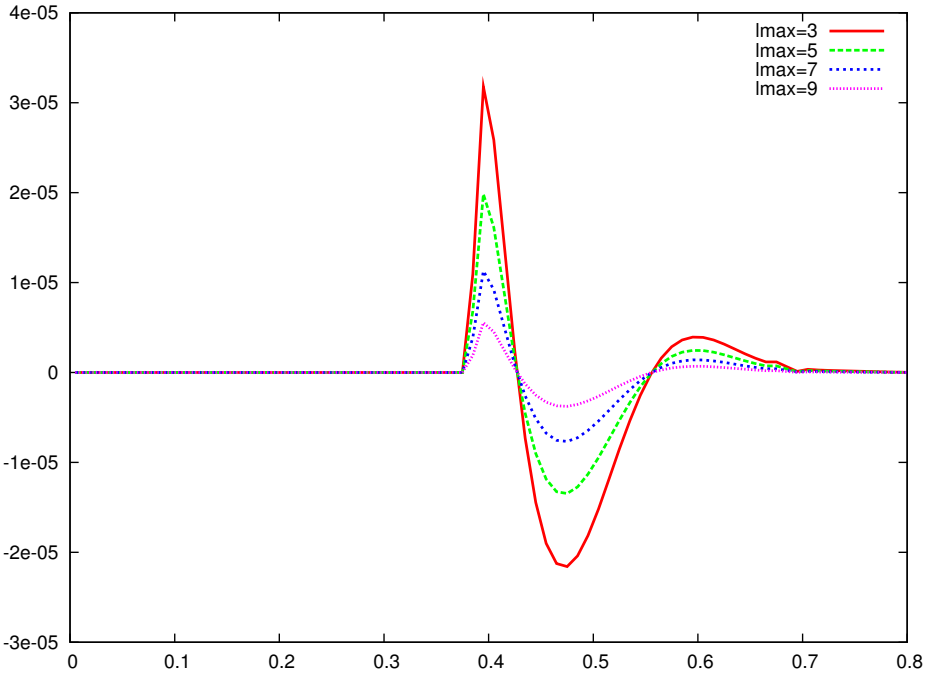

(b) Convergence with increasing ℓ_m at $N = 80$.

Figure 6.6: The initial toroidal Lorentz acceleration converges to zero with increasing spatial resolution.

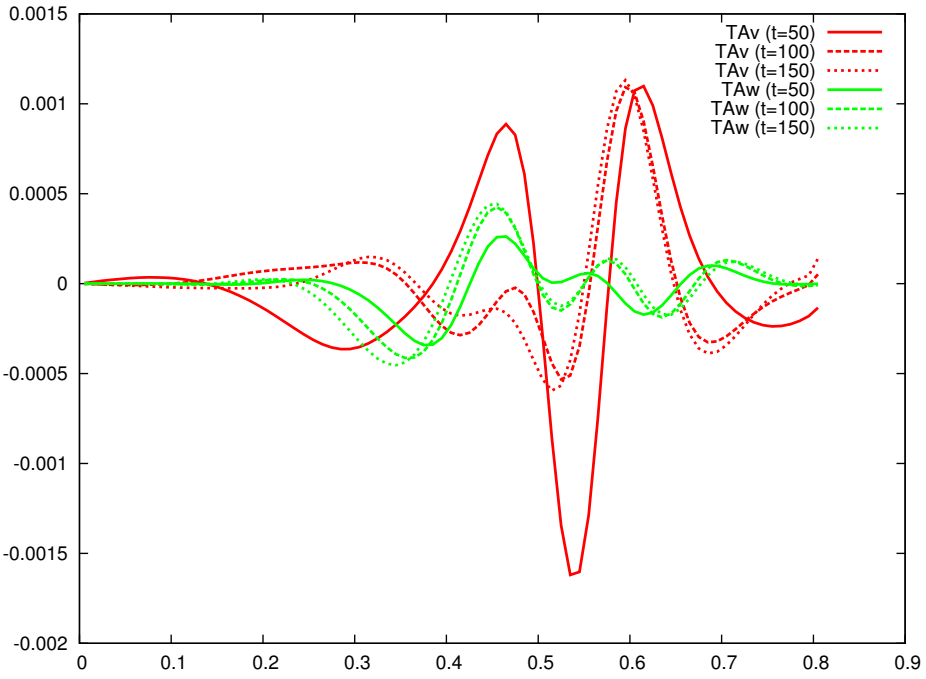

Figure 6.7: The radial and toroidal accelerations at different time steps during relaxation. The former has decreased in magnitude from that given by the initial data by a factor of 10^{-2} and the latter has increased by 10.

6.4 Stability

Tayler [86, 87, 89] showed, using an analytical method, that purely poloidal and toroidal fields should (usually) be unstable to certain kinds of perturbations over an Alfvén time scale $t_A = R\sqrt{M/\mathfrak{B}}$, even within stably stratified stars. In recent years there have been several numerical models built to study these results; in particular a series of papers by Braithwaite [17, 18, 19] confirm the existence of these instabilities for various stratified configurations with and without exterior field components.

Various instability effects are known for magnetized stars with rotation or thermal effects included, for example, the magneto-rotational instability [7]. Spruit [81] showed that the so-called *Tayler effect* is perhaps the most important class of toroidal instability: purely toroidal fields are subject to *kinking*, where circular, horizontal field lines are displaced in different directions. The effect is often compared with the displacement of vertebrae from spinal cord compression. Toroidal fields should always be unstable to $|m| = 1$ perturbations, with stability to other m's if the density and field configuration satisfies a particular condition relating to the potential energy [17].

Poloidal fields should also exhibit a similar vertical kink effect when perturbed by $|m| \geq 2$, but adding a toroidal stabilizes the configuration at some point (usually quoted as $\mathfrak{B}_T/\mathfrak{B}$ being somewhere between 20% and 30%). Tayler showed that mixed field stability requires the magnetic pressure to be weak compared to the fluid pressure, comparable toroidal and poloidal field strengths, and no current flowing along the magnetic axis.

Given the estimated ages of some pulsars – PSR B0531+21, lying at the heart of the Crab Nebula, is the pulsar remnant of a supernova observed in 1054 CE, and the current closest known neutron star, PSR J0108-1431, may be over 200 million years old [85] – it is likely to be the case that a typical neutron star magnetic field is of mixed configuration. Any that are wound up to have a too-strong (and thus unstable) toroidal component perhaps lose energy in the form of powerful γ-ray flares [35, 60].

However the stability properties of generic mixed fields embedded in polytropic stars are not well known, despite a wealth of literature dealing with such configurations. It is perhaps the case that polytropes have no stable equilibria: Reisenegger [74] has pointed out that there is no known mechanism to stop a perturbed toroidal field from rising vertically out of the star as strong fluid pressure displaces it. Additionally, a simple comparison of the number of independent functions indicates that balancing A_φ, B_φ against a single variable ρ gives, at best, only a particular subset of all possible configurations. A stratified fluid with $P(\rho, s)$ generating a positive buoyancy effect should be able to maintain a stable, long lived mixed field.

6.4.1 Axisymmetric perturbations

To test the stability of the relaxed mixed field discussed in section 6.3.2 we evolve non-linear, axisymmetric perturbations to the $\ell_m = 4, t = 100$ relaxed background. We indeed find that this configuration is stable to various perturbations when evolved freely or with unwanted background oscillations artificially removed.

We achieve the latter by subtracting the *initial* time derivative of the unperturbed, frictionless, relaxed state, from every subsequent time-step of the perturbed evolution. We shall refer to this method as *subtracting the residual acceleration*. As we saw in section 5.7.4 residual acceleration decreases with increasing resolution so this subtraction is consistent.

In addition we only consider adding perturbations in modes[3] that are not naturally excited by this mixed-field configuration in order to reduce the search-space. For initial data where the density/velocity components have even-ℓ and the magnetic field components odd-ℓ this means we perturb in odd-ℓ fluid and/or even-ℓ magnetic terms.

In evolutions of this mixed field background with the residual acceleration subtracted, we find perturbations of any variable with initial amplitude set to $10^{-3}, 10^{-4}, 10^{-5}$ remain stable and perfectly proportional by a factor of 10, whilst the even-ℓ velocities and odd-ℓ field perturbations remain proportional by a factor of 10^2, indicating that they are driven by quadratic source terms. These evolutions remain stable until at least $t = 100 + 400$. Small $\ell = 1$ fluid oscillations of $\mathcal{O}(10^{-10}), \mathcal{O}(10^{-11})$ are proportional although the quadratic $\ell = 2$ components are noisy and $\mathcal{O}(10^{-16})$ indicating they are overwhelmed by floating-point error.

6.4.2 Nonaxisymmetric perturbations

On purely poloidal axisymmetric backgrounds, $\bar{w}_2^2$ perturbations cause significant decay of the poloidal component. Mixed fields with a sufficiently strong toroidal component are stable to such perturbations; the purely toroidal fields we evolve are unstable only to perturbations $\bar{w}_\ell^1$.

The poloidal instability occurs over a time dependent on both the background field strength and the perturbation amplitude, rather than simply one Alfvén time crossing. For example, with $\psi_1 = 0.01$ and $\bar{w}_2^2 = 10^{-3}, 10^{-4}$, the field begins to noticeably decay at around $t = 25, 50$ and has somewhat settled into a new configuration at around $t = 70, 95$ ($t_A \simeq 13$). Perturbations of $\bar{\rho}_2^2$ and $\bar{D}_2^2$ do not cause this decay, or even dampen it when $\bar{w}_2^2$ is present. We have already seen that axisymmetric perturbations do not lead to similar behaviour.

Varying the dissipation amount and order, the friction coefficient, the resolution (in radius or angles) ℓ_m, or the extrapolation order at the outer boundary makes little, if any, difference to the decay time scale and so we conclude that we are observing a physical effect.

[3] In referring to *modes* we exclusively refer to the ℓ, m harmonic numbers involved.

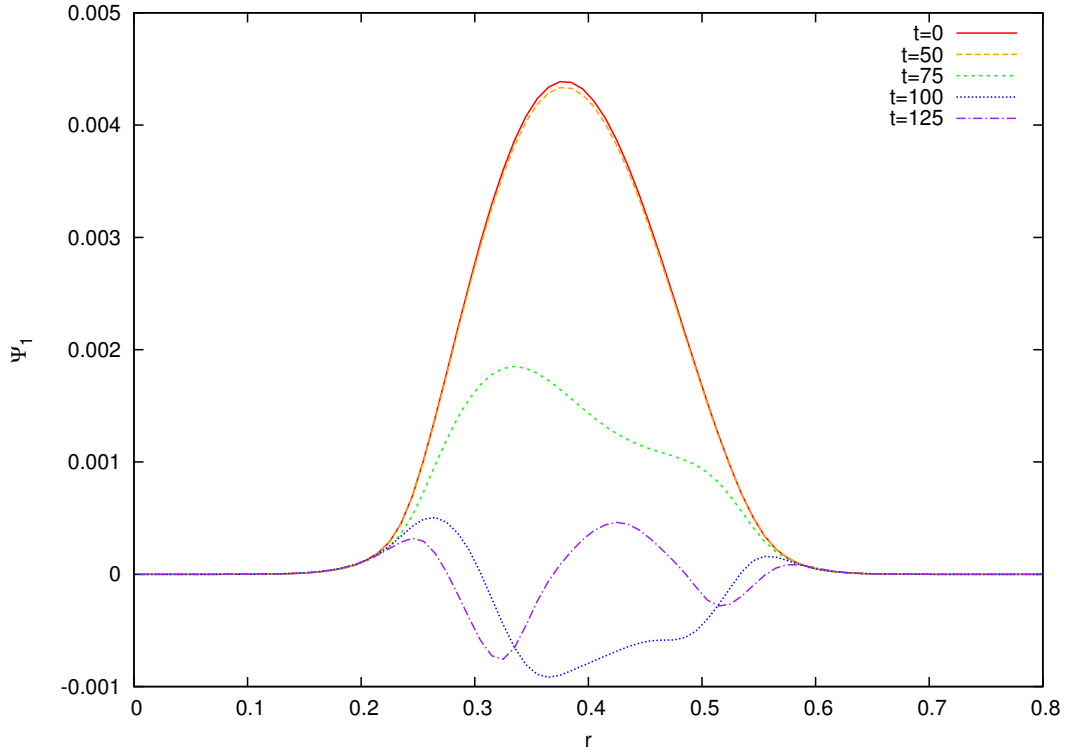

Figure 6.8: Evolution and decay of $\bar{\Psi}_1^0$ when a constant perturbation $\bar{w}_2^2 = 10^{-4}$ is applied. The field has no $\ell = 1, m = 0$ toroidal component but a $\bar{D}_3^2$ term grows to a similar order.

The decay of $\bar{\psi}_1^0$ to a $\bar{w}_2^2 = \mathcal{O}(10^{-4})$ perturbation is shown in figure 6.8. Evolving without subtracting a residual acceleration speeds up the decay but does not appear to affect the stability of any of the fields we study in this section.

Additionally, it is not just $\ell = m = 2$ toroidal modes that lead to the poloidal instability but apparently any quadrupole-led w-perturbation (section 2.4), e.g. $\bar{w}_2^2, \bar{w}_3^3, \bar{w}_4^4, \bar{w}_4^2$. Since these modes induce $\bar{D}_{\ell+1}^m$ terms, it is expected (and observed for $\ell = 2, m = 2$) that $\ell = 1, m = 0$ poloidal fields are unstable to dipolar D perturbations.

We define the quantity $Z_\psi(r,t) = \bar{\psi}_0^1(r,t)/\bar{\psi}_0^1(r,0)$ and record the *decay time* as $Z(0.4,t) \leq 0.99$ for varying perturbation modes. This particular fraction is chosen simply because it gives a rough estimate as to when the field is noticeably beginning to decay. Modes that do not decay within time $t = 400$ are marked as such.

Figure 6.9 lists such decay times for $\ell = 1$ poloidal fields with rotation $\bar{w}_\ell^m = \mathcal{O}(10^{-4})$. The indications are that quadrupolar perturbations of w are stable, unlike dipolar modes, which, for a given ℓ, collapse faster at higher m. This higher-m-faster-collapse result appears to be in agreement with a result from Tayler and Markey [89], although more tests with higher modes (and hence higher ℓ_m) are necessary to rigorously confirm this. It is not clear to us why quadrupolar perturbations are stable, and if this is an inherent property of the perturbation, or rather the couplings with the background density and/or magnetic field; perhaps it it the case that these perturbations, satisfying $f^{(\theta)}(\theta,\varphi) = -f^{(\theta)}(\pi-\theta,\varphi)$, are

ℓ	m	Decay time
1	1	167
2	1	N/A
2	2	48
3	2	N/A
3	3	42
4	2	77.5
4	3	N/A
4	4	41.5

Figure 6.9: Decay time of a purely poloidal $\ell = 1$ field ($\psi_1 = 0.01$) at $\ell_m = 6$ to $\bar{w}^m_\ell = \mathcal{O}(10^{-4})$. The figures for $m = 1$ were found with $\ell_m = 4$. The Alfvén time for this field is approximately 30; the fields that did not decay were tested up to a time of 400.

suppressing the usual poloidal field *kinking* that gives the instability (figure 2.3, and figure 2 of [16]).

3–dimensional visualization helps us to observe a strong toroidal component is quickly generated during these evolutions (figure 6.10), through the excitation of (exclusively) quadrupolar $\bar{D}^m_\ell$ terms, for example $\bar{D}^2_3, \bar{D}^3_4$.

Purely toroidal fields, centred at $r = 0.4$, appear to be stable to $w^{m>1}_\ell$ perturbations, in the same sense that the value of $Z_D(t) = D_1(r = 0.4, t)/D_1(r = 0.4, t = 0)$ oscillates around some value close to one, irrespective of the perturbation being dipole- or quadrupole-led. Evolving a field perturbed by $\bar{w}^2_2$ without subtracting the residual acceleration does lead to a gradual shrinking of $\bar{D}^0_1$ ($Z(100) = 0.95, Z(200) = 0.91$) but the perturbation does not grow at an exponential rate. The effect is illustrated in figure 6.11 Those $m = 1$ perturbations with a lower ℓ collapse the field faster but as we are using $\bar{w}$ = constant perturbations it is not easy to tell if this is due to larger $w \propto r^\ell$. Lander and Jones [60] recently investigated a similar background with linear $m = 1$ perturbations, finding decay over one Alfvén crossing, and went on to confirm that adding rotation increases the time taken to decay without ever stabilizing the star.

To investigate the poloidal/toroidal energy proportion a generic mixed field requires for stability when subject to $\bar{w}^2_2$ perturbations, we again record the quantity Z_ψ with varying d_1 (figure 6.12). As with the purely poloidal case, those fields that are unstable are generally observed to collapse and oscillate around a new configuration, which remains closer to the initial data with a stronger toroidal component. Larger amplitude perturbations cause unstable fields to decay faster and do not cause otherwise stable fields to collapse.

The results indicate that, for a stratified star initially set from a range of different polytropes, and with a magnetic field dominated by $\ell = 1$ components, an initial fraction

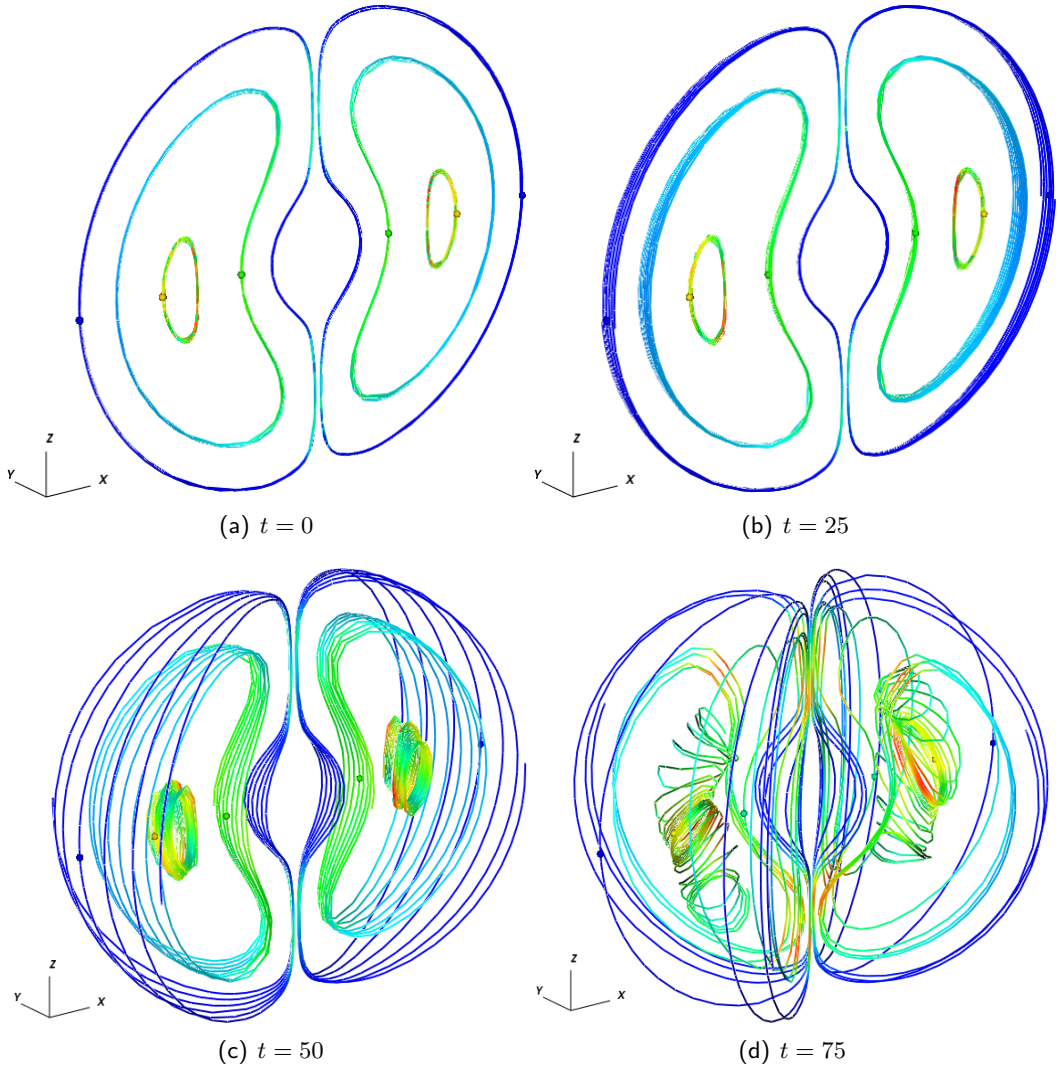

(a) $t = 0$ (b) $t = 25$

(c) $t = 50$ (d) $t = 75$

Figure 6.10: Some (truncated) field lines of an evolution of an initially poloidal magnetic field, with colours indicating $|\mathbf{B}|$. When subjected to an $\mathcal{O}(10^{-4})$ $\bar{w}_2^2$ perturbation a substantial nonaxisymmetric toroidal term $\bar{D}_3^2$ is rapidly generated. By $t = 50$ the $\bar{\Psi}_1^0$ component has started to noticeably decay.

$\mathfrak{B}_T/\mathfrak{B} > 0.3$ is stable to $\ell = m = 2$ toroidal perturbations. This appears to be a *linear* instability: poloidal fields still collapse with $\bar{w}_2^2 = \mathcal{O}(10^{-10})$ perturbations (which grow exponentially in time) and when all modes with $|m| > 2$ are discarded.

In section 7.3 we shall look at the oscillation modes of (stable) nonaxisymmetric perturbations to some of the same magnetic fields. Although some basic stability properties have been investigated there are still many questions that could be addressed using this spectral framework: for example, how varying the radial- and angular-profiles of these magnetic fields might alter their stability properties (particularly with regards to toroidal fields), what (if any) differences there are with linear evolutions, and if the same toroidal/poloidal energy proportions required for stability hold for all toroidal perturbation modes ℓ, m.

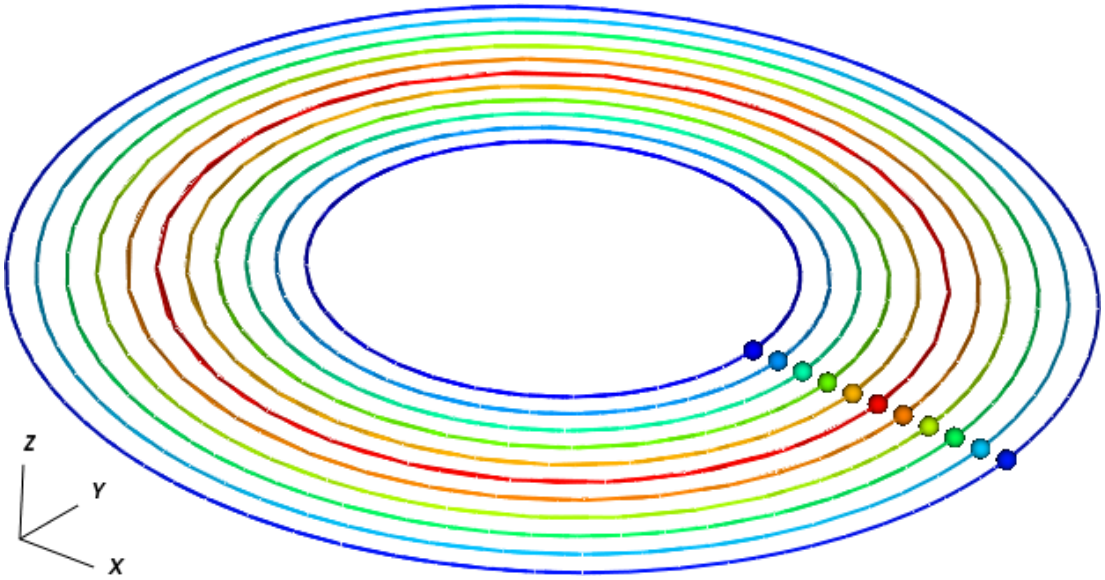

(a) $t = 0$

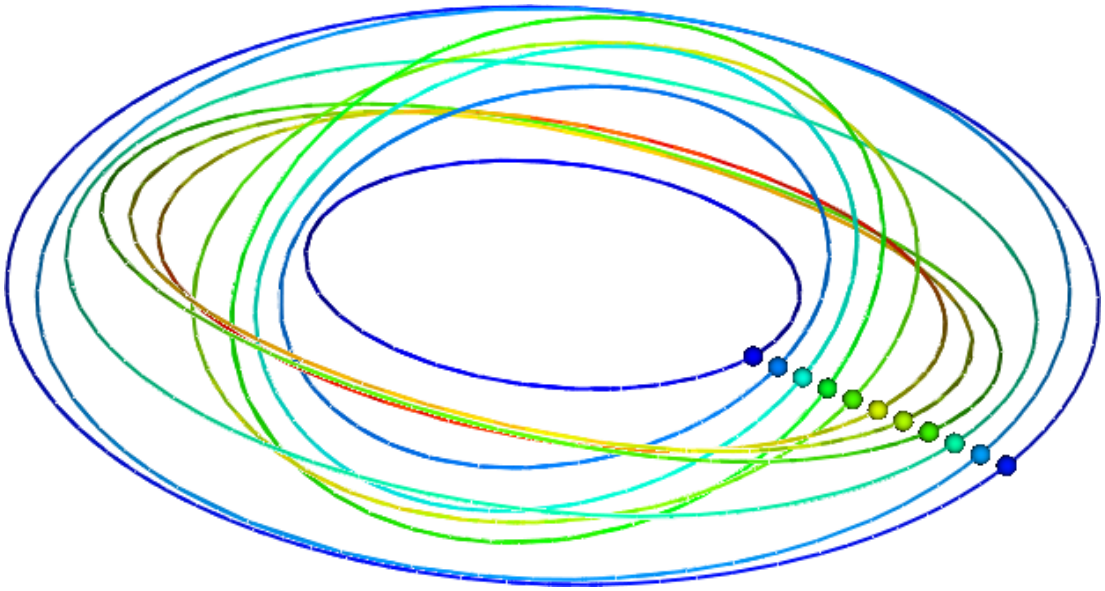

(b) $t = 200$

Figure 6.11: Some streamlines of an initially toroidal magnetic field that pass through the equator, subsequently evolved non-linearly with a $\bar{w}_1^1$ perturbation. Due to an instability the background field decreases in strength whilst a strong $\ell = 2, m = 1$ poloidal field component is generated. This is the Tayler instability: field lines remain circular but are displaced from the horizontal.

d_1	Initial $\mathfrak{B}_T/\mathfrak{B}$	Relaxed $\mathfrak{B}_T/\mathfrak{B}$	Decay time $n = 1.5$
0	0	0	78
0.01	0.032	0.036	81
0.02	0.117	0.131	90
0.03	0.229	0.252	121
0.0325	0.259	0.283	143.5
0.035	0.288	0.314	210
0.0375	0.317	0.344	∞

(a) $\psi_1 = 0.005$

d_1	Initial $\mathfrak{B}_T/\mathfrak{B}$	Relaxed $\mathfrak{B}_T/\mathfrak{B}$	Decay time $n = 1.1$	$n = 1.5$	$n = 2$
0	0	0	58.5	49	41
0.02	0.032	0.042	60.5	50	42.5
0.04	0.117	0.150	70.5	57	48
0.06	0.229	0.282	105.5	80	67.5
0.065	0.256	0.315	135.5	98	82
0.07	0.288	0.347	256.5	161	124.5
0.075	0.317	0.408	∞	∞	∞

(b) $\psi_1 = 0.01$

d_1	Initial $\mathfrak{B}_T/\mathfrak{B}$	Relaxed $\mathfrak{B}_T/\mathfrak{B}$	Decay time $n = 1.5$	$n = 2$
0	0	0	31	26
0.1	0.171	0.255	43.5	36.5
0.14	0.288	0.398	116	88.5
0.144	0.300	0.411	234.5	131.5
0.145	0.303	0.414	∞	161
0.146	0.306	0.416		241
0.147	0.309	0.420		∞

(c) $\psi_1 = 0.02$

Figure 6.12: The time it takes $\bar{\Psi}_1^0$, with a varying toroidal component, to decay in magnitude by 1% when perturbed by $\bar{w}_2^2 = \mathcal{O}(10^{-4})$. Increasing the stratification (greater n) lowers the mass of the modelled NS, and hence shortens the Alfvén time, which is approximately halved between the $n = 1.1, 2$ models (for $\psi_1 = 0.01, d_1 = 0.07$ it is approximately $31, 18$ for $n = 1.1, 2$).

Chapter 7

Oscillation Modes

As we have already noted, the oscillation modes observable in X-ray or γ-ray signals from pulsars and magnetars are important for tuning NS models. Whilst we are not overtly concerned here with the phenomenology of neutron star models, it is still worthwhile to adapt the mathematical apparatus for the analysis of modes to our spectral framework.

To quickly outline the process we follow to find oscillation frequencies with our code, we start by finding a background equilibrium through relaxation, then set $\bar{\rho}$ or $\bar{w}$ perturbations for a particular ℓ, m and save the output of a sufficiently long evolution every few time steps. Finally we take the 1D discrete Fourier transform (DFT) of these complex data at various points in r using the free and widely used FFTW library[1].

7.1 Method

7.1.1 Transforming from the inertial frame

Our evolution equations are described in the inertial frame, yet oscillation frequencies of rotating neutron stars are almost always given in a co-rotating frame (denoted here by hatted variables). Noting that such a transformation shifts coordinates $\varphi = \hat{\varphi} + \Omega t$, and any oscillation with frequency ω can be written in terms of spherical harmonics as $e^{i(m\varphi+\omega t)}$, for some perturbation $\zeta(r,\theta)$ we have a relation

$$\zeta e^{i(m\hat{\varphi}+\hat{\omega}t)} = \zeta e^{i(m\varphi+\omega t)} \tag{7.1.1}$$

$$\implies \hat{\omega} = \omega + m\Omega = 2\pi f + m\Omega, \tag{7.1.2}$$

where f is the normal frequency returned by a DFT.

[1] Available from http://www.fftw.org

7.1.2 Background equilibria

To investigate the inertial mode frequencies of unstratified polytropes with our code, we first need to find the unperturbed axisymmetric equilibria of a range of rotation frequencies $\Omega = \sqrt{3}\bar{w}_1^0$. These are straightforward to find by starting with the known analytical solution and then relaxing for some time with a small friction coefficient to find a better numerical equilibrium.

For the length of time the code is subsequently run, typically tens of thousands of time steps, an evolution of the unperturbed background might evolve significantly away from the starting configuration – that is, our supposed equilibria are not stable for as long as we require – and the rotation rate can increase greatly. To remedy this we remove the friction and evolve by subtracting a residual acceleration at every time step (section 6.3.2). Setting a low truncation $\ell_m = 2$ for rigid rotation is sufficient to find the background.

7.1.3 Frequency analysis

To calculate oscillation frequencies we will need to perform multiple one-dimensional DFTs in the time domain. These are defined as

$$X_k = \sum_{n=0}^{N_t} x_n e^{-\frac{2\pi i}{N_t} kn}, \qquad k = 0, ..., N_t \tag{7.1.3}$$

where $N_t + 1$ is the total number of time steps and the x_n are complex-valued data[2] sampled every few time steps at some particular value of r: if the modes we are interested in are global then it should not matter what r we choose. For example, the input may be the values of $\bar{w}_2^2$ at the first grid point sampled every 10 time steps. The x_n are of course assumed to be representative of a continuous function, but as they are not necessarily periodic we may choose to multiply by a window function to reduce *edge noise*. Using a fast Fourier transform algorithm means this operation can usually be performed in $\mathcal{O}(N_t \log_2 N_t)$ steps, instead of $\mathcal{O}(N_t^2)$ [33].

The complex-valued discrete points in the frequency domain X_k need to be rescaled to give the angular frequency spectrum. FFTW returns positive frequencies, with each point $k = \frac{T\omega}{2\pi}$, in the region $k \in [1 : N_t/2]$, and negative frequencies $N_t - k = \frac{T\omega}{2\pi}$ in the region $k \in [N_t/2 + 1 : N_t]$, where $T = \delta t\, N_t$ is the run-time and ω is the angular frequency[3]. DC offset is returned at X_0.

The DFT of a real-valued sinusoid returns equal amplitude positive and negative

[2] Recall that our mode components are complex valued, *c.f.* section 4.2, so we find the complex transform of every variable and mode $\rho_m^\ell, \hat{v}_m^\ell$ etc. at sampled r, t.

[3] Another way of saying this is that FFTW returns frequencies in the range $[0^+, N_Y]$ in the first half of the output, and $[-N_Y : 0^-]$ in the second half where N_Y is the Nyquist frequency (half the sampling frequency).

frequencies, since, for example,

$$f(t) = \cos(\omega t) = \tfrac{1}{2}(e^{i\omega t} + e^{-i\omega t}). \tag{7.1.4}$$

Complex valued-sinusoids can of course return purely positive or negative frequencies which correspond to clockwise or anti-clockwise motion in time.

7.2 Inertial modes

Inertial modes are axial-led modes [65] that appear in rotating stars as a result of the Coriolis force. In particular, the r-mode is the lowest frequency of these, as well as the most interesting. It was first identified in an astrophysical context by Papaloizou and Pringle [68] who named it after the recently discovered Rossby waves. Recently it was found that the r-modes should become unstable in the relativistic regime through what is known as the CFS instability [4, 5, 28, 37, 38] which we explain below. In particular, hot, rapidly rotating proto-neutron stars may well emit detectable gravitational waves through this instability, although various damping mechanisms have been proposed.

Passamonti *et al.* [70] recently developed a code to investigate the oscillation modes of both stratified and unstratified non-magnetic neutron stars. This code differs from ours in a number of ways: it includes the stellar surface by working on coordinates adapted to contours of constant pressure, it makes the Cowling approximation, and it operates in the linear regime. Nonetheless a comparison will help highlight some of the strengths and weaknesses in our approach.

It is possible to show [68, 77] that the r-mode frequency is, to $\mathcal{O}(\Omega)$, proportional to the rotation rate when observed from a co-rotating frame:

$$\hat{\omega}_\ell^m = \frac{2m\Omega}{\ell(\ell+1)} + \mathcal{O}(\Omega^3). \tag{7.2.1}$$

The rapid-rotation corrections are odd order in Ω because the observed frequencies should not depend on the orientation of the observer [5]. From (7.1.2) the inertial frame frequency is

$$\omega_\ell^m = -m\Omega\frac{(\ell-1)(\ell+2)}{\ell(\ell+1)}, \tag{7.2.2}$$

which is always negative for positive m. We can also derive these frequencies directly from the spectral expansion without taking a curl. The term of interest is

$$\dot{\bar{w}}_\gamma = r^{\ell_\alpha+\ell_\beta-\ell_\gamma-1}\chi_\gamma\,\hat{G}_{\alpha\beta-\gamma}\,\bar{w}_\alpha\bar{w}_\beta\frac{\ell_\alpha+\ell_\alpha^2-\ell_\beta(1+\ell_\beta)+L_\gamma^2}{2L_\gamma^2}+\ldots \tag{7.2.3}$$

which reduces to

$$\dot{\bar{w}}_\gamma \simeq -\left(\frac{(\ell-1)(\ell+2)}{\sqrt{3}L_\gamma^2}\Omega\chi_\gamma\,\hat{G}_{1\gamma-\gamma}\right)\bar{w}_\gamma \tag{7.2.4}$$

if we ignore all other coupling terms, including the polar velocity components. Since S_1^0 only has a φ component, the antisymmetry of $\hat{G}$ gives

$$\hat{G}_{1\gamma-\gamma} = \int Y_1^0 Z_\gamma^a S_{-\gamma a} d\Omega = -\int Y_{-\gamma} Z_\gamma^a S_{1a}^0 d\Omega \tag{7.2.5}$$

$$= -im_\gamma\sqrt{3}\int Y_{-\gamma}Y_\gamma d\Omega$$

$$= 4\pi i m_\gamma(-1)^{m_\gamma+1}\sqrt{3}. \tag{7.2.6}$$

Hence

$$\dot{\bar{w}}_\gamma \simeq -im\Omega\frac{(\ell-1)(\ell+2)}{\ell(\ell+1)} = i\omega_I\bar{w}_\gamma \tag{7.2.7}$$

which has an r-independent frequency and is thus a *global* mode.

These modes travel around the star with a *pattern speed* [5]

$$\sigma_I^\ell = \Omega\frac{(\ell-1)(\ell+2)}{\ell(\ell+1)}. \tag{7.2.8}$$

This concept is illustrated in figure 7.2 and elsewhere [5, 77]. Since $\sigma_I^2 = 2\Omega/3 < \Omega$ (prograde motion) it is the case that a co-rotating observer will notice the pattern moving in a direction opposite to rotation (retrograde). Consider a passenger jet flying eastwards: it will appear to be moving west according to an inertial observer because it is travelling slower than the Earth's rotation, which is about 30% faster than the speed of sound.

It is this feature that leads to the CFS instability in GR. Angular momentum is clearly positive for prograde motion, and negative for retrograde motion. If the oscillation mode is prograde in the inertial frame, some mechanism (such as gravitational wave emission or MRI [7, 8]) could cause a loss of positive angular momentum from the neutron star. As a result the angular momentum of the retrograde mode becomes more and more negative, which boosts the oscillation amplitude, which in turn increases the amount of angular momentum being shed. Thus this acts as an unstable feedback mechanism.

7.2.1 Non-magnetized, non-stratified modes

Naïvely the first mode to investigate could be perturbations of $\bar{w}_1^1$, but these will have zero frequency according to (7.2.2), as well as (7.2.4). It has been long known that such perturbations are stationary convective currents. This makes for a good sanity-check in any 3D code.

Component	Ang. frequency	Relative power
$\bar{w}_2^2$	$\sigma \simeq -1$	1
$\bar{w}_3^2$	0	
$\bar{w}_4^2$	σ	3×10^{-2}
$\bar{w}_4^4$	0	
$\bar{w}_5^2$	0	
$\bar{w}_5^4$	2σ	4×10^{-6}
$\bar{w}_6^2$	σ	10^{-3}
$\bar{w}_6^4$	0	
$\bar{w}_6^6$	4σ	4×10^{-9}

Figure 7.1: r-mode frequency and relative power for perturbations in varying ℓ, m at $\Omega = 0.45, \ell_m = 6$.

The next mode of interest are perturbations in $\ell = m = 2$. To investigate these we set $\bar{w}_2^2 = 10^{-4}$ with $\ell_m = 4, N = 90, r_{\mathsf{max}} = 0.9$. In addition we use a forth-order dissipation scheme with second-order accurate extrapolation at the outer boundary: higher order methods lead to instabilities at the outer boundary in increasingly shorter time-scales.

Figure 7.4 shows how the evolution initially progresses with high rotation as ℓ_m is increased, with figure 7.3 displaying the angular frequencies returned by the code at different rotation rates. We note that setting $\ell_m = 2$ gives the $\mathcal{O}(\Omega)$ frequencies exactly, and $\ell_m \geq 3$ results in equivalent frequencies with differing amplitude. We have chosen $\ell_m = 4$ in particular as it appears to be a good trade off between accuracy and speed. In addition there appears to be a low-frequency, high-ℓ amplitude modulation of these modes.

Figure 7.5 shows the $\ell = m = 2$ r-mode frequencies given by our code, transformed into a co-rotating frame, against those of Passamonti [70]. Although their code is linear it does still take into account the $\mathcal{O}(\Omega^3)$ terms, hence the deviation as one approaches the breakup velocity. Our code is obviously not exhibiting this behaviour, i.e. our inertial-frame frequencies are higher than expected, most likely due to the spherical boundary: applying the Cowling approximation and/or altering the surface fraction changes the observed frequencies very little.

We can analyze the frequencies of higher ℓ, m modes by looking again at the $\Omega = 0.45, \ell_m = 6$ evolution. Higher ℓ components oscillate at higher frequencies, some of which are quite noisy (most of the polar terms) and only some of the axial terms (e.g. $\bar{w}_4^2, \bar{w}_5^4, \bar{w}_6^6$) have a very strong signal at, or close to, a single (negative) frequency. The r-mode is primarily visible in $\bar{w}_2^2$ at $\sigma \simeq -1.1$, and all of the $\bar{w}_{2i}^2$ have peaks at the same frequency, with decreasing power (1, .., .. relative to the $\bar{w}_2^2$ power). The higher ℓ, m components that are excited appear to have strong signals at a particular multiple of the r-mode frequency, for example $\bar{w}_5^4$ exhibits a frequency$\sim 2\sigma$ and $\bar{w}_6^6$ at around $\sim 4\sigma$ (figure 7.1).

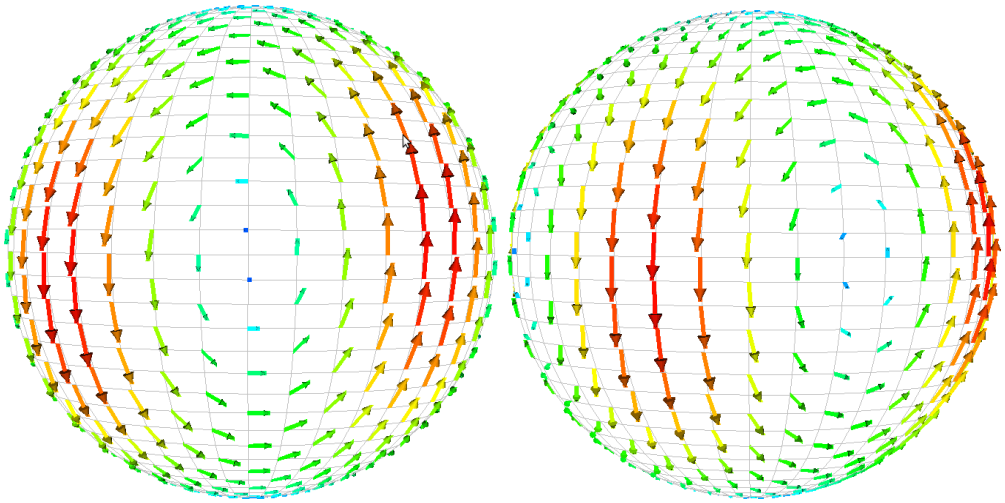

(a) $t = 0$

(b) $t = 0.1/\Omega$

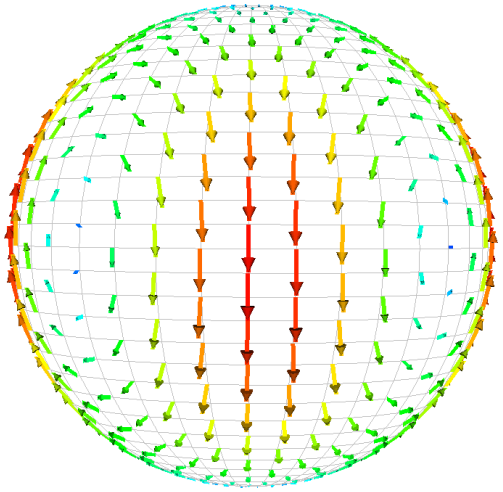

(c) $t = 0.2/\Omega$

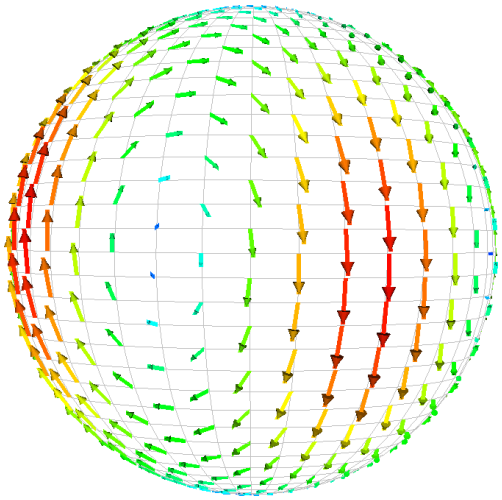

(d) $t = 0.3/\Omega$

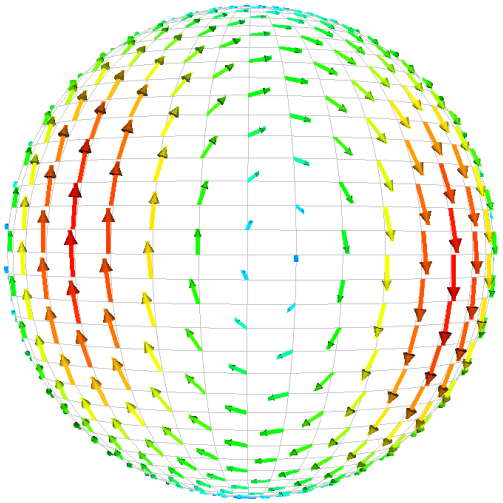

(e) $t = 0.4/\Omega$

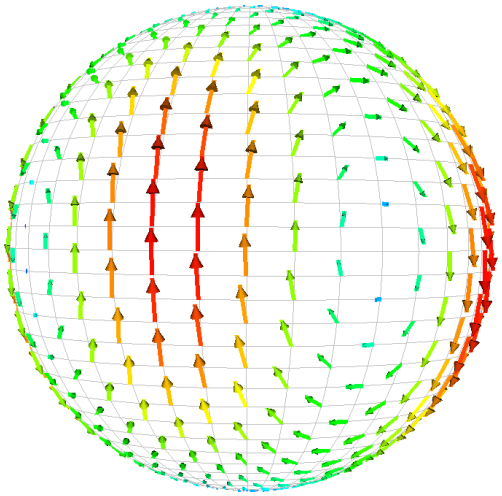

(f) $t = 0.5/\Omega$

Figure 7.2: An illustration of the pattern speed at which the $\ell = m = 2$ r-modes move across spherical surfaces of a star, correct to $\mathcal{O}(\Omega)$ and with rotation about the vertical axis. These are shown for one half of a complete rotation and seem to have angular frequency $2\Omega/3$, agreeing with (7.2.8).

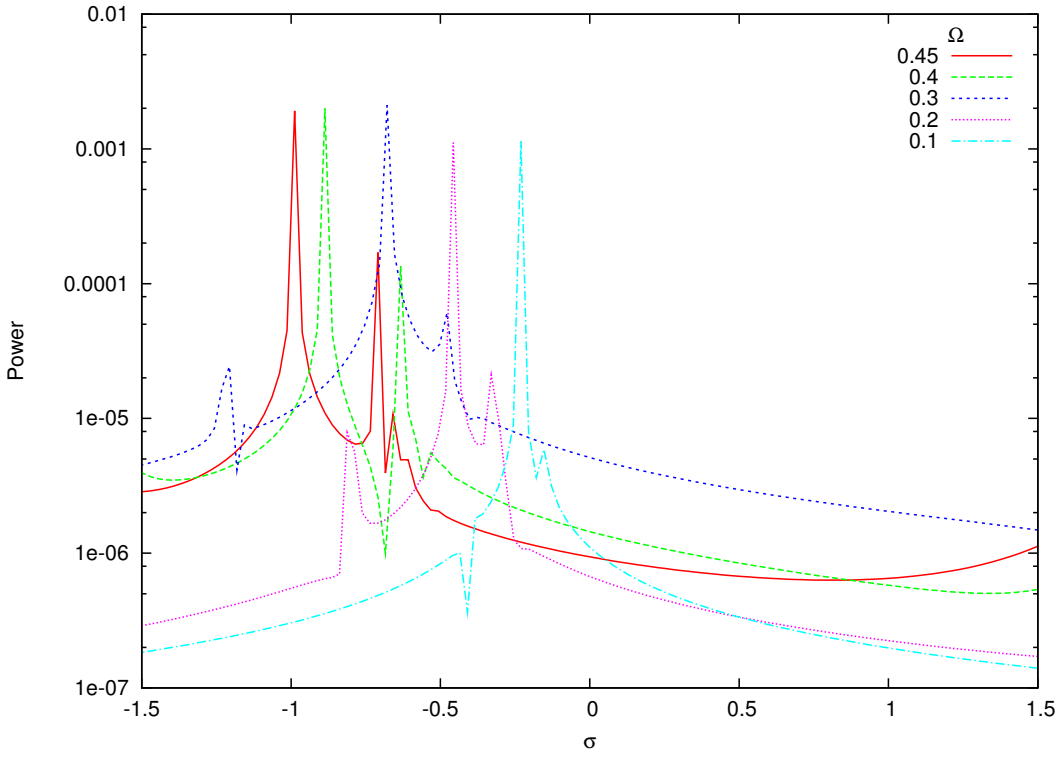

(a) $\ell_m = 3$ frequencies

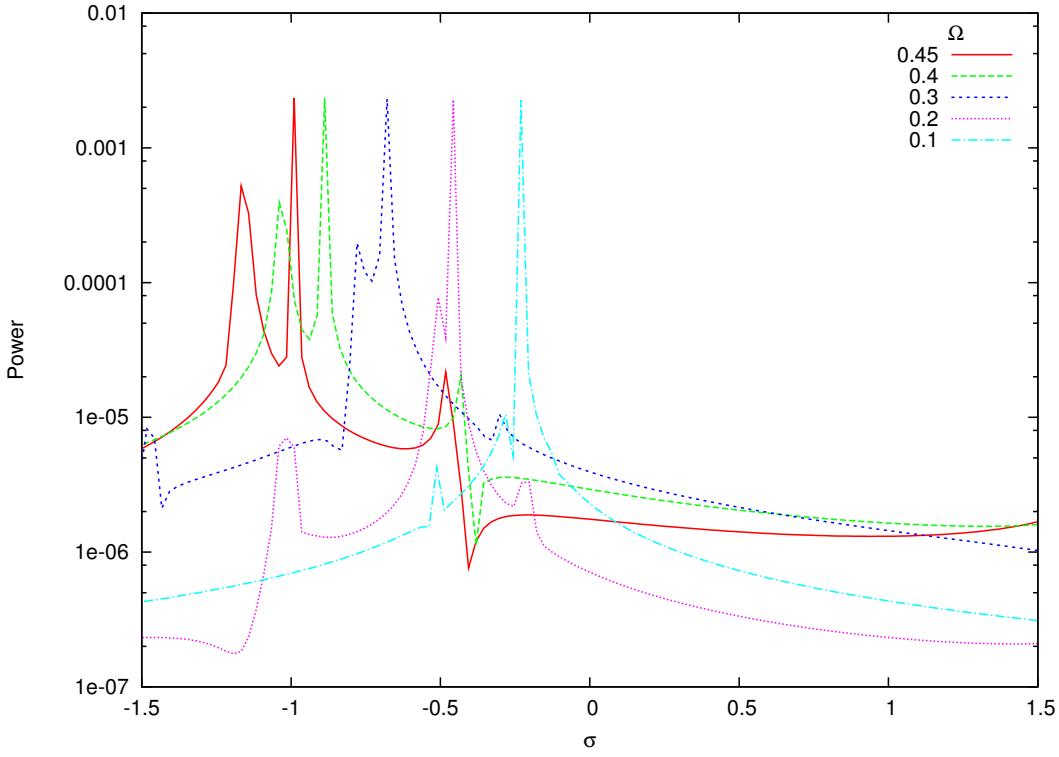

(b) $\ell_m = 4$ frequencies

Figure 7.3: Power spectral density of the $\bar{w}_2^2$ evolution with $\ell_m = 4$ and varying Ω. The highest amplitude peaks correspond to the r-modes and have are of fixed frequency when $\ell_m \geq 3$.

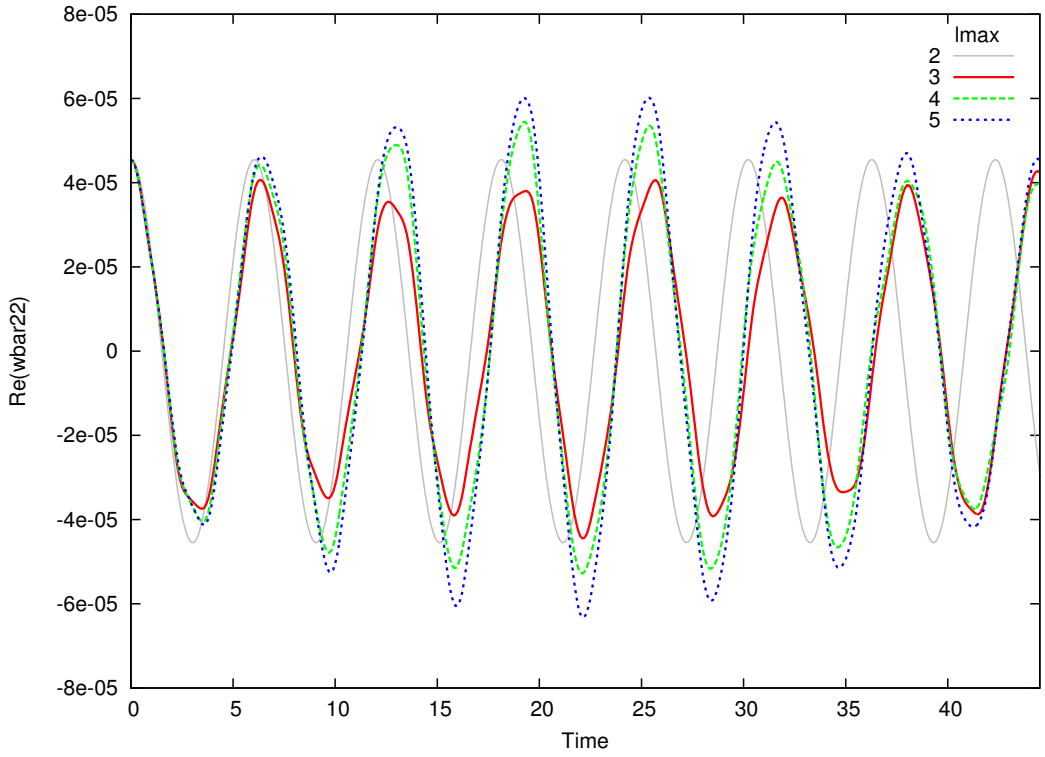

Figure 7.4: The evolution of $\mathrm{Re}(\bar{w}_2^2)$ with increasing ℓ_m. Setting $\ell_m \geq 3$ gives a set of equivalent r-mode frequencies with differing amplitudes.

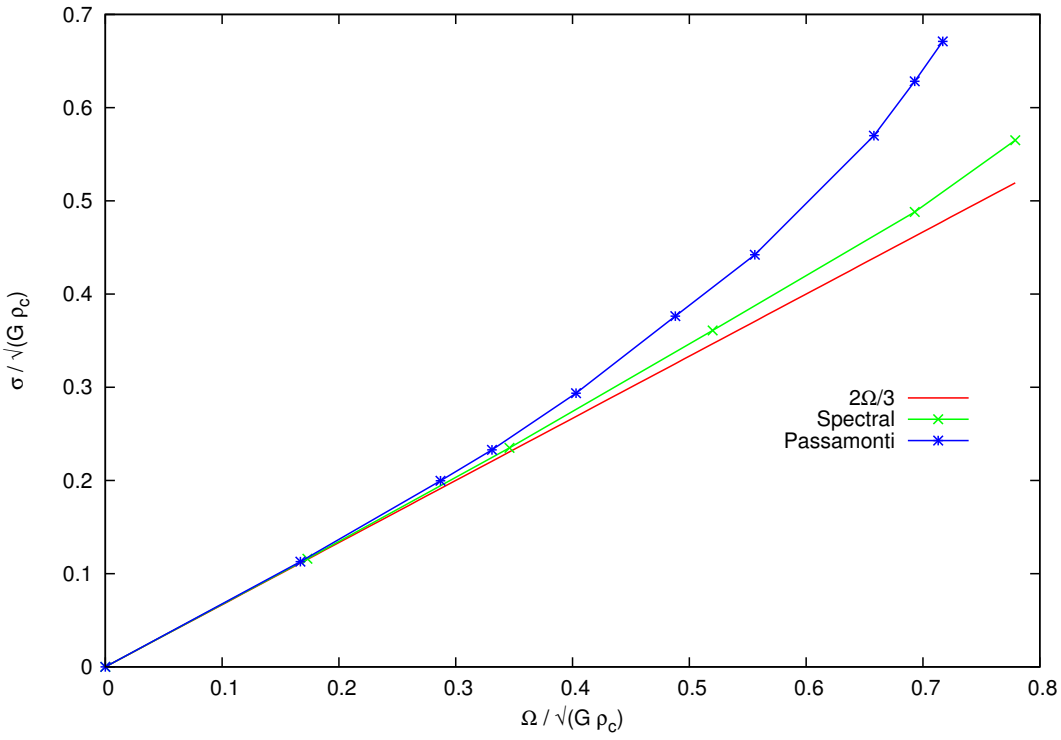

Figure 7.5: The r-mode frequencies of our spectral code with $\ell_m = 4$ against those of Passamonti, figure 3 [70].

7.3 Non-rotating magnetic modes

Although we are unable to investigate the effects of rotation on magnetic stability and modes due to the failure of the friction method to properly relax to equilibrium (section 5.7.4), the modes of a non-rotating ($\bar{w}^0_\ell = 0$) stratified star are still of interest as an approximation to those neutron stars whose rotation is relatively small. This could include, for example, young magnetars whose rotational energy has been mostly deposited into the magnetic field.

7.3.1 Toroidal background

In section 7.2 we re-derived the frequencies of linear-order r-modes . In a similar vein we can naïvely attempt to find the linear order inertial frequencies of stars with a generic equation of state and an $\ell = 1$ toroidal field: such a field can, mathematically at least, satisfy an equilibrium condition.

Consider the couplings with $\bar{w}^0_1 = \Omega/\sqrt{3}, \bar{D}^0_1 = \Delta(r)$, and where we simplify $1/\rho \simeq 1/\bar{\rho}_0$ as the background field is sufficiently weak. Perturbed quantities would evolve as

$$\dot{\bar{w}}_\gamma \simeq im\frac{\ell(\ell+1)-2}{\ell(\ell+1)}\left(\frac{\sqrt{3}\Delta\bar{D}_\gamma}{\mu_0\bar{\rho}_0} - \Omega\bar{w}_\gamma\right) \tag{7.3.1}$$

$$\dot{\bar{D}}_\gamma \simeq im\left(\sqrt{3}\Delta\bar{w}_\gamma - \Omega\bar{D}_\gamma\right). \tag{7.3.2}$$

It is not difficult to find the (lengthy) solutions to this system, which admits frequencies

$$\sigma = m\Omega\frac{(1-\ell-\ell^2)}{\ell(\ell+1)} \pm \sqrt{\frac{\Omega^2}{\ell^2(\ell+1)^2} + 3\frac{\Delta(r)^2}{\mu_0\rho_0(r)}\frac{(\ell-1)(\ell+2)}{\ell(\ell+1)}}. \tag{7.3.3}$$

In the limit of no background magnetic field,

$$\bar{w}_\gamma = w_0(r)e^{i\omega t}, \quad \bar{D}_\gamma = D_0(r)e^{-im\Omega t} \tag{7.3.4}$$

where ω is the r-mode frequency (7.2.2) and w_0, D_0 are some initial data. Note that $\bar{D}_\gamma$ has a vanishing frequency when observed from a co-rotating frame. Without background rotation, one recovers m-independent frequencies proportional to $\Delta/\sqrt{\mu_0\rho_0}$, i.e. Alfvén waves, which are

$$\sigma_2^2 = \sqrt{2}\frac{\Delta}{\sqrt{\mu_0\rho_0}} \tag{7.3.5}$$

for $\ell = m = 2$ perturbations. These frequencies are however r-dependent – there is a *continuum* of modes – unless $\Delta(r) \propto \sqrt{\rho_0(r)}$.

Unfortunately this analysis is invalidated by the reintroduction of the poloidal $\ell + 1$ velocity terms, which we have observed to grow to the same order of magnitude as $\bar{w}_\gamma$ through couplings with Ω. Nevertheless the frequencies of $\bar{w}_\gamma$ will be strongly Δ-dependent

with weak/no rotation, and so we will look at perturbations to the relaxed states of section 6.3.2 to investigate this relationship and how close it may come to our axial-only analysis.

We investigate a constant $\bar{w}_2^2$ perturbation to a non-rotating star with a relaxed Gaussian toroidal $\bar{D}_1^0$ field of the form

$$\Delta = \bar{D}_1^0 = d_1(R^2 - r^2)\left(e^{-(r-c)^2/w^2} + e^{-(r+c)^2/w^2}\right) \tag{7.3.6}$$

where $R = 0.8, c = 0.4, w = 0.1, d_1 = 0.1$. As usual we evolve with the initial time derivative of the unperturbed, relaxed state subtracted at every time step, and then take the Fourier transform over time at varying r.

Despite the non-constant background field, $\bar{w}_2^2(0.3 \leq r \leq 0.5)$ appears to oscillate at a single, fixed frequency that is proportional to Max$(\Delta/\sqrt{\mu_0\rho_0})$, as shown in figure 7.6 for varying background field strength. Only the oscillation amplitude is $\Delta(r)$-dependent. The frequencies of the excited $\bar{\Psi}_3^2$ component are harder to discern as its evolution appears to be damped, and thus it is difficult to ascertain if these $\ell + 1, m$ polar magnetic modes scale linearly with field strength (as per Lander *et al.* [61] figure 3).

$\bar{D}_2^2$ perturbations evolve with almost identical amplitude and frequency to the corresponding $\bar{w}_2^2$. For either class, $\Delta(r)$ or its derivatives does not explicitly appear in the expression for the time derivative, although it is perhaps worth noting they each evolve as

$$\begin{aligned}\dot{\bar{w}}_2^2 &= ... + \alpha\bar{w}_2^2 + \zeta\bar{w}_2^{2\prime},\\ \dot{\bar{D}}_2^2 &= ... + \beta\bar{D}_2^2 + \zeta\bar{D}_2^{2\prime}\end{aligned} \tag{7.3.7}$$

where

$$\alpha \neq \beta, \qquad \zeta = \hat{v}_0 - \frac{1}{7}\sqrt{5}r^2\hat{v}_2^0 - \frac{2}{7}\sqrt{5}r\bar{u}_2^0. \tag{7.3.8}$$

Gaussian $\bar{\Psi}_2^2$ perturbations to this toroidal background oscillate weakly around their initial configurations, and as such the Fourier transform of this variable is dominated by the 0-frequency component (figure 7.7). This is a different result to the findings from non-stratified stars [59], but perhaps a result of the stable stratification. The $m = 2$ components that are excited are $\bar{w}_{2n-1}^2, \bar{\Psi}_{2n}^2$. Higher m components are those with $P_{2n\geq m}^m, \bar{D}_{2n+1\geq m}^m$ for even $m/2$ and $\bar{w}_{2n-1\geq m}^m, \bar{\Psi}_{2n\geq m}^m$ for odd $m/2$ (P represents polar fluid terms $\bar{\rho}, \hat{v}, \bar{u}, f$), i.e. poloidal-toroidal fluid-field components, and vice-versa, in alternating m.

When a toroidal field is perturbed by $\bar{\rho}_2^2$, magnetic and f-modes can be observed in the DFT of the $\bar{D}_3^2$ component, (figure 7.8). The double-spikes give a somewhat large error, but it appears that the lowest frequency magnetic modes oscillate at approximately $5\,\sigma_A$. We have not evolved for sufficient time steps to determine the shift in f-mode frequency with increasing field strength; Lander *et al.* [61] suggest any shift would be less than 1% for our field strengths.

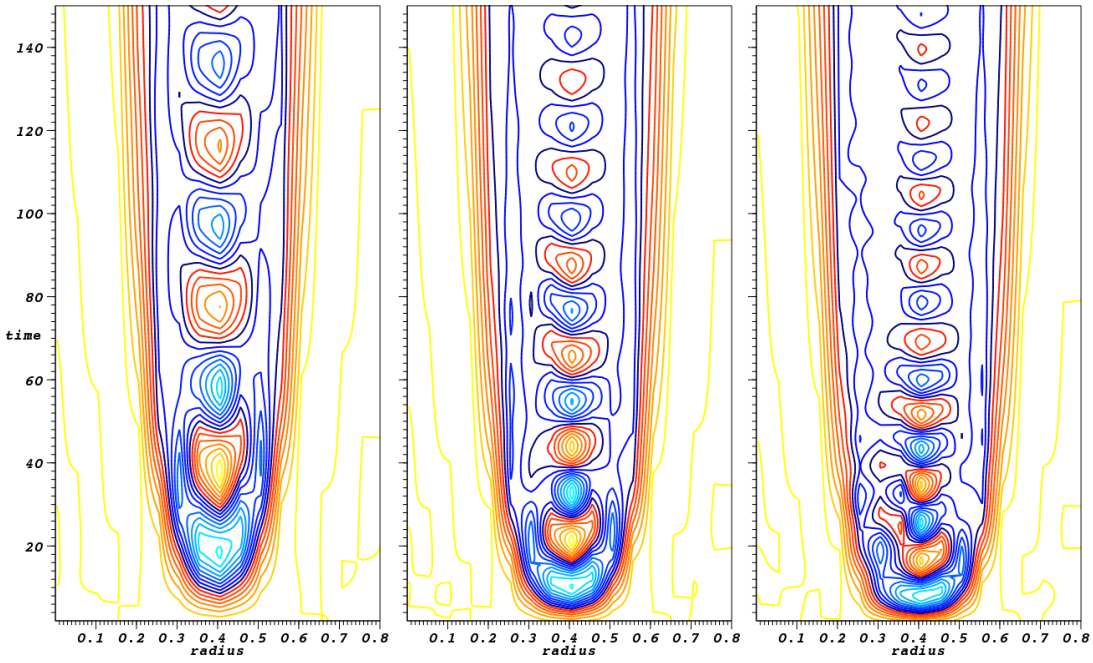

(a) $\bar{w}_2^2,\ d_1 = 0.1$ (b) $\bar{w}_2^2,\ d_1 = 0.2$ (c) $\bar{w}_2^2,\ d_1 = 0.3$

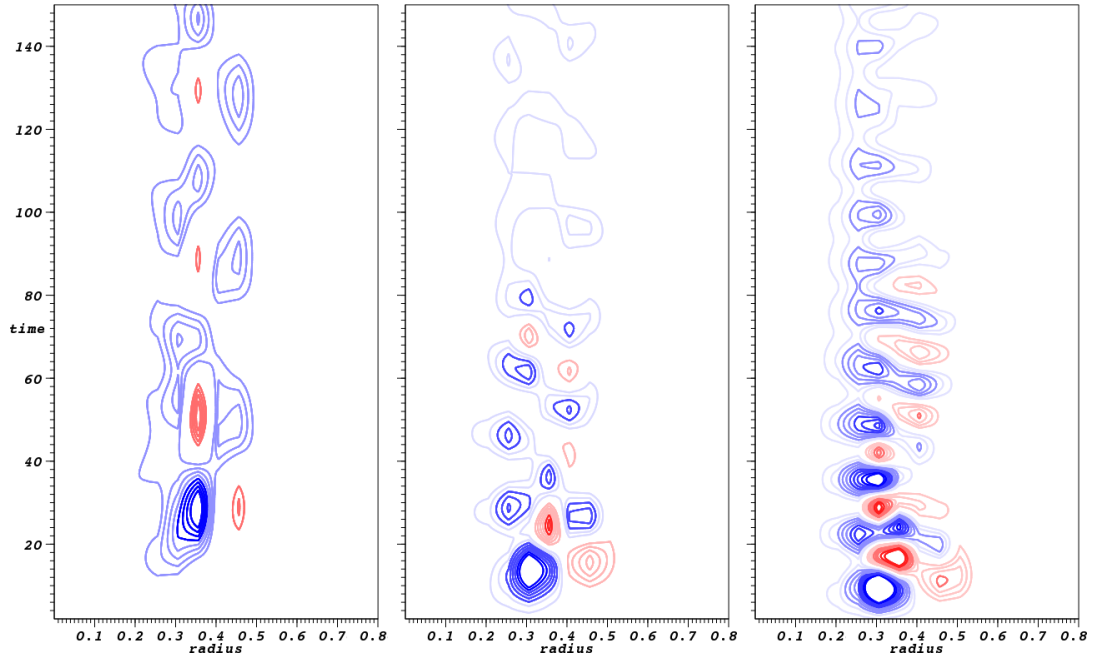

(d) $\bar{\Psi}_3^2,\ d_1 = 0.1$ (e) $\bar{\Psi}_3^2,\ d_1 = 0.2$ (f) $\bar{\Psi}_3^2,\ d_1 = 0.3$

Figure 7.6: $\bar{w}_2^2$ oscillations (top) on Gaussian $\bar{D}_1^0$ backgrounds with amplitude between $\sim 10^{-4}$ (yellow contours) and -10^{-4} (light blue). The normal frequencies of the central oscillations are approximately $\pm\frac{1}{2}D_1(0.4)/\sqrt{\rho_0(0.4)}$, i.e. around half the Alfvén frequency. The excited $\bar{\Psi}_3^2$ components are also shown (bottom, $\mathcal{O}(10^{-6})$ non-constant colour scaling) although these oscillations appear to be damped.

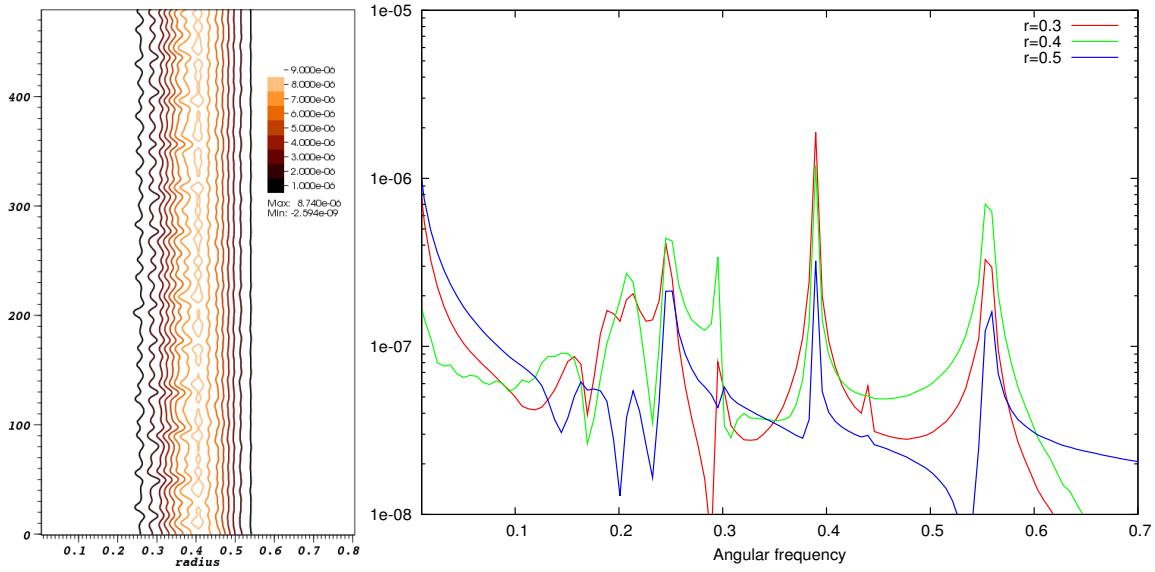

(a) The evolution of a $\bar{\Psi}_2^2$ perturbation (left) and its Fourier transform at varying r (right).

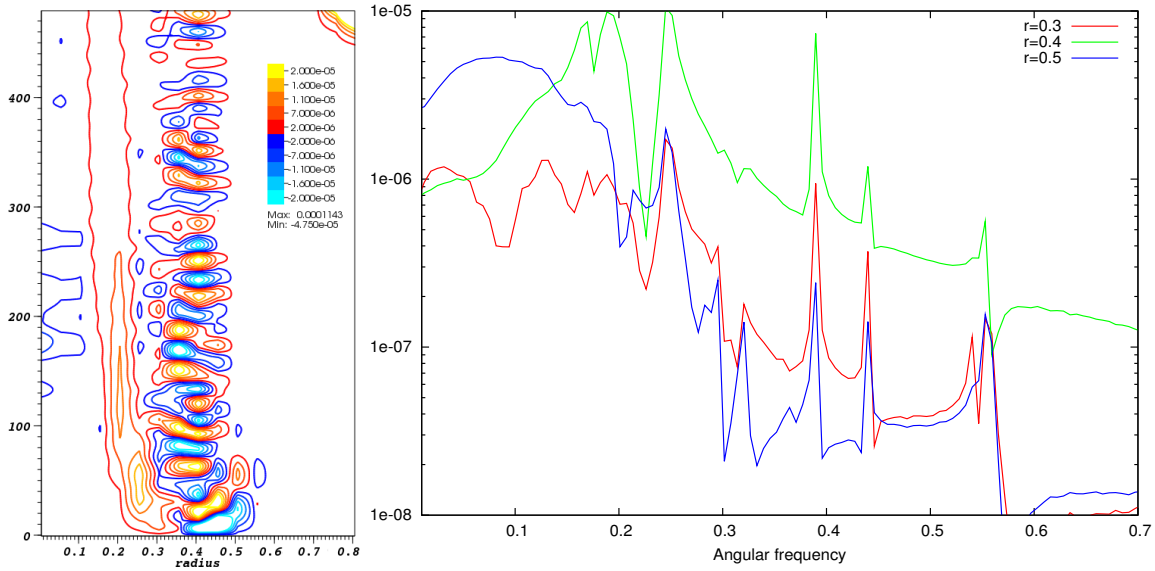

(b) The corresponding excited $\bar{w}_3^2$ evolution (left) and its Fourier transform at varying r (right)

Figure 7.7: A $\bar{\Psi}_2^2$ perturbation to a Gaussian $\bar{D}_1^0$ background oscillates weakly around its original configuration (top). The DFT of the excited $\bar{w}_3^2$ component has several shared frequency peaks.

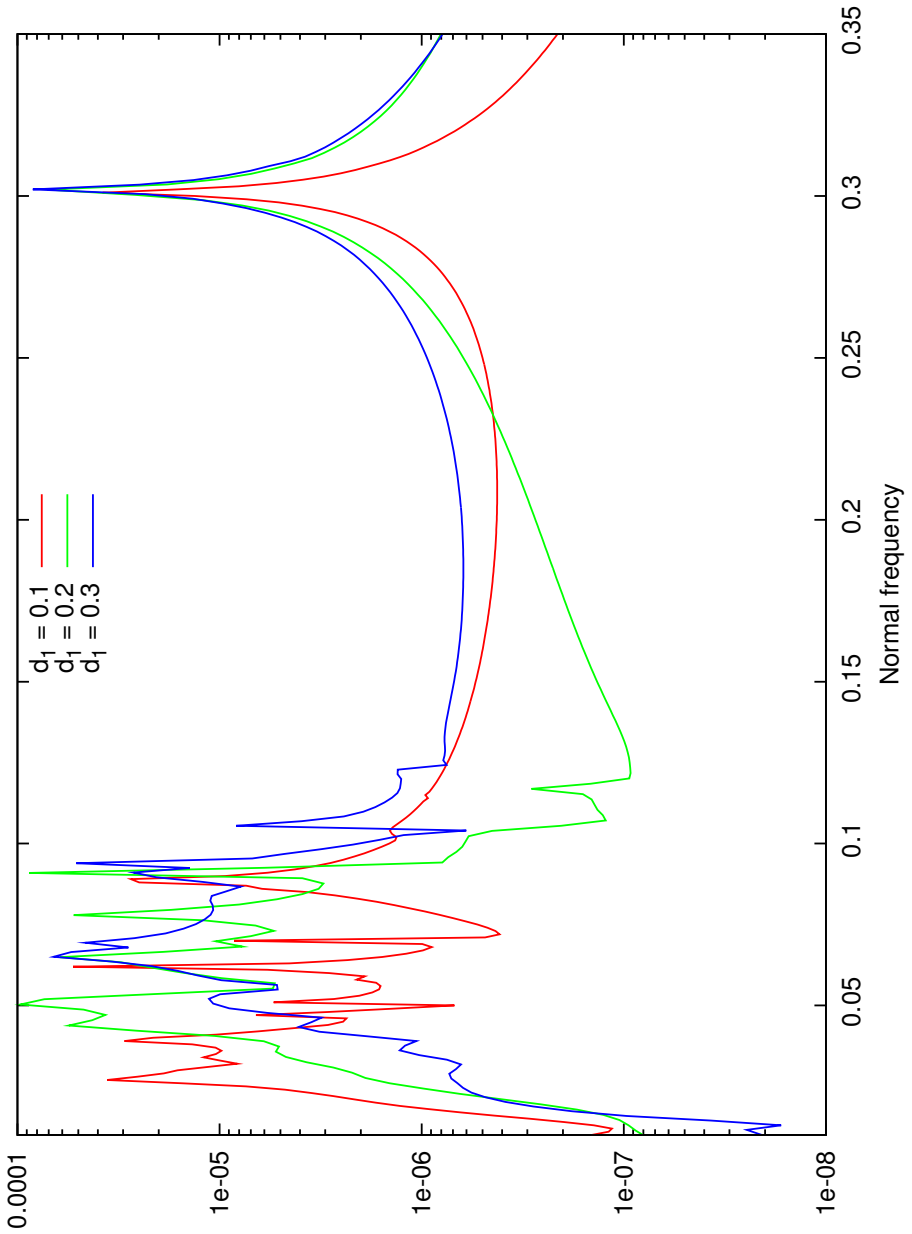

Figure 7.8: $\bar{\rho}_2^2$ perturbations on a toroidal background excite a $\bar{D}_3^2$ component, whose DFT is shown here for varying field strength. An f-mode at $\sigma = 0.3$ is visible, as are magnetic modes with $\sigma < 0.1$. There appear to be several low frequency peaks that are dependent on the background field.

7.3.2 Poloidal and mixed backgrounds

As previously observed, (non-rotating) poloidal backgrounds can be wound up into mixed fields with a strong nonaxisymmetric component by a certain class of w, D perturbations. Stable, quadrupole-led D perturbations oscillate at a fixed frequency proportional to Ψ_1^0 as illustrated in figure 7.9. It thus appears that D perturbations on both toroidal and poloidal backgrounds oscillate at approximately half the Alfvén frequency.

Interestingly, on mixed-field backgrounds a $\bar{D}_2^2$ perturbation will excite a $\bar{\Psi}_2^2$ component to oscillate at the same frequency, which is approximately three times the Alfvén frequency (figure 7.10). We studied a small range of varying poloidal and toroidal background field strengths and found the same ratio, but more simulations are necessary to determine the full picture, particularly the transition to purely toroidal/poloidal backgrounds.

Other evolutions that would be worth investigating include studying the frequency of $\bar{w}_2^2$ perturbations on backgrounds that tend towards being purely-poloidal, increasing the perturbation ℓ, m mode, and a comprehensive survey of how low frequency magnetic modes may vary over such backgrounds.

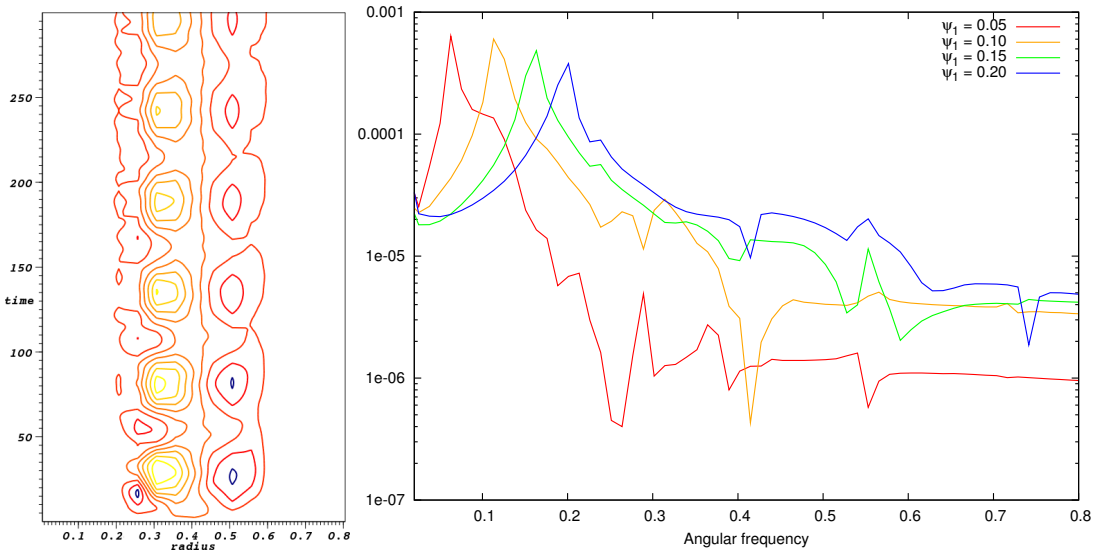

Figure 7.9: A $\bar{D}_2^2$ perturbation on a $\psi_1 = 0.01$ background (left) and Fourier transforms (right) for varying background poloidal field strength. The DFT is taken over $0 \leq t \leq 500$ at $r = 0.3$, near to where the oscillations are largest in amplitude: the highest-amplitude oscillations are proportional to the background field strength and oscillate at approximately half the Alfvén frequency.

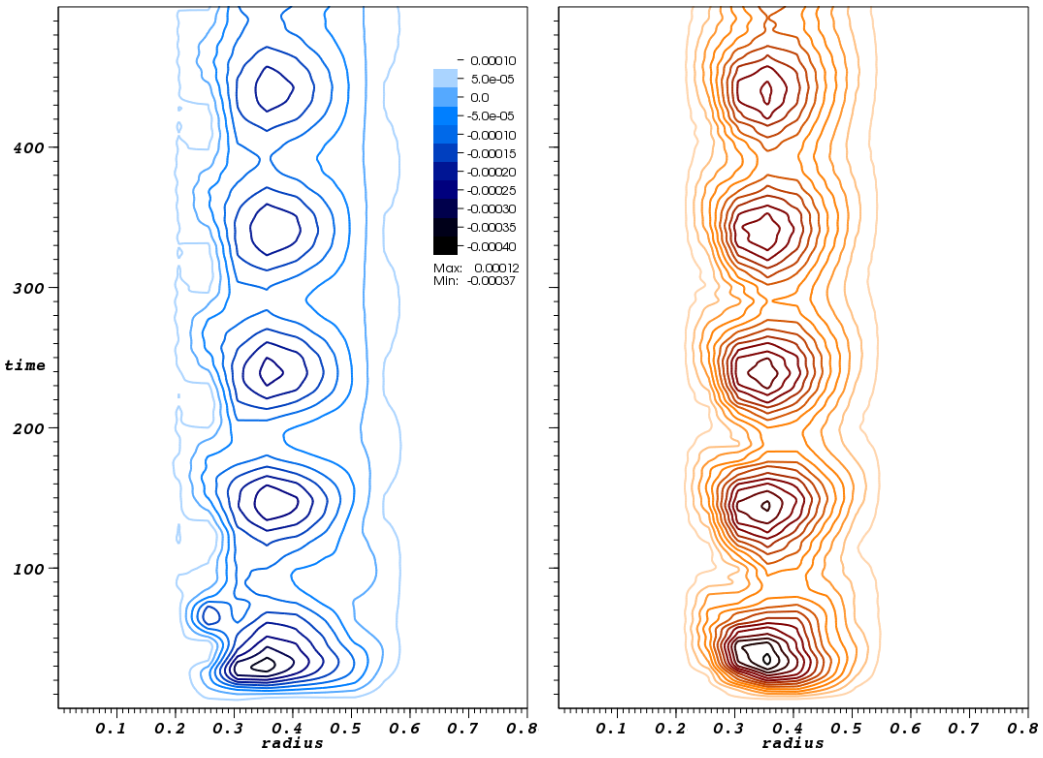

(a) $\bar{D}_2^2$ (b) $\bar{\Psi}_2^2$

Figure 7.10: $\bar{D}_2^2$ perturbations on mixed field backgrounds excite a $\bar{\Psi}_2^2$ component, and both oscillate at approximately three times the Alfvén frequency.

Conclusions

We have demonstrated a hybrid spectral approach to nonlinear MHD, using coordinates in the radial direction and convolution for angles. Although this hybrid technique is not new [22, 40, 56] we have been the first to apply it to the general problem of finding (and investigating the stability of) nonlinear rotating and/or magnetic equilibria of Newtonian neutron stars, and consider it to be fast and flexible, despite several (hopefully solvable) problems.

One of its biggest drawbacks is that the outer boundary is handled by a crude spherical cut-off, implemented for both technical limitations and to avoid singularities; other techniques [59] fully implement a boundary for situations that a typical desktop machine has sufficient computational power to handle in reasonable time. It is also much harder (if not sometimes impossible) to adapt existing analytical and numerical methods [80, 90] into our framework.

On the other hand, various linear and nonlinear problems can be configured with ease and, in the case of high radial resolution and low angular resolution, executed with incredible speed. The same could potentially be said for situations involving very high ℓ, m if one could justify discarding *distant* modes to these. The convolution technique lets us study the behaviour of individual modes, and leads us to a system apparently excellently suited for multi-core parallelization.

In order to overcome an instability observed at the origin for the wave equation – other authors do not report seeing such a phenomenon, or instead evolve in a shell, or use spectral methods in radius – we have found a simple technical solution for second-order systems; work on gaining higher-order accuracy is ongoing [47]. By re-casting the Euler equation in new variables to make it more wave-like, we prevent the same instability from occurring.

We have also recast the MHD equations using a vector potential so that the divergence-free constraint of magnetic fields is inherent. The vector Laplacian of the magnetic field is greatly simplified by this and leaves the door open for future studies of non-ideal MHD. Exterior poloidal fields, embedded in vacuum, can also be handled as they reduce to simple ℓ-dependent functions of radius with matching conditions on the boundary. The extra derivative that using a vector potential introduces does not seem to cause any issues.

The method scales very well for linear problems ($\mathcal{O}(N_R\ \ell_m)$) and accurate rotating equilibria were found for non-stratified, non-magnetic stars, using a novel relaxation technique

with very low radial and angular resolution. These equilibria are found without approximations made to the gravitational potential, as the convolution technique reduces Poisson's equation to a (relatively) easily solved linear equation.

Our investigations into nonlinear axisymmetric problems ($\mathcal{O}(N_R \ell_m^3)$), involving magnetization, stratification and rotation, met with varying success. We found that non-stratified magnetized stars could not be stabilized with the relaxation technique, perhaps indicating that such equilibria are impossible [74]. We were unable to stabilize stratified, rotating stars (magnetized or not), although we do not know if this is due to an inherent instability mechanism, somehow related to the boundary conditions, or indeed a problem caused by the spherical boundary. We attempted to relax a system with a different stratification (i.e. trying some $D\mathcal{K}/Dt \neq 0$) and found that, although we can not justify any of these choices, the relaxation appeared to work.

We were able to stabilize stratified, non-rotating, magnetized stars given arbitrary initial data [18] and by perturbing in nonlinear, nonaxisymmetric modes ($\mathcal{O}(N_R \ell_m^5)$) we could roughly investigate their stability characteristics and oscillation frequencies. By only evolving the necessary harmonic modes, and using the exponential convergence properties of the spectral method, these problems can be made to scale much better than $\mathcal{O}(\ell_m^5)$, although the time evolution of some magnetic configurations can still take several hours to run.

We looked at (and compared with existing results) the r-modes of rotating, non-stratified, non-magnetized stars and found some difference due to the outer boundary, although the spectral method does often mean these mode frequencies can be calculated by hand. As already mentioned we are currently unable to go any further with regards to investigating stratified rotating configurations, unless we attempt to modify our pressure law or boundary conditions.

We found that certain purely poloidal/toroidal fields are linearly unstable, only becoming stable when mixed with sufficiently strong counterpart fields with the amount of mixing in broad agreement with results [88]. We observed that $\ell = 1, m = 0$ toroidal fields were only unstable to toroidal perturbations with $m = 1$, as expected [60], and stable for $m > 1$. Various $\ell = 1, m = 0$ poloidal fields were unstable to dipolar toroidal perturbations, yet stable to all of the poloidal perturbations we tested. The stability of pure fields to certain perturbation modes is somewhat surprising and do not appear to be predicted [87, 89].

Appendix A

Spherical Harmonics

A.1 Table of Scalar and Vector Spherical Harmonics

As per the definition (2.1.15) we do not work with orthonormal spherical harmonics. The first few values of $Y_\ell^m(\theta,\varphi)$ are

$$
\begin{aligned}
&Y_0^0 = 1, \\
&Y_1^0 = \sqrt{3}\cos\theta, && Y_1^1 = -\sqrt{\frac{3}{2}}e^{i\varphi}\sin\theta, \\
&Y_2^0 = \frac{1}{2}\sqrt{5}(3\cos^2\theta - 1), && Y_2^2 = -\frac{1}{2}\sqrt{\frac{15}{2}}e^{2i\varphi}(\cos^2\theta - 1), \\
&Y_3^0 = \frac{1}{2}\sqrt{7}\left(5\cos^3\theta - 3\cos\theta\right), && Y_3^3 = -\frac{1}{4}\sqrt{35}\sin^3\theta e^{3i\varphi}.
\end{aligned}
$$

The vector harmonics are given by definitions (2.4.2). We typically work with the contravariant forms; on a 2-sphere in a (θ,φ) direction (ignoring the radial components) the first few of these are

$$
\begin{aligned}
&(Z_\ell^m)^a = \left(\partial_\theta Y_\ell^m, \frac{1}{\sin^2\theta}\partial_\varphi Y_\ell^m\right), \\
&Z_1^0 = (-\sqrt{3}\sin\theta, 0), && Z_1^1 = \left(-\sqrt{\frac{3}{2}}e^{i\varphi}\cos\theta, -i\sqrt{\frac{3}{2}}e^{i\varphi}\csc\theta\right), \\
&Z_2^0 = (-3\sqrt{5}\sin\theta\cos\theta, 0), \\
&Z_3^0 = \left(\frac{3\sqrt{7}}{2}\sin\theta\left[1 - 5\cos^2\theta\right], 0\right).
\end{aligned}
$$

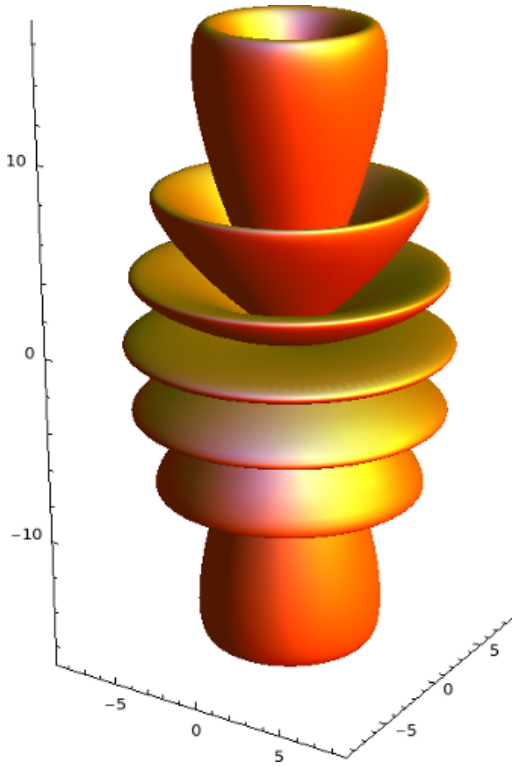

Figure A.1: The θ-component of Z^0_7.

and

$$(S^m_\ell)^a = \left(\frac{1}{\sin\theta}\partial_\varphi Y^m_\ell, \frac{-1}{\sin\theta}\,\partial_\theta Y^m_\ell\right),$$

$$S^0_1 = (0, \sqrt{3}), \qquad S^1_1 = \left(-i\sqrt{\frac{3}{2}}e^{i\varphi}, \sqrt{\frac{3}{2}}\cot\theta\right),$$

$$S^0_2 = (0, 3\sqrt{5}\cos\theta),$$

$$S^0_3 = \left(0, -\frac{3\sqrt{7}}{2}\left[1 - 5\cos^2\theta\right]\right).$$

In axisymmetry, noting that $S^\varphi = \frac{-1}{\sin\theta}Z^\theta$ is useful for plotting in 3D.

Appendix B

Code snippets

B.1 Fortran $\hat{C}_{\alpha\beta-\gamma}$ calculator

This Fortran code calculates the Gaunt coefficient $\hat{C}_{\alpha\beta-\gamma}$ by finding Wigner $3j$ coefficients (2.2.10). One needs to write a `factrl` function to calculate factorials.

```
FUNCTION wigner3j(l1,l2,l3,m1,m2,m3)
  IMPLICIT NONE
  REAL*8 :: wigner3j
  INTEGER,INTENT(IN) :: l1,l2,l3,m1,m2,m3
  REAL*8 :: ssum,tsum
  LOGICAL :: found_t
  INTEGER :: numsum,j,t,t1,t2,t3,t4,t5,check
  IF(m1==0 .AND. m2==0 .AND. m3==0) RETURN wigner3jzero(l1,l2,l3)
  !Triangle co-efficient
  wigner3j = ((-1.d0)**(l1-l2-m3)) * SQRT( factrl(l1+l2-l3)&
    *factrl(l1-l2+l3)*factrl(-l1+l2+l3)/factrl(l1+l2+l3+1) )
  wigner3j = wigner3j * SQRT(factrl(l1+m1)*factrl(l1-m1)*factrl(l2+m2)&
     *factrl(l2-m2)*factrl(l3+m3)*factrl(l3-m3))
  !There are "numsum" terms in the sum, given by the smallest of:
  numsum = MIN(l1+m1,l1-m1,l2+m2,l2-m2,l3+m3,l3-m3,l1+l2-l3,l1-l2+l3,&
     -l1+l2+l3) + 1
  !Need to find allowable t that we can sum over; numsum of these.
  t1 = m1 + l3 - l2
  t2 = l3 - l1 - m2
  t3 = l1 + l2 - l3
  t4 = l1 - m1
  t5 = l2 + m2
  tsum = 0
  t = -1
  !Loop over permissible t
  DO j = 1,numsum
    t = t + 1
    found_t = .FALSE.
    check = 0
```

```
    DO WHILE(found_t .EQV. .FALSE.)
      IF(t+t1 < 0 .OR. t+t2 < 0 .OR. t3-t < 0 .or. t4-t < 0 .OR. t5-t < 0) THEN
        t = t+1
      ELSE
        found_t = .TRUE.
      END IF
      check = check+1
      IF(check>1000) STOP 'ERROR Cannot find t'
    END DO
    ssum = factrl(t) * factrl(t+t1) * factrl(t+t2) * factrl(t3-t)&
      * factrl(t4-t) * factrl(t5-t)
    IF(ssum==0) STOP 'ERROR Found ssum = 0'
    tsum = tsum + ((-1.d0)**t)/ssum
  END DO
  !Return the answer
  wigner3j = wigner3j * tsum
  RETURN
END FUNCTION


FUNCTION wigner3jzero(l1,l2,l3)
  IMPLICIT NONE
  REAL*8 :: wigner3jzero
  INTEGER,INTENT(IN) :: l1,l2,l3
  INTEGER :: l,k
  wigner3jzero = 0
  l = l1+l2+l3
  k = l/2
  IF(MOD(l,2) == 0) then
    wigner3jzero = ((-1.d0)**k) * SQRT( factrl(l-(2*l1))*factrl(l-(2*l2))&
      *factrl(l-(2*l3))/factrl(l+1) )
    wigner3jzero = wigner3jzero * factrl(k) / ( factrl(k-l1)*factrl(k-l2)&
      *factrl(k-l3) )
  END IF
  RETURN
END FUNCTION wigner3jzero


FUNCTION chat(l1,l2,l3,m1,m2,m3)
  IMPLICIT NONE
  REAL*8 :: chat
  INTENGER,INTENT(IN) :: l1,l2,l3,m1,m2,m3
  IF(MOD(l1+l2+l3,2) /= 0 .OR. (m1+m2+m3) /= 0) THEN
    chat = 0.d0
  ELSE
    chat =  4.d0*pi*SQRT(DBLE( (2*l1+1)*(2*l2+1)*(2*l3+1) ))&
      *wigner3j(l1,l2,l3,m1,m2,m3)&
      *wigner3jzero(l1,l2,l3)
  END IF
  RETURN
END FUNCTION
```

B.2 Fortran $\hat{G}_{\alpha\beta\gamma}$ calculator

This function returns the non-axisymmetric integral $\hat{G}_{\alpha\beta\gamma}$ using the method described in section 2.4.4. The function `chat(x,y,z)` returns $\hat{C}_{x,y,z}$.

```
RECURSIVE FUNCTION g_hat(l1,m1,l2,m2,l3,m3)
  IMPLICIT NONE
  DOUBLE COMPLEX :: g_hat
  INTEGER,INTENT(IN) :: l1,m1,l2,m2,l3,m3
  DOUBLE COMPLEX,PARAMETER :: ii = (0.d0,1.d0)
  INTEGER :: l0,zeta,oneone
  REAL*8 :: coef_a,c_hat_one
  g_hat = 0.d0
  IF((l2 == l3 .AND. m2 == m3) .OR. (l1 == 0) .OR. (l2 == 0) .OR. (l3 == 0)&
  .OR. (m2 == 0 .AND. m3 == 0)) THEN
    RETURN !Axisymmetric integral
  ELSE IF(m1 .LE. 0 .AND. m2 .LE. 0 .AND. m3 .LE. 0) THEN
    STOP 'ERROR All m are negative'
  ELSE IF(m1 .GE. m2 .AND. m1 .GE. m3) THEN
    oneone = multiindex(1,1) !ell=m=1 <=> zeta=3
    c_hat_one = c_hat(oneone,multiindex(l1-1,m1-1),multiindex(l1,-m1))
    IF(c_hat_one == 0.d0) STOP 'ERROR c_hat = 0'
    coef_a = 4.d0*pi/((-1.d0)**m1*c_hat_one)
    !Jump down through non-zero c_hat's
    DO l0 = l1-1,0,-2
      zeta = multiindex(l0,m1-1)
      IF(m2+1 .LE. l2) g_hat = g_hat + coef_a*m3*SQRT(DBLE((l2-m2)*(l2+m2+1)))&
        *c_hat(zeta,multiindex(l2,m2+1),multiindex(l3,m3))
      IF(m3+1 .LE. l3) g_hat = g_hat - coef_a*m2*SQRT(DBLE((l3-m3)*(l3+m3+1)))&
        *c_hat(zeta,multiindex(l2,m2),multiindex(l3,m3+1))
      IF(l0-2 .GE. m1-1) THEN
        coef_a = -coef_a*c_hat(oneone,zeta,multiindex(l0-1,-m1))&
          /c_hat(oneone,multiindex(l0-2,m1-1),multiindex(l0-1,-m1))
      ELSE
        coef_a = 0.d0
      END IF
    END DO
    !Rescale Y11
    g_hat = -ii*g_hat*SQRT(3.d0/2.d0)
  ELSE IF(m2 .GE. m1 .AND. m2 .GE. m3) THEN
    !Sort the m's
    g_hat = -g_hat(l2,m2,l1,m1,l3,m3)
  ELSE IF(m3 .GE. m1 .AND. m3 .GE. m2) THEN
    !Sort the m's
    g_hat = -g_hat(l3,m3,l2,m2,l1,m1)
  ELSE
    STOP 'ERROR Unexpected loop'
  END IF
  RETURN
END FUNCTION
```

B.3 Fortran/Silo integration

Our three dimensional plots were made by writing data to the Silo format [1] and visualizing in VisIt [2]. The following code shows how one may write a single precision scalar field to a $10 \times 10 \times 10$ 3D mesh, although it is also possible to save vector and tensor information. The code should be compiled using the `-lsilo` compiler flag, which requires the file `silo.inc` to be in the library path.

```
PROGRAM silowriter
  IMPLICIT NONE
  INCLUDE 'SILO.INC'
  INTEGER :: err,nx,ny,nz,dims(3),ndims,silofile,i,j
  PARAMETER (nx = 10)
  PARAMETER (ny = 10)
  PARAMETER (nz = 10)
  REAL*4 :: x(nx),y(ny),z(nz), sp_var(nx,ny,nz) !We write single precision to disk
  REAL*8 :: dp_var(nx,ny,nz)
  DATA dims/nx,ny,nz/
  ndims = 3
  !Set the mesh somehow
  set_mesh(x,nx,y,ny,z,nz)
  !Set the data somehow
  set_data(dp_var,nx,ny,nz)
  !Then convert to single precision
  sp_var = REAL(dp_var)
  !Now create the Silo file
  err = DBCREATE('out.silo',8,DB_CLOBBER,DB_LOCAL,DB_F77NULL,0,DB_PDB,silofile)
  IF(err /= 0) STOP 'ERROR Could not create file'
  err = DBPUTQM(silofile,"quadmesh",9,"x",1,"y",1,"z",1,x,y,z,dims,ndims,DB_FLOAT,&
    DB_COLLINEAR,DB_F77NULL,ierr)
  IF(err /= 0) STOP 'ERROR Could not write mesh'
  err = DBPUTQV1(silofile,"var",3,"quadmesh",8,sp_var,dims,ndims,DB_F77NULL,0,DB_FLOAT,&
    DB_NODECENT,DB_F77NULL,ierr)
  IF(err /= 0) STOP 'ERROR Could not write sp_var'
  err = DBCLOSE(silofile)
END PROGRAM
```

[1] Available from http://wci.llnl.gov/codes/silo
[2] Available from http://visit.llnl.gov

B.4 Mathematica Lane-Emden solver

This *Mathematica* script calculates numerical solutions to the Lane-Emden equation with index n (5.1.20). The quantity `start` defines how close to zero the solver begins (typically the value of h) as the numerical integrator cannot handle the removable singularity at the origin. `stop` defines the maximum value of ζ to integrate out to (typically $2\ell + 3$). It starts by series expanding θ and finding the coefficients near the origin, then inserts back into the ODE which it then numerically integrates.

```
LESolver[n_, start_, stop_] := Module[
   {degree = 6, expansion, series, unknowns, expression, coefflist, coeffsolve},
   series = 1 + Sum[Subscript[a, i] \[Zeta]^i, {i, 2, degree, 2}] + O[\[Zeta]]^(degree + 1);
   unknowns = Table[Subscript[a, i], {i, 2, degree, 2}];
   expression = Expand[(1/\[Zeta]^2 D[\[Zeta]^2 D[\[Theta][\[Zeta]], \[Zeta]], \
      \[Zeta]] + \[Theta][\[Zeta]]^n) /. {
      \[Theta][\[Zeta]] -> series,
      \[Theta]'[\[Zeta]] -> D[series, \[Zeta]],
      \[Theta]''[\[Zeta]] ->  D[series, \[Zeta], \[Zeta]]
      }];
   coefflist = CoefficientList[Normal[expression], \[Zeta]];
   coeffsolve = Solve[Thread[coefflist == 0], unknowns] // First;
   expansion = {Normal[series], D[Normal[series], \[Zeta]]} /.
     coeffsolve /. \[Zeta] -> start;
   Return[\[Theta][\[Zeta]] /. NDSolve[{
         SetPrecision[
            1/\[Zeta]^2 D[\[Zeta]^2 D[\[Theta][\[Zeta]], \[Zeta]], \[Zeta]] \
            + \[Theta][\[Zeta]]^n == 0,
         24],
         \[Theta][start] == expansion[[1]],
         \[Theta]'[start] == expansion[[2]]
      },
      \[Theta][\[Zeta]],
      {\[Zeta], start, stop},
      AccuracyGoal -> 24, PrecisionGoal -> 12
      ] // First
   ];
 ]
```

References

[1] S. Akiyama et al. The magnetorotational instability in core-collapse supernova explosions. *Ap. J.*, 584:954–970, 2003.

[2] A.S. Aladl, A. Deakin and H. Rasmussen. Nonreflecting boundary condition for the wave equation. *Journal of Computational and Applied Mathematics*, 138:309–323, 2002.

[3] M. Anderson et al. Relativistic MHD with adaptive mesh refinement. *C.Q.G.*, 23:6503–6524, 2006.

[4] N. Andersson. A new class of unstable modes of rotating relativistic stars. *Ap. J.*, 502:708–713, 1998.

[5] N. Andersson and K. Kokkotas. The r-mode instability in rotating neutron stars. *International Journal of Modern Physics D*, 10:381–441, 2000.

[6] W. Baade and F. Zwicky. Remarks on super-novae and cosmic rays. *Phys. Rev.*, 46:76–77, 1934.

[7] S.A. Balbus and J.F. Hawley. A powerful local shear instability in weakly magnetized disks. *Ap. J.*, 376:214–233, 1991.

[8] S.A. Balbus and J.F. Hawley. Instability, turbulence, and enhanced transport in accretion disks. *Rev. Mod. Phys.*, 70:1–53, 1998.

[9] T.W. Baumgarte, S.L. Shapiro, and M. Shibata. On the maximum mass of differentially rotating neutron stars. *Ap. J. Lett.*, 528:L29, 2000.

[10] A. Bayliss and E. Turkel. Radiation boundary conditions for wave-like equations. *Communications on Pure and Applied Mathematics*, 33:707–725, 1980.

[11] S.J. Bell and A. Hewish. Angular size and flux density of the small source in the Crab Nebula at 81.5 Mc/s. *Nature*, 213:1214–1216, 1967.

[12] G. Bertomieu, J. Provost, and J. Rocca. Low frequency oscillations of a slowly rotating star: quasi-toroidal modes. *Astron. Astrophys.*, 94:126–133, 1981.

[13] R.D. Blandford and K.S. Thorne. Applications of classical physics. http://www.pma.caltech.edu/Courses/ph136, 2004.

[14] J.M. Blondin et al. Stability of standing accretion shocks, with an eye toward corecollapse supernovae. *Ap. J.*, 584:971–980, 2003.

[15] S. Bonazzola and L. Villain. Inertial modes in slowly rotating stars: An evolutionary description. *Phys. Rev. D*, 66:123001, 2002.

[16] J. Braithwaite. The stability of poloidal magnetic elds in rotating stars. *Astron. Astrophys.*, 469:275–284, 2007.

[17] J. Braithwaite. Axisymmetric magnetic fields in stars: relative strengths of poloidal and toroidal components. *Mon. Not. R. Astron. Soc.*, 397:763–774, 2009.

[18] J. Braithwaite and Å. Nordlund. Stable magnetic fields in stellar interiors. *Astron. Astrophys.*, 450:1077–1095, 2005.

[19] J. Braithwaite and H.C. Spruit. Evolution of the magnetic field in magnetars. *Astron. Astrophys.*, 450:1097–1106, 2006.

[20] D. Brizuela, J.M. Martín-García, and G.A. Mena Marugán. Second and higher-order perturbations of a spherical spacetime. *Phys. Rev. D*, 74:044039, 2006.

[21] A.S. Brun. On the interaction between differential rotation and magnetic fields in the sun. *Solar Phys.*, 220:333–345, 2003.

[22] E. Bullard and H. Gellman. Homogeneous dynamos and terrestrial magnetism. *Phil. Trans. R. Soc.*, 247:213–278, 1954.

[23] G. Calabrese and C. Gundlach. Discrete boundary treatment for the shifted wave equation. *C.Q.G.*, 23:S343, 2006.

[24] C. Canuto et al. *Spectral Methods in Fluid Dynamics*. Springer-Verlag, 1988.

[25] N. Chamel and P. Haensel. Physics of neutron star crusts. *Living Reviews in Relativity*, 2008. http://www.livingreviews.org/lrr-2008-10.

[26] S. Chandrasekhar. Axisymmetric magnetic fields and fluid motions. *Ap. J.*, 124:232–243, 1956.

[27] S. Chandrasekhar. *An introduction to the study of stellar structure*. Dover Publications, 1958.

[28] S. Chandrasekhar. Solutions of two problems in the theory of gravitational radiation. *Phys. Rev. Lett.*, 24:611–615, 1970.

[29] S. Chandrasekhar and E. Fermi. Magnetic fields in spiral arms. *Ap. J.*, 118:113–115, 1953.

[30] S. Chandrasekhar and K.H. Prendergast. The equilibrium of magnetic stars. *Proc. Natl. Acad. Sci.*, 42:5–9, 1956.

[31] S. Chandrasekhar and L. Woltjer. On force-free magnetic fields. *Proc. Nat. Ac. Sci.*, 44(4):285–289, 1956.

[32] U.R. Christensen et al. A numerical dynamo benchmark. *Phys. Earth Planet. Inter.*, 128:25–34, 2001.

[33] J.W. Cooley and O.W. Tukey. An algorithm for the machine calculation of complex Fourier series. *Math. Comput.*, 19:297–301, 1965.

[34] M. Duez et al. Collapse of magnetized hypermassive neutron stars in general relativity. *Phys. Rev. Lett.*, 96, 2006.

[35] R.C. Duncan and C. Thompson. Formation of very strongly magnetized neutron stars - implications for gamma-ray bursts. *Ap. J.*, 392:L9–L13, 1992.

[36] V. Ferrari et al. Relativistic models of magnetars: the twisted torus magnetic field configuration. *Mon. Not. R. Astron. Soc.*, 397:913–924, 2009.

[37] J.L. Friedman and S.M. Morsink. Axial instability of rotating relativistic stars. *Ap. J.*, 502:714–720, 1998.

[38] J.L. Friedman and B.F. Schutz. Secular instability of rotating Newtonian stars. *Ap. J.*, 222:281–296, 1978.

[39] C.L. Fryer and K.C.B. New. Gravitational waves from gravitational collapse. *Living Reviews in Relativity*, 6(2), 2003. http://www.livingreviews.org/lrr-2003-2.

[40] U. Geppert and J.A. Pons. Magnetic field dissipation in neutron star crusts: from magnetars to isolated neutron stars. *Astron. Astrophys.*, 470:303–315, 2007.

[41] U. Geppert and H.J. Wiebicke. Amplification of neutron star magnetic fields by thermoelectric effects I. general formalism. *Astron. Astrophys.*, 87:217–228, 1991.

[42] U.H. Gerlach and U.K. Sengupta. Gauge-invariant perturbations on most general spherically symmetric space-times. *Phys. Rev. D*, 19:2268–2272, 1979.

[43] P. Goldreich and W.H. Julian. Pulsar electrodynamics. *Ap. J.*, 157, 1969.

[44] H. Grad and H. Rubin. Hydromagnetic equilibria and force-free fields. *Proc. 2nd Intern. Conf. on Peaceful Uses of Atomic Energy (U.N.)*, 31:190, 1958.

[45] P. Grandclément and J. Novak. Spectral methods for numerical relativity. *Living Reviews in Relativity*, 12(1), 2009. http://www.livingreviews.org/lrr-2009-1.

[46] C. Gundlach and J.M. Martín-García. Gauge-invariant and coordinate-independent perturbations of stellar collapse: the interior. *Phys. Rev. D*, 61:084024, 2000.

[47] C. Gundlach, J.M. Martín-García, and D. Garfinkle. Summation by parts methods for spherical harmonic decomposition of the wave equation in arbitrary dimensions. *In preparation*, 2010.

[48] B. Gustaffsson, H.O. Kreiss, and J. Oliger. *Time Dependent Problems and Difference Methods*. New York Wiley, 1955.

[49] I. Hachisu. A versatile method for obtaining structures of rapidly rotating stars. *Ap. J. Supplement Series*, 61:461–499, Nov. 1986.

[50] J. Hansson and F. Sandin. Preon stars: a new class of cosmic compact objects. *Phys. Lett. B*, 616:1–7, 2004.

[51] B. Haskell et al. Are neutron stars with crystalline color-superconducting cores relevant for the LIGO experiment? *Phys. Rev. Lett.*, 99:231101, 2007.

[52] J.W. Hessels et al. A radio pulsar spinning at 716 Hz. *Science*, 311(5769):1901–1904, 2006.

[53] W. Ho and C. Heinke. A neutron star with a carbon atmosphere in the Cassiopeia A supernova remnant. *Nature*, 462:71–73, 2009.

[54] M. Hoffberg et al. Anisotropic superfluidity in neutron star matter. *Phys. Rev. Lett.*, 24:775–777, 1970.

[55] M.A. Ivanov and G.A. Shulman. Photodissociation of iron nuclei during the collapse of a magnetic star. *Astron. Zh.*, 67:326–333, 1990.

[56] D.J. Ivers and C.G. Philips. A vector spherical harmonic spectral code for linearised magnetohydrodynamics. *ANZIAM J.*, 44:C423–C442, 2003.

[57] N. Iwamoto. Quark beta decay and the cooling of neutron stars. *Phys. Rev. Lett.*, 44:1637–1640, 1980.

[58] F. John. Blow-up of solutions of nonlinear wave equations in three space dimensions. *Manuscripta Math*, 28:235–268, 1979.

[59] S. Lander and D.I. Jones. Magnetic fields in axisymmetric neutron stars. *Mon. Not. R. Astron. Soc.*, 395:2162–2176, 2009.

[60] S.K. Lander and D.I Jones. Instabilities in neutron stars with toroidal magnetic elds. *http://arxiv.org/abs/1009.2453*, 2010.

[61] S.K. Lander, D.I. Jones, and A. Passamonti. Oscillations of rotating magnetised neutron stars with purely toroidal magnetic fields. *Mon. Not. R. Astron. Soc.*, 405:318–328, 2010.

[62] Y. Levin. Qpos during magnetar flares are not driven by mechanical normal modes of the crust. *Mon. Not. R. Astron. Soc.*, 368:L35–L38, 2006.

[63] L. Lindblom and B.J. Owen. Effect of hyperon bulk viscosity on neutron-star r-modes. 65:063006, 2002.

[64] B. Link et al. Pulsar glitches as probes of neutron star interiors. *Nature*, 359:616–618, 1992.

[65] Keith H. Lockitch and John L. Friedman. Where are the r-mode s of isentropic stars? *Ap. J.*, 521:764–788, 1999.

[66] R. Moenchmeyer et al. Gravitational waves from the collapse of rotating stellar cores. *Astron. Astrophys.*, 246:417–440, 1991.

[67] D.M. Palmer et al. A giant gamma-ray flare from the magnetar SGR 1806-20. *Nature*, 434:1107–1109, 2005.

[68] P. Papaloizou and J.E. Pringle. Non-radial oscillations of rotating stars and their relevance to the short-period oscillations of cataclysmic variables. *Mon. Not. R. astr. Soc.*, 182:423–442, 1978.

[69] E.N. Parker. Hydromagnetic dynamo models. *Ap. J.*, 122:293, 1955.

[70] A. Passamonti et al. Oscillations of rapidly rotating stratified neutron stars. *Mon. Not. R. Astron. Soc.*, 396:951–963, 2009.

[71] D. Pines and M. Alpar. Superfluidity in neutron stars. *Nature*, 316:27–32, 1985.

[72] J.A. Pons et al. Evolution of proto-neutron stars. *Ap. J.*, 512:780–804, 1999.

[73] A. Reisenegger. Chemical equilibrium and stable stratification of a multicomponent fluid: Thermodynamics and application to neutron stars. *Ap. J.*, 550:860–862, 2000.

[74] A. Reisenegger. Stable magnetic equilibria and their evolution in the upper main sequence, white dwarfs, and neutron stars. *Astron. Astrophys.*, 499:557–566, 2009.

[75] M. Rieutord. Linear theory of rotating fluids using spherical harmonics. *Geophys. Astrophys. Fluid Dynamics*, 39:163–182, 1987.

[76] P.H. Roberts. The equilibrium of magnetic stars. *Ap. J.*, 122:508–512, 1955.

[77] H. Saio. R-mode oscillations in uniformly rotating stars. *Ap. J.*, 256:717–735, 1982.

[78] S.J. Schwartz et al. The gamma-ray giant flare from SGR 1806-20: evidence of crustal cracking via initial timescales. *Ap. J.*, 627:129–132, 2005.

[79] S. Shapiro. Differential rotation in neutron stars: magnetic braking and viscous damping. *Ap. J.*, 544:397–408, 2000.

[80] S.L. Shapiro and S.A. Teukolsky. *Black Holes, White Dwarfs, and Neutron Stars*. John Wiley & Sons, 1983.

[81] H.C. Spruit. Differential rotation and magnetic fields in stellar interiors. *Astron. Astrophys.*, 349:189–202, 1999.

[82] B.C. Stephens et al. Collapse and black hole formation in magnetized, differentially rotating neutron stars. *C.Q.G.*, 24:S207–S219, 2007.

[83] R. Stoeckly. Polytropic models with fast, non-uniform rotation. *Ap. J.*, 140:552, 1965.

[84] J-L. Tassoul. *Stellar rotation*. Cambridge University Press, 2000.

[85] T.M. Tauris et al. Discovery of psr j0108-1431: The closest known neutron star? *Ap. J.*, 428:L53–L55, 1995.

[86] R.J. Tayler. Hydromagnetic instabilities of an ideally conducting fluid. *Proc. Phys. Soc. B*, 70:31–48, 1957.

[87] R.J. Tayler. The adiabatic stability of stars containing magnetic fields - I - toroidal fields. *Mon. Not. R. Astron. Soc.*, 161:365–380, 1973.

[88] R.J. Tayler. The adiabatic stability of stars containing magnetic fields - IV - mixed poloidal and toroidal fields. *Mon. Not. R. Astron. Soc.*, 191:151–163, 1981.

[89] R.J. Tayler and P. Markey. The adiabatic stability of stars containing magnetic fields - II - poloidal fields. *Mon. Not. R. Astron. Soc.*, 163:77–91, 1973.

[90] Y. Tomimura and Y. Eriguchi. A new numerical scheme for structures of rotating magnetic stars. *Mon. Not. R. Astron. Soc.*, 359:1117–1130, 2005.

[91] A.L Watts and T.E. Strohmayer. High frequency oscillations during magnetar ares. *Adv. Space Res.*, 40:1446, 2007.

[92] E.W. Weisstein. Clebsch-Gordan coefficients. http://mathworld.wolfram.com/Clebsch-GordanCoefficient.html.

[93] E.W. Weisstein. Wigner 3j-symbol. http://mathworld.wolfram.com/Wigner3j-Symbol.html.